UNIVERSIDAD DE CANTABRIA

PROGRAMA DE DOCTORADO EN
ciencia y tecnología

TESIS DOCTORAL

UNA VISIÓN MULTIFRECUENCIA DE NÚCLEOS DE GALAXIAS ACTIVAS

PH.D. THESIS

A MULTIFREQUENCY VIEW OF ACTIVE GALACTIC NUCLEI

Realizada por:
Ignacio Ordovás Pascual

Dirigida por:
Dra. Silvia Mateos Ibáñez
Prof. Francisco Jesús Carrera Troyano

Escuela de Doctorado de la Universidad de Cantabria

Santander 2019

Declaración de Autoría

Silvia Mateos Ibáñez, Doctora en Ciencias Físicas y Profesora Contratada Doctora de la Universidad de Cantabria,

y

Francisco Jesús Carrera Troyano, Doctor en Ciencias Físicas y Catedrático de la Universidad de Cantabria,

CERTIFICAN que la presente memoria

Una visión multifrecuencia de Núcleos de Galaxias Activas

ha sido realizada por **Ignacio Ordovás Pascual** bajo nuestra dirección.
Consideramos que esta memoria contiene aportaciones suficientes para construir la tesis Doctoral del interesado.

En Santander, a 30 de Octubre de 2019

Silvia Mateos Ibáñez

Francisco Jesús Carrera Troyano

A Aurelia, la maestra que apuntó mis ojos al cielo…
A Aurelia, mi abuela…

Agradecimientos

Aquí se acaba una etapa de un camino que empecé a recorrer hace tiempo al introducirme en la astrofísica, tras el paso por múltiples lugares. El doctorado ha supuesto, sin lugar a dudas, una inolvidable etapa de desafío intelectual y emocional en la que, a parte del desarrollo de un tema de investigación, me ha supuesto crecer tanto en la parte profesional como en la personal. Y ya llegados al final del doctorado, es el momento para mirar atrás y dar reconocer a todos aquellos que, de forma activa o pasiva, cerca o lejos de mí, han sido apoyos para que esta tesis haya podido completarse con éxito.

En primer lugar agradezco a mis codirectores Silvia Mateos y Francisco Carrera su mentoría y su dedicado apoyo con este proyecto, pues gracias a su guía y sus útiles consejos han hecho posible que lleve a cabo esta investigación. A Silvia tengo que agradecerle su ayuda para exprimir toda la información que ha sido posible de su muestreo de AGN para poder acabar con un estudio realmente interesante. De ella me quedo con su meticulosidad en el trabajo diario y no dar por terminado nada hasta que tenemos por seguro que tenemos un trabajo "a prueba de referees". Agradezco también la oportunidad que me dió para poder volver unos días al Gran Telescopio Canarias y poder disfrutar de La Palma otra vez. De Francisco me llevo su paciencia en el análisis estadístico de todos los datos que se nos ponen por delante y su puntillosidad hasta no dejar ningún cabo suelto. Con él y sus toques de humor y frikismo, ha sido más sobrellevable esta tesis.

Como agradecimiento institucional, reconocer al Ministerio de Economía que convocó las ayudas para la formación de doctores con la que accedí al contrato predoctoral, y a la Universidad de Cantabria y su Escuela de Doctorado, en la cual he desarrollado la presente tesis.

A lo largo de la tesis tuve también la oportunidad de ser ayudado lejos de mi casa. Durante las estancias en el Observatorio de Brera en Milán con Alessandro, Paola, Roberto, Alberto y Lucia, y más tarde en el Observatorio Nacional de Atenas con Ioannis, Amalia, Georgios y Thanassis, pude disfrutar del trato familiar y el interés por el trabajo que estaba haciendo. *Grazie per tutti* y *ευχαριστώ πολύ* por vuestra mentoría, colaboración y por hacerme sentir escuchado en el trabajo como uno más de vuestro equipo. Amalia se incorporó más tarde a nuestro grupo. Además de brindarme amistad, también contribuyó con el tratamiento de espectros de rayos X de forma determinante. Sin su ayuda la investigación que hemos desarrollado estos años habría sido muy diferente.

Al llegar a Santander me encontré con un grupo de compañeros que trabajaban con sus proyectos y me acogieron como su amigo. He disfrutado mucho de la compañía de Anuar, Judit y Diego Tuccillo, mis compañeros de despacho y también estudiantes de doctorado, con los que espero seguir en contacto tras mi estancia aquí. Más tarde se incorporó un viejo conocido de Tenerife, Ismael, con quien he tenido interesantes discusiones de trabajo, como de quedadas. Por último, mucha suerte a Lorenzo que se ha unido recientemente al grupo de AGN, y que nos ha ayudado también con su trabajo.

Agradezco también al grupo de rayos-X del IFCA en el que he estado estos años. Gracias a Almudena, Antonio, Ángel, Bea, Esther, Maite, Nuria, Pilu, Silvia Martinez y Xavier (además de los mencionados anteriormente) por la compañía y por haber hecho mejorar mi cocina con estos "Jueves Gastronómicos". Por este grupo también me he introducido a la divulgación científica.

La compañía de los amigos que he conocido en Santander ha sido una parte muy importante para las distracciones, lo cual hay que agradecer en especial, además de a mis compañeros de doctorado y postdocs que ya he nombrado, a David, Rosa, Belén, Diego Herranz, Alberto, Luis y tantos otros compañeros del IFCA con los que hemos ido a incontables miércoles de cine, cenas, roleado y frikeado en general. También a todos aquellos que he conocido fuera del mundo académico en Santander, compañeros de piso y demás, que me han acompañado y soportado en mi estancia. Además, "más allá del muro", siempre han estado mis amigos en otras partes de España y del mundo, pues entre mis Alucheros y otros madrileños, gentes de Canarias, alustantinos y otras regiones, y también personas que a lo largo de estos años he conocido por todo el globo me han apoyado con su amistad. Por supuesto, también agradezco a mis padres, abuelos, tíos, primos y demás coincidencias variopintas de ADN su soporte a las duras y a las maduras.

Por último, me gustaría mencionar a una serie de personas que, a lo largo de mi vida, han sido determinantes en su momento para que tomara este camino. Así, me gustaría agradecer a Jorge Sánchez por su mentoría en el el trabajo de fin de máster, que además me introdujo de lleno en la investigación profesional y con quien publiqué mi primer artículo. Quería también nombrar a Eduardo García y Félix Grijalbo, profesores en el instituto y en el colegio respectivamente, con los que he crecido y me han marcado como persona. Por último, pero más importante personalmente para mi, agradecer a alguien que me enseñó por primera vez los nombres de los planetas y con ello empezó mi curiosidad por el cosmos. Ese alguien es mi abuela Aurelia, culpable en primera instancia de que yo esté hoy aquí.

Resumen de la tesis en castellano

Objetivos de la Investigación

Los Núcleos de Galaxias Activas (AGN en inglés) presentan emisión a lo largo de todo el espectro electromagnético caracterizada por una luminosidad muy alta y persistente, distribución espectral de energías (SED) no térmica y variabilidad en escalas de tiempo que van de años a minutos, indicando estas últimas que la emisión se produce en regiones muy compactas. Estas características indican que el origen de esta emisión es debido a la acreción de material a un agujero negro supermasivo (SMBH) con masa en torno a 10^{6-9} masas solares localizado en el núcleo de la galaxia activa. Principalmente, los AGN en el UV/óptico se dividen en fuentes de tipo-1, aquellos con líneas de emisión anchas (con anchura a media altura FWHM > 1500 km s^{-1}), y objetos de tipo-2, sin presencia de las mencionadas líneas de emisión anchas. Estas diferencias se explican con el conocido como Modelo Unificado de AGN que, en su versión más simple, interpreta estas diferencias como efectos de orientación. La forma de explicarlo es con la existencia de una estructura toroidal de polvo y gas que rodea el SMBH: el toro. Según la inclinación del plano ecuatorial del toro con respecto a nuestra línea de visión, si la emisión de las regiones más internas del AGN (como la región de líneas anchas; BLR) intercepta el toro, estará oscurecida y por tanto se clasifica como tipo-2. En el caso de que la línea de visión no intercepte el toro, la emisión del AGN no estará oscurecida y se clasifica como tipo-1. Este modelo es capaz de describir las propiedades observadas para la mayoría de AGN. Sin embargo, existe un porcentaje importante de fuentes cuyas propiedades discrepan en diferentes frecuencias del espectro electromagnético, y por tanto no pueden ser justificadas con la versión más simple del Modelo Unificado basado en orientación.

En esta tesis tratamos de estudiar la relación entre la extinción en el UV/óptico y la absorción medida en rayos X de los AGN de tipo-1. La caracterización del oscurecimiento de la emisión nuclear es un aspecto importante en el estudio de AGN ya que es necesaria para poder recuperar su emisión intrínseca y propiedades derivadas de ella. Además nos permite comprender las propiedades del medio que rodea el SMBH. A día de hoy sigue habiendo muchas incógnitas acerca del oscurecimiento en AGN, y por tanto de la validez de los modelos basados en orientación del toro. Son necesarios estudios con muestras que introduzcan los menores sesgos posibles.

Planteamiento y metodología

En esta tesis doctoral hemos realizado un estudio centrado en AGN de tipo-1, provenientes del muestreo de AGN Bright Ultra-hard XMM-Newton Survey (BUXS). Se trata de una muestra de 255 AGN seleccionada en la banda de los rayos X duros (4.5 − 10 keV). Esta selección permite tener una muestra de AGN de tipo-1 casi completa para AGN no oscurecidos y con absorciones en rayos X bajas, perdiendo aquellos muy oscurecidos con densidades de columna de hidrógeno $N_{\rm H} \gtrsim 10^{23}$ cm^{-2} (nivel de absorción en rayos X a lo largo de la línea de visión). Como en esta tesis doctoral trabajamos sólamente con AGN de tipo-1, la selección en rayos X duros no debería introducir ningún sesgo importante en la muestra porque no se espera que objetos con estas $N_{\rm H}$ muestren líneas anchas en el UV/óptico. Disponemos de datos en rayos X de XMM-Newton de buena calidad para todos los objetos, así como de espectros en el UV/óptico del muestreo público Sloan Digital Sky survey (SDSS) y observaciones dedicadas de diversos telescopios terrestres para sus contrapartidas ópticas. La información disponible de los espectros UV/ópticos es muy buena, ya que la identificación espectroscópica de las fuentes de BUXS es casi completa (>99 % de fuentes identificadas, con 172 tipos-1 y 80 tipos-2).

Hemos planteado dos estudios diferentes. En primer lugar tenemos dos AGN con clasificación UV/óptica indicativa de extinción óptica elevada, pero sus espectros en rayos X indican que en la línea de visión hay baja absorción. Según la versión simple del Modelo Unificado de AGN, los objetos con extinción óptica elevada deberían tener también una absorción en rayos X elevada, por lo que deben explicarse de alguna forma diferente. Para determinar el origen de la mencionada discrepancia en estos dos objetos realizamos un estudio detallado separando la contribución del AGN y la galaxia anfitriona, obteniendo así la extinción óptica e información sobre las líneas de emisión anchas y estrechas en longitudes de onda UV/óptica. Usamos espectros de VLT/X-Shooter con alta resolución espectral y con cobertura desde el ultravioleta hasta en infrarrojo cercano, además de espectros de alta calidad en rayos X obtenidos con el observatorio XMM-Newton. Hemos investigado diferentes escenarios para descubrir el origen de la diferencia entre las clasificaciones ópticas y en rayos X.

En el segundo estudio, hemos llevado a cabo un análisis estadístico de una muestra representativa de AGN de tipo-1 (132 AGN). Para esta muestra hemos excluido todos los AGN con luminosidad intrínseca en la banda 2 − 10 keV con $\log(L_{2-10\ \rm keV}/\rm erg\ s^{-1}) < 42$, para aumentar el contraste entre el AGN y la galaxia anfitriona. Además, analizamos únicamente los objetos con $z < 1$, para que los ajustes para obtener $N_{\rm H}$ den resultados lo suficientemente robustos. Esto es porque con z creciente perdemos cobertura de la emisión en rayos X a más baja energía, que es donde mejor permite ajustar el $N_{\rm H}$.

Para el estudio científico que hemos llevado a cabo, analizamos los espectros ópticos y de rayos X para obtener la extinción óptica ($A_{\rm V}$) y la absorción en rayos X ($N_{\rm H}$). Además, hemos obtenido parámetros como la luminosidad intrínseca de los AGN y de determinadas líneas de emisión y de la dispersión de velocidades de la BLR. En el caso de los espectros ópticos, tras corregir de la extinción Galáctica,

hemos separado la emisión de la galaxia anfitriona y la del AGN. Los modelos usados para la emisión de la galaxia anfitriona provienen de ajustes de SEDs. A la emisión de AGN se le aplica el modelo de extinción de la Pequeña Nube de Magallanes de Gordon *et al.* (2003), que es más apropiado para reproducir la extinción óptica de la emisión nuclear del AGN. Así podemos aislar la emisión nuclear y obtener la extinción óptica. Ajustando las regiones en longitud de onda de líneas de emisión usando una ley de potencias además de perfiles gaussianos, nos permite obtener el flujo y la anchura en velocidad de las líneas de emisión estrechas y anchas de los AGN.

En cuanto al tratamiento de los espectros en rayos X modelamos su emisión ajustando diferentes contribuciones (continuo de ley de potencias, absorción por gas, emisión de gas caliente, etc.), derivando la absorción en rayos X y la luminosidad intrínseca de la fuente. Para los espectros de rayos X de los dos AGN con clasificaciones discordantes, los ajustes han sido realizados en esta tesis doctoral, mientras que los espectros del segundo trabajo han sido ajustados por miembros del grupo y en esta tesis se ha trabajado con los resultados de los ajustes. Agrupando todas las observaciones de XMM-Newton disponibles para cada objeto, nos permite determinar la absorción en rayos X con una precisión mayor, ya que somos capaces de medir el $N_{\rm H}$ hasta $\log(N_{\rm H}/{\rm cm}^{-2}) = 19$, frente a $\log(N_{\rm H}/{\rm cm}^{-2}) = 20$, que es el mínimo $N_{\rm H}$ que se suele dar en trabajos similares anteriores cuando no se detecta absorción. Este hecho es crítico para nuestro estudio ya que los AGN tipo-1 generalmente presentan poca absorción en rayos X.

Para el estudio estadístico de AGN de tipo-1 hemos obtenido las distribuciones individuales de probabilidad de $A_{\rm V}$ y $N_{\rm H}$ para cada objeto, siendo el primer estudio que utiliza estas distribuciones para el análisis del oscurecimiento de los AGN. Ésto, sumado a la buena calidad de los datos de los que disponemos nos permite realizar una investigación mucho más completa que en estudios anteriores. Con los parámetros que se han obtenido de los espectros en cada frecuencia, podemos conocer mejor la relación entre la clasificación de los AGN y su oscurecimiento, y podemos dar posibles explicaciones para aquellos AGN cuya clasificación óptica y en rayos X no coincide. Además comparamos la extinción en el óptico y la absorción en rayos X para conocer cómo de relacionadas están estas dos cantidades en una muestra completa.

Aportaciones originales

Los dos AGN con clasificación discordante muestran un origen diferente de la discrepancia. En uno de los casos, la explicación más probable es que el medio que oscurece la emisión nuclear tiene más polvo que gas comparado con un medio con una composición similar a la Galáctica. Ésto provoca que observemos más extinción en el UV/óptico que en rayos X. En cuanto al segundo objeto, el cociente gas/polvo es compatible con una composición relativa como la Galáctica. La discrepancia se debe a efectos de dilución de la emisión nuclear por la emisión estelar, ya que la relación entre las masas de la galaxia anfitriona y del agujero negro es muy superior a lo esperado comparado con las relaciones

típicas en la literatura. Hemos descartado en ambos casos que sean AGN Compton-thick ($N_{\rm H} > 10^{24}$ cm^{-2}). También hemos descartado que el flujo de las líneas anchas sea intrínsecamente débil comparado con el rango de cocientes típicos de los flujos de líneas anchas y estrechas que suelen presentar los AGN.

El análisis de la muestra representativa de tipos-1 ha permitido encontrar que la fracción de objetos extinguidos en el óptico y absorbidos en rayos X es significativamente mayor en la submuestra de la que disponemos de clasificación completa (aquellos con $z < 0.2$) que en la muestra total de tipos-1 ($40 - 50$ % frente a 20 %). La fracción de objetos de la muestra completa que son tipos-1 absorbidos pero no enrojecidos y viceversa es de un 32 %, que es un factor $\sim$2 más elevado que lo que se encuentra en la literatura. Ésto indica que, sin trabajar con muestras con clasificaciones completas, los resultados extraídos están sesgados hacia objetos con menor oscurecimiento. Conforme aumenta z, perdemos objetos oscurecidos que son clasificados como tipos-2, ya que sus líneas de emisión anchas quedan fuera de la cobertura del espectro UV/óptico.

En nuestro estudio hemos obtenido una relación creciente entre subtipo de AGN (de 1.0 a 1.9) y el oscurecimiento, tanto en el rango óptico como en rayos X. En el caso de la extinción óptica, $A_{\rm V}$ crece gradualmente con el subtipo, mientras que la absorción en rayos X crece abruptamente desde los tipos-1.0/2/5 a los tipos-1.8/9. Aunque pueda haber escenarios diferentes que puedan influir en el cociente relativo entre el flujo de líneas anchas y estrechas, algo que da lugar a la clasificación óptica, en nuestro análisis hemos obtenido que la extinción es la principal contribución a la clasificación de AGN. Concluimos finalmente, que tanto $A_{\rm V}$ como $N_{\rm H}$ tienen una relación directa con el subtipo de AGN.

Hemos analizado la fiabilidad de los métodos que estiman la extinción óptica basados en los cocientes de los flujos de las líneas anchas de H_α y H_β (Balmer decrement) con nuestras estimaciones basadas en el análisis del continuo UV/óptico emitido por el disco de acreción. Si bien los cocientes intrínsecos medios que obtenemos se ajustan a los usados en la literatura, las estimaciones de $A_{\rm V}$ no están muy correlacionadas. Estos resultados están en concordancia con estudios que sostienen que el cociente intrínseco de los flujos de las líneas anchas de H_α y H_β puede variar de unos objetos a otros dependiendo de las condiciones físicas del material donde se emiten las líneas. Por tanto, el análisis realizado en esta tesis indica que las estimaciones de $A_{\rm V}$ basadas en el Balmer decrement deben ser tomadas con precaución.

En cuanto a la relación $A_{\rm V}$-$N_{\rm H}$, que da cuenta de la cantidad relativa de polvo y gas, los resultados obtenidos muestran que no hay una relación clara entre la extinción óptica y la absorción en rayos X, por lo que no podemos extrapolar directamente un nivel determinado de absorción en rayos X a partir del oscurecimiento en el óptico y viceversa. Para aproximadamente la mitad de la muestra, aquellos con $A_{\rm V}$ y $N_{\rm H}$ más bajos, el cociente $A_{\rm V}/N_{\rm H}$ está sesgado debido a errores sistemáticos. Ésto implica que para una parte importante de la muestra no es posible estimar el cociente entre polvo y gas, aun teniendo datos de gran calidad. En estudios previos, el cociente $A_{\rm V}/N_{\rm H}$ obtenido muestra

valores compatibles o por debajo del cociente Galáctico, mientras que sólo una minoría ($3-9$ %) tiene un exceso de polvo con respecto al gas comparado con la relación Galáctica. Con nuestro análisis riguroso y conservador basado en las distribuciones de probabilidad de $A_{\rm V}$ y $N_{\rm H}$, encontramos un mínimo de un 47 % de objetos con un cociente de polvo/gas más alto que el Galáctico para la muestra completa. Si usamos únicamente los tipos-1.0/2/5, como hacen otros trabajos, esta fracción mínima es de un 32 %, que sigue siendo más alta que la de estudios anteriores. Esta elevada fracción de objetos con $A_{\rm V}/N_{\rm H}$ más altos que el cociente Galáctico comparada con estudios anteriores puede ser debida a la clasificación equivocada de tipos-1 como tipos-2, por métodos de selección que sesgan la muestra en contra de AGN con extinción elevada, o porque este análisis no ha sido formalmente realizado por no ser el objetivo de estos trabajos.

Conclusiones

En esta tesis hemos demostrado que las discrepancias entre las clasificaciones ópticas y en rayos X pueden deberse a diversos factores. Por esta razón, aquellos AGN con clasificación óptica que indica elevada extinción en el óptico pero cuyo espectro en rayos X presenta poca absorción en rayos X no pueden considerarse una familia física de objetos, al tener propiedades distintas. En el estudio detallado de las dos fuentes encontramos dos explicaciones completamente diferentes al hecho de que estos AGN presenten un espectro en rayos X poco o nada absorbido mientras que su clasificación UV/óptico indica elevada extinción.

En la muestra de AGN de tipo-1 de que hemos estudiado de forma estadística, hemos obtenido que las muestras de tipos-1 sin cobertura espectral de la región de $\rm H_{\alpha}$ para todos los AGN son incompletas para los tipos-1.8/9. Por tanto estas muestras presentan sesgos en contra de $N_{\rm H}$ y $A_{\rm V}$ altos. Hemos demostrado que el cociente intrínseco de los flujos de las líneas de $\rm H_{\alpha}$ y $\rm H_{\beta}$ anchas es dispar, afectando por tanto a las estimaciones de $A_{\rm V}$ basadas en el Balmer decrement. Hemos comprobado finalmente que la cantidad de absorción en rayos X y el oscurecimiento óptico no presentan una relación robusta, favoreciendo modelos que asumen que la absorción en rayos X y la extinción en el óptico se producen mayoritariamente en estructuras diferentes, o alternativamente que los cocientes $A_{\rm V}/N_{\rm H}$ pueden ser muy distintos de fuente a fuente.

Futuras líneas de investigación

Los resultados de esta tesis indican que la extensión de la espectroscopía hasta el infrarrojo cercano para poder detectar posibles objetos oscurecidos que por cobertura del espectro no detectamos para $z > 0.2$ permitiría determinar cuántos objetos oscurecidos se pierden a altas luminosidades y mejorar la estadística de los resultados obtenidos en esta tesis doctoral. Además permitiría analizar de forma

robusta los efectos con la luminosidad intrínseca del AGN. Extender la muestra a $z > 0.2$, al sacar espectros en el UV/óptico con rendija estrecha para aquellos de los que sólo disponemos de espectro UV/óptico con fibra, también permitiría identificar objetos de tipo-1 clasificados tipo-2 debido a la dilución de la emisión nuclear por la emisión estelar. De entre los 60 tipos-2 en el rango $z = 0.05 - 1$ y con $\log(L_{2-10\ \mathrm{keV}}/\mathrm{erg\ s^{-1}}) > 42$ identificados en BUXS, 12 no están absorbidos en rayos X y es posible que sean en realidad tipos-1 afectados por esta dilución. Para $z < 0.2$ el impacto no es importante, ya que sólamente 3 (menos de un 8 %) son tipos-2 no absorbidos. Por último, con los datos obtenidos en esta tesis y futuras extensiones, se podría obtener la tasa de acreción del SMBH y ver su dependencia con la subclasificación de AGN.

UNIVERSIDAD DE CANTABRIA

PROGRAMA DE DOCTORADO EN
ciencia y tecnología

TESIS DOCTORAL

UNA VISIÓN MULTIFRECUENCIA DE NÚCLEOS DE GALAXIAS ACTIVAS

PH.D. THESIS

A MULTIFREQUENCY VIEW OF ACTIVE GALACTIC NUCLEI

Dissertation by:
Ignacio Ordovás Pascual

Supervised by:
Dr. Silvia Mateos Ibáñez
Prof. Francisco Jesús Carrera Troyano

Escuela de Doctorado de la Universidad de Cantabria

Santander 2019

"Mathematics is a suspicious activity.
All those hypotenuse drawings must be plans for assassination attempts.
Algebra is treacherous code."

Flavia Albia
(Lindsey Davis, The Ides of April)

"Break out the champagne if we won't be seein' tomorrow.
Let's get on with the shitshow."

Amanda Shires

Summary

Objectives of the investigation

Active Galactic Nuclei (AGN) present emission through the entire electromagnetic spectrum characterized by a very high and persistent luminosity, a non-thermal Spectral Energy Distributions (SED) and variability in time scales from years to minutes, the latter indicating that this emission takes place in very compact regions. These characteristics indicate that the origin of this emission is due to the accretion of material to a supermassive black hole (SMBH) whose mass ranges between 10^{6-9} solar masses and is located in the nucleus of the active galaxy. Mainly, in the UV/optical, AGN are divided into type-1 sources, that have broad emission lines (with full width at half maximum FWHM > 1500 km s^{-1}), and type-2 AGN, with-out detected broad emission lines. These differences are explained with what is known as the Unified Model of AGN. This model, in its simplest version, interprets these differences as orientation effects. The way to explain this is with the existence of a toroidal structure of dust and gas surrounding the SMBH: the torus. Depending on the inclination of the torus equatorial plane with respect to our line-of-sight, if the innermost regions of the AGN (as the Broad Line Region; BLR) intercepts the torus, it is obscured and therefore we classify the AGN as type-2. If the line-of-sight does not intercept the torus, the AGN emission is unobscured and therefore we classify the AGN as type-1. This model is able to explain the observed properties for most AGN. However, there is a significant fraction of sources whose properties are discordant at different frequencies of the electromagnetic spectrum, and therefore cannot be explained with the simplest version of the orientation-based Unified Model.

In this Thesis we aim to study the relationship between the extinction in the UV/optical and the absorption in X-rays of type-1 AGN. The characterization of the obscuration of the nuclear emission is an important aspect in the study of AGN since it is necessary to recover their intrinsic properties. It also allows us to understand the properties of the environment surrounding the SMBH. Today there are still many unresolved questions about obscuration in AGN and hence the validity of torus-based models as well. Studies that use samples as unbiased as possible are needed in order to bring light into this issue.

Planning and methodology

In this Thesis we have conducted a study focusing on type-1 AGN from the Bright Ultra-hard XMM-Newton Survey (BUXS). This is a survey composed by 255 AGN selected in the hard X-rays (4.5 – 10 keV). This selection allows to obtain a sample of type-1 AGN that reduces the strong bias against heavily absorbed AGN with hydrogen column densities of $N_{\rm H} \gtrsim 10^{23}$ cm^{-2} (the $N_{\rm H}$ is indicative of the absorption in X-rays). As in this Thesis we work only with type-1 AGN, the selection in hard X-rays should not introduce significant bias in the sample as objects with these high $N_{\rm H}$ levels are not expected to present broad lines in the UV/optical. We have good quality XMM-Newton X-ray data for this sample, as well as UV/optical spectra from the Sloan Digital Sky Survey (SDSS) public survey and dedicated observations at several ground-based telescopes for their optical counterparts. We have high quality information for the UV/optical spectra, since the spectroscopic identification of the BUXS AGN is almost complete (>99 per cent of identified sources, with 172 type-1 and 80 type-2 AGN).

In this Thesis we conducted two different studies. In the first one we have two type-1.9 AGN, but whose X-ray spectra indicates that in the line-of-sight the absorption is low. According to the simplest version of the Unified Model of AGN, objects with high optical extinction should also have a high X-ray absorption, so they must be explained in some different way. To determine the origin of the mentioned discrepancy in these two objects, we carried out a detailed study dividing the AGN and host galaxy emission, so we could obtain the optical extinction and information about broad and narrow emission lines at UV/optical frequencies. We used VLT/X-Shooter spectra with high spectral resolution and wavelength coverage from the UV to the Near InfraRed. We also have high quality spectra in the X-rays obtained with the XMM-Newton observatory. We have investigated different scenarios to uncover the origin of the discordant optical and X-ray classifications.

In the second work, we have carried out a statistical study of a representative sample of 132 type-1 AGN. For this sample we have excluded all AGN with intrinsic luminosities in the 2 – 10 keV band with $\log(L_{2-10\ \rm keV}/\rm erg\ s^{-1}) < 42$, to increase the contrast between AGN and the host galaxy. In addition, we analyse only objects with $z < 1$, to ensure that the $N_{\rm H}$ is measured with robustness. This is because with increasing z we lose coverage of the X-ray emission at lower energies, which is where it is best to constrain the $N_{\rm H}$.

We analysed the optical and X-ray spectra to obtain the optical extinction ($A_{\rm V}$) and X-ray absorption ($N_{\rm H}$). In addition, we have obtained parameters such as the AGN intrinsic luminosity, the flux of certain emission lines and the gas velocity dispersion in the BLR. In the case of the optical spectra, after correcting from Galactic extinction, we separated the host galaxy starlight and the AGN emission. The models used for the host galaxy emission are selected using SED fits. The extinction model of the Small Magellanic Cloud of Gordon *et al.* (2003) is applied to the AGN emission, which is the most appropriate to reproduce the optical extinction of the nuclear emission of AGN. With this, we can isolate the nuclear emission and obtain the optical extinction. By fitting the wavelength regions with

emission lines using a power law in addition to Gaussian profiles, we obtained the flux and width in velocity of the broad and narrow emission lines of the AGN.

With respect to the analysis of the spectra in X-rays, we model their emission by fitting different contributions (power law continuum, gas absorption, hot gas emission, etc.), obtaining the X-ray absorption and the intrinsic luminosity of the AGN. For the X-ray spectra of the two AGN with discordant classifications, the fits have been made in this Thesis, while the spectra of the second work have been fitted by members of our group, and so in this Thesis we have worked with the models already fitted. Combining all the available XMM-Newton observations for each object allows us to determine the X-ray absorption with great precision, since we are able to measure the $N_{\rm H}$ up to $\log(N_{\rm H}/{\rm cm}^{-2}) = 19$, whereas in previous studies normally set a minimum of $\log(N_{\rm H}/{\rm cm}^{-2}) = 20$ when no absorption is detected. This is critical for our study since type-1 AGN generally present low X-ray absorption.

For the statistical study of type-1 AGN we obtained the individual probability distributions of $A_{\rm V}$ and $N_{\rm H}$ for each object, being the first study that uses these distributions for the analysis of the obscuration in AGN. This, along with the good quality of the available data, allows us to conduct a much more robust investigation than in previous studies. With the obtained parameters from each spectra at each frequency, we can better understand the relationship between the classification of AGN and their obscuration, and hence we can provide possible explanations for those objects whose optical and X-ray classification does not match. We also compared the extinction in the optical and the absorption in the X-rays to explore how these quantities are correlated in a complete sample.

Original contributions

The two AGN with discordant classification show a different origin of the discrepancy. In one case, the most likely explanation is that the medium that obscures the nuclear emission has more dust than gas compared to the Galactic dust-to-gas relation. This causes us to observe more extinction in the UV/optical than in X-rays. As for the second object, the dust-to-gas ratio is compatible with a relative composition such as the Galactic. We found that the discrepancy is due to the effects of dilution of the nuclear emission by stellar emission, since the relationship between the masses of the host galaxy and the black hole is much higher than expected compared to the typical relation in the literature. We have ruled out in both cases that they are AGN Compton-thick. We have also ruled out that the flux of the broad lines is intrinsically weak compared to the typical broad and narrow line fluxes ratios that AGN usually present.

The analysis of the representative sample of type-1 AGN allowed to obtain that the fraction of optically reddened and X-ray absorbed objects is significantly higher than in the sample that we have complete classification (those with $z < 0.2$) that in the full sample of type-1 AGN (40 − 50 per cent versus 20 per cent). The fraction of objects for the complete sample that are absorbed type-1 AGN but are

unreddened and viceversa is 32 per cent, that is ∼2 times higher than the one in the literature. This indicates that, without working with complete samples, the obtained results are biased against highly obscured objects. With increasing z, we lose obscured sources as they are misclassified as type-2 AGN, as their broad emission lines are not covered in their UV/optical spectrum.

In our study we have obtained an increasing relation between subtype of AGN (from type-1.0 to type-1.9) and obscuration, both in the optical range and in X-rays. In the case of optical extinction, A_V gradually rises with the subtype, while the X-ray absorption rises steeply from type-1.0/2/5 to type-1.8/9. Although there may be different scenarios that can contribute to the broad and narrow emission lines relative flux, that defines the optical classification, in our analysis we have obtained that extinction is the main contribution to the subclassification of AGN. We finally conclude that both A_V and N_H have a direct relation with the subtype of AGN.

We have compared the optical extinction estimation methods based on the H_α and H_β broad emission line fluxes (Balmer decrement) with our estimates based on the analysis of the UV/optical continuum emitted by the accretion disk. While the mean intrinsic ratios we obtain are consistent with those used in the literature, the A_V measurements are not very correlated. These results are in agreement with studies that support that the intrinsic broad H_α and H_β emission line flux ratio can vary from one object to another depending on the physical conditions of the material where the lines are emitted. Therefore, the analysis performed in this Thesis indicates that Balmer decrement estimations of A_V should be taken with caution.

As for the A_V-N_H ratio, which accounts for the relative amount of gas and dust, we have found that there is no clear relationship between optical extinction and X-ray absorption, so we cannot directly extrapolate a certain level of absorption in X-rays from the extinction in the optical and vice versa. For approximately half of the sample, those AGN with low A_V and N_H, their A_V/N_H ratio is biased due to systematic errors. This implies that for an important part of the sample it is not possible to estimate the dust-to-gas ratio, even with high quality data. In previous studies the A_V/N_H is found to be compatible or below the Galactic ratio, while only a minority ($3-9$ per cent) has higher amounts of dust with respect to gas compared to the Galactic ratio. In our case we found a minimum of 47 per cent with higher dust-to-gas ratio objects than the Galactic for the complete sample of type-1. If only type-1.0/2/5 AGN are considered, as other studies do, we obtain a minimum of 32 per cent of objects with higher dust-to-gas ratios than the Galactic. This higher fraction of A_V/N_H ratios higher than the Galactic standard compared to previous studies might be due misclassification of type-1 objects, AGN selection methods that miss low reddened sources or because this analysis is not formally performed in these works.

Conclusions

In this thesis we have shown that the discrepancies between the optical and X-ray classifications observed for a significant fraction of AGN may be caused by diverse factors. For this reason, those AGN with an optical classification that indicates high optical extinction but whose X-ray spectrum has low X-ray absorption cannot be considered a physical family of objects. In the detailed study of the two sources we discussed several contributions as high dust-to-gas ratios or dilution of the nuclear emission by stellar emission that can explain AGN to have a low or not absorbed X-ray spectrum and UV/optical classification indicating high extinction.

In the type-1 AGN sample that we studied statistically, we obtained that type-1 samples without H_α spectral coverage for all sources are incomplete for type-1.8/9. This means that these samples are biased against high A_V and high N_H. We have proven than the intrinsic broad H_α and H_β flux ratio is very wide, affecting the Balmer decrement A_V estimations. We have obtained that the amount of X-ray absorption and the optical extinction do not present a clear relationship, favouring models that assume that the bulk of the X-ray absorption is produced in a different structure than the optical extinction, or alternatively that A_V/N_H ratios can be very different from source to source.

Future research lines

The results of this Thesis indicate that the extension of the spectroscopy to the NIR in order to be able to detect obscured objects misclassified as type-2 AGN at $z > 0.2$ would allow to to analyse the effects with the intrinsic luminosity of the AGN. This would also improve the statistics of the results obtained in this Thesis. By extending the sample to $z > 0.2$, as we would obtain narrow slit spectra for those for which we only have fibre spectra, would allow to identify type-1 AGN misclassified as type-2 due to dilution of the nuclear emission by the host stellar emission. Among the 60 type-2 sources in the $z = 0.05 - 1$ range and with $\log(L_{2-10\ \mathrm{keV}}/\mathrm{erg\ s^{-1}}) > 42$ identified in BUXS, 12 are X-ray unabsorbed and might be type-1 AGN affected by this dilution. Lastly, with the data obtained in this Thesis and future extensions, we could compute the mass and accretion rate of the SMBH and investigate its dependence with the classification.

Contents

List of Figures

List of Tables

Chapter 1

Introduction

During the 18th and 19th centuries, it was not clear whether the 'nebulae' seen in the sky were part of our galaxy, or they were 'island-universes' composed of stars (Kant 1755). Since the discovery in 1924 of a Cepheid variable star in M31 (Hubble 1929), it became clear that some of them were extragalactic objects, or more precisely, they were galaxies like the Milky Way. Using spectroscopic analyses, it soon became clear as well that some of the galaxies showed emission lines of highly ionized elements in their nuclei (Seyfert 1943) that cannot be explained just by the emission mechanisms of the stars, and so this emission is originated by a completely different phenomenon. In some of these galaxies, this non stellar radiation completely outshines the galaxy starlight. These objects are called 'Active Galactic Nuclei' (AGN).

Nowadays, it is widely accepted that the origin of this emission is due to supermassive black holes (SMBH) of $>10^{6-9}$ solar masses ($M_{\odot}$) in the centre of the active galaxies. The material that falls into the immense gravitational potential of the SMBH, releases energy in a process called accretion which is the origin of the electromagnetic emission (see Sec. 1.1 for a more detailed explanation). The reasons to accept that SMBH are responsible of this highly energetic phenomena are various. The emission of normal or quiescent galaxies is produced almost entirely by stars, gas and dust, and is mainly constrained between the UltraViolet (UV) and InfraRed (IR) ranges. However, AGN show intense emission across all the electromagnetic spectrum, from gamma rays to radio frequencies. This means that active galaxies present emission in over twenty orders of magnitude in frequency (Padovani *et al.* 2017). The luminosity of AGN range from bolometric luminosities[1] ($L_{\rm bol}$) of 10^{40} erg s^{-1}, lower or comparable to the emission of quiescent galaxies ($L_{\rm bol} < 10^{43}$ erg s^{-1}, Bell and de Jong 2001, Vitale *et al.* 2013), to luminosities of 10^{48} erg s^{-1} (Padovani *et al.* 2017). Depending on the energy band observed, AGN show strong time variability on time-scales from years to minutes (Ulrich, Maraschi, and Urry 1997, Mateos *et al.* 2007, Krumpe *et al.* 2010, García-González *et al.* 2015, Hernández-García *et al.* 2015, LaMassa *et al.* 2015). The shortest time scales of variability, specially in the X-ray

[1]The bolometric luminosity is the total energy emitted across the whole electromagnetic spectrum.

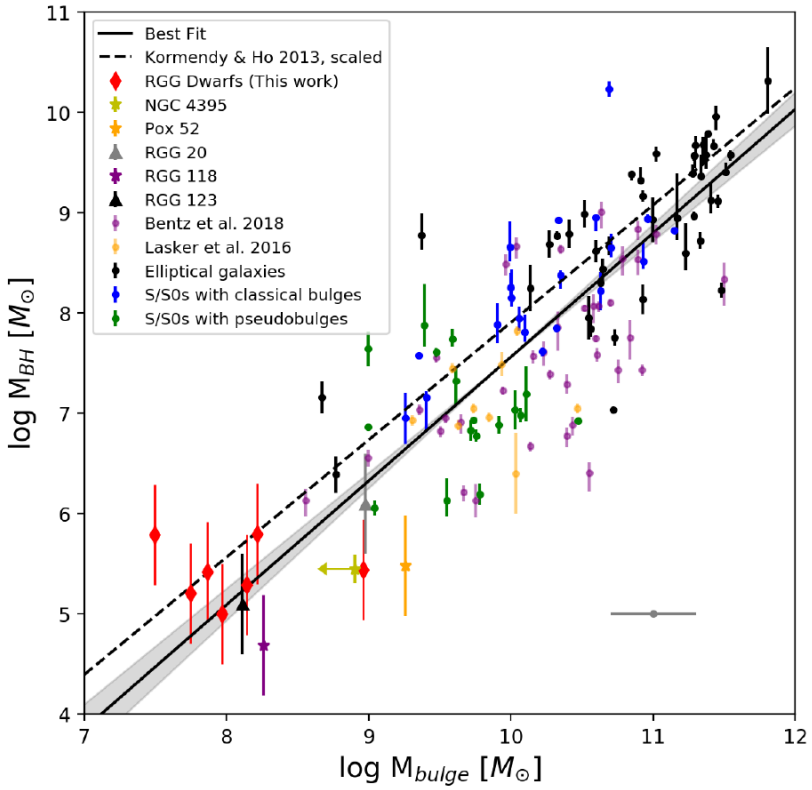

FIGURE 1.1: SMBH mass versus bulge stellar mass of the host galaxy extracted from Schutte, Reines and Greene (2019).

band, leave no doubt that the emission originates in a very compact region of the order of miliparsecs, roughly the size of the Solar System (Padovani *et al.* 2017). Taking together the high luminosity and the compact region where most of the emission originates, AGN are objects with tremendous energy densities, only explainable by accretion onto SMBH in the core of their host galaxies.

There are evidences that almost every massive galaxy harbours a SMBH in its nucleus (Magorrian *et al.* 1998), but as the one in the Milky Way (10^6 $M_\odot$; Ghez *et al.* 2008), not all of them are active. The SMBH mass (M_{BH}) has a tight relation with its host galaxy properties, more precisely with the stellar velocity dispersion, the mass and the luminosity (σ, M_{bulge} and L_{bulge}, respectively; Turner and Miller 2009). The M_{BH}/σ, M_{BH}/M_{bulge}, M_{BH}/L_{host} diagrams (see Fig. 1.1) show evidence that there is a coevolution of the growth of SMBH through the accretion of matter and their hosts through star formation, so AGN could be considered a stage in galactic evolution that can be triggered by accretion or galaxy mergers (Hopkins *et al.* 2008, Hirschmann *et al.* 2010, Kormendy and Ho 2013, Silk, Di Cintio and Dvorkin 2014). A hypothesis to explain the observed relation is that the energy emitted by the AGN affects the material that feeds it and that feeds star formation, as this feedback affects the full galaxy (Fabian 2012). This would mean that the growth of AGN is linked with galaxy evolution (Kormendy and Ho 2013).

As active galaxies are the most luminous persistent objects in the Universe and are long lived as well, they are visible at a large range of distances. The most distant AGN to date is at $z = 7.54$ (Bañados *et*

al. 2018), when the Universe was only about 10 per cent of its present age. This object is one of the visible objects closest in time to the Big Bang. The study of AGN therefore is key to understand the evolution of the cosmos since the Universe was very young.

The Cosmic X-ray Background (CXRB) radiation is believed to be the emission from AGN integrated over Cosmic history (Szokoly *et al.* 2004, Barger *et al.* 2005, Gilli, Comastri, and Hasinger 2007). To reproduce the CXRB it has been demonstrated that the nuclear region of most AGN must be obscured by large amounts of gas and dust (Gilli, Comastri, and Hasinger 2007, Treister, Urry, and Virani 2009, Akylas *et al.* 2012). Thus, revealing the nature of the obscuring material is key to understand the physical properties of AGN.

All of these facts are pieces of evidence for the big importance of the study of AGN. In this Thesis we work on understanding the nuclear environment of the AGN. Moreover, our studies provide relevant observational tests for the so-called Unified Models of AGN (Antonucci 1993, Urry and Padovani 1995, Netzer 2015; see Sec. 1.2). This is an crucial aspect of AGN, as there are some open questions to the date that challenges the Unified Model.

1.1 Physical mechanisms of emission

We pointed out that AGN are detected in a wide range of frequencies. In this section we explain the origin of the AGN emission in each of the available observational windows. In the following section we explain where is this emission originates according to the Unified Model of AGN. In Fig. 1.2 we show the complete Spectral Energy Distribution (SED) of an average AGN.

1. **Radio emission:** it is well described with a power law, $L_\nu \propto \nu^{-\alpha_R}$, indicating a non-thermal origin. Core-dominated sources present flatter spectra than lobe-dominant ones ($\alpha_R \sim 0.5 \pm 0.5$ and $\alpha_R \sim 1.0 \pm 0.5$, respectively; Wilkes 2004). The radio emission in the so-called Radio Loud AGN (see Sec. 1.3) is due to synchrotron emission of electrons moving at relativistic energies through magnetic fields, while in Radio Quiet AGN (see Sec. 1.3) different mechanisms are involved, such as AGN driven winds, low power jets, free-free emission from photoionized gas or by the innermost accretion disc coronal activity (Panessa *et al.* 2019).

2. **IR emission:** in the MIR, its emission range can be approximated by a power law ($L_\nu \propto \nu^{-\alpha}$) of $\alpha \sim 1$ (see Alonso-Herrero *et al.* 2001 and references therein). It is due to thermal emission. The nuclear emission is absorbed and scattered, and it heats the dust located at circumnuclear scales (see Sec. 1.2) that re-emits it at Near InfraRed and Far InfraRed (NIR/FIR) frequencies (Nenkova *et al.* 2008). The resulting emission is known as the IR bump. This bump peaks at 60 μm and falls dramatically, at longer wavelengths. The inflection at the blue side of the bump is produced at ~1 μm. This corresponds to the maximum temperature at which dust can

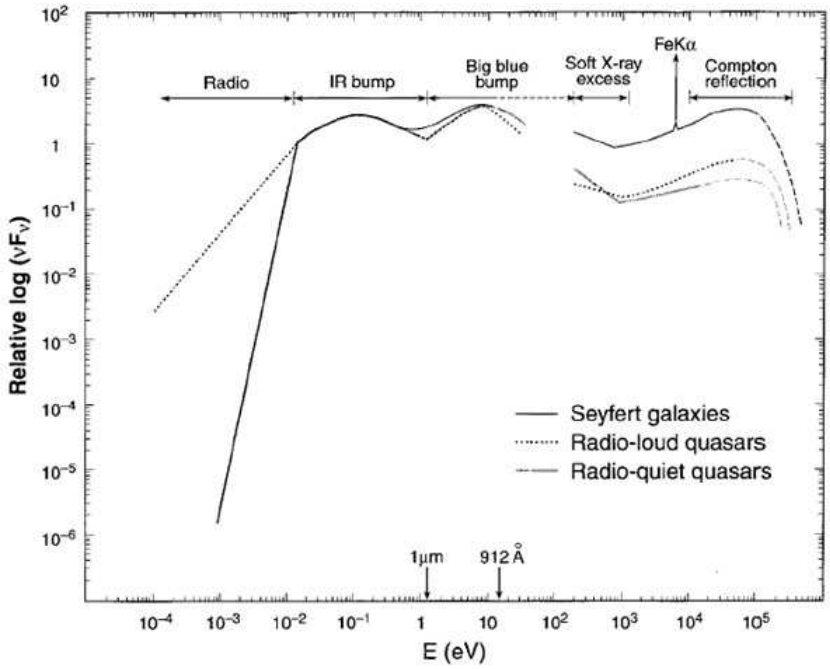

FIGURE 1.2: Typical SEDs of AGN (see Sec. 1.3 for details of different AGN classes). Figure from Beckmann and Shrader (2012).

survive, 1000 – 2000 K, depending on the composition of the dust grains (Granato, Danese, and Franceschini 1997, Netzer 2013).

3. **UV/optical emission:** the shape of the UV/optical continuum emission can be modelled with a multi-component black body of temperature $T \sim 10^{5\pm1}$ K that peaks at ∼1000 Å. The origin of this feature is thermal emission at different temperatures caused by inflowing material to the SMBH, which forms an accretion disk. This SED component is referred to as the Big Blue Bump (BBB) and it is usually the one where the AGN peaks in luminosity. The relative strengths of the IR and Big Blue bumps are generally comparable, but is not the same for all AGN (Wilkes 2004). Superimposed to this featureless continuum there are permitted, semi-forbidden and forbidden emission lines coming from material at different distances from the SMBH (0.01 – 0.1 pc or 100 – 1000 pc). Depending on the distance to the SMBH, there are broad emission lines with full width at half-maximum (FWHM) velocities of >1000 km s^{-1}, and narrow emission lines with FWHM velocities comparable to the stellar velocity dispersion (<1000 km s^{-1}). In addition, there are blends that form pseudo continuum regions originated by two elements: the FeII pseudo continuum, with velocities comparable to the ones of the broad lines or slightly lower, and the continuum produced by high order Balmer lines. In particular there is a bump at the wavelength region of the MgII line called the Small Blue Bump, that is formed by a combination of those two blends (Risaliti and Elvis 2004).

4. **X-ray emission:** the broad band continuum emission in the X-rays extends from 1 keV to over 100 keV. In energy space, the flux can be modelled with a power law $F_{\rm E} \propto E^{1-\Gamma}$, with a typical

photon index of $\Gamma \sim 1.9$[2] (Caccianiga *et al.* 2004, Galbiati *et al.* 2005, Mateos *et al.* 2005b, Mateos *et al.* 2005a, Tozzi *et al.* 2006, Mateos *et al.* 2010, Corral *et al.* 2011). The power law continuum is produced by the interaction of low energy photons (at UV/optical frequencies) from the accretion disk with electrons moving at relativistic energies in a hot corona above the accretion disk, resulting in a gain of energy by the photons (inverse Compton scattering). A fraction of X-ray photons are radiated to directions that intersect the accretion disk (see Sec. 1.2). Below 2 keV, an excess of emission with respect to the extrapolation of the power law continuum (the so-called 'soft excess') is detected in ∼50 per cent of AGN (Beckmann and Shrader 2012). The origin of this component is not clear, but is often explained by gas emission in the corona or blurred ionized reflection, among others (Boissay, Ricci and Paltani 2016). A high energy cutoff at energies ∼100 keV is sometimes detected (Malizia *et al.* 2014). Other component is the 'Compton reflection hump', that is roughly between 8-300 keV and peaks at 30 keV, where the reflection efficiency reaches its maximum. This spectral feature is often explained as reflection of the direct X-ray continuum in the accretion disk or the molecular torus (Turner and Miller 2009, see Sec. 1.2). This emission depends on the geometry, chemical composition and orientation with respect to the line of sight (Beckmann and Shrader 2012). Another reprocessing signature in the X-ray spectrum of AGN that is often detected, is an emission line at 6.4 keV. This is the Fe-K_α line (Corral *et al.* 2008, Ricci *et al.* 2014). The narrow component of this line, with a typical FWHM∼ 2000 km s^{-1}, can be explained by neutral material with low orbital velocity far away from the SMBH (such as the torus, see Sec. 1.2). In addition, there is a relativistic Fe-K_α line that is seen in some objects and it is believed to originate by fluorescence of material located in the inner accretion disk (Liu *et al.* 2016).

5. **Gamma ray emission:** photons above 100 MeV are believed to be formed by Compton scattering within the AGN jet, either from synchrotron self-Compton mechanism or from up-scattering of photons from a source external from the jet (Beckmann and Shrader 2012, see Sec. 1.2).

As we have already said, the source of the AGN enormous power is the accretion of material into the SMBH. Comparing the bolometric luminosity of the AGN with the maximum luminosity at which the SMBH can irradiate for a M_{BH} (the Eddington luminosity, L_{Edd}[3]), we can estimate the accretion rate of the AGN (related to the Eddington ratio, λ), assuming normally accretion efficiencies of about $\epsilon \sim 0.1$ (Marconi *et al.* 2004). We can find from objects accreting at very low Eddington ratios ($\lambda = 10^{-2}$–10^{-3}, Raimundo and Fabian 2009) to objects accreting at super-Eddington ratios, up to $\lambda \sim 10$ (Willott *et al.* 2010).

[2]The photon index Γ is related with the energy index with the expression $\Gamma = \alpha_X + 1$, and hence $F_E \sim E^{-\alpha_X}$.

[3]The maximum luminosity of an AGN with a black hole of mass M that is fed by spherical accretion of gas, taking into account the balance between radiation pressure and gravity. L_{Edd} is defined as $L_{Edd} = 1.26 \times 10^{38}(M/M_\odot)$ erg s^{-1}, assuming a medium composed by pure hydrogen.

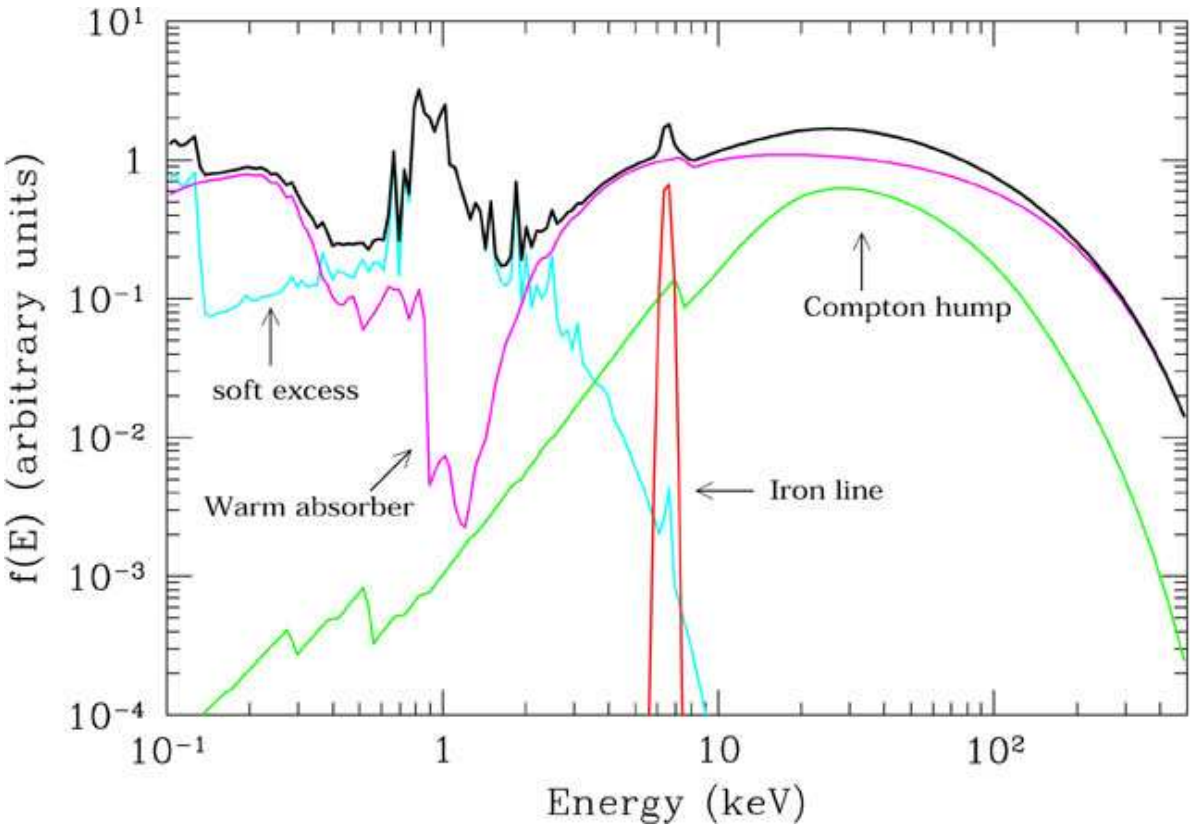

FIGURE 1.3: X-ray spectrum of a AGN, with the components of the X-ray emission overplotted with different colours. Figure from Risaliti and Elvis (2004).

This Thesis focuses on the study of the X-ray and UV/optical emission properties of AGN, so in Fig. 1.3 we show the main components of the X-ray emission of an AGN, in Fig. 1.4 we show a composite rest-frame UV/optical AGN spectrum from Meusinger and Brunzendorf (2002) and below we explain in more detail the emission mechanisms at UV/optical frequencies.

1.1.1 Emission lines at UV/optical wavelengths

The most likely origin for the UV/optical AGN emission lines is photoionization (Netzer 1990). The radiation that ionizes the material is the direct UV and optical emission from the accretion disk. There are models that separate the region where the low ionization (Balmer lines, FeII, MgII) and high ionization (Ly$_\alpha$, CIV, CIII]) broad emission lines are emitted. The latter are likely produced by a diluted outflowing medium, while the low ionization broad lines come mainly from material located in the outer regions of the accretion disk (Netzer 1990).

In this Thesis we focus at rest-frame wavelengths redwards of ~2000 Å. In this region the most conspicuous broad emission lines are, from blue to red rest-frame wavelengths, MgII λ2798 Å, H$_\beta$ λ4861 Å and H$_\alpha$ λ6563 Å. Other, less prominent broad emission lines are the Balmer series of Hydrogen (H$_\gamma$ and higher order lines), and in the infrared, the ones from the Paschen series. The FeII emission

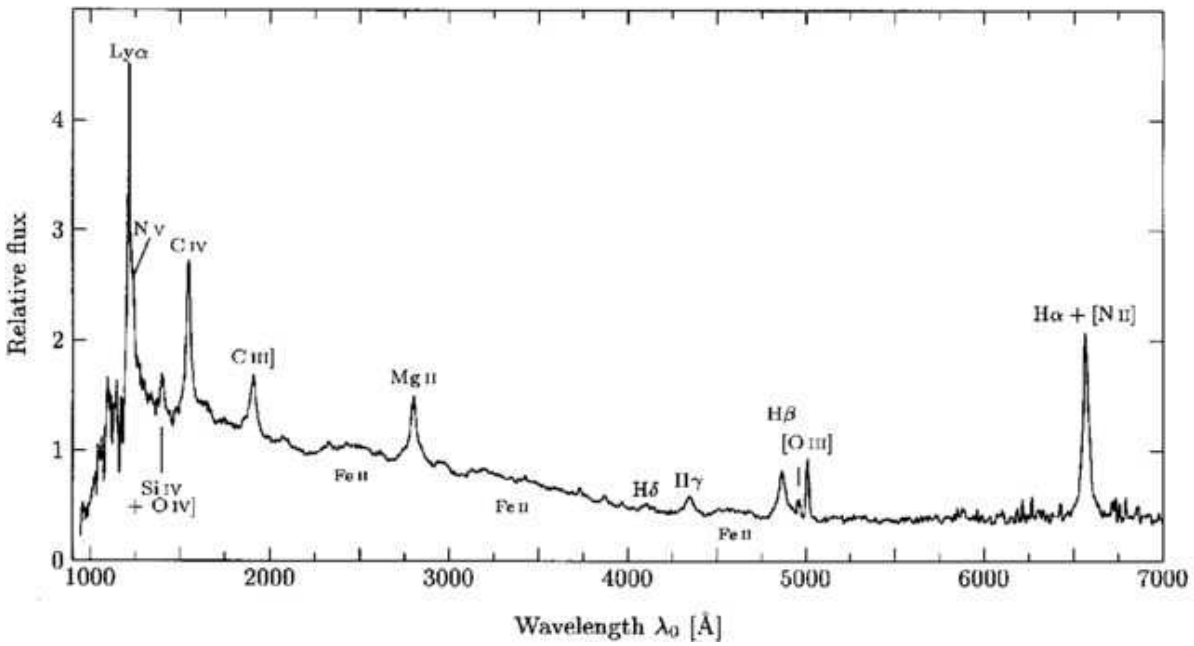

FIGURE 1.4: Composite spectrum (in the rest-frame) obtained from the low-resolution spectra of all QSOs and Seyfert 1s from Meusinger and Brunzendorf (2002) (Credit: Jens Brunzendorf).

comes from the outer parts of the Broad Line Region (BLR), as they are usually found to have FWHM velocities of 0.8 − 1.0 times the H_β ones (Osterbrock 1991). They form a pseudo continuum, that is most prominent in the region of the MgII line (the Small Blue Bump, SBB), and two narrow regions bluewards and redwards H_β. Nearly all broad line AGN have optical FeII emission in their spectrum. The FeII strength is usually measured by the quantity R4570 = FeII λ4570/H_β, being FeII λ4570 the flux of the FeII lines measured in the range λ = 4434 − 4684 Å and H_β the flux of the sum of the fluxes from the narrow and broad H_β components. As shown in Véron-Cetty and Véron (2000), this ratio is ∼0.1 − 1 for the vast majority of objects. Only 5 per cent of AGN have R4570 > 1. Other pseudocontinuum from the BLR is the one formed by the stacking of the high order Balmer lines and bluewards 3646 Å the bound-free Balmer Continuum. This contribution appears in the SBB, along with part of the FeII emission.

Normally, the forbidden narrow emission lines that are most prominent are the ones from [OII] $\lambda\lambda$3726,3729 Å, the [OIII] $\lambda\lambda$4959,5007 Å emission near H_β, [OI] λ6302 Å, and the doublets near H_α from [NII] $\lambda\lambda$6549,6585 Å and [SII] $\lambda\lambda$6718,6733 Å. In addition, the narrow emission lines of the Hydrogen Balmer series are often visible.

The emission lines have an intrinsic lorentzian profile. The velocity dispersion of the material where the lines are produced makes their shape closer to a Gaussian profile due to Doppler broadening. For the broad emission lines, the centre of the line can be displaced with respect to the rest-frame in some cases by inflows and outflows of material in the BLR (Sulentic, Marziani, and Dultzin-Hacyan 2000, Steinhardt *et al.* 2012, Gaskell and Goosmann 2013). The narrow lines, produced in the Narrow Line

Region (NLR), are not displaced but sometimes, if the material where the line is emitted is outflowing, an extra blue component can be detected in addition to the rest-frame narrow emission lines.

1.2 Unified Model of AGN

AGN show a very broad range of observational properties across the whole electromagnetic spectrum. The Unified Model was proposed to explain this diversity (Antonucci 1993, Urry and Padovani 1995, Netzer 2015). In the standard model, the observed differences between classes of AGN stems primarily from the orientation of the line-of-sight with respect to an axisymmetric dusty structure (the torus; see Fig. 1.5) that is obscuring the AGN central engine. The components of the AGN, schematically represented in Fig. 1.5, are the following:

1. **Accretion disk:** the material falling into the SMBH forms a geometrically thin optically thick disk whose outer radius is estimated to be of $\sim 10^{-2}$ pc (Hawkins 2007). The inner disk radius has an approximated size of $10^{-5\pm1}$ pc (Beckmann and Shrader 2012).

2. **X-ray corona:** this is where the X-ray emission is produced and it is thought to be linked to the accretion disk forming a balanced system in which both components interact. The hot plasma of electrons in the corona reaches temperatures of $T \sim 10^9$ K (Di Matteo, Blackman, and Fabian 1997). This corona is illuminated by optical/UV photons from the disk, some of which are reemitted at X-ray energies due to inverse Compton scattering. A strong observational support to the direct relation between the corona and the accretion disk is the relation found between the X-ray and UV luminosities over more than 5 decades in luminosity (Lusso *et al.* 2010).

3. **BLR:** this region is formed by dust-free clouds of highly ionized gas. From the difference of line ratios from the core to the wings of the broad lines, it is inferred that this region is not a thin spherical shell (Crenshaw 1986). The material on the BLR is believed to form clouds orbiting at high velocities at a distance of $0.01 - 0.1$ pc from the SMBH. The opening angle of this region (the vertex angle of the cone formed by the material and the vertical axis) is unknown to date. UV/optical photons from the accretion disk ionize the gas in the BLR producing broad permitted emission lines. From line diagnostics, it is inferred that these clouds are dense ($\sim 10^9$ cm^{-3}) and the gas has temperatures of $T \sim 20000$ K (Popović 2003).

4. **Torus:** further away from the BLR, there is a dusty region with a toroidal geometry surrounding the SMBH and extending up to a few parsecs (García-Burillo *et al.* 2016). The torus is expected to share its symmetry axis with the disk and the SMBH, although in some AGN the torus and disk are misaligned (e.g. Lawrence and Elvis 2010, Lopez-Rodriguez *et al.* 2016). Most of the dust in the torus is distributed in optically thick dense clouds (Krolik and Begelman 1988, Nenkova, Ivezić and Elitzur 2002, Nenkova *et al.* 2008, Elitzur 2012). This component is the

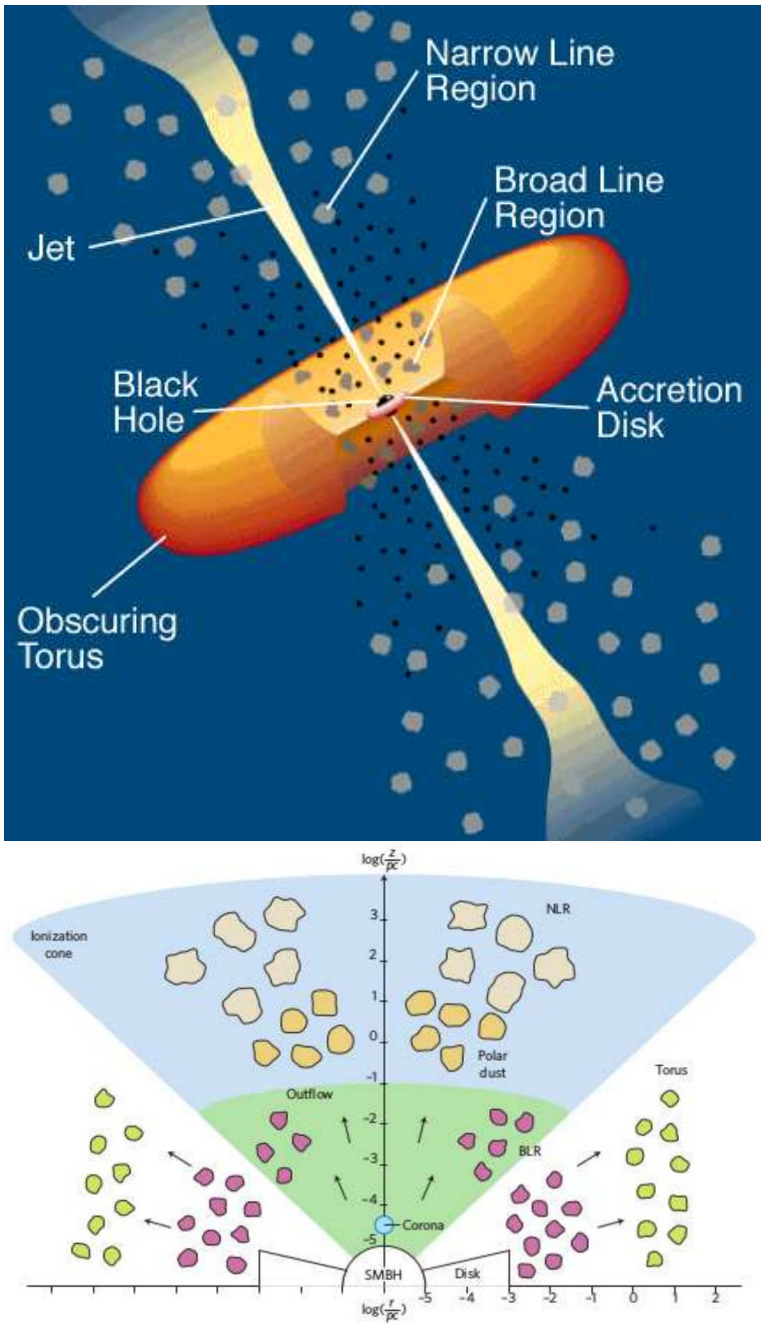

FIGURE 1.5: Top: artistic representation of the simplest model of the structure of an AGN (credit: C.M. Urry and P. Padovani). Bottom: modern sketch of the components of an AGN and their distance to the central SMBH (Ramos Almeida and Ricci 2017). In the origin of the axes it is represented the SMBH, and in the horizontal direction the accretion disk. The corona is represented as a blue circle. The BLR, torus, polar dust and NLR are represented by clouds of different colors and sizes. The green cone represents the region of the material of the BLR that is outflowing. The blue region is the ionization cone that excites the clouds forming the NLR.

key ingredient of Unified Models to explain the variations in the observed properties of AGN. If the material in the torus intercepts the observer's line-of-sight, the emission from the corona, the accretion disk and the BLR will be obscured and the AGN will be optically classified as type-2. If the torus does not intercept the observer's line-of-sight, we have a direct view of the AGN nuclear engine. These objects are optically classified as type-1. The Unified Model initially assumed that the torus properties were the same in all AGN, but recent studies show that there is a dependence with AGN properties such as the luminosity and the Eddington ratio (Alonso-Herrero *et al.* 2011, Kishimoto *et al.* 2011, Elitzur, Ho, and Trump 2014, Mateos *et al.* 2017, Ramos Almeida and Ricci 2017, Ricci *et al.* 2017b, Hickox and Alexander 2018, García-Bernete *et al.* 2019). Not all the dust responsible for the IR emission of AGN is located in the torus. Recent studies suggest that a significant fraction of the dust might be located in AGN-driven bipolar outflows perpendicular to the plane of the accretion disk (see Fig. 1.5; Hönig *et al.* 2017).

5. **NLR:** the narrow lines observed in the UV/optical spectrum of AGN have FWHM velocities comparable to the host galaxy bulge stellar velocity. These lines are produced by the emission of gas clouds further away from the central engine ($\sim 100 - 1000$ pc), and hence, with lower ionization than in the BLR. The ionization cone formed by the opening angle of the torus irradiates the material of the NLR ionizing it (see Fig. 1.5). The forbidden and permitted lines produced in the NLR are excited by the accretion disk emission. The clouds are less dense (10^3 cm^{-3}) and cooler ($T \sim 15000$ K) than those in the BLR (Osterbrock 1991).

6. **Radio Jet:** the jets are originated at sub-parsec scales and can often be traced up to distances from kpc to Mpc (Schwartz *et al.* 2003). Radio-emitting AGN are often divided into Fanaroff–Riley Class I and Fanaroff–Riley Class II jets (FR I and FR II, respectively; Fanaroff and Riley 1974). FR I jets have low luminosity ($<10^{41}$ erg s^{-1}) and end in radio lobes. FR II jets are more luminous ($>10^{41}$ erg s^{-1}) and end in hotspots. The fraction of AGN that have powerful jets is believed to be of ~15 per cent, but recent studies suggest that this fraction could drop to <1 per cent (Padovani *et al.* 2017).

1.3 Classification of AGN

In the framework of the standard Unified Model, the large variety of observed properties of AGN depend, mainly, on the relative orientation of the plane of the torus with respect to the observer's line-of-sight. If the torus blocks our view of the AGN central engine, the nuclear region might be partially obscured or completely hidden from us. The presence or absence and the relative strength of some of the features shown in Sec. 1.1 leads to a vast variety of AGN classes. In this section we will detail the different classifications in the AGN zoo putting them in context with the Unified Model and the

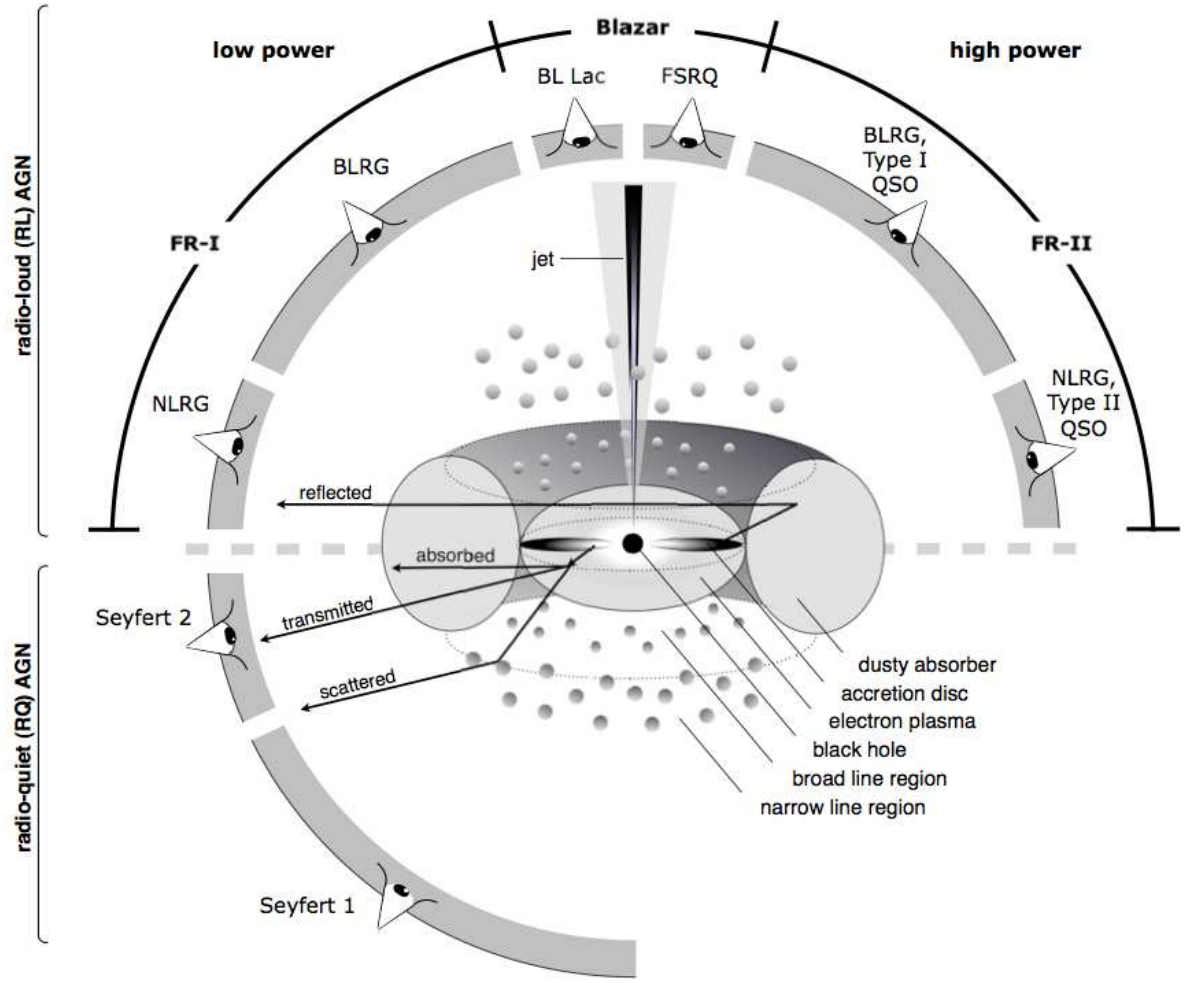

FIGURE 1.6: Schematic representation of the Unified model of AGN from Beckmann and Shrader (2012) and the different classification of the AGN depending on the viewing angle.

radiation that is detected by the observer. To help the reader understand the differences and the variety of AGN classes we include a scheme in Fig. 1.6.

In addition to orientation, to explain the diversity of AGN properties other parameters are invoked, such as AGN luminosity, variability, intrinsic differences in the broad band continuum SEDs, presence or absence of broad and narrow emission or absorption lines and host galaxy contamination. In Table 1.1 we list the AGN classes most frequently used in the literature.

The radio loudness parameter R is defined as the ratio of the fluxes at 5 GHz and in the optical B-band (Urry and Padovani 1995). RL AGN have $R > 10$ and RQ AGN have $R < 10$. RL AGN are approximately 10 per cent of the total AGN population. Their radio emission is between 2 and 4 orders of magnitude larger than in RQ AGN (Wilkes 2004). Nowadays, this distinction is rather obsolete, as the major physical difference is the presence of strong relativistic jets rather than the radio loudness (Padovani *et al.* 2017).

Table 1.1: The AGN zoo

Class/Acronym	Meaning	Main properties/reference
Quasar	Quasi-stellar radio source (originally)	Radio detection no longer required
Sey1	Seyfert 1	FWHM $\gtrsim$ 1000 km s^{-1}
Sey2	Seyfert 2	FWHM $\lesssim$ 1000 km s^{-1}
QSO	Quasi-stellar object	Quasar-like, non-radio source
QSO2	Quasi-stellar object 2	High power Sey2
RQ AGN	Radio-quiet AGN	see ref. 1
RL AGN	Radio-loud AGN	see ref. 1
Type 1		Sey1 and quasars
Type 2		Sey2 and QSO2
BLO	Broad-line object	FWHM $\gtrsim$ 1000 km s^{-1}
BLAGN	Broad-line AGN	FWHM $\gtrsim$ 1000 km s^{-1}
CT	Compton-thick	$N_{\rm H} \geq 1.5 \times 10^{24}$ cm^{-2}
NLAGN	Narrow-line AGN	FWHM $\lesssim$ 1000 km s^{-1}
NLRG	Narrow-line radio galaxy	RL Sey2
NLS1	Narrow-line Seyfert 1	ref. 2
Sey1.5/1.8/1.9	Seyfert 1.5, 1.8 or 1.9	ref. 3
XBONG	X-ray bright optically normal galaxy	AGN only in X-rays/weak lined AGN

Table adapted from Padovani *et al.* (2017). The top part of the table relates to major/classical classes. The last column describes the main properties. When these are too complex, it gives a reference to the first paper, which defined the relevant class or, when preceded by "see", a recent paper, which gives up-to-date details on it. Reference key: 1. Padovani (2016); 2. Osterbrock and Pogge (1985); 3. Osterbrock (1981).

The most luminous members of the AGN population are sometimes referred to as QSO or Quasars, with a more formal threshold defined as $M_B < -21.5$ mag.

In this Thesis we used an AGN classification based on the observed properties at rest-frame UV/optical wavelengths. AGN are divided into optical type-1 and type-2. Type-1 AGN show UV/optical broad emission lines with FWHM $\gtrsim$ 1000 km s^{-1}. Additionally, the optical spectrum normally presents narrow emission lines with FWHM $<$ 1000 km s^{-1}. Type-1 AGN typically show a strong blue continuum from the accretion disk. This emission is very intense and frequently outshines the host galaxy at these wavelengths. In type-2 AGN the continuum from the accretion disk is reddened and hence the host galaxy emission is more prominent. Hence type-2 AGN show an optical spectrum that presents only narrow emission lines superimposed on the host galaxy spectrum. The broad emission lines are obscured and thus, undetected. The narrow line emission spectra of type-1 and type-2 are very similar, but in some type-1 AGN there are much stronger highly ionized lines, that are emitted closer to the central engine (Ferguson, Korista, and Ferland 1997). In order to clarify the differences between types of AGN, we show in Fig. 1.7 the typical rest-frame UV/optical spectrum of a type-1, a type-2 AGN and a red galaxy.

In low luminosity AGN, the emission features can be partially or totally outshined by stellar light from

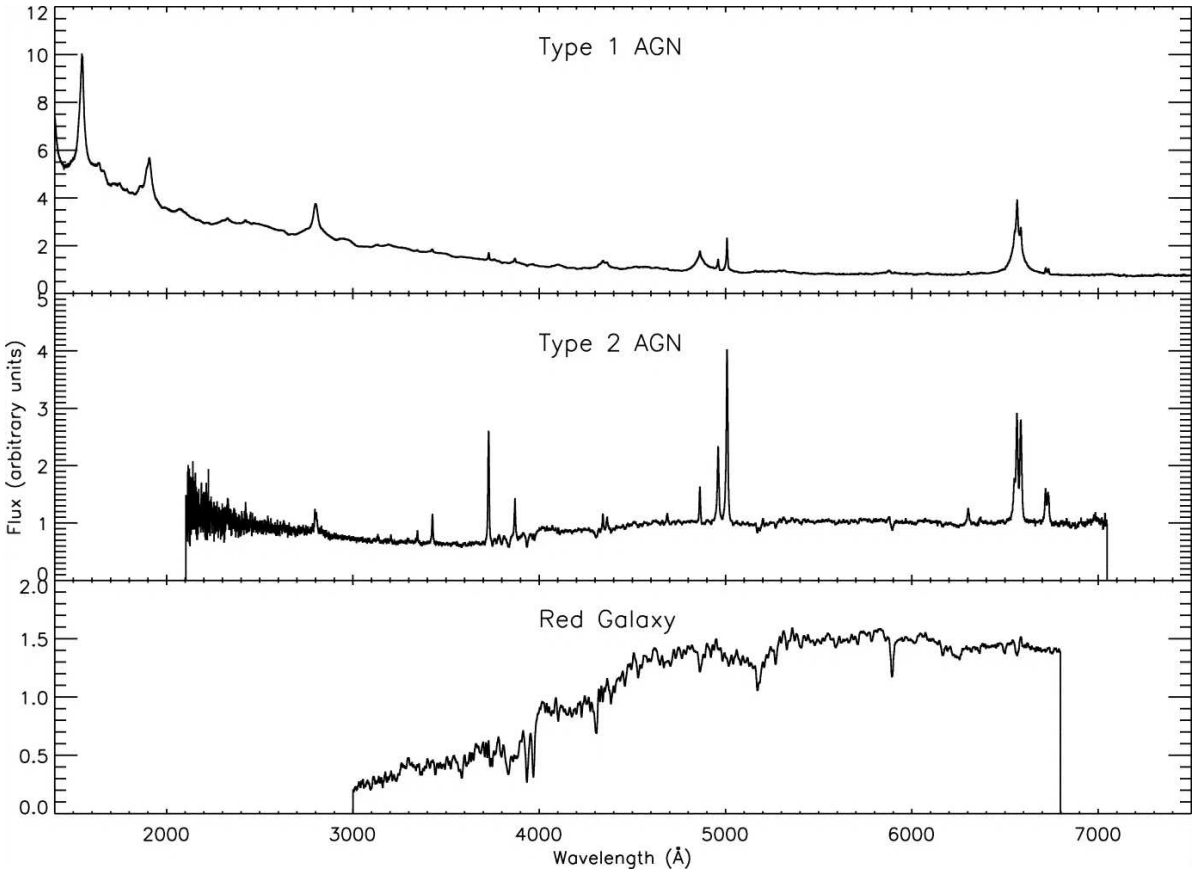

FIGURE 1.7: Typical spectrum in the rest-frame UV/optical of a type-1 AGN (top), a type-2 (middle) and a galaxy (bottom). Figure from Trump *et al.* (2007).

the galaxy (Severgnini *et al.* 2003, Georgantopoulos and Georgakakis 2005, Caccianiga *et al.* 2007, Caccianiga *et al.* 2008). If these low luminosity AGN have some level of extinction, its emission will be even harder to detect. This could make the source to be misclassified, or to be classified as an X-ray bright optically normal galaxy (XBONG).

Additionally there are examples of objects without detected UV/optical broad emission lines, but which show Paschen broad emission lines in the infrared (Goodrich, Veilleux, and Hill 1994). This is not surprising, since high dust extinction could make UV/optical lines undetectable, while in the infrared, the emission is less affected by dust extinction. Finally, in some AGN, broad emission lines are only detected in the polarized spectrum (Antonucci and Miller 1985, Miller and Goodrich 1990, Tran, Miller, and Kay 1992, Ramos Almeida *et al.* 2016).

There are as well subdivisions in the type-1 classification based on the visual relative strength of the broad and narrow emission lines (Osterbrock 1977, 1981, Urry and Padovani 1995), that are type-1.0/1.2/1.5/1.8/1.9 (Osterbrock 1977, 1981). Several works have presented quantitative schemes to subclassify type-1 AGN (e.g. Whittle 1992, Winkler 1992). The one used in this work is from Whittle (1992) and is schematized in Fig. 3.3 (see Sec. 3.4). It is possible to explain intermediate classification of type-1 AGN using only extinction extinction of the broad lines with respect to the narrow lines

(Goodrich 1995, Urry and Padovani 1995, Komossa and Fink 1997, Sparke and Gallagher 2007, Deo *et al.* 2007, Heard and Gaskell 2016, Schnorr-Müller *et al.* 2016). Nevertheless, there are recently reported several alternative explanations that can explain the intermediate classification, which are listed below:

- It has been found that type-1.8/9 AGN are more likely found in edge-on galaxies (Maiolino and Rieke 1995). There are studies suggesting that extinction by the host galaxy alone could explain intermediate type AGN (e.g. Alonso-Herrero *et al.* 2003, Prieto *et al.* 2014).
- Variability of the intrinsic continuum flux that ionizes the BLR can decrease reduce the intensity of the broad emission lines, resulting in a change of the AGN classification (Trippe *et al.* 2010). Such changes in the BLR flux can occur on time scales of the order of days (Kaspi *et al.* 2000b). The NLR emission, as is at much further scales (see Sec. 1.2), is integrated in time, so intrinsic continuum flux variations do not affect the flux of the narrow lines.
- Recent studies point out that AGN could follow an evolutionary sequence from type-1.0 to type-1.8/9, as accretion rate and luminosity can modify the structure of the BLR (Stern and Laor 2012, Elitzur, Ho, and Trump 2014).

1.4 X-ray absorption and UV/optical obscuration

It is clear that nuclear obscuration plays a key role in the observed properties of AGN. One of the main goals of this Thesis is to study the impact of obscuration on AGN appearance at UV/optical and X-ray wavelengths, so in this section we explain how do we model it in the optical range and in the X-rays.

The nuclear radiation emitted by the AGN may traverse various materials until it reaches the observer. The emission that propagates in the equatorial direction of the disk, has a high chance of being absorbed by the torus and thus, of being completely blocked (Elitzur 2012). Meanwhile, the radiation that does not intercept the material in the torus will escape from the AGN practically unaffected. The AGN emission could be affected by material in the interstellar medium of the host galaxy, such as dust lanes or gas clouds. Our own Galaxy also contributes to the line-of-sight extinction by a known quantity and, hence, can be corrected using existing $N_{\rm H}$ Galactic maps (Dickey and Lockman 1990) and assuming the dust-to-gas relation of the Milky Way.

1.4.1 Optical obscuration

Dust grains are the main ingredient responsible of the UV/optical extinction via scattering and absorption of the accretion disk and BLR photons (Hickox and Alexander 2018). Since it is more effective at wavelengths comparable to the dust grain size ($\lambda = 2\pi a$, being a the size of the dust grain), its effect is

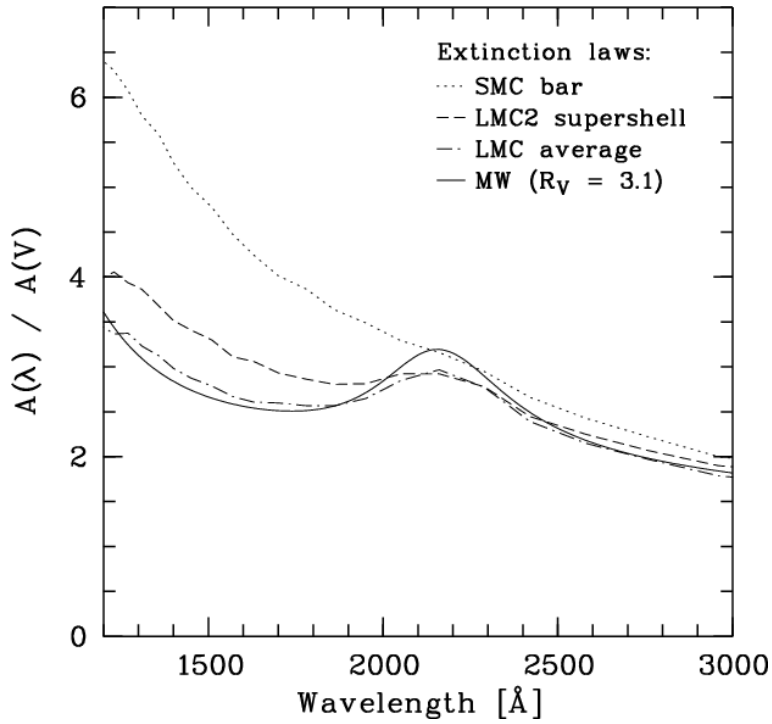

FIGURE 1.8: Different models of dust extinction versus wavelength. Figure from Noll and Pierini (2005).

higher at shorter wavelengths. In Fig. 1.8 we show different extinction models. For AGN, the extinction model that best explains their reddening properties is the one from the Small Magellanic Cloud (Hopkins *et al.* 2004), being one of the most used the one from Gordon *et al.* (2003).

One of the methods used to constrain the optical reddening is to fit the observed nuclear continuum with an extinction model and an AGN template. There is a population of AGN whose continuum is intrinsically redder than the average, and so the method might not be able to distinguish between intrinsically red objects and AGN with a strong blue continuum with small amounts of optical reddening (Hall *et al.* 2006, Young, Elvis, and Risaliti 2008). Other method to estimate the nuclear extinction is by computing Balmer decrements. This consists in comparing the relative strengths of emission lines, mainly H_α and H_β, although H_ϵ or even Paschen lines are sometimes used, and comparing with the intrinsic relative strengths expected from some standard ionization model. For the most used case, that is H_α/H_β, a case B recombination and an optically thin photoionized plasma is assumed (Osterbrock 1989). The intrinsic value is normally found to be around 3.1 for the NLR and 3.4 for the BLR, in the latter case without a clear and universally accepted value. Indeed, recent studies are finding that this value has a considerable spread (Jin, Ward, and Done 2012b, Schnorr-Müller *et al.* 2016), as it depends on the conditions of the line emitting region (Netzer 2013).

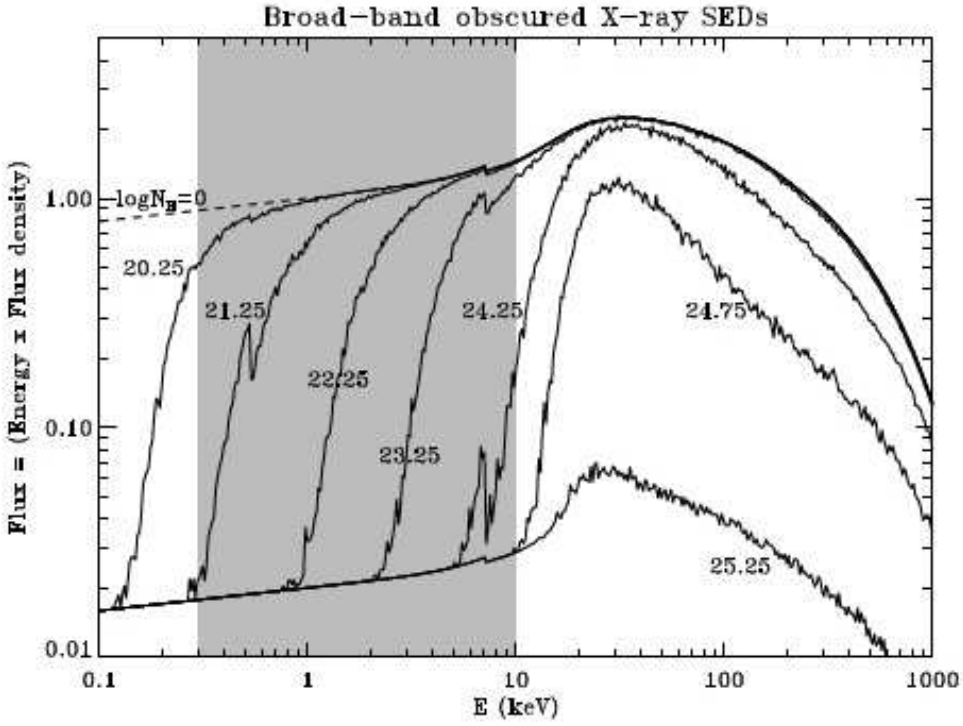

FIGURE 1.9: The effect of gas absorption in the X-ray emission. Figure from the adaptation of Wilman and Fabian (1999) shown in Singh (2013). The numbers on top of each spectrum are $N_{\rm H}$ values in logarithmic units in $\rm cm^{-2}$.

1.4.2 X-ray absorption

To first order, gas along the line-of-sight absorbs the X-ray photons. The elements of the gas that absorbs the X-ray emission are heavier than hydrogen, as its ionisation potential is too low. Nevertheless, hydrogen is the most abundant element of the material along the line-of-sight, and it is relatively easy to measure using the 21 cm emission. This is why the amount of absorbing material is quantified in terms of the $N_{\rm H}$ column density. The probability for an X-ray photon to be absorbed is defined as:

$$P(E) = 1 - e^{(-\sigma(E)\times N_{\rm H})} \tag{1.1}$$

where σ(E) is a the cross section for photoelectric absorption. The effect of the gas on the X-ray photons is higher at soft energies. In Fig. 1.9 we show the effects of photoelectric absorption for different column densities of gas on AGN emission. In that figure the nuclear emission is simulated using a $\Gamma = 1.9$ power law plus reflection and an exponential cut-off at 360 keV (see Wilman and Fabian 1999 for details).

1.4.3 Discrepancies between X-ray absorption and optical extinction

According to the Unified Model, AGN with significant extinction in the optical range should also show high levels of absorption in X-rays and vice versa, but this is not observed in all sources. Approximately 10 – 23 per cent of AGN optically classified as type-1 present an X-ray absorbed spectrum (the thresholds to classify a source as absorbed are normally $\log(N_{\rm H}/{\rm cm}^{-2}) = 21.5 - 22$; Ueda *et al.* 2003, Merloni *et al.* 2014), while 3 – 17 per cent of type-2 AGN are X-ray unabsorbed. The fraction of AGN with apparently discordant UV/optical and X-ray properties appears to be independent of the AGN selection method. The mismatch between optical extinction and X-ray absorption described above is observed in both optical/infrared and X-ray selected samples at all redshifts (Panessa and Bassani 2002, Caccianiga *et al.* 2004, Mateos *et al.* 2005b, 2005a, Mainieri *et al.* 2005, Caccianiga *et al.* 2008, Mateos *et al.* 2010, Corral *et al.* 2011, Scott, Stewart, and Mateos 2012, Page *et al.* 2011, Merloni *et al.* 2014). The origin of such apparent discrepancies remains unclear, and hence so it is the validity of the Unified Model for such AGN.

There have been many attempts to explain the origin of the discrepancies for X-ray unabsorbed optical type-2 AGN. Here we list several possible explanations:

- For some AGN it is found that they have a dust-to-gas ratio higher than the Galactic value (Caccianiga *et al.* 2004, Trippe *et al.* 2010, Huang *et al.* 2011, Malizia *et al.* 2012, Masetti *et al.* 2012, Mehdipour, Branduardi-Raymont, and Page 2012). The X-ray emission would arrive to us less affected by the material in the line of sight than the optical emission.

- A dusty-ionized absorber can produce less relative absorption in the X-rays than in the optical (Della Ceca *et al.* 2001).

- Compton-thick AGN (objects with intrinsic $N_{\rm H}$ equal or larger than the inverse of the Thomson cross-section: $N_{\rm H} > \sigma_T^{-1} = 1.5 \times 10^{24}$ cm^{-2}) can be misclassified as X-ray unabsorbed type-2 objects, since the direct X-ray emission below 10 keV is completely absorbed and we would only detect scattered nuclear radiation, which might be mistaken by direct emission (Braito *et al.* 2003, Akylas and Georgantopoulos 2009, Braito *et al.* 2011, Malizia *et al.* 2012). This contribution is about 1 – 3 per cent of the primary X-ray emission (Gilli, Salvati, and Hasinger 2001b, Comastri 2004, Georgantopoulos *et al.* 2011a), therefore comparing it to AGN bolometric tracers at other wavelengths (e.g. the [OIII] line) can unveil whether the source is Compton-thick. In addition, there may be reflected nuclear radiation would have a lower power law index as well ($\Gamma \sim 1.0$; Winter *et al.* 2008, Georgantopoulos *et al.* 2011b, Brightman *et al.* 2014, Del Moro *et al.* 2016). The equivalent width (EW) of the Fe line at 6.4 keV would be high as well, due to the suppressed intrinsic broad-band continuum.

- The broad UV/optical emission lines could be completely diluted by the host galaxy starlight. This is the case for XBONGs (Severgnini *et al.* 2003, Georgantopoulos and Georgakakis 2005, Caccianiga *et al.* 2007).

AGN with low optical extinction and high X-ray absorption could be explained as follows:

- The majority of the material that absorbs the X-ray emission of the AGN is located inside the dust sublimation radius (Risaliti, Elvis and Nicastro 2002, 2011, Mehdipour *et al.* 2017). The dust-to-gas ratio decreases due to dust sublimation close to the central X-ray source, as within this radius, the temperature is high enough to eradicate the dust grains (Granato, Danese, and Franceschini 1997, Markowitz, Krumpe, and Nikutta 2014).
- Dust grains are bigger in the environment of AGN, because small grains coagulate forming larger grains. In the inner region of the torus, as the density is larger than in the outer parts, the formation of large grains is favoured, reducing the A_V/N_H ratio if this material is obscuring the central emission (Gilli *et al.* 2001).

An independent explanation of discordant X-ray and optical properties without having to invoke non standard physics or material with dust-to-gas ratio different than the Galactic is variability in the sources. If the optical and X-ray data had been taken at different epochs, we can not discard that the discrepancies are originated by eclipses of gas and/or dusty clouds from the BLR and/or the torus moving into or outside the line-of-sight. The clumpy structure of the BLR and the torus would be compatible with this explanation. In fact, there are reports in the literature of changing look sources (LaMassa *et al.* 2015, Miniutti *et al.* 2014). Nevertheless, even with simultaneous optical and X-ray observations, there are sources with discordant optical and X-ray properties (Corral *et al.* 2005, Bianchi *et al.* 2008, 2012a). The region responsible for the X-ray absorption might not be the same as the one that obscures the optical emission (Weingartner and Murray 2002). If the majority of the X-ray absorption comes from dust-free gas from the BLR and the optical extinction is produced in regions further away, such as the torus or the host galaxy (with light travel times from days to months in the BLR and from months to years in the torus, see Sec. 1.2), this could explain the differences even in simultaneous observations.

1.5 Aims of this Thesis

A good understanding of the properties of the material responsible for the X-ray absorption and optical extinction of AGN is needed to recover the intrinsic properties of the objects, and, taking into account the existing mismatch between X-ray and optical properties in many sources, to better interpret the results of studies using X-ray and optical AGN classifications. The knowledge of the properties of

the obscuring medium is also needed to properly understand the AGN model and all the components included in it.

AGN samples based on optical colour selection methods provide a large number of AGN (Padovani *et al.* 2017). However, these surveys miss AGN even with nuclear extinction values of just $A_V \sim 1.5$ mag (Richards *et al.* 2003). Since only less than 10 per cent of all AGN present powerful radio emission, radio selection techniques are also incomplete (Mushotzky 2004). IR selection techniques are able to select Compton-thick objects, but they are biased to highly luminous sources, as the host contamination can be very important at these wavelengths. Searching for AGN at X-ray energies below 10 keV (as we did in our work) we are able to reduce the strong bias against heavily absorbed sources (up to $\log(N_H/\mathrm{cm}^{-2}) \gtrsim 23$). This implies that we are almost complete for type-1 AGN and for mildly absorbed type-2 AGN, missing only the most highly absorbed objects. In this Thesis we work with a sample selected in X-rays, the most complete and unbiased AGN selection method for our aims.

Some studies estimate the optical extinction of the AGN through fits of the AGN SEDs. Although is relatively easy to obtain good quality fits of the observed fluxes, this method lacks the spectral resolution to detect AGN and host galaxy typical features, and thus to robustly constrain the exact nuclear and host relative contribution. Our method to constrain A_V using the UV/optical continuum, allows us to build a complete sample with reliable results to study the intrinsic distributions of X-ray absorption and UV/optical extinction in type-1 AGN.

In this Thesis we provided insight into the relation between obscuration and source type and between optical extinction and X-ray absorption in AGN over a broad range of accretion luminosities and z. To do so we used the AGN sample from the hard X-ray selected Bright Ultra-hard XMM-Newton Survey (Mateos *et al.* 2012, see Sec. 3.1). In Chap. 2 we described the instrumentation and data used to build the sample, while in Chap. 3 we explained the selection of the objects included in our study and the methods used to analyse them.

In Chap. 4, we examined in detail two puzzling sources from the BUXS survey. These objects show an optical spectrum of type-1.9 AGN, i.e. objects that are generally optically obscured with A_V of $\sim 2-4$ mag. In the X-rays they show low levels of absorption, as the measured value or the upper limit on the N_H column density is lower than $\log(N_H/\mathrm{cm}^{-2}) = 21.5 - 22$. From a detailed analysis of their UV-to-NIR emission using observations from the instrument X-Shooter on the Very Large Telescope (VLT) and their X-ray emission, based on spectroscopic observations from the XMM-Newton observatory, we recovered the optical nuclear extinction (A_V) and X-ray absorption (N_H). With this information we tested several scenarios to explain the discrepant optical and X-ray classification of these sources.

In Chap. 5, we studied the impact of obscuration on the classification of AGN. As this is an X-ray selected sample it is possible to measure higher levels of extinction than in UV/optical surveys, and hence we are able to obtain more robust estimates of the fraction of type-1 AGN having an optical and X-ray classification mismatch. We also provided robust constrains on the distribution of obscuration

for type-1 AGN with intermediate optical classifications. As before, we estimated the X-ray absorption from XMM-Newton spectral fits, and the optical extinction from the reddening of the UV/optical AGN continuum from the Sloan Digital Sky Survey (SDSS) public survey and dedicated observations at several ground-based telescopes. As we have independent measurements of $A_{\rm V}$ and $N_{\rm H}$, we can check the relation (or absence of it) between these two quantities.

Summarizing, along this Thesis we will tackle the following issues to understand better the obscuration at optical and X-ray frequencies, along with the associated phenomena:

- Discover the origin of the discrepancy of optical and X-ray classification in lightly X-ray absorbed type-1.9 AGN, taking into account different scenarios proposed in the literature.
- Critically examine the robustness of the extinction measurement methods normally used in AGN analysis.
- Accurately measure the dependence of the type-1 AGN subclassification with the optical extinction and X-ray absorption.
- Obtain the intrinsic percentage of type-1 objects that have an obscuration typical of a type-2 AGN, either optically extinguished or X-ray absorbed.
- Determine how strong is the correlation between the optical extinction and the X-ray absorption in type-1 AGN.
- Unveil whether there is a single dust-to-gas ratio able to match the results in this study and if it is compatible with the Galactic value.

Chapter 2

Instrumentation

The AGN sample used in this Thesis was drawn from the wide-angle (44.43 sq. degree) Bright Ultra-hard XMM-Newton Survey (BUXS; Mateos *et al.* 2012). This is a flux limited ($f_{4.5-10\ \mathrm{keV}} \geq 6 \times 10^{-14}$ erg s^{-1} cm^{-2}) hard X-ray selected (4.5 − 10 keV) sample of AGN detected with the XMM-Newton observatory. The details of the BUXS survey and the properties of the AGN drawn for this study are described in Chap. 3.

In this chapter we detail the instrumentation used to obtain all the data used in this Thesis. The X-ray instrumentation onboard the spacecraft XMM-Newton is described in Sec. 2.1, and the characteristics of the spectrographs used for follow up of the BUXS objects at UV/optical/NIR in ground based telescopes are presented in Sec. 2.2.

2.1 X-ray observations

The atmosphere of the Earth is completely opaque to photons of certain energies as seen in Fig. 2.1. For some wavelength bands, the instruments must be at a certain altitude to detect cosmic radiation. Optical emission can be detected by instruments located at the ground, as well as radio and some infrared energy windows. But to collect cosmic X-ray radiation, detectors have to be placed in rockets or space observatories.

In this Thesis the X-ray data used comes from the X-ray Multi-Mirror Mission (XMM-Newton; Jansen *et al.* 2001). This is one of the four 'Cornerstone' missions defined in the Horizon 2000 Programme of the European Space Agency (ESA).

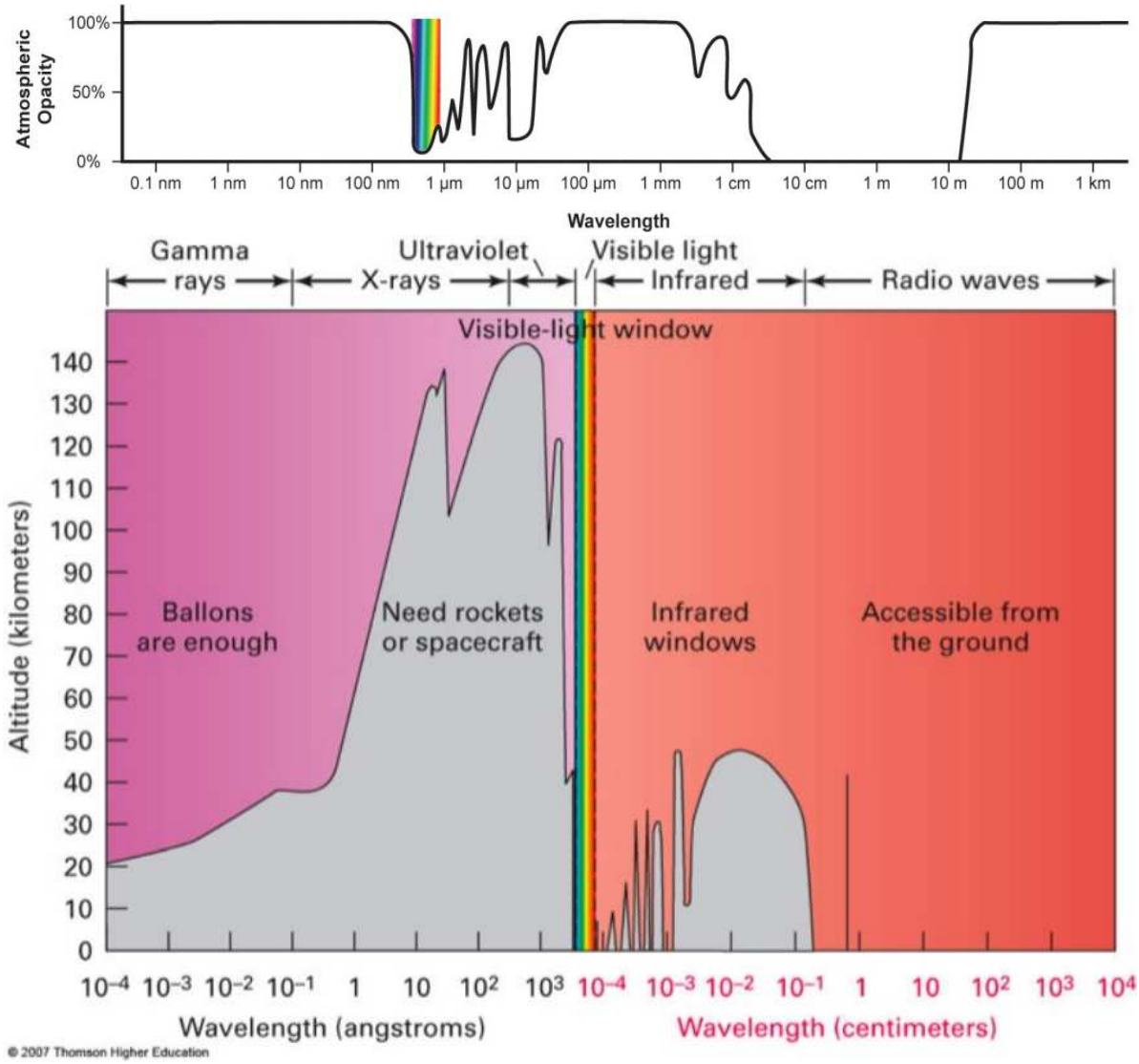

FIGURE 2.1: Top: opacity of the atmosphere in terms of the observed wavelength (credit: NASA). Bottom: the altitude in kilometres represents where the absorption of the atmosphere reduces by a factor of two the incident radiation (credit: Thomson Higher Education 2007).

2.1.1 XMM-Newton

XMM-Newton was launched by an Ariane 504 from Kourou, French Guiana on December 10th 1999. The satellite is in a elliptical orbit around the Earth, with an inclination of 40°, being the apogee at a distance between 99000 and 115000 km and the perigee between 6000 and 22000 km of altitude. The spacecraft takes 48 hours to complete an orbit.

XMM-Newton carries one optical/UV telescope: the Optical Monitor (OM; Mason *et al.* 2001, see Sec. 2.1.1.1), and two X-ray instruments: the European Photon Imaging Camera (EPIC; Turner *et al.* 2001, Strüder *et al.* 2001, see Sec. 2.1.1.2) and the Reflection Grating Spectrometer (RGS; den Herder *et al.* 2001, see Sec. 2.1.1.3). This allow simultaneous optical and X-ray observations. We show a sketch of the XMM-Newton spacecraft in Fig. 2.2.

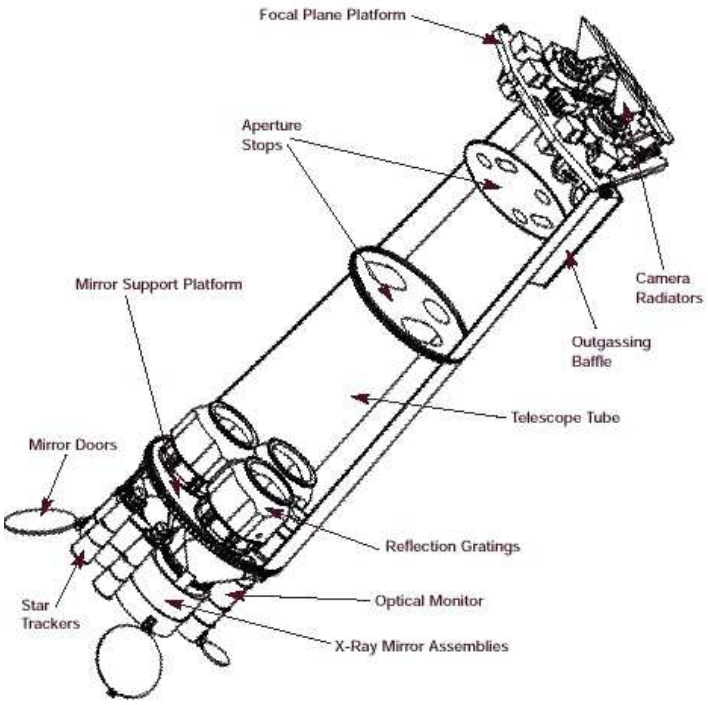

FIGURE 2.2: Diagram of the XMM-Newton spacecraft (credit: ESA).

XMM-Newton also carries three X-ray telescopes that are built with 58 Wolter I grazing-incidence mirrors, being the diameter of the largest mirrors 70 cm. They are nested in coaxial and cofocal configuration with a grazing angle of 30 arcmin. The focal length of these telescopes is 7.5 m. This configuration allows the instruments to achieve an effective area of ∼1500 cm^2 over a wide energy range (0.1-15 keV).

2.1.1.1 Optical Monitor

The Optical Monitor, is a 30 cm Ritchey-Chretien telescope that works in the wavelength range 1800-6500 Å. It can collect photons on the same regions as the X-ray telescope simultaneously with a ∼17 arcmin square field of view and ∼1 arcsec spatial resolution.

2.1.1.2 European Photon Imaging Camera (EPIC)

The detectors of the European Photon Imaging Camera (EPIC) are Charge-Coupled Device cameras (CCD) that can register extremely weak X-ray radiation and can detect flux variation in the range of microseconds.

They are located at the prime focus of each of the three X-ray telescopes. The EPIC cameras have the following detectors: two Metal Oxide Semi-conductor (EPIC-MOS; Turner *et al.* 2001) and one EPIC-pn (Strüder *et al.* 2001). In front of each detector there is a filter wheel to reduce the contamination of

the X-ray signal by IR, visible and UV light. Both types of detectors are sensitive to the energy range $0.1 - 15$ keV with similar spectral resolution ($E/\Delta E = 20 - 50$).

- The EPIC-MOS consists of two sets of CCDs sensitive in the 0.1-15 keV energy range. Each EPIC-MOS camera consists of a mosaic of 7 CCDs where each CCD is 600×600 pixels. Every single CCD has a size of 10.9×10.9 arcmin and the total Field of View (FOV) of the MOS camera is 33×33 arcmin.
- The EPIC-pn camera is a mosaic of 12 CCDs (64×200 pixels each), with a FOV of 12.6×4.4 arcmin each, to obtain a total FOV of 27.5×27.5 arcmin.

2.1.1.3 Reflection Grating Spectrometer (RGS)

In the telescopes illuminating the MOS, roughly 40 per cent of the incoming radiation is reflected to a secondary focus, where the Reflection Grating Spectrometers (RGS) are located. The two RGS allow higher resolution spectroscopic observations of bright objects at low X-ray energies ($E/\Delta E = 100 - 500$ at $0.3 - 2$ keV) than with the EPIC cameras.

2.2 Ground-based telescopes

To determine the z and optical class of our X-ray selected AGN, an intensive campaign of optical follow-up observations was carried out from 2009 to 2012. All the sky area of BUXS is covered by the Sloan Digital Sky Survey (SDSS, see Sec. 2.2.1) imaging survey, which was used to look for optical counterparts of our sources. The median 5σ photometric depth for SDSS observations is 22.15, 23.13, 22.70, 22.20 and 20.71 mag for the u, g, r, i and z filters of the survey, respectively. We show in Fig. 2.3 the response of the SDSS filters. The median FWHM seeing of these observations is between 1.53 and 1.26 arcsec, depending on the filter, and the global astrometric precision is $0.1''$ rms. To cross-match the X-ray and optical sources the algorithm of Pineau *et al.* (2011) was used, whose likelihood ratio is based on the one from de Ruiter, Willis and Arp (1977). This is conducted using a likelihood ratio for each X-ray source with the optical candidate counterparts. Among the 255 AGN from BUXS, only 5 were not detected by SDSS. For these 5 sources, deeper proprietary observations with the Telescopio Nazionale Galileo (TNG, see Sec. 2.2.2.2) reaching photometric depths of $24 - 25$ mag were used to detect the optical counterparts.

Since the beginning of the BUXS survey in 2009, we also collected SDSS public spectra through different data releases of the spectroscopic survey (at the time of our studies we had SDSS spectra for 174 sources). For the sources without SDSS spectra or for those for which the available spectrum do not have enough quality, dedicated observations at several ground-based telescopes counterparts were conducted.

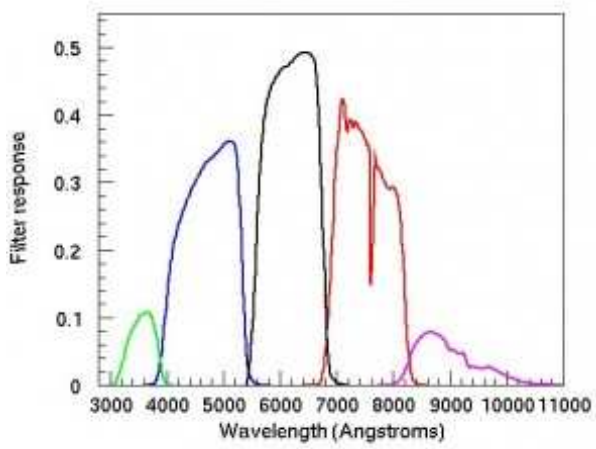

FIGURE 2.3: Response of the *ugriz* SDSS filters (credit: SDSS).

In the cases where more than one UV/optical spectra is available for an AGN, we choose the most appropriate one based on the wavelength coverage and the signal-to-noise ratio (SNR, that we compute in the continuum windows used in the fits of the UV/optical continuum, see Sec.3.3.2). If all spectra from different instruments have SNR < 8 we choose the one with the highest SNR. If we have more than one spectrum with SNR > 8, we choose the one among them with the widest wavelength coverage to constrain better the optical extinction, as it is measured using the UV/optical continuum emission.

In Sec. 2.2.1 we describe the SDSS instrumentation used to collect the public spectra for the BUXS AGN. Then, in Sec. 2.2.2 we describe in detail the optical telescopes and instrumentation used to acquire the proprietary observations. In particular we put special emphasis in Sec. 2.2.2.1 on the VLT/X-Shooter, as there is one chapter in this Thesis dedicated to a detailed analysis conducted with data from this instrument (Chap. 4). For the rest of the proprietary observations we describe the telescopes and instrumentation used more succinctly.

2.2.1 Fibre spectra from the SDSS survey

We used spectra from the Sloan Digital Sky Survey (SDSS) until Data Release 14 (Abolfathi *et al.* 2018). The SDSS is an international collaboration that uses a dedicated 2.5 m modified Ritchey-Chrétien alt-azimuth telescope placed at the Apache Point Observatory, New Mexico, USA, 2788 m above sea level.

To obtain optical spectra, SDSS uses plates. Each hole in the plate is connected to a fibre to drive the incoming radiation to the two spectrographs mounted on the image rotator.

For this Thesis we used the data collected with the old SDSS-I/II spectrograph (Gunn *et al.* 2006) and the most modern one, the Baryon Oscillation Spectroscopic Survey (BOSS) spectrograph (Smee *et al.* 2013).

2.2.1.1 SDSS-I/II Spectrograph

The first spectroscopic instrument from SDSS acquired spectra from 640 positions in the sky for each plate. The holes in the plate are connected with optical fibres whose diameter is 3 arcsec. The fibres carry the incoming light from the focal plane to slitheads attached to a cartridge that can be put on and off. The light is split into two spectrographs, to cover the wavelength ranges from 3800 to 6100 Å, and from 5900 to 9100 Å, respectively. The beam is split with a dichroic with the dividing wavelength at around 6000 Å. Each spectrograph collects the radiation with one SITe/Tektronix 2048×2048 CCD for each arm. This setup allows to have a resolution ranging from 1850 to 2200 over the whole spectral range.

2.2.1.2 BOSS Spectrograph

The BOSS spectrograph is a redesign of the original SDSS spectrograph. The plates are drilled with 1000 holes corresponding to the sky positions for each target in the observed field, and the fibres connected to each hole have a diameter of 2 arcsec. The new instrument can provide spectra with a wavelength range from 3600 to 10400 Å. The light for each object is split with a dichroic at roughly 6000 Å. The light is then carried to two arms. The blue channel has a wavelength range of $3700 - 6000$ Å and the red arm covers $5650 - 10400$ Å. The spectral resolution ranges from 1560 to 2650.

2.2.2 Long Slit spectra

In this section we describe the telescopes and instrumentation of the follow-up campaign of spectroscopic identifications of the BUXS X-ray sources.

2.2.2.1 VLT/X-Shooter

The Very Large Telescope (VLT) is operated by the European Southern Observatory (ESO) at Paranal Observatory in the Atacama Desert of Chile, 2635 m above sea level. It consists of four individual telescopes (UT1: Antu, UT2: Kueyen, UT3: Melipal, UT4: Yepun), each one with a diameter of the primary mirror of 8.2 m. X-Shooter (Vernet *et al.* 2011), is placed on the Cassegrain focus of UT2. In Fig. 2.4 we show an sketch of the instrument. It consists of a combination of three echelle spectrographs that provide simultaneous UV-to-NIR spectroscopy ($3000 - 25000$ Å) with intermediate

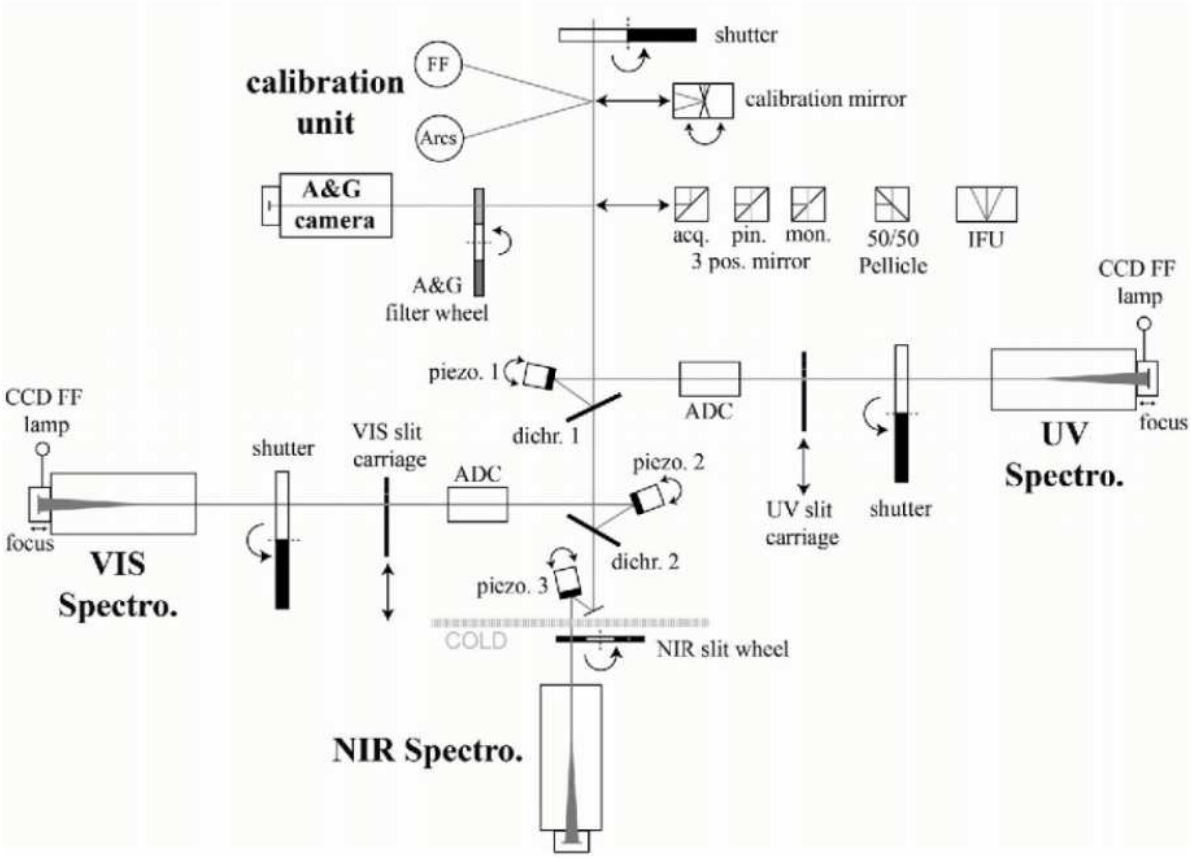

FIGURE 2.4: Schematic overview of VLT/X-Shooter (credit: ESO).

spectral resolution (R $\sim$ 4000 – 17000, depending on wavelength and slit width). All the slits have a fixed length of 11 arcsec. The incident light is divided in three different paths, each one reaching a different echelle spectrograph. This is conducted using two dichroic beamsplitters, with dividing wavelengths of 5595 Å and 10240 Å. One arm collects the UV light (UVB: 3000 – 5595 Å), other optical light (VIS: 5595 – 10240 Å), and the last one near infrared light (NIR: 10240 – 24800 Å). The UVB and VIS paths incorporate an Atmospheric Dispersion Corrector (ADC) that allows to compensate the effects of differential atmospheric refraction. This removes the restriction to orient the slit to the parallactic angle, as it will correct the refraction wavelength dependent slit losses independently from the airmass and the orientation of the slit. The effect on the infrared is low, so no NIR ADC is used in X-Shooter.

The setup used for the X-Shooter observations in Chap. 4 is shown in Tables 2.1 and 2.2.

2.2.2.2 Other ground based optical telescopes

In this section we detail the instrumentation used for the BUXS observing runs.

TABLE 2.1: X-Shooter setup used in this Thesis.

Arm	Slit Width (arcsec)	R ($\lambda/\Delta\lambda$)	Sampling (pix/FWHM)
UVB	1.0	5100	6.3
VIS	0.9	8800	6.0
NIR	0.9	5100	6.3

Notes: (1): X-Shooter arm; (2): slit width in arcsec used in the observations; (3): resolving power ($\lambda/\Delta\lambda$); (4): sampling of the setup used in our observations.

TABLE 2.2: X-Shooter spectra acquisition information.

Object (1)	Date (2)	Nodding (3)	Airmass (4)
2XMMiJ000441.2+000711 (J00)	2010-09-07	+2.5 -2.0	1.14
2XMMJ025218.5-011746 (J02)	2010-09-04	+2.5 -1.5	1.09

Notes: (1): object identifier and their short names used in this Thesis in brackets; (2): observation date (YYYY-MM-DD); (3): nodding separation in arc sec; (4): airmass.

- GTC/OSIRIS: the Optical System for Imaging and low-Intermediate-Resolution Integrated Spectroscopy (OSIRIS) is located in the Nasmyth-B focus of the 10.4 m Gran Telescopio CANARIAS (GTC). This telescope is placed at the Roque de los Muchachos Observatory on the island of La Palma, Spain, 2396 m above sea level. The GTC was built by the public company GRANTECAN S.A., that also operates it.

- VLT/FORS2: the FOcal Reducer/low dispersion Spectrograph 2 (FORS2) is installed at the Cassegrain focus of the VLT telescope Antu (UT1).

- SUBARU/FOCAS: The Faint Object Camera and Spectrograph (FOCAS) is an optical imaging and spectroscopy unit installed at the Cassegrain focus of the Subaru Telescope. This is a 8.2 m telescope operated by the National Astronomical Observatory of Japan that is located at the summit of Mauna Kea (Hawaii, USA), 4205 m above sea level.

- WHT/ACAM: the Auxiliary-port CAMera (ACAM) is mounted at the Cassegrain focus of the 4.2 m William Herschel Telescope (WHT), that is part of the Isaac Newton Group of Telescopes[1] (ING) situated at the Roque de los Muchachos Observatory.

- WHT/ISIS: the Intermediate dispersion Spectrograph and Imaging System (ISIS), mounted at the Cassegrain focus of the WHT, consists of two arms. A dichroic divides the incoming light in two beams with the dividing wavelength at roughly 5300 Å.

[1]The ING is operated by the Particle Physics And Astronomy Research Council (PPARC) of the United Kingdom, the Nederlandse Organisatie voor Wetenschappelijk Onderzoek (NWO) of the Netherlands and the Instituto de Astrofísica de Canarias (IAC) of Spain.

- NTT/EFOSC2: the ESO Faint Object Spectrograph and Camera v.2 (EFOSC2) is placed at the 3.58 m ESO New Technology Telescope (NTT). This telescope is located in La Silla, at an altitude of 2400 m in the southern part of the chilean Atacama desert.
- TNG/DOLORES: the Device Optimized for the LOw RESolution (DOLORES, or LRS), that is placed at one of the Nasmyth focus of the 3.58 m Telescopio Galileo Galilei (TNG) located in the Roque de los Muchachos Observatory. TNG is operated by the 'Fundacion Galileo Galilei, with is financed by the Istituto Nazionale di Astrofisica (INAF).
- NOT/ALFOSC: the Andalucia Faint Object Spectrograph and Camera (ALFOSC) is placed at the 2.5 m Nordic Optical Telescope (NOT). It is located at the Roque de los Muchachos Observatory, and it is operated by the Nordic Optical Telescope Scientific Association (NOTSA).
- UH/WFGS: the Wide Field Grism Spectrograph (WFGS), installed at the University of Hawaii telescope (2.2 m) is located on Mauna Kea (Hawaii, USA), at 4213 m.

In Table 2.3 we summarize the technical information of the grisms and slits used for spectroscopy in this Thesis.

TABLE 2.3: Instrument setup used for the BUXS follow-up campaign.

Instrument	$D_{Telescope}$ (m)	Grism name	λ range (Å)	Slit width (arcsec)	R ($\lambda/\Delta\lambda$)
GTC/OSIRIS	10.4	R500R	4800 – 10000	1.0	352
				1.23	286
VLT/FORS2	8.2	300V	4450 – 8650	1.0	440
				1.3	338
SUBARU/FOCAS	8.2	300B	4700 – 9100	0.8	500
WHT/ACAM	4.2	V400	3300 – 9500	1.0	570
				1.5	380
WHT/ISIS (Blue arm)	4.2	R300B	3200 – 5300	1.46	640
				1.52	620
WHT/ISIS (Red arm)	4.2	R158R	5300 – 9300	1.46	640
				1.52	620
NTT/EFOSC2	3.58	Grism 4	4085 – 7520	1.0	2798
		Grism 13	3685 – 9315	1.5	1058
TNG/DOLORES	3.58	LR-B	3000 – 8430	1.0	585
				1.5	390
				2.0	293
NOT/ALFOSC	2.5	Grism 4	3200 – 9600	1.0	360
				1.3	277
				1.8	200
		Grism 7	3650 – 7110	1.0	650
UH/WFGS	2.2	Green(400)	3800 – 9700	1.6	300

Notes: (1): telescope and instrument; (2): diameter of the telescope; (3): name of the grism used; (4): wavelength range of the grism; (5): slit width; (6): Resolving power.

Chapter 3

The BUXS Sample

In this Thesis we carried out two different studies to provide insight into the obscuration of AGN:

- Detailed analysis of the origin of the apparent mismatch between the X-ray and optical properties of two lightly X-ray absorbed type-2 AGN: 2XMMiJ000441.2+000711 and 2XMMJ025218.5-011746 (hereafter J00 and J02, respectively; see Chap. 4).
- Statistical study of the X-ray absorption and optical extinction of a large, uniformly selected sample of type-1 AGN. The objects span over four orders of magnitude in accretion luminosity and have $z < 1$ (see Chap. 5).

All sources analysed were drawn from BUXS. The properties of the survey are explained in detail in Sec. 3.1. In this chapter we also describe the analysis of the X-ray and UV/optical spectroscopic observations (see Sec. 3.2 and Sec. 3.3, respectively). Finally, in Sec. 3.4 we present the properties the samples of AGN used for this Thesis.

3.1 Sample definition

As already stated, the sources were detected with the XMM-Newton observatory at X-ray energies above 4.5 keV and have fluxes in the 4.5-10 keV band $f_{4.5-10\,\mathrm{keV}} \geq 6 \times 10^{-14}$ erg s^{-1} cm^{-2}. This selection, as mentioned in Chap. 2, is able to reduce the strong bias against heavily absorbed AGN (up to $\log(N_{\mathrm{H}}/\mathrm{cm}^{-2}) \gtrsim 23$). The X-ray observations used to build the BUXS survey were drawn from the second XMM-Newton serendipitous source catalogue[1] (2XMM; Watson *et al.* 2009). This catalogue covers a sky area of more than 500 deg^2 (non-overlapping sky area of ∼360 deg^2), and provides 191 870 unique sources.

[1] https://heasarc.gsfc.nasa.gov/W3Browse/xmm-newton/xmmssc.html

The BUXS sample is build from EPIC pn observations with more than 10 ks of clean exposure time without bright and/or extended X-ray sources in the pn FOV. The BUXS sky area was selected based on the one covered by the SDSS imaging survey. From them, only fields at high Galactic latitude ($|b| > 20$ deg) were used to obtain a sample with the least Galactic contamination as possible, resulting in a total sky area of 44.43 sq. degree.

Parts of the BUXS sky area have been observed more than once with XMM-Newton. For this reason, for some AGN in this Thesis there are multiple observations in the public XMM-Newton Science Archive[2] that we combined with the original data set to increase the SNR of the X-ray spectroscopic observations of our objects.

The identification process of the optical counterparts was explained in Sec. 2.2. BUXS contains 255 AGN after removing Galactic stars (less than 2 per cent) and BL Lacs (1 per cent). At the time of writing, the optical spectroscopic identification completeness is >98 per cent (only 5 objects left), using either SDSS or dedicated UV/optical spectroscopic observations.

3.2 X-ray spectral modelling

The extraction of the X-ray spectroscopic observations was conducted by team members of our group using the XMM-Newton Science Analysis System (SAS) tasks. We use only the 0.25-10 keV energy range, where the X-ray instruments are best calibrated, to reduce the noisy regions of the XMM-Newton spectra. We use the XMM-Newton Science Archive to extract all the available public observations for our objects up to October 2018. X-ray spectra were extracted from the three EPIC cameras (MOS1, MOS2 and pn) and the MOS1 and MOS2 observations were combined (MOS1+MOS2 is named MOS hereafter). We combined all pn spectra and all MOS spectra, so we fit just two spectra of each source. In Fig. 3.1 we show the distribution of the total number of EPIC (MOS+pn) net counts (background subtracted) for the BUXS type-1 AGN sample (132 objects; see Sec. 3.4). The median number of counts is 2062, so clearly, the sample used in this Thesis is quite unique, since all AGN studies in the literature at similar X-ray fluxes have X-ray spectroscopic observations of substantially lower quality (Mateos *et al.* 2010, Corral *et al.* 2011, Castelló-Mor *et al.* 2013, Lanzuisi *et al.* 2013, Merloni *et al.* 2014, Corral *et al.* 2015, Koulouridis *et al.* 2016).

To constrain the properties of our AGN we fit their X-ray spectra with XSPEC (Arnaud 1996). We used a combination of different models to determine the shape of the direct and scattered broadband continuum components (modelled with power laws), soft excess (modelled with a collisionally-ionized diffuse gas or a phenomenological black body model) and rest-frame line-of-sight X-ray absorption. We also take into account the Galactic absorption using column densities taken from Dickey and Lockman (1990). We fit the pn and MOS spectra of the same source simultaneously with the parameters

[2] http://nxsa.esac.esa.int/nxsa-web/

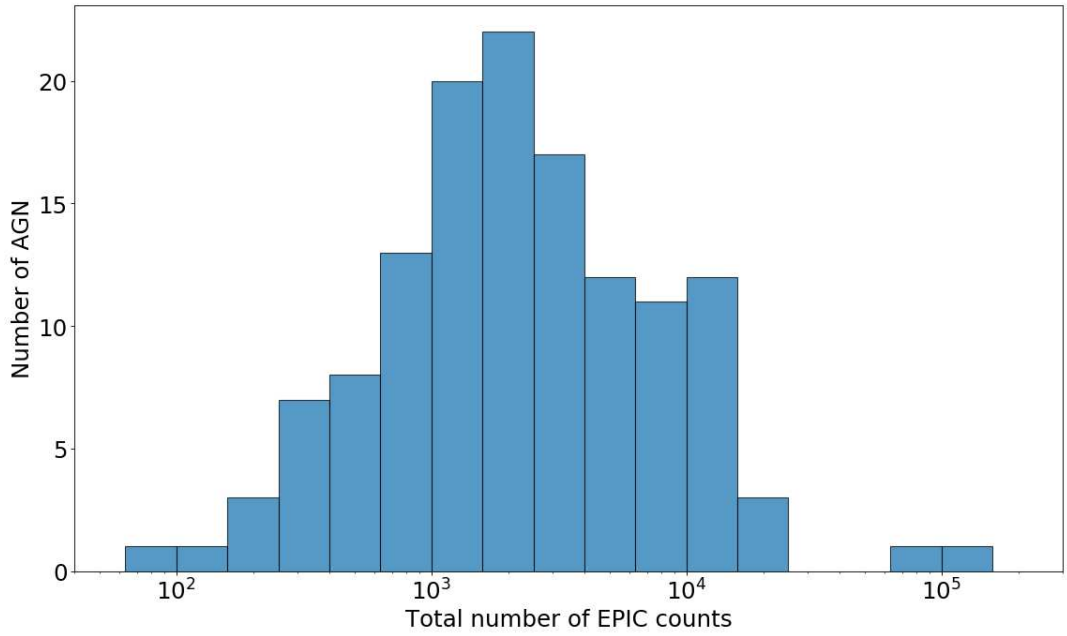

FIGURE 3.1: Total number of EPIC (MOS+pn) net counts in the 0.25 − 10 keV energy range for the BUXS type-1 AGN sample.

of the model tied, except for all normalisations to take into account cross-calibration uncertainties between the MOS and pn cameras (Mateos *et al.* 2009).

We fitted the two sources of Chap. 4 using the χ^2 statistic. We have used the F-test (Press *et al.* 1992) to measure the significance of the detection for every spectral component additional to the power law model with Galactic and intrinsic absorption for the direct broadband continuum emission. We have selected a confidence level threshold of 95 per cent to accept an additional spectral component.

The X-ray spectra of our sample of type-1 AGN used in the statistical study presented in Chap. 5 were fitted by team members of our group. To properly take into account in our study the uncertainties of the model parameters, we compute the probability distributions of $N_{\rm H}$ and the intrinsic luminosity in the rest-frame 2-10 keV energy range. To do so, Markov chain Monte Carlo simulations (MCMC) were used (see Sec. 3.2.2). The Deviance Information Criterion (DIC, Spiegelhalter *et al.* 2002) was used to select the best fit model taking into account both the complexity of the models and the quality of the fits.

3.2.1 X-ray spectral models

X-ray spectra are measured in units of counts per energy channel $C(I)$ instead of flux, $F_E(E) = dE/dtdS\,d\varepsilon$. The incident flux of the source is modified by the response matrix of the instrument $R(I, E)$. This response matrix $R(I, E)$ stands for the probability that incoming X-ray photons of energy E give rise to a certain amount of counts in a given energy channel I. Therefore we can relate the observed spectrum with the incident radiation as follows,

$$C(I) = \int F_E(E) R(I, E) dE \tag{3.1}$$

The integral is evaluated over the energy range where the detector is sensitive to X-ray photons, i.e., where the response matrix $R(I, E) > 0$. This model is associated to the emission spectrum of the source, that is $F_E(E)$. The models used in this study are[3]:

- **Power law**

  The power law, as mentioned in Chap. 1, is the mathematical expression that is used to model the X-ray emission from the corona. The broad band X-ray continuum is the main contributor to the AGN emission at the energies sampled in our study. We have used the `zpowerlw` implementation of this model in XSPEC. We fix the redshift to that of the source.

- **Collisionally-ionized diffuse gas**

  The emission from collisionally-ionized diffuse gas, that is radiation produced by the deceleration of two charged particles when they are deflected, is needed to model the soft excess. This can be done with the additive models `apec` or `mekal`. The emission spectrum `apec` is based on data from the AtomDB atomic database[4], and `mekal` is based on the model calculations of Mewe and Kaastra with Fe L calculations by Liedahl (Mewe, Gronenschild, and van den Oord 1985, Mewe, Lemen, and van den Oord 1986, Kaastra 2000, Liedahl, Osterheld, and Goldstein 1995). We fix the redshift to that of the source and the abundances to the values of Anders and Grevesse (1989), and we leave the H density (only used in `mekal`), the temperature of the plasma and the normalization as free parameters.

- **Black body**

  The black body, implemented with the `zbbody` command, is an additive model used to fit the soft excess emission. This is just a phenomenological model, so it is used to fit the soft excess in those cases where we want to avoid overfitting, or because this phenomenological model fits better the soft excess or when `apec` or `mekal` does not provide a good quality fit to the soft excess emission. This model is fixed at the redshift of the source and the temperature is a free parameter.

- **Gaussian line profile**

  Using `zgauss`, we model the profile of the Fe Kα emission line. As the spectra used in this work do not have enough resolution to accurately fit the width of the line, the width of the line is fixed at $\sigma = 0.01$ keV and the rest-frame energy at 6.4 keV to prevent the fits giving unphysical results. If an emission line is not obviously seen in the spectrum, we try to fit a narrow line, only accepting it if it fulfilled the F-test. Additionally, we fix the redshift to that of the source.

[3] https://heasarc.gsfc.nasa.gov/xanadu/xspec/manual/Models.html
[4] http://atomdb.org/

- **Galactic absorption**

  The radiation coming from the AGN is absorbed by material in the Milky Way. This absorption is modelled using `wabs`. We use the Galactic $N_{\rm H}$ column densities ($N_{H,G}$) at the coordinates of each object from Dickey and Lockman (1990) at the coordinates for each source. For the study in Chap. 4 we fix this value, but in Chap. 5 we allow it to vary using a Gaussian prior (see Sec. 3.2.2) where the mean μ is the value $N_{H,G}$ and σ is the standard deviation of the $N_{H,G}$ values measured in a in a 4×4 degrees box centred in the object. The range of allowed values for $N_{H,G}$ are restricted to 3 times the standard deviation to prevent the fits from overlapping with the intrinsic absorption. All values were retrieved using the routine `nh` from HEAsoft.

- **Intrinsic absorption**

  Using the multiplicative model `zwabs` we measure the intrinsic X-ray absorption at the redshift of the source. We fix the redshift value to that of the source and the $N_{\rm H}$ column density is left as a free parameter.

- **Torus model**

  For one object with $N_{\rm H}$ column density close to the Compton-thick limit, none of the models described above (and combinations of them) is appropriate to model the emission. In this case, we used the torus model from Brightman and Nandra (2011) that takes into account Compton scattering and reprocessed radiation of the Compton-thick material around the central engine. In this model, the parameters are the redshift, the absorption and two angles: the opening angle of the torus (defined as the vertex angle of the cone formed by the torus and the vertical axis) and its inclination with respect to the line-of-sight. Except for the redshift, which we fix to that of the source, all of them are free parameters.

The X-ray spectra were fitted with the following models:

- **zwapo:** `wabs*zwabs*zpowerlw`
- **zwapopo:** `wabs*(zpowerlw+zwabs*zpowerlw)`
- **zwabbpo:** `wabs*(zbbody+zwabs*zpowerlw)`
- **zwapecpo:** `wabs*(apec+zwabs*zpowerlw)`
- **zwmekalpo:** `wabs*(mekal+zwabs*zpowerlw)`
- **zwapecpopo:** `wabs*(apec+zpowerlw+zwabs*zpowerlw)`
- **zwapectorus:** `wabs*(apec+zpowerlw+torus)`

TABLE 3.1: Priors used to fit the XMM-Newton spectra using Bayesian statistics.

Parameter	Fit limits	Prior
Γ	0 – 4	Gaussian prior (μ = 1.9, σ = 0.25)
$N_{\rm H}$	10^{19} – 10^{25} cm^{-2}	Flat logarithmic
$N_{H,G}$	$\mu\pm3\sigma$ (see Notes)	Gaussian prior (see Sec. 3.2.1 and notes)
kT	0.01 – 1 keV	Flat
Flux normalization	10^{-7} – 1	Flat logarithmic
log(L$_{2-10\ \rm keV}$/erg s^{-1})	39 – 47	Gaussian prior (μ = 44, σ = 2)

Notes: We denote a uniform prior in linear space as flat and a uniform prior in logarithmic space (Jeffreys prior, Jeffreys 1946) as flat logarithmic. We describe the Gaussian prior mean and standard deviation with μ and σ, respectively. In the case of $N_{H,G}$, μ and σ are fixed for each source as described in Sec. 3.2.1. The luminosity prior is obtained performing preliminary fits of the X-ray spectra to obtain the expected luminosity range of our AGN.

3.2.2 Markov Chain Monte Carlo spectral fitting simulations

For the type-1 AGN sample in Chap. 5 we used Markov Chain Monte Carlo simulations to obtain the probability distributions of $N_{\rm H}$. This was performed by members of our group. We first grouped the spectra with one count per bin and used a Cash likelihood (implemented in XSPEC as C-stat; Cash 1979) with Bayesian statistics to fit the spectra, defining for each parameter a prior probability, shortened as prior. This is an initial estimated probability of the numerical values of each free parameter. We list in Table 3.1 the priors used.

Using the results from the previous step, to obtain the probability distributions of the fitted parameters, we conduct MCMC with a chain length of 100000 using the Goodman and Weare (2010) algorithm. We ignore the first 10000 data points to ensure that we use only convergent simulations (all chains were individually checked). We chose the model that minimizes the DIC. We only select more complex models than an absorbed power law if the DIC improvement is not marginal (>5 per cent, which is the maximum random difference observed by running the same chains multiple times for the same source and model). We follow this criterion with the following exceptions:

1. If the selected model is a double power law model with very high absorption ($N_{\rm H} \gtrsim 10^{24}$ cm^{-2}), but is chosen due to high energy residuals that are likely artefacts from the spectral extraction. These cases are detected via visual inspection of the fitted spectra and residuals, and only happened in four cases.

2. Due to the lack of enough counts at high energies, either because of low count spectra and/or high absorbing column density, in five cases we were forced to fix Γ to 1.9, which is the typical photon index value in AGN (Caccianiga *et al.* 2004, Galbiati *et al.* 2005, Mateos *et al.* 2005a, Mateos *et al.* 2005b, Tozzi *et al.* 2006, Mateos *et al.* 2010, Corral *et al.* 2011).

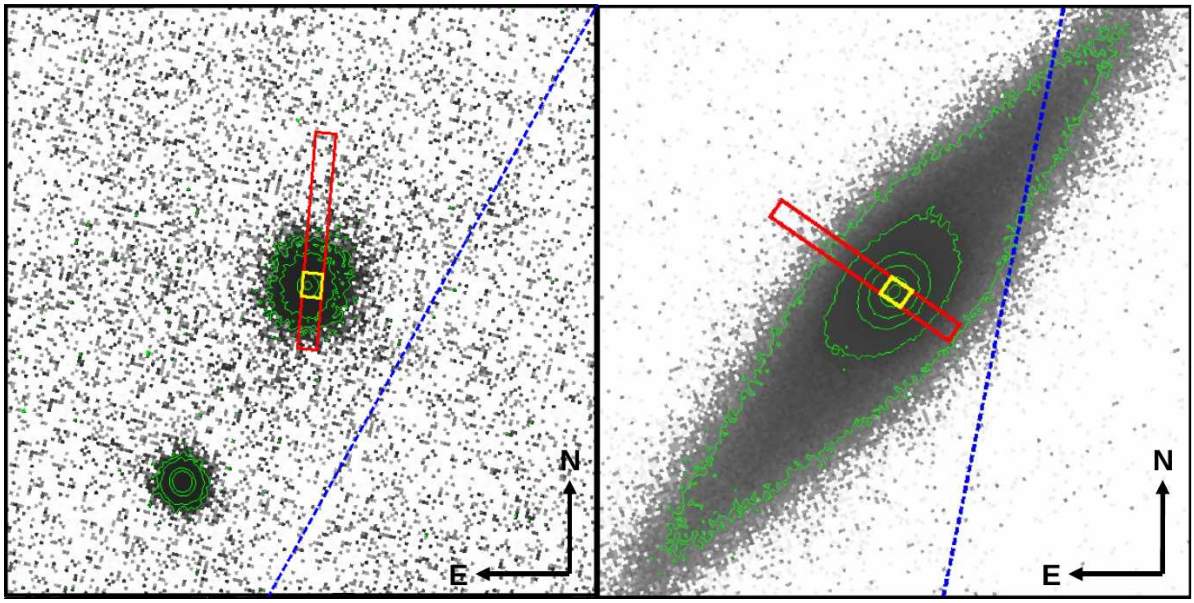

FIGURE 3.2: Section of $0.5' \times 0.5'$ of the acquisition image of J00 (left) and J02 (right) with the projection of the slit in the red box, $1'' \times 11''$, for one of the nodding positions. Both images were taken with the *i*-band filter. The small yellow box inside the slit is the extraction region of the spectrum, $1'' \times 1.22''$. The blue dashed line represents the parallactic angle at the end of of the acquisition of the first nodding position.

3.3 Modeling of the UV/optical continuum

We used the UV/optical spectra to recover the nuclear extinction, the intrinsic AGN continuum emission and the most conspicuous UV/optical broad and narrow emission lines. For the proprietary observations, except for one of the sources observed with X-Shooter, the spectra were taken with the slit at parallactic angle. The only source not taken at this angle is J02, because, as it is very extended, almost the totality of the slit would cover only galaxy (see Fig. 3.2), and hence it would not provide sufficient sky background, needed for the modelling of the spectrum. Nevertheless, using an angle different than the parallactic is not a problem as X-Shooter is equipped with an ADC (see Sec. 2.2.2.1). We present in Fig. 3.2 the acquisition images of both objects and indicate the slit projected in the sky, the extraction region of the spectra and the parallactic angle.

The spectra were reduced using the software IRAF[5], except the ones from X-Shooter. In this Thesis we reduced some of the TNG/DOLORES spectra (runs 09A, 09B and 10B), one from OSIRIS (run 15A) and the two objects from X-Shooter. The rest of the observations were already reduced at the time of the analysis. We used the standard procedures for the reduction of the spectra. This is: bias subtraction, flat field correction, extraction of the 2D spectra to 1D, wavelength and flux calibration using an standard star. IRAF's Laplacian Cosmic Ray Identification task for spectroscopy (`lacos_spec`, van Dokkum 2001) was applied to the raw images for cosmic ray rejection. In the conversion of 2D to 1D spectra using `apall` we estimate the error of each spectrum as well. We then shifted the UV/optical spectra to

[5]http://ast.noao.edu/data/software

vacuum wavelengths and corrected them for Galactic extinction using IRAF's `deredden` task using the Dickey and Lockman $N_{\rm H}$ map (Dickey and Lockman 1990) by transforming the $N_{\rm H}$ column density into $A_{\rm V}$ in each section of the sky for this step. We used the dust-to-gas ratio of the Milky Way $A_{\rm V}/N_{\rm H} = 5.3 \times 10^{-22}$ mag/cm^{-2} (Bohlin, Savage, and Drake 1978). There are six objects whose optical spectra have been reduced by collaborators, and we only have flux without error estimation. For these, we compute the SNR using the continuum fluctuations with the algorithm set forth by the Spectral Container Working Group of ST-ECF, MAST and CADC (Stoehr *et al.* 2008)[6].

The X-Shooter observations for J00 and J02 were taken close to the meridian and with low air mass, hence, the effect of the atmospheric dispersion is small. In addition, during our observations, the ADC was functional. We reduced the spectrum using the public X-Shooter pipeline version 2.3.0 with Gasgano, following the instructions described in the X-Shooter pipeline manual[7]. We used a binning in the wavelength direction of 0.02 nm pixel^{-1} for the UVB and VIS arms and 0.06 nm pixel^{-1} for the NIR arm, and a binning in the slit direction of 0.16 arcsec pixel^{-1} for the UVB and VIS arms and 0.21 arcsec pixel^{-1} for the NIR arm. For these objects `lacos_spec` was applied to the raw images for cosmic ray rejection, and then each arm was reduced individually. There are three different recipes to do the flux calibration: the offset mode, the staring mode and the nodding mode. We used the recipe for the staring mode, as it provides a better background subtraction. We used IRAF to extract the 1D spectra being careful to follow the trace. This was carried out with the routine `apall`. This is because the spectra have a trace whose centre was not constant in the cross-dispersion direction due to an imperfect order rectification of the pipeline. We joined the spectrum from different X-Shooter arms following the information about the dichroic crossover region in the X-Shooter user manual. To join the UVB and VIS arms, the crossover region is at 5595 Å, while between the VIS and NIR is at 10140 Å. The transition regions are 5560-5638 and 10095-10350 Å, respectively. A 0.9-1.1 scaling factor between arms is sometimes needed to match in flux the complete spectrum (López *et al.* 2016; Nisini *et al.* 2016). We used the average continuum in these regions around the crossover points to compute the flux scaling factors for each arm using the VIS one as reference. We scaled the UVB arm spectra using a factor of 0.9 while for the NIR arm a 1.0 flux scaling factor was acceptable. Errors were propagated through this process. The air wavelengths were transformed to vacuum, and then we applied the heliocentric correction. The spectra were corrected for the Galactic extinction as for the other proprietary data.

The aperture used to extract the spectra was defined to maximize the signal to noise of the AGN emission. This was carried out using the software IMFIT[8] on the acquisition images of the VLT observations. Both images were taken using the *i*-band filter. In both targets, a bright nuclear source was detected. To compute the fraction of the AGN light that enters through the slit, for J00 we decomposed the emission into a Gaussian function for the AGN, and a Sérsic profile for the host galaxy. J02 is an

[6] http://www.stecf.org/software/ASTROsoft/DER_SNR/der_snr.py
[7] ftp://ftp.eso.org/pub/dfs/pipelines/X-Shooter/xshoo-pipeline-manual-12.2.pdf
[8] http://www.mpe.mpg.de/~erwin/code/imfit/

edge-on galaxy (de Vaucouleurs *et al.* 1991) so we used a Gaussian profile for the AGN and two Sérsic profiles for the host galaxy, to fit the bulge and the disc. The parameters of the Sérsic and Gaussian models (intensity, σ, effective radius, Sérsic index) were computed with errors of ∼20 per cent or less, indicating reliable fits of the photometric images. The widths of the Gaussian profiles are ∼2.5 and ∼3.5 pixels for J00 and J02, respectively. We estimated that about 75 per cent and 56 per cent of the AGN emission is included in the slit for J00 and J02, respectively.

In order to measure the relative contribution of the AGN and the host galaxy, we model the continuum of the spectrum with templates reproducing the emission from the AGN and their host galaxies. We applied to the AGN continuum an extinction law, to take into account the nuclear extinction in terms of A_V, which is a free parameter in the fits. The extinction model chosen is the one from the SMC from Gordon *et al.* (2003). To conduct these fits, we use two different methods, depending on the spectrum available.

The UV-to-NIR spectra from X-Shooter have a wavelength continuum wide enough to constrain the shape of the host galaxies. Moreover, the AGN observed with this instrument have a high host contamination. These facts make it possible to accurately model in a robust way the host continuum using a set of Single Stellar Populations (SSP). For these cases we use the software STARLIGHT, (see Sec. 3.3.1). In the case of the statistical type-1 AGN sample, their UV/optical spectra have a more restricted wavelength range (it does not extend into the NIR as with the X-Shooter spectra) to conduct the previous analysis, so we have to use a different approach. In these cases we first determine a host galaxy model using SED analysis and then we decompose the observed spectra into host galaxy and nuclear emission with the host galaxy model fixed and its normalization left as a free parameter (see Sec. 3.3.2).

3.3.1 Detailed decomposition into AGN and host galaxy of X-Shooter spectra

To decompose the X-Shooter spectra into AGN and host galaxy emission at UV-to-NIR wavelengths, we used the software STARLIGHT (Cid Fernandes *et al.* 2005, Mateus *et al.* 2006).

In order to model the galaxy starlight we used a set of individual SSP templates from the Bruzual and Charlot (2003) library. We used 45 models with metallicities $Z = 0.05$, 0.02 and 0.004 in units of the solar value and ages ranging from 1 Myr to 13 Gy. The considered range of SSP provides a good modelling of our AGN hosts (Tremonti *et al.* 2004). The model is a linear combination of all the templates. The SSP templates are convolved with a certain velocity to take into account the stellar velocity dispersion, so the stellar features are well modelled. The input spectrum has to be in rest-frame wavelengths but the code allows for a shift in velocity.

The software allows as well to add additional templates, such as a power law continuum, and different extinction models. Moreover, it allows to obscure some of the templates by an additional extinction component. We use STARLIGHT to model the host galaxy with a combination of obscured SSP

(obscuration associated to dust in the host) and an additional template for the AGN emission, that can also be obscured to take into account the nuclear extinction. The UV-to-NIR spectra obtained by X-Shooter have enough wavelength range and SNR to measure the intrinsic shape of the host galaxy, so no additional information is needed to constrain the host galaxy emission.

There is some scatter in the continuum shapes of individual AGN which also depend on the SMBH mass and can vary with time (Koratkar and Blaes 1999, Schmidt *et al.* 2012, Baron *et al.* 2016). Since our aim is to reproduce the intrinsic AGN continuum by finding the model that best fits each source, we have adopted a broken power law ($F_\lambda \propto \lambda^\alpha$) with the break at 10000 Å and spectral index range of $\alpha = -1.9$ to -1.4 below the break and $\alpha = -0.8$ to -0.6 above it. These values fit well hard X-ray selected (2-10 keV) type-1 AGN (Polletta *et al.* 2007). The break is likely associated with the change in the AGN continuum slope between the IR bump and the Big blue bump (Koratkar and Blaes 1999). We created a set of broken power laws with steps in the power law index of $\Delta\alpha = 0.125$ for the blue region and $\Delta\alpha = 0.05$ for the red. STARLIGHT does not allow to leave the spectral index as a free parameter, so we chose the model among the described set of broken power laws that best fits each object.

To reduce noise and to follow the recommendations of the STARLIGHT manual we rebinned the spectra to 2 Å per bin. In the fitting we used the χ^2 statistic, taking into account the error of the input spectrum. The software does not compute uncertainties, so the extinction uncertainty was measured afterwards by other methods.

3.3.2 AGN and host galaxy modelling of UV/optical spectra

The line parameters and the spectral continuum fits for the BUXS type-1 sample were obtained with the CIAO's SHERPA fitting tool (Freeman et al. 2001) by minimizing the χ^2 statistic. This software takes into account the error of the input data. In order to fit the continuum of the sources, we have built a model similar to the one described in the previous section: a combination of a host galaxy plus AGN emission, the latter affected by a certain amount of extinction. We had to add Fe II emission and the Balmer continuum to the featureless AGN continuum, as for some objects only AGN emission does not provide acceptable fits. In order to reduce the many degrees of freedom of our model, we made some assumptions:

- To accurately choose the best host galaxy model we need to determine the overall shape in a wide wavelength range to avoid degeneracies. We use best-fit host galaxy templates from the SED decomposition presented in Mateos *et al.* (2015), if in the SED fitting it was necessary to introduce this component. This was decided by conducting the fits with and without host galaxy template, and if the $\Delta\chi^2$ between those models is higher than 2σ, we accepted the detection of the stellar component.

- The AGN is obscured using the Gordon *et al.* (2003) extinction model. As mentioned in Sec. 1.4, it is the one that better explains the absorption in QSOs. This model has $R = A_V/E(B-V) = 2.74$ and $A_V/N_H = (13.18 \pm 1.02) \times 10^{-22}$ cm^{-2} mag^{-1}. We do not allow $A_V < 0$ mag to prevent unrealistic results.

- To take into account the featureless continuum emission, we used the QSO template from Richards *et al.* (2006). It does not include the emission lines nor pseudocontinuum emission, as both components were subtracted to build the template. This is not a problem since the spectral ranges with the strongest AGN emission lines were not used in our fits (see below).

- To model the contribution of the FeII lines, we used the theoretical model of Verner *et al.* (2009). This is a QSO FeII emission spectra with data from 1000 to 10000 Å, constructed using a 830-level model atom for FeII. Various templates are available depending on the N_H density, the microturbulence and the ionizing flux. We used the one that best fits I Zw 1, the prototypical AGN for the FeII emission. This is an approach often used in the literature to fit the FeII emission in AGN (e.g. Dong *et al.* 2008, Jin *et al.* 2012a, Castelló-Mor *et al.* 2014). The conditions are a density of $\log(N_H/\text{cm}^{-3}) = 11$, a microturbulence of $\xi = 30$ km/s and an ionizing flux of $\log(\Phi/\text{cm}^{-3}\ \text{s}^{-1}) = 20.5$. This template has to be convolved with the velocity dispersion of the material in the BLR (Netzer 1990, Greene and Ho 2006, Shields, Ludwig, and Salviander 2010). A velocity between 1.0 and 0.8 times the one of H_β provides a good fitting of the FeII emission as it comes from the outer parts of the BLR (Osterbrock 1991). We used an intermediate value of 0.9 times the BLR velocity, that we calculate fitting the H_α, H_β and/or MgII regions (see Sec. 3.3.3). This allows fixing the velocity dispersion of the lines, the only degree of freedom being the normalization of the FeII complex.

- The last component of the AGN emission that we have incorporated is the Balmer continuum, i.e. the free-bound continuum bluewards $\lambda < 3646$ Å. It depends on the temperature of the electrons T_e, and the optical depth τ_{BC}. Redwards of 3646 Å, the high order Balmer lines pile up forming a rise from $\lambda = 3646$ Å. To model the rise we use the Balmer lines between the energy levels $n = 5$ and $n = 50$, using the Case B ratios with $T = 15000$ K, $n_e = 10^{10}$ cm^{-3} from Storey and Hummer (1995), as used in Kovačević, Popović, and Kollatschny (2014). The FWHM was fixed to the observed value of the FWHM of the BLR lines in the same source (as mentioned above, see Sec. 3.3.3). The peak in flux is matched with the Balmer continuum at $\lambda = 3646$ Å, (see Eq. 3.2, Grandi 1982). We use $T_e = 15000$ K and $\tau_{BC} = 1$ as in Kovačević, Popović, and Kollatschny (2014). In the equations just below $B_\lambda(T_e)$ is the Planck function at the temperature T_e (see Eq. 3.3), and τ_λ is the optical depth at a certain λ:

$$F(\lambda) = K \times B_\lambda(T_e)\,(1 - e^{-\tau_\lambda}),\ \lambda \leq 3646\text{Å} \tag{3.2}$$

where

$$B_\lambda(T_e) = \frac{2hc^2/\lambda^5}{e^{hc/\lambda kT} - 1} \tag{3.3}$$

and

$$\tau_\lambda = \tau_{BE}\left(\frac{3646\text{Å}}{\lambda}\right) \tag{3.4}$$

With this model we have five free parameters: the nuclear extinction and the normalizations of the AGN, the FeII complex, the Balmer continuum and the normalisation of the host galaxy. Following the approximations explained above we can carry out a proper fit of the UV/optical continuum of AGN to measure the extinction in terms of A_V.

As opposed to the objects with X-Shooter spectra (see Sec. 3.3.1), in this case we fixed the shape of the AGN featureless continuum to the one of the QSO template from Richards *et al.* (2006), with a spectral index of $\alpha = -1.78$. This is because the objects in this part of the study have not enough wavelength coverage to resolve the degeneracies. In this case, the estimations of A_V are calculated with respect to this template and mild variations may be found if other templates are used (Selsing *et al.* 2016). We show in Sec. 5.6.1 that the fitted values for A_V would not change substantially of other slopes are used.

We visually inspected all fitted spectra in order to identify and mask out wavelength regions that present structures that may affect the results of the fits. This includes the telluric absorption bands or the most conspicuous broad and narrow emission lines present in each spectrum, such as the Balmer lines, MgII, and the doublets of narrow emission lines of [OIII], [NII] and [SII] mainly.

The fits made by CIAO's SHERPA allow computing errors using 1σ confidence intervals from $\Delta\chi^2$, so normally errors are not symmetrical. To be as precise as possible, we compute the χ^2 statistic for the best fits using different A_V values. This allows to obtain the probability of A_V as $P(A_V) \sim e^{-\Delta\chi^2/2}$. In this case, the errors for A_V are estimated using the smallest 1σ probability interval that contains the mode (the best fit value). In these calculations we have to include the uncertainty of the extinction model. To do so, we convolve the probability distributions of A_V with a Gaussian with the same width as the mean error of the SMC model of Gordon *et al.* (2003) in the wavelength region of the fits, that is computed for each spectrum.

3.3.3 Optical emission line fits

Fitting the UV/optical emission lines give us information, such as the bulk velocity of the line emitting material or the classification and subclassification of the AGN. In this Thesis we fitted the wavelength regions surrounding H_α, H_β and MgII to recover the emission line parameters. The model we used to approximate the profile of the lines is a Gaussian. We assumed the same width, in velocity, for all the narrow emission lines, as we do expect that all of them are coming from the same region, and so, the material is moving with the same velocity dispersion. The fits were made using CIAO's SHERPA. In these fits we used the observed spectra without subtracting stellar emission fitting the local continuum with a power law. This is because the available host galaxy templates used in the SED fitting do not have enough wavelength resolution to accurately correct the stellar absorption features of H_α and H_β.

Since the stellar absorption features are narrow, they are not expected to affect the broad emission line measurements.

For the H_α region, we fitted the rest-frame [NII]$\lambda\lambda$ 6549,6585 Å , [SII]$\lambda\lambda$ 6716,6731 Å , and H_α narrow lines, all of them with the same width, the relative ratios of the line centers fixed and the flux left free to vary. For the broad component of H_α, the flux, line width and centroid were left free to vary. Lastly, we modelled the local continuum with a power law. The wavelength region that we used to fit the H_α line is from rest-frame 6400 and 6800 Å. For twelve objects we had to use a wider wavelength interval to robustly measure the continuum around the line, since some broad lines are very wide, and so the mentioned wavelength range does not cover any region without broad line emission.

The H_β region was fitted generally in the 4700 – 5100 Å rest-frame wavelength range, but as in the H_α region, some spectra (in this case seven objects) needed a wider wavelength range to measure better the continuum, also modelled as a power law. We fitted the H_β and the rest-frame [OIII]$\lambda\lambda$ 4959,5007 Å narrow emission lines. The widths were the same for all the narrow lines, the relative distance of the line centers are fixed but their fluxes are free. To model the broad component of H_β the flux, width and centroid are free parameters. If our spectra cover both the H_α and H_β lines and they are both detected, the width and the offset of the line with respect to the narrow component were fixed generally to the same as the broad H_α values in velocity, if the measurement of the H_α line width is able to fit the H_β region with the same width. For eight objects, we did not fix the width between H_α and H_β, as due to the peculiar shape of the lines (for example asymmetrical profiles or narrow lines with two components) the fit results were problematic. We checked in these cases that the velocity obtained for the broad lines is consistent within the uncertainties. For eight objects, the residuals of the broad component suggested that the FeII continuum was affecting the fits in the H_β region, so we removed this emission using the FeII template described in Sec. 3.3.2.

We used the rest-frame 2700 – 2900 Å region to fit the MgII emission line. To measure the broad component we used a Gaussian with three degrees of freedom (flux, width and centre) and a local continuum with the form of a power law. For five objects we also added two additional Gaussian profiles in order to fit absorption lines, that are sometimes present in the same region of the broad line (Steidel *et al.* 1997). The pseudocontinuum present in that region can affect the FWHM estimation, so we initially fitted the observed MgII region and then we subtracted the pseudocontinuum contribution. After that we fitted again only the continuum plus the MgII line contribution.

The detection of the broad component is crucial as it determines if the object is classified as either type-1.9 or type-2 and thus, whether it should be included in the type-1 BUXS sample (assuming that the broad component is not detected in H_β). To robustly confirm the detection of a broad component in H_α, we tested whether there was a possible outflow of NLR material, that can be mistaken as a broad H_α emission line (Shimizu *et al.* 2018). For the objects in which it is difficult to confirm the detection of a faint broad H_α line, we helped the fits by fixing the fluxes of the [NII] lines at [NII]λ 6585 Å= 2.96× [NII]λ 6549 Å. To do this, we fitted each of the narrow lines in the H_α wavelength region with two

components for all objects originally classified as type-1 AGN. To confirm the presence of an outflow, we also fitted the H_β region to check whether the [OIII] lines need as well two components. This exercise allowed us to build a sample with the most robust classification as possible with our data, avoiding false broad line detections. We used $\Delta\chi^2 > 3\sigma$ between the fit with and without a broad emission line as a threshold to ensure that a broad line is detected in the spectrum. We used the same 3σ threshold to detect the presence of outflowing components in the narrow lines. We found 2 type-2 objects whose possible broad H_α line was an effect of an outflowing material from the NLR and not a real broad emission line.

There are six objects whose broad line has a highly asymmetric profile and thus, a single Gaussian can not accurately measure the profile of the line, as the residuals indicated a poor fit. In these cases, we modelled the line with up to three Gaussian profiles. The FWHM of the asymmetrical broad components and its errors were computed with simulations using the median and 1σ percentiles.

As in the case of the optical continuum fits, the errors of every fit parameter are computed using $\Delta\chi^2$ using 1σ asymmetric errors for each free parameter.

3.4 AGN samples used in this Thesis

In this Thesis we use two different samples of AGN drawn from the BUXS survey. The first is a small sample of two lightly X-ray absorbed type-1.9 AGN. The two objects, J00 and J02, were included in a proposal for follow-up with X-Shooter (see Sec. 2.2.2.1 for technical details). These objects are not the only lightly X-ray absorbed type-2 AGN in BUXS, but they are the only two which were successfully observed by X-Shooter.

The second part of this Thesis consists on a statistical study of the nuclear obscuration in AGN. To maximize the contrast between AGN and host galaxy emission, we focus on optical type-1 AGN, i.e., in those objects with detected rest-frame UV/optical broad emission lines.

We discard in this study the objects with $\log(L_{2-10\ \mathrm{keV}}/\mathrm{erg\ s^{-1}}) < 42$ in order to ensure that the X-ray emission is coming from the AGN and to minimize the contamination from the host galaxy. All type-1 AGN in BUXS with $\log(L_{2-10\ \mathrm{keV}}/\mathrm{erg\ s^{-1}}) < 42$ have $z < 0.05$, therefore this is the effective lower limit in the full sample of type-1 AGN. As one of the objectives is to determine the intrinsic distribution of N_H for type-1 AGN and its relation (or lack of it) with the optical extinction, we also set a limit in redshift of $z < 1$. This is because we want to measure in a robust way the X-ray absorption, which in type-1 AGN is expected to be low (Lusso *et al.* 2013, Shimizu *et al.* 2018). With increasing z, it is harder to detect the attenuation at soft X-ray energies since such spectral feature will fall outside the observed X-ray energy range (Mushotzky 2004). Additionally, we discard two objects whose SNR in the UV/optical spectrum is SNR < 4. Lastly, we discard 2XMMJ144411.3+291508 whose TNG spectrum shows broad MgII emission, but the broad H_β emission line is not detected, even though it is covered

TABLE 3.2: BUXS type-1 sample.

	Type-1 (MgII)	Type-1.0	Type-1.2	Type-1.5	Type-1.8	Type-1.9	Total
Full sample	21	35	36	20	7	13	132
$z < 0.65$	1	23	32	17	6	13	92
$z < 0.2$	0	4	9	8	1	10	32

Sources and classification according to the scheme described in Fig. 3.3 for the 132 objects in the BUXS type-1 selected sample and the $z < 0.65$ and $z < 0.2$ subsamples.

by the spectrum. This is likely produced by host dilution of the H_β region, while in the MgII spectral region the starlight is much less important. The continuum spectrum fits (see Sec. 3.3.2) give an upper limit in A_V of 4 mag, so it is not informative and complicates the discussion and subclassification of this source.

The final number of type-1 AGN fulfilling the conditions above is 132, including type-1.8 and type-1.9, often classified as type-2 AGN in the literature. The total number of type-2 in the BUXS sample between $z = 0.05$ and $z = 1$ is 67. At redshifts closer to $z = 1$, we do not cover H_β so some of the sources with enough extinction to suppress MgII but not H_β or H_α would be classified as type-2 due to wavelength coverage.

Taking this into account, we have defined two samples:

- 92 sources with $z < 0.65$: we have intermediate classifications from 1.0 to 1.8 (our spectra cover H_β, but H_α is not covered for all of them) for all sources (except for one particular object observed with NTT, that we can only classify it as a type-1 with only MgII covered, but it is not excluded from this sample) in this spectral range.
- 32 sources with $z < 0.2$: a complete sample with intermediate classifications from 1.0 to 1.9 for all sources (our spectra cover both H_α and H_β). This is a subsample of the previous subsample.

Our AGN classification scheme is based on the one from Whittle (1992) and is described in Fig. 3.3. We note that, if we use instead the classification scheme from Winkler (1992), that is used in the Véron-Cetty and Véron (2001) QSO catalog, we get similar results. We summarize in Table 3.2 the classification of the type-1 BUXS sample used in this Thesis. There are AGN where only broad MgII is available (21 out of 132; 16 per cent), as H_α and H_β are not covered with our UV/optical spectroscopic observations. These sources are labelled as type-1 (MgII), as we can only classify them as a generic type-1 AGN.

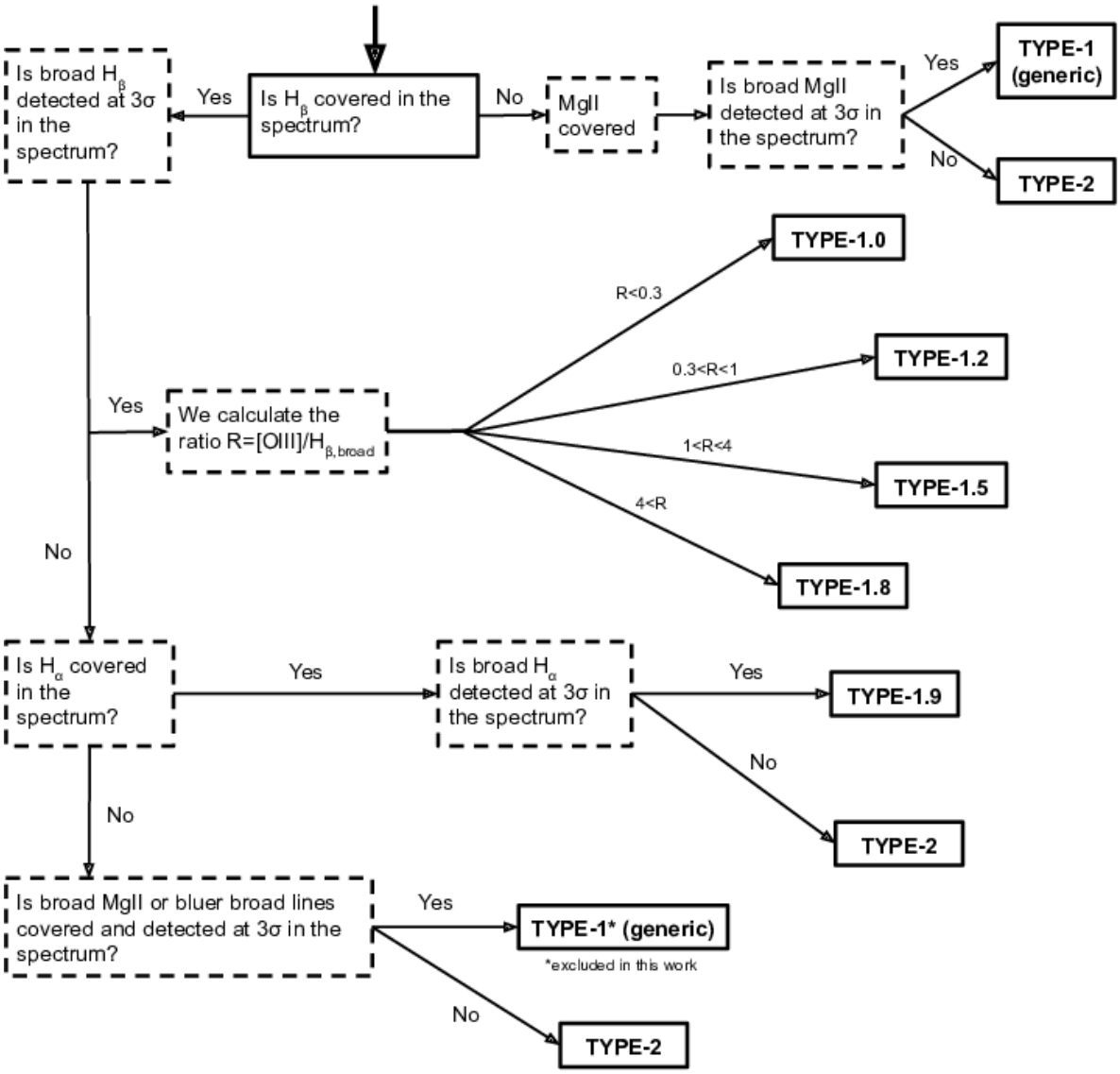

FIGURE 3.3: Classification scheme used in this work, based on the one from Whittle (1992).

Chapter 4

Detailed study of two AGN

The objective of this study is to get insight into the physics behind the apparent mismatch between UV/optical and X-ray classification of two lightly X-ray absorbed type-1.9 AGN at low-z selected from BUXS (see Sec. 3.4). In this chapter we check whether the Unified Model can explain the observed properties of these AGN.

By comparing the properties derived from the X-rays (absorption) and at UV/optical wavelengths (extinction), we have tested several possible scenarios: a) the presence of a Compton-thick AGN; b) the obscuration and intrinsic properties in these AGN are standard but they are hosted in very massive galaxies, or a low luminosity AGN in normal host galaxies and where the broad UV/optical emission lines are diluted by the host galaxy emission; c) intrinsic non-standard nuclear properties, such as a high dust-to-gas ratio or an intrinsically weak BLR.

4.1 AGN sample

The two objects studied are J00 and J02 (see Chap. 3), at z = 0.1075 and 0.0246, respectively. While both sources are lightly X-ray absorbed, J00 has been optically classified as type-1.9 using optical spectroscopic observations from the SDSS-DR7 (Abazajian *et al.* 2009) and J02 is optically classified as a type-2 AGN using the spectrum from the Six-Degree Field Galaxy Survey (6dF; Jones *et al.* 2009). As we will show below, during the work for this Thesis we have reclassified J02 as a type-1.9 AGN.

For both sources, we have proprietary high resolution UV-to-NIR X-Shooter spectra (P.I.: S. Mateos, see Table 2.2 for the details of the observations), as well as good quality (2490 and 1696 net EPIC counts for J00 and J02, respectively) XMM-Newton X-ray spectra in the observed energy range from 0.25 to 10 keV (Table 4.1).

TABLE 4.1: Summary of X-ray properties of our AGN.

Object	z	Obs. ID	T_{exp}	Cts	F	log(L)	$N_{\rm H}$	$N_{H,G}$	Γ	kT	Model	χ^2/d.o.f
					10^{-13}		10^{21}	10^{21}				
			ks		erg cm^{-2} s^{-1}	erg s^{-1}	cm^{-2}	cm^{-2}		keV		
(1)	(2)	(3)	(4)	(5)	(6)	(7)	(8)	(9)	(10)	(11)	(12)	(13)
		0305751001	26.57	1172								
J00	0.108	(2005-12-10)	(11.48)	(1318)	2.04±0.22	42.76±0.05	<0.67	0.31	1.66±0.09	$0.16^{+0.01}_{-0.02}$	*zwabbpo*	169.2/139
		0151490101	55.20	830								
J02	0.025	(2003-07-16)	(22.02)	(866)	$1.31^{+1.07}_{-0.99}$	41.25±0.03	$1.7^{+2.0}_{-1.4}$	0.51	2.08±0.09	-	*zwapo*	135.1/100

Notes: (1): J00=2XMMiJ000441.2+000711, J02=2XMMJ025218.5-011746. X-ray source identifier as listed in the Second XMM-Newton Serendipitous Source Catalogue (2XMM-DR3; Watson *et al.* 2009); (2): redshift; (3): XMM-Newton Observation ID. In brackets we show the date of the observation; (4): net MOS and pn (in brackets) exposure time after removal of high background flares; (5): net counts of the MOS and pn (in brackets) spectra between 0.25 and 10 keV; (6): 2-10 keV flux; (7): logarithm of the intrinsic, absorption corrected, 2-10 keV luminosity; (8): intrinsic X-ray column density; (9): Galactic column density from Dickey and Lockman (1990); (10): power law photon index; (11): temperature of the black body; (12): best-fitting model (see Sec. 3.2.2); (13): χ^2 value and number of degrees of freedom. All reported errors are at the 1σ level.

4.2 X-ray spectral fits

We fitted the X-ray spectra of our sources with a combination of different models to determine the shape of the direct broad-band continuum components and the rest-frame line-of-sight X-ray absorption using a minimum grouping of 15 counts per bin. The description of the fitting procedure is detailed in Sec 3.2. We used χ^2 statistics to fit both the pn and MOS spectra with the parameters of the model tied, except for all normalisations, as mentioned in Sec. 3.2. The X-ray luminosities were computed in the rest-frame 2-10 keV energy band. They were corrected for X-ray absorption both Galactic and intrinsic to the sources.

- **J00:** it is X-ray unabsorbed. The 1σ upper limit on the column density is 6.7×10^{20} cm^{-2}. The best-fitting model is a combination of a black body with temperature $kT = 0.16^{+0.01}_{-0.02}$ keV and an unabsorbed power law with photon index $\Gamma = 1.66 \pm 0.09$. The X-ray spectra (MOS and pn) are shown in Fig. 4.1 (top). The black body emission is a phenomenological model often used in the literature to fit the soft X-ray excess (Corral *et al.* 2015). Nevertheless this is not physically correct for J00, as it is well known that the black body temperature of an accretion disk around a SMBH such as the one for J00 (see Sec. 4.4.1) is too low to explain the soft X-ray excess. Since the photon index obtained for J00 is somewhat low, for a sanity check we computed the X-ray absorption with a fixed photon index of $\Gamma = 1.9$, the typical value for type-1 AGN (Caccianiga *et al.* 2004, Galbiati *et al.* 2005, Mateos *et al.* 2005b, Mateos *et al.* 2005a, Tozzi *et al.* 2006, Mateos *et al.* 2010, Corral *et al.* 2011). Even with this fixed value of the photon index, we still classify this object as a low absorption AGN ($N_{\rm H} \leq 1.3 \times 10^{21}$ cm^{-2}). We also tried a more physically motivated model, albeit more complex, replacing the black body with a hot diffuse gas model (`mekal` model in XSPEC). This gives us an upper limit on the column density of 2.4×10^{20} cm^{-2}

(with $\Gamma = 1.83 \pm 0.07$, χ^2/d.o.f = 173.7/139). The results, in terms of the X-ray classification as absorbed/unabsorbed, do not change using one model or the other. Therefore we use in this work the results with the black body since we obtain a more conservative value of $N_{\rm H}$. The Equivalent Width (EW) of the Fe line at rest-frame 6.4 keV is formally EW = $0.30^{+0.16}_{-0.17}$ keV, but adding this line is not statistically significant ($\Delta\chi^2 = 3$ for Δd.o.f. = 1, a 1.73σ detection). As it is below the 3σ threshold, we did not include the Fe line in the final model. Looking at the spectrum of J00 (Fig. 4.1) we can see a bump at the hard X-ray energies (>5 keV), but we believe that it is not real, since it is only present in one of the EPIC cameras. This feature is probably associated with residuals in the background subtraction. Nevertheless, since the shape of the continuum is very well determined at lower energies, the above mentioned bump is not affecting our best-fit estimates.

- **J02:** the best-fit model is an absorbed power law with photon index $\Gamma = 2.08 \pm 0.09$ and intrinsic $N_{\rm H} = 1.7^{+2.0}_{-1.4} \times 10^{21}$ cm^{-2}. The EW of the Fe line is formally EW = $1.12^{+0.49}_{-0.39}$ keV, that is large, but the detection is not significant ($\Delta\chi^2 = 6$ for Δd.o.f. = 1, a 2.45σ detection, see also Fig. 4.1). As in J00, we did not include the Fe line in the final model.

4.3 UV-to-NIR spectra fits

4.3.1 AGN and host galaxy continuum decomposition

We fit both spectra using the STARLIGHT software using a broken power law model for the nuclear emission and a set of SSP for the host emission (see Sec. 3.3.1). The spectral range used in the fit is between 3700 and 16000 Å (rest-frame). In order to fit the AGN and host galaxy continuum emission only, we masked out the spectral ranges where the strongest AGN emission lines and the telluric absorption lines are expected (see grey and yellow bands in Fig. 4.2). We excluded the regions between 6850 – 6950 Å, 7165 – 7210 Å and 7550 – 7725 Å, where some residuals of telluric features in the Bruzual & Charlot library are present.

Fig. 4.2 shows the results of the spectral decomposition. In both objects, the observed emission is dominated by the host galaxy across the full range of wavelengths sampled with our observations. The best-fit slopes of the AGN continuum at rest-frame UV/optical wavelengths are $\alpha_{\rm blue} = -1.90$ and $\alpha_{\rm red} = -0.6$ for J00 and for J02 $\alpha_{\rm blue} = -1.78$ and $\alpha_{\rm red} = -0.6$ below and above the break at 10000 Å, respectively. The intrinsic extinctions of the AGN continua are $A_{\rm V} = 2.04 \pm 0.30$ mag and $A_{\rm V} = 2.19 \pm 0.33$ mag for J00 and J02, respectively.

We computed the errors in the extinction by varying the power-law indices and obtaining the χ^2 value. The errors are very small (<1 per cent) using this approach. We added an additional 15 per cent error

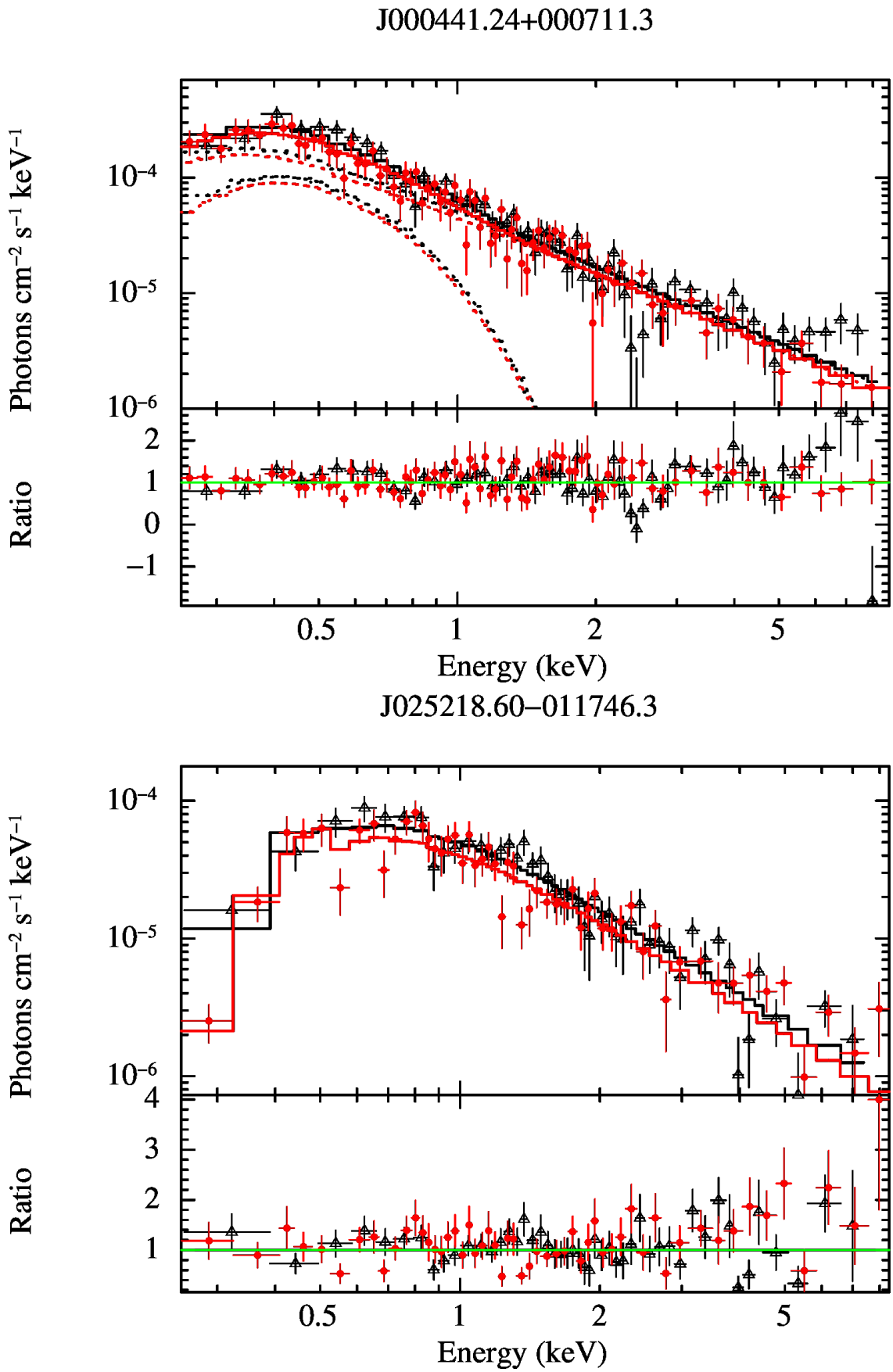

FIGURE 4.1: Top: MOS (black triangles) and pn (red dots) spectra of J00 and the best fit model (blackbody + power law) in solid lines. Each model component is plotted with dotted lines. Bottom: MOS (black triangles) and pn (red dots) spectra of J02. The best fit model (absorbed power law) is shown with solid lines. We also represent the ratio between the data and the best-fit model. These are `ufspec` plots from XSPEC, i.e. with the Response Matrix Files (RMF) and Ancillary Response Files (ARF) deconvolved using the best fit model.

contribution to account for the overall uncertainty of the SMC extinction model used (Gordon *et al.* 2003). This contribution to the error is the one that dominates.

We believe that the results from our AGN and host galaxy decomposition analysis are robust because the X-Shooter spectra have a sufficiently large wavelength range to constrain the host galaxy contribution. Moreover, the stellar features present in the spectra, such as the CaII $\lambda\lambda$3934, 3969 absorption-lines, help constraining the emission from the hosts (see Fig. 4.2). If more relative contributions of the nuclei were present in the spectra, this would in fact, flatten the stellar features to a more featureless contribution contrary to what we observe in the fitting model and the residuals.

4.4 Analysis of the UV/optical emission from the AGN

We extract the information of the emission lines by fitting the H_α and H_β wavelength regions of the host-galaxy-subtracted spectrum. We fit these regions using a local power law and Gaussian emission as described in Sec. 3.3.3. In Fig. 4.3 we show the results from the fitting of the H_α and H_β, while best-fitting values are indicated in Table 4.2.

Since the broad H_β component was not detected in any of the spectra, only an upper limit could be computed for the Balmer decrement from the BLR. Line parameters and Balmer decrements are reported in Table 4.2. The Balmer decrement derived from the flux ratio of the narrow components of the H_α and H_β emission lines will be compared in Sec. 4.5.3 with the absorption measured in the X-rays and the extinction of the rest-frame UV-to-NIR continuum.

4.4.1 SMBH masses

We estimate SMBH masses for our targets using the luminosity and the FWHM of the H_α broad emission line and the expression from Greene and Ho (2005),

$$\begin{aligned} log\left(\frac{M_{SMBH}}{M_\odot}\right) = (0.45 \pm 0.05)\log\left(\frac{L_{H_\alpha}}{10^{42} ergs\ s^{-1}}\right) + \\ +(2.06 \pm 0.06)\log\left(\frac{FWHM_{H_\alpha}}{10^{3} km\ s^{-1}}\right) + 6.40^{+0.09}_{-0.07} \end{aligned} \tag{4.1}$$

where $M_{\rm SMBH}/M_\odot$ is the mass of the SMBH in solar masses. L_{H_α} is the intrinsic luminosity of the H_α emission line in erg s^{-1}, corrected for both the nuclear and the host galaxy extinction. Finally $\rm FWHM_{H_\alpha}$ is the FWHM of the broad H_α emission line in km s^{-1}. We have corrected the FWHM of the lines by the instrumental spectral dispersion by subtracting the instrumental broadening in quadrature.

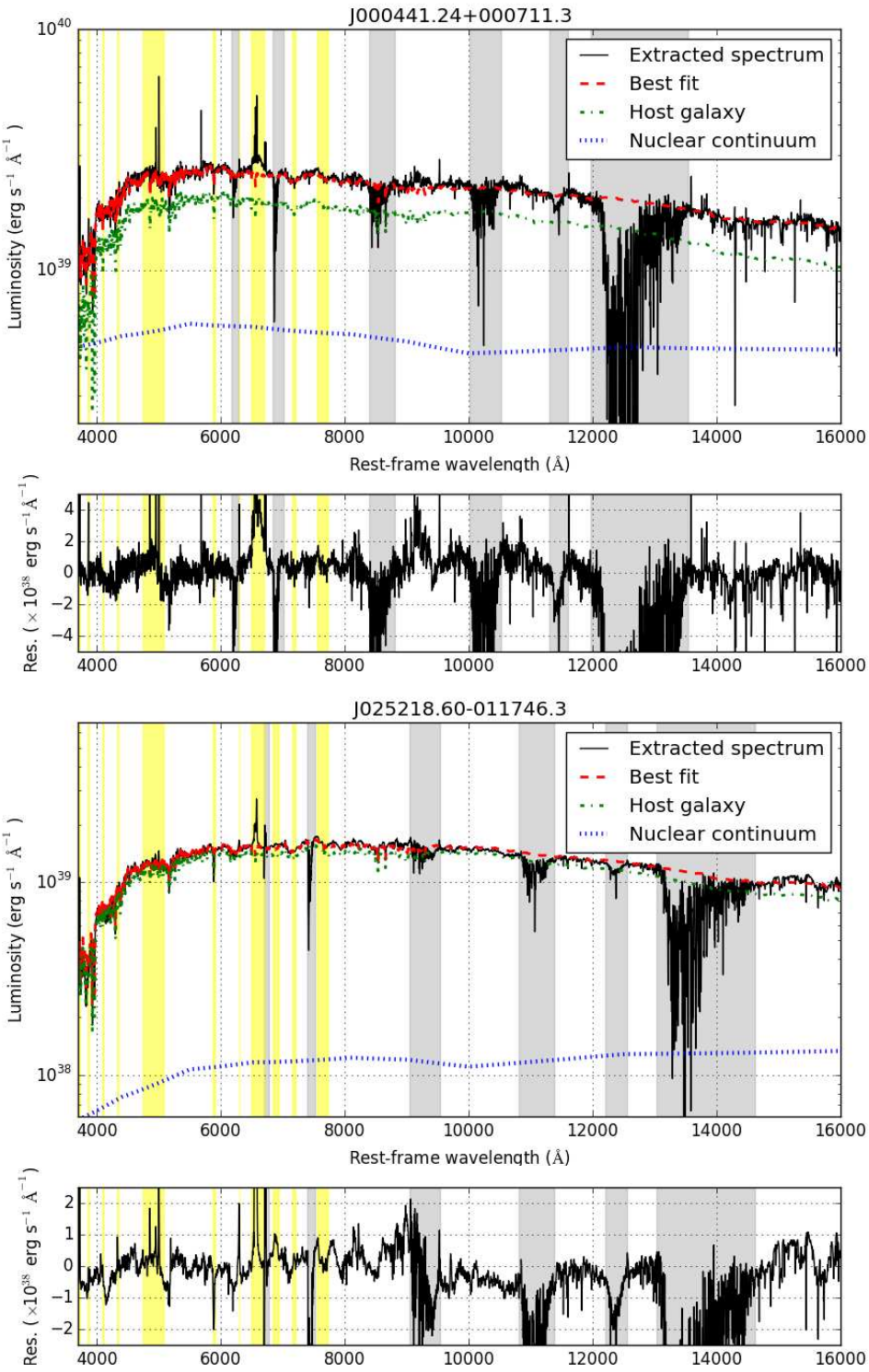

FIGURE 4.2: Decomposition of the UV-to-NIR spectra of J00 (top) and J02 (bottom) into host galaxy and AGN components. The upper panels represent the results of the fits while the bottom panels show the residuals of the fits. The grey and yellow bands indicate the telluric absorption features and the spectral regions with the AGN strongest emission lines, respectively, which are ignored in the fits.

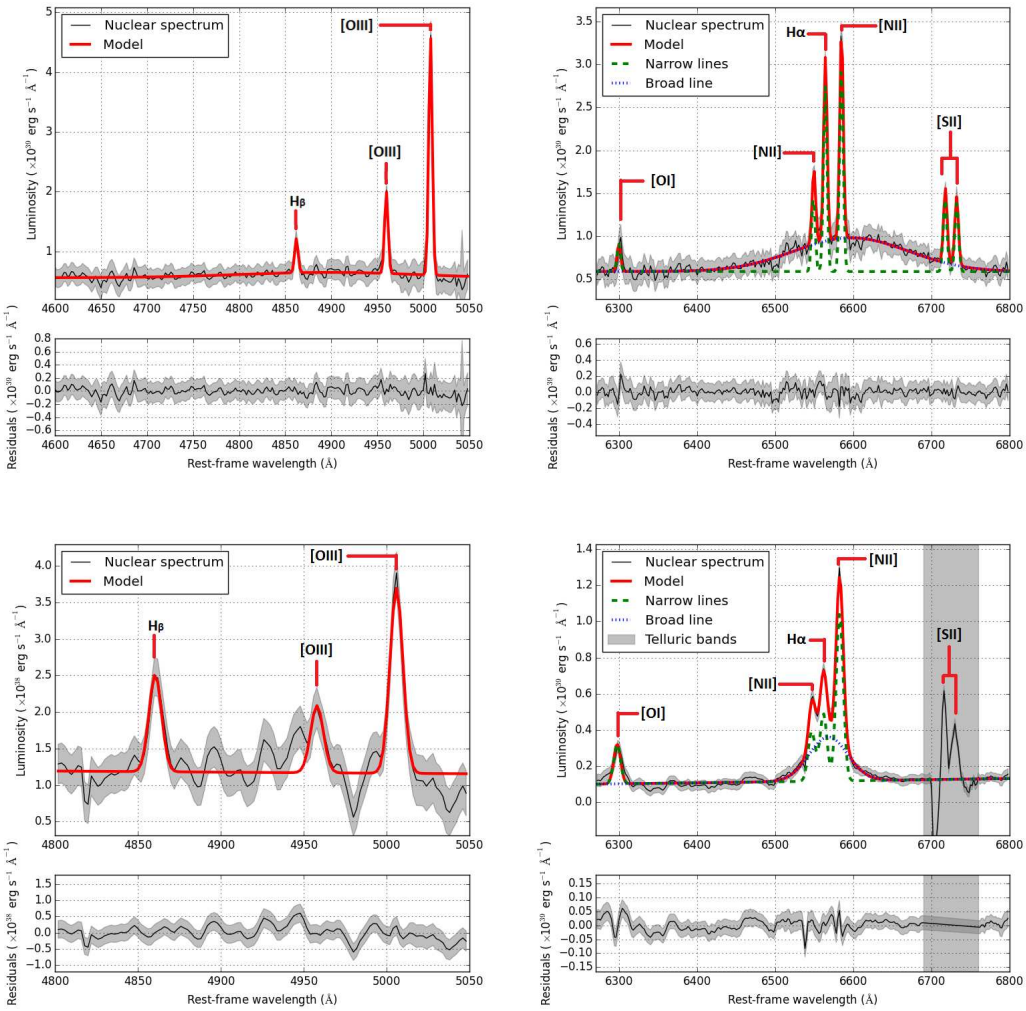

FIGURE 4.3: Decomposition of the AGN emission into continuum plus narrow and broad emission lines for J00 (top) and J02 (bottom). Left panels: H_β+[OIII] region. Right panels: H_α region. In grey we show the uncertainties on each spectrum. We also indicate the observed narrow emission lines.

We show the SMBH masses computed using Eq. 4.1, as well as the relevant luminosities, in Table 4.2. In addition we list the bolometric and Eddington luminosities for our sources, as well as the Eddington ratios ($L_{bol}/L_{Edd.}$). The bolometric luminosities are calculated using the expression $L_{\rm bol} = 9 \times \lambda L_{5100}$ (Kaspi *et al.* 2000b), being L_{5100} the monochromatic luminosity of the dereddened nuclear emission at rest-frame 5100 Å. The Eddington ratios are within the expected values for nearby AGN with similar bolometric luminosities and SMBH masses (Panessa *et al.* 2006).

4.4.2 Host galaxy masses

It is well known that the SMBH mass and the spheroidal mass of the host galaxies follow a linear relation in log space (Merritt and Ferrarese 2001, Park *et al.* 2012). In this study we calculate both the dynamical mass and the stellar mass from the spheroidal component of the host galaxy.

TABLE 4.2: Emission line fitting results.

	J00	J02
$FWHM_{H_\alpha,b}$ (km/s)	7830 ± 1221	2499 ± 175
$FWHM_{H_\alpha,n}$ (km/s)	246 ± 19	376 ± 17
$L_{H_\alpha,b}$	22.0±2.0	6.15±0.61
$L_{H_\alpha,n}$	2.63±0.13	0.52±0.08
$L_{H_\beta,b}$	≤16.2	≤1.51
$L_{H_\beta,n}$	$0.89^{+0.19}_{-0.21}$	0.17±0.03
$L_{[OIII],5007Å}$	$8.37^{+0.49}_{-0.62}$	$0.81^{+0.8}_{-0.12}$
$L^o_{H_\alpha,b}/L^o_{H\beta,b}$	≥3.13	≥11.40
$L^o_{H_\alpha,n}/L^o_{H\beta,n}$	$4.41^{+0.92}_{-1.34}$	$3.34^{+0.80}_{-1.05}$
L_{bol}	1192± 118	243 ± 30
$\log(M_{SMBH}/M_\odot)$	$7.96^{+0.23}_{-0.25}$	$6.74^{+0.26}_{-0.22}$
$L_{Edd.}$	$1.19^{+0.97}_{-0.56}\times10^6$	$0.071^{+0.052}_{-0.036}\times10^6$
$L_{bol}/L_{Edd.}$	$0.0010^{+0.0004}_{-0.0010}$	$0.0034^{+0.0011}_{-0.0034}$

Notes: Properties of the different broad and narrow emission lines (subindex 'b' and 'n', respectively) used in our analysis and properties of the SMBH. We show the full width at half-maximum for narrow and broad H_α lines. All luminosities are in units of 10^{40} erg/s. The fits to the lines used to determine the Balmer decrement use as baseline the host-galaxy-subtracted spectrum. All luminosities are extinction corrected, except for those with the superindex 'o'.

4.4.2.1 Stellar masses

STARLIGHT provides stellar masses for its best fit models. We have corrected those for slit losses using the information obtained using IMFIT (see Sec. 3.3). We computed the fraction of flux of the Sersic profile of the spheroidal component that enters through the slit and compared it with the total flux of the Sersic profile to calculate the slit losses. The fractions of the spheroid light that went through the slit are 9.0 and 6.2 per cent for J00 and J02, respectively.

The stellar mass, M_{stell}, derived using STARLIGHT is computed using mass-to-light relations, converting each SSP contribution to stellar mass. STARLIGHT does not compute errors in the best-fitting values. In Bell and de Jong (2001) the uncertainties associated to the stellar mass-to-light ratio are discussed. These uncertainties are all of the order of 0.1 − 0.2 dex. We use the largest value to be conservative. Our results are shown in Table 4.3.

4.4.2.2 Dynamical masses

As a sanity check, we also computed the dynamical mass of the spheroidal component of the host galaxies, M_{dyn}. We obtained M_{dyn} using the line-of-sight velocity dispersion (σ_e) as described below.

The observed width of the NaI doublet at rest-frame $\lambda\lambda$5896, 5890 Å (Na ID) is a stellar absorption feature that can be used to calculate σ_e (Spiniello *et al.* 2012). The observed width of the Na ID feature

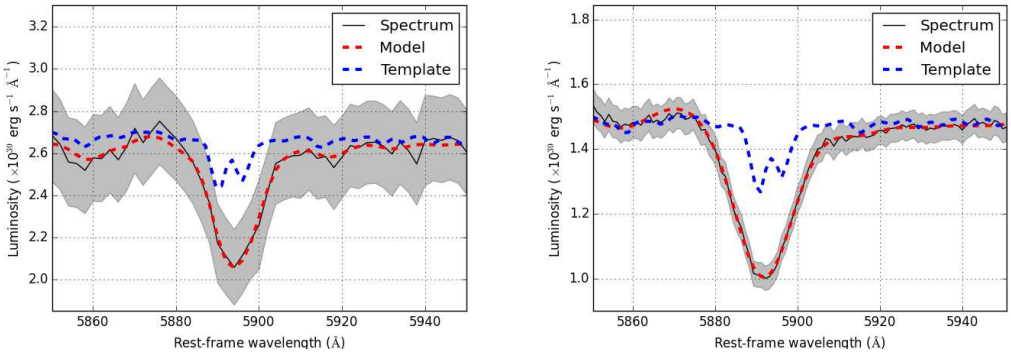

FIGURE 4.4: Spectrum (in black) of the Na ID of J00 (left) and J02 (right) and the best-fit results (in red). In grey we show the uncertainties on each spectrum. In blue we plot the SSP template. The template has a spectral resolution of 1.28Å.

results from the convolution of the resolution of the instrument (from Sec. 2.2.2.1), the intrinsic width of the stellar population and σ_e. The spectral resolution is computed using the FWHM of the closest arc line of the X-Shooter observation. For the stellar population, we used the SSP template from the Bruzual and Charlot 2003 library (Bruzual and Charlot 2003) that, based on the results of STARLIGHT, is the SSP that contributes the most for each host galaxy: the SSP of 0.9 Gyr and $Z = 0.05$ for J00, and 11 Gyr and $Z = 0.02$ for J02. These SSP contribute roughly 30 per cent and 55 per cent over the total host contributions for J00 and J02, respectively. In any case the NaID doublet shape does not change dramatically from one template to other, so we think the estimation provided in this work is reliable enough to compute the stellar velocity dispersion.

In Fig. 4.4 we show the NaID and the results of the fits. We also plot the template used in each object with the spectral resolution at the region of the doublet. To calculate the M_{dyn} of our AGN hosts we used the Virial relations from Cappellari *et al.* (2006) and Taylor *et al.* (2010),

$$M_{dyn} = k(n) \times \frac{r_e \sigma_e^2}{G} \tag{4.2}$$

where r_e is the effective radius of the spheroidal mass of the host galaxy, σ_e is the line-of-sight velocity dispersion, $k(n)$ is a factor that depends on the Sersic index and G is the universal gravitational constant. Using the software IMFIT we obtained r_e and the Sersic index by fitting the acquisition images from the VLT. These values are shown in Table 4.3. To compute the error in the spheroidal mass we propagate errors.

We summarize in Table 4.3 the properties of our AGN hosts. We clearly see that our dynamical mass estimates are compatible with the stellar masses calculated before. The studied galaxies are massive but not atypical (Vitale *et al.* 2013).

Table 4.3: Host galaxy properties.

	J00	J02
σ_e (km s^{-1})	145 ± 109 km s^{-1}	260 ± 87 km s^{-1}
r_e (kpc)	4.21 ± 0.39 kpc	0.84 ± 0.04 kpc
n	1.17	0.96
$k(n)$	7.92	7.96
$\log(M_{dyn}/M_\odot)$	$11.07^{+0.23}_{-0.42}$	$10.85^{+0.11}_{-0.12}$
$\log(M_{stell}/M_\odot)$	$10.73^{+0.20}_{-0.20}$	$10.89^{+0.20}_{-0.20}$

Notes: σ_e is the line-of-sight velocity dispersion and r_e the effective radius. The factor $k(n)$ in Eq. 4.2 depends on n, the Sersic index. Lastly we show the dynamical and stellar masses.

4.5 Discussion

In the following subsections we discuss one by one the possible causes of the apparent discordant properties of our AGN in the UV/optical range and in X-rays.

4.5.1 Compton-thick or Compton-thin obscuration

Based on the observed X-ray properties, we can rule out that our objects are Compton-thick. First of all the broad band continuum shape is too steep to be produced mainly by reflected emission as demonstrated in Sec. 4.2. Compton-thick sources usually have $\Gamma \sim 1.0$ (Winter *et al.* 2008, Georgantopoulos *et al.* 2011b, Brightman *et al.* 2014, Del Moro *et al.* 2016), while our sources have $\Gamma = 1.7 - 1.8$.

The EW of the Fe K emission line can be used as a hint of whether there is significant absorption of the direct, broad-band continuum emission. Compton-thick AGN are expected to have Fe K emission lines with EW$\geq$ 1 keV (Gandhi *et al.* 2014), due to the highly suppressed underlying continuum. Only for J02, if we include a Fe line in the model, its EW is large (formally EW = $1.12^{+0.49}_{-0.39}$ keV), but it is likely due to noise as the detection is not significant. No Fe line is detected with high significance in any of our sources.

The Compton-thin nature of the sources in this study is supported by the high $L_{2-10\ \mathrm{keV}}/L_{[\mathrm{O\,III}]}$ ratio, where $L_{[\mathrm{O\,III}]}$ is the intrinsic luminosity of the [O III] emission line at rest-frame λ5007 Å. This is because if we only detect in X-rays the scattered component (which is only a few per cent of the intrinsic AGN power) or the reflected component (which again is much lower than the intrinsic AGN power), and we mistakenly associate it with the direct broad band continuum, the X-ray luminosity can be largely underestimated. The [OIII] emission comes from the NLR, at $\sim$100 − 1000 pc from the central engine (see Sec. 1.2), and hence is unaffected by the nuclear extinction. Therefore we can use $L_{[\mathrm{O\,III}]}$ as a proxy of the accretion luminosity, and compare it to the $L_{2-10\ \mathrm{keV}}$. Compton-thick sources have $L_{2-10\ \mathrm{keV}}/L_{[\mathrm{O\,III}]} < 0.1 - 1.0$ (Bassani *et al.* 1999, Akylas and Georgantopoulos 2009). As the

TABLE 4.4: Gast-to-dust and $M_{\rm SMBH}/M_{bulge}$ ratios.

Object	$A_{\rm V}/N_{\rm H}$ (mag cm^{-2})	$\log(M_{\rm SMBH}/M_{bulge})$
J00	$\geq 2.61 \times 10^{-21}$	$-2.77^{+0.36}_{-0.34}$
J02	$1.30^{+1.8}_{-1.1} \times 10^{-21}$	-4.15 ± 0.39
Reference value	5.3×10^{-22}	-2.9 ± 0.5

Notes: The reference value for $A_{\rm V}/N_{\rm H}$ is the Galactic and for $\log(M_{\rm SMBH}/M_{bulge})$ is the mean value from Merritt and Ferrarese (2001).

$L_{2-10\ \rm keV}/L_{[\rm O\,III]}$ ratio is 69 for J02 and 22 for J00 (see Tables 4.1 and 4.2), this effectively excludes the Compton-thick character of both of our sources.

4.5.2 Host galaxy dilution

We check whether the discrepancy of the AGN classification of the AGN in our sample can be explained just by host galaxy dilution. To do so, we compare the mass of the host galaxy with the mass of its SMBH. This allows to check if the host galaxy is proportionally more massive than the SMBH by comparing with the relations between those quantities in the literature (Ferrarese and Merritt 2000, Gebhardt *et al.* 2000). We estimated the SMBH-to-host galaxy mass ratio for our two sources (see Table 4.4) and we compared them with the value reported by Merritt and Ferrarese (2001), $\langle \log(M_{\rm SMBH}/M_{bulge}) \rangle = -2.9$ with a rms of 0.5 dex. This relation has been derived using the masses of the bulges for a sample of elliptical galaxies from Ferrarese and Merritt (2000) and Gebhardt *et al.* (2000).

For J00 we obtain $\langle \log(M_{\rm SMBH}/M_{bulge}) \rangle = -2.77^{+0.36}_{-0.34}$, which is consistent with the Meritt & Ferrarese relation. This means that the galaxy is as massive as expected from the mass of its SMBH.

J02 has $\langle \log(M_{\rm SMBH}/M_{bulge}) \rangle = -4.15 \pm 0.39$, that is more than 2 times the rms below the standard relation. Thus for J02 host galaxy dilution could explain, at least in part, the lack of broad emission line detection in the 6dF spectrum. This is because we expect more impact of the star-light dilution on the AGN emission compared to AGN with less massive host galaxies.

There are many examples in the literature of apparently normal galaxies (e.g. XBONGs) in which, after the host galaxy contamination is removed, AGN emission is revealed (Severgnini *et al.* 2003, Georgantopoulos and Georgakakis 2005, Caccianiga *et al.* 2007). In the next sections we will investigate if this is the only factor that contributes to the observed optical/X-ray discrepancy for J02.

4.5.3 Dust-to-gas ratio of the nuclear medium

Typically AGN have dust-to-gas ratios lower than or compatible with the Galactic value (Maiolino *et al.* 2001, Vasudevan *et al.* 2009, Parisi 2011, Marchese *et al.* 2012, Hao *et al.* 2013, Burtscher *et al.*

TABLE 4.5: AGN optical extinction.

	J00	J02
$A_{\rm V,NLR}$	$1.07^{+0.67}_{-0.81}$	$0.30^{+0.77}_{-0.81}$
$A_{\rm V,cont.}$	2.04 ± 0.30	2.19 ± 0.33
$A_{\rm V,X-ray}$	≤ 0.36	$0.90^{+1.06}_{-0.74}$

Notes: optical extinction of the NLR and AGN continuum in mag. The NLR extinction is derived from the Balmer decrement (Bassani *et al.* 1999, Pappa *et al.* 2001, Carrera, Page, and Mittaz 2004) using the expression $E(B-V) = 2.07\times \log((\mathrm{H}_\alpha/\mathrm{H}_\beta)/3)$ with $R_{\rm V} = 3.1$. For comparison we include $A_{V,X-ray}$ the optical extinction derived using the $N_{\rm H}$ column density measured in X-rays and the SMC extinction model from Gordon *et al.* (2003).

2016, but see our new results in Chap. 5), i.e. $A_{\rm V}/N_{\rm H}$ =5.3×10^{-22} mag cm^{-2}. This result holds for AGN selected at X-ray, optical and IR wavelengths (Wilkes *et al.* 2002, Young, Elvis, and Risaliti 2008). We have compared $A_{\rm V}$ (see Table 4.5) and $N_{\rm H}$ (see Table 4.1) for our sources. For J00 $A_{\rm V}/N_{\rm H} \geq 2.61 \times 10^{-21}$ mag cm^{-2}, while for J02 $A_{\rm V}/N_{\rm H} = 1.30^{+1.8}_{-1.1} \times 10^{-21}$ mag cm^{-2}. J00 has a $A_{\rm V}/N_{\rm H}$ more than 5 times the Galactic value. For J02 the observed and Galactic values are consistent. As mentioned in Sec. 4.3.1, the SMC extinction model provides one of the lowest measurements of $A_{\rm V}$ of all models taken into account. Nevertheless, if we use $A_{\rm V}$ based on different extinction models (the Milky Way extinction curve from Allen 1973, the Large Magellanic Cloud models from Gordon *et al.* 2003, the Calzetti *et al.* 2000 law and the Cardelli, Clayton, and Mathis 1989 extinction model), our results do not change.

A dust-to-gas ratio higher than the Galactic value could explain the observed properties of J00. It is a scenario offered in Panessa and Bassani (2002), to explain X-ray unabsorbed type-2 AGN since absorption detected in X-rays is mostly produced in gas. There are a few examples in the literature of AGN with higher dust-to-gas ratios than the Galactic value (Trippe *et al.* 2010, Mehdipour, Branduardi-Raymont, and Page 2012, Huang *et al.* 2011), although in previous studies these sources are estimated to be 3 – 9 per cent of the sources of the entire population (Maiolino *et al.* 2001, Caccianiga *et al.* 2004, Malizia *et al.* 2012).

4.5.4 Intrinsically weak BLR region

To investigate whether our AGN have a BLR with non-standard properties (e.g. underluminous) we have determined the luminosity ratio $\mathrm{L_{NLR}/L_{BLR}}$ from the broad and narrow components of the H_α emission line (see Table 4.2). Then we compare our values with the relation between $\mathrm{L_{NLR}/L_{BLR}}$ and $\mathrm{L_{BLR}}$ found for AGN of similar z and luminosities to ours from Stern and Laor (2012). The $\log(L_{H_\alpha,\mathrm{n}}/L_{H_\alpha,\mathrm{b}})$ are −0.92 and −1.07 for J00 and J02, respectively. The expected $\log(L_{H_\alpha,\mathrm{n}}/L_{H_\alpha,\mathrm{b}})$ values are −0.66 and −0.47 for J00 and J02, respectively. Taking into account the 0.4 dex scatter of the mentioned relation the differences are not significant. We conclude that none of our sources appear to have intrinsically weak BLR.

4.5.5 Variability

AGN are highly variable sources across the whole electromagnetic spectrum at both long and short time scales (Ulrich, Maraschi, and Urry 1997, Mateos *et al.* 2007, Krumpe *et al.* 2010, García-González *et al.* 2015, Hernández-García *et al.* 2015, LaMassa *et al.* 2015). As the X-ray and UV/optical observations used here have not been taken simultaneously, we cannot rule out that variability could explain, at least in part, the observed mismatch between the optical and X-ray properties of our AGN.

As a check, we carried out the UV-to-optical spectral decomposition into AGN and host galaxy emission using a public SDSS-DR7 spectrum available for J00 (taken in 2000-09-05). We carry out the analysis using the same AGN, galaxy templates and extinction law as for the X-Shooter data (see Sec. 4.3.1). To compare the intrinsic flux and the extinction of the AGN between both spectra, we have to take into account that that a higher fraction of light from both the AGN and the host enters through the 3 arcsec fibre of the SDSS spectrum. There is some variation, that is best described by an extinction change ($A_{V,SDSS} = 0.69 \pm 0.10$ mag versus $A_{V,XSH} = 2.04 \pm 0.29$ mag) instead of a change in the luminosity of the AGN. For this source we only observe a marginal variation of the intrinsic flux with 1.6σ significance. The A_V measured gives a higher dust-to-gas ratio than Galactic ($A_V/N_H > 8.8 \times 10^{-22}$ mag cm^{-2}), as with the X-Shooter data. The 6dF optical spectrum of J02 is not of sufficient quality for conducting a spectral decomposition analysis.

We conclude that extinction variability could be present in at least one of our sources (J00, the one with the largest A_V/N_H ratio). Even so, we confirm that the dust-to-gas ratio of the material responsible for the extinction of the nuclear emission in this source is higher than the Galactic value. Simultaneous X-ray and optical observations are needed to assess the actual importance of variability on these objects.

4.6 Conclusions

In this work we have investigated the origin of the apparent mismatch between the optical and X-ray properties of two AGN with high optical extinction but low X-ray absorption. In the two objects analysed we detected a broad emission line in H_α using the data from X-Shooter after a careful removal of the host galaxy contribution.

We test several scenarios that could explain the observed optical and X-ray properties. We ruled out a Compton-thick nature of our sources, on the basis of the $L_{2-10\ \mathrm{keV}}/L_{[O\,III]}$ ratio and the absence of the Fe K emission line. We also discarded that the observed weakness of the broad emission lines, in particular the Balmer H_α line, is caused by an intrinsically weak BLR emission.

Interestingly, the origin of the mismatch is found to be different for each AGN. An A_V/N_H higher than the Galactic value is the best explanation for the properties of J00 without the need to invoke variability of either the X-ray absorption and/or the UV/optical extinction. J02 has a massive host

galaxy in comparison with its SMBH mass so that the broad emission lines and the AGN nuclear continuum are swamped by the host galaxy star-light, which makes them very difficult to detect.

We conclude that discordant optical and X-ray classifications can be provoked by very different scenarios, and hence, X-ray unabsorbed type-1.9 AGN are not a physical family of objects with the same properties.

Chapter 5

Analysis of the BUXS type-1 sample

In this Thesis we have accurately measured in an statistical way the impact of obscuration on the optical classification of type-1 AGN using the individual probability distributions of $A_{\rm V}$ and $N_{\rm H}$, being the first study of this kind that uses these distributions. They are obtained from the analysis of high quality UV/optical and X-ray spectra (see Chap. 3). We derive the optical extinction (by dust) and X-ray absorption (by gas) of the obscuring medium of type-1 objects in a robust way. As this sample was selected using hard X-rays and we accurately optically classified the AGN, we have a complete sample of type-1 objects with almost no bias against heavily obscured sources.

With this unique information we studied the following issues: a) we analysed the completeness of the full sample with respect to a subsample with complete classification; b) we evaluated the origin of the subclassification of AGN; c) we also checked the reliability of the Balmer decrement of the broad H_α and H_β emission lines as an extinction measurement method; d) by comparing the individual probability distributions of $A_{\rm V}$ and $N_{\rm H}$ we statistically studied whether there is correlation between the obscuration at both energy bands; e) we have assessed the dust-to-gas ratios of type-1 sources with respect to that of our Galaxy.

5.1 Sample and subsamples definition

We selected from the essentially fully spectroscopically identified BUXS sample all objects that show at least one broad emission line in their optical spectrum, i.e. AGN with optical classifications from type-1.0 to type-1.9. In type-2 AGN the nuclear emission is entirely suppressed, so estimating the amount of optical extinction is extremely difficult. This is why we centred this study only on AGN with at least one broad emission line in their UV/optical spectrum, so we ensure that at least a fraction of UV/optical nuclear emission is detected, and hence we can estimate its $A_{\rm V}$. We used only the $z = 0.05 - 1$ range and objects with $\log(L_{2-10\ \rm keV}/\rm erg\ s^{-1}) > 42$, as described in Sec. 3.4. The

TABLE 5.1: BUXS type-1 sample.

	Type-1 (MgII)	Type-1.0	Type-1.2	Type-1.5	Type-1.8	Type-1.9	Total
Full sample	21	35	36	20	7	13	132
$z < 0.65$	1	23	32	17	6	13	92
$z < 0.2$	0	4	9	8	1	10	32

This is Table 3.2 repeated here for clarity. Sources and classification according to the scheme described in Fig. 3.3 for the 132 objects in the full BUXS type-1 sample and the $z < 0.65$ and $z < 0.2$ subsamples.

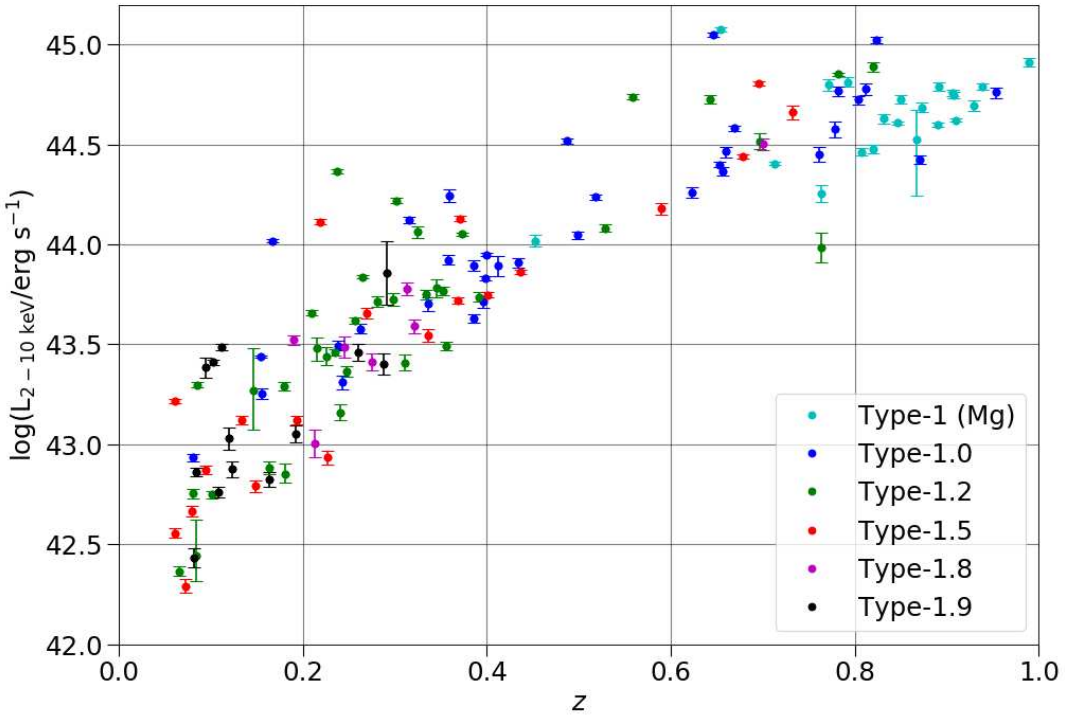

FIGURE 5.1: 2-10 keV luminosity versus z of all the 132 objects in the full BUXS type-1 sample. Colours represent each subclass. We represent as well the 1σ errors of the luminosity.

luminosity cut applied to minimize the contamination from the host galaxy. The $z < 1$ cut is to robustly constrain the $N_{\rm H}$ column density. We note that all sources with $\log(L_{2-10\ \rm keV}/\rm erg\ s^{-1}) > 42$ have $z > 0.05$. In Fig. 5.1 we show the $L_{2-10\ \rm keV}$ vs z diagram r for our full sample of 132 type-1 AGN, henceforth "full sample". We list again the number of AGN in each subclass from Table 3.2 in Table 5.1 for clarity.

As stated in Sec. 3.4, we divided the objects into smaller subsamples based on whether the UV/optical spectra covered the H_α and/or H_β spectral regions, i.e., using $z < 0.2$ and $z < 0.65$ cuts. The former is a subsample of the latter.

We used the $z < 0.65$ sample to analyse the properties (such as $A_{\rm V}$ or $N_{\rm H}$) of the subtypes from type-1.0 to type-1.8, as for this cut the classification is complete for all those subtypes, since the H_β region is covered in all the objects in that subsample.

In the $z < 0.2$ sample the classification is complete for all the objects because our optical spectroscopic observations cover both the H_α and H_β wavelength regions for all of them. There are 10 type-1.9 AGN out of 32, plus an additional type-1.8 object in this sample. This gives a 31 and 34 per cent of type-1.9 and type-1.8/9 AGN, respectively. This is higher than the $10-20$ per cent of type-1.8/9 AGN normally obtained by other studies (Caccianiga *et al.* 2004, Winter *et al.* 2009, Stern and Laor 2012, Malizia *et al.* 2012, Elitzur, Ho, and Trump 2014, Shimizu *et al.* 2018). As the $z < 0.2$ sample is relatively small, we checked whether this difference is statistically significant using binomial statistics and obtaining the confidence intervals using a Bayesian approach (using the shortest confidence interval that includes the mode). A type-1.8/9 fraction of 10 per cent is within the 2σ interval around the mode of our distribution, so the difference is not very significant.

The diverse fractions of type-1.9 reported in the literature are likely to be caused by differences in the criteria used for the detection of a broad emission line (e.g. visual inspection or $\Delta\chi^2$) or difficulties to detect it in optical spectra of poor quality (Netzer 2015). In some cases the broad emission lines could be hidden by the host galaxy starlight (Severgnini *et al.* 2003, Georgantopoulos and Georgakakis 2005, Caccianiga *et al.* 2007, 2008). If the spectra have high host galaxy contamination (e.g. fibre spectra, that include more galaxy light than using slits), we could be misclassifying some type-1.8/9 AGN as type-2 objects, specially at low AGN luminosities (Ordovás-Pascual *et al.* 2017).

Sometimes in the literature type-1.8/9 are classified as type-2 AGN (e.g. Caccianiga *et al.* 2008, Corral *et al.* 2011). To allow direct comparison with previous results, in some cases we consider only the objects with subtypes from 1.0 to 1.5. To do so we use only the ones with $z < 0.65$ because, as previously stated, the classification using this z cut is complete for these subtypes.

There are objects in the BUXS type-1 AGN sample which can only be classified as generic type-1 due uniquely to the presence of broad MgII emission. These objects are named shortly in this work as type-1 (MgII) and they are not removed from our study as they form part of the full sample, but we can not provide detailed subclassification for them. Despite being included in the tables, in this work we do not analyse these objects in detail, but we find that their properties are similar to the type-1.0/2/5 AGN.

5.2 Analysis of UV/optical and X-ray data

To obtain the optical extinction affecting the nuclear emission in each AGN, we followed the method described in Sec. 3.3.2. The degeneracy between the slope of the AGN UV/optical continuum and the host contribution can affect the A_V estimation. The continuum fitting proposed in this work can provide reliable estimates of A_V in type-1 AGN, as it is conducted as follows: first, based on a thorough SED fitting analysis from rest-frame UV-to-mid-IR wavelengths, we constrain the emission from the AGN hosts. As mentioned in Sec. 3.3.2, the stellar emission is needed if in the SED decomposition

TABLE 5.2: Summary of the detection of nuclear extinction and host galaxy emission.

Full sample (132)	Upper limit in A_V	Detection in A_V
No host galaxy emission	15 (11 %)	16 (12 %)
Host galaxy emission	38 (29 %)	63 (48 %)

Notes: Number of AGN that are compatible or not with nuclear extinction within 1σ. In addition we indicate the number of sources for which host galaxy emission is negligible and for which is not.

the $\Delta\chi^2$ between the best-fit model with and without host galaxy emission is higher than 2σ (Mateos *et al.* 2015). After that we use the best-fit host galaxy template to estimate the galaxy contribution to each of our UV/optical spectra. In this way we measure in a robust way the relative contribution of the host galaxy and the AGN emission (the latter affected by optical extinction). We can only compute an upper limit in A_V for a source if, using the probability distributions of A_V, the narrowest 1σ interval around the mode includes $A_V = 0$ mag. In this case, the 1σ upper limit is given as the value of the 84.2 percentile. In Table 5.2 we list the number of objects for which the inclusion of host galaxy emission is needed to model the spectrum according to the SED decomposition and the number that have only an upper limit in the optical extinction. We found that, for 77 per cent of the sample, the host galaxy starlight contribution is significant so it has to be taken into account in the spectral fits.

In Sec. 3.2, we mentioned that members of our group extracted and analysed the X-ray spectra for all the sources in this study. This allows us to obtain the probability distribution of the intrinsic N_H for all AGN, and then compare it with the classification of our sources and with the A_V probability distributions. To compute the errors for the X-ray absorption, we use the median and narrowest 1σ interval of the N_H distribution (Hogg and Foreman-Mackey 2018). If the interval includes $\log(N_H/\mathrm{cm}^{-2}) = 19$, which is the minimum N_H column density value allowed in the fits, this is indicative that we do not have a detection of X-ray absorption. In these cases we compute the 1σ upper limits for N_H as the value of the 84.2 percentile. This is the same criterion used for A_V.

In Table 5.3 we show the number and fraction of objects for which we can detect optical nuclear extinction and/or intrinsic X-ray absorption. We find that for 91 type-1 AGN, 68 per cent of the sample, we can only compute an upper limit on N_H. Compared to the extinction in the UV/optical, for which 53 sources, 40 per cent of the sample, show only an upper limit in A_V, so the fraction of upper limits on the optical extinction is lower than on the X-ray absorption.

Finally, we summarize in Appendix A the A_V and the reddening corrected monochromatic flux at 5100 Å from the optical fits, as well as the N_H and the intrinsic luminosity in the 2-10 keV energy range, among other important information about the fits in both energy bands.

TABLE 5.3: A_V and N_H detection in the full BUXS type-1 sample.

Full sample (132)	Upper limit in A_V	Detection in A_V
Upper limit in N_H	48 (36 %)	43 (33 %)
Detection in N_H	5 (4 %)	36 (27 %)

Notes: Number of AGN that are compatible or not with optical extinction and X-ray absorption within 1σ.

5.3 UV/optical extinction

5.3.1 Complete classification subsample at $z < 0.2$

We show the optical extinction versus z in Fig. 5.2. We note that the objects with the highest extinction ($A_V \gtrsim 2$ mag) are found preferentially at lower z. In Fig. 5.3 we represent the combined probability distributions of A_V for the full sample and the $z < 0.2$ subsample (i.e. the one whose classification is complete). Instead of plotting the best fit values of the optical extinction of each AGN, we used the A_V probability distributions, so each object in the histogram contributes with an equal area. We observe that the full sample has an A_V distribution much more concentrated at low extinctions, compared to the distribution for the $z < 0.2$ sample. This is because the latter has a higher fraction of high A_V objects, since those are mainly at low z. The samples without H_α wavelength coverage are biased against high A_V. Likewise, type-2 samples that do not cover the H_α wavelength region will include some type-1.9 AGN, affecting their A_V distributions.

In the following section we study the A_V probability distributions of each subclass.

5.3.2 Extinction of the subclasses

The distribution of A_V of the full sample separated in subtypes is shown in Fig. 5.4. It is clear that below $A_V = 2$ mag the main contribution is from type-1.0/2/5 AGN and the type-1 (MgII) objects, while above $A_V = 2$ mag, the contribution of type-1.8/9 and some type-1.5 is dominant.

In Fig. 5.5 we present the probability distribution of each AGN subclass normalized to one. From type-1.0 to type-1.8 we show only the distribution for the objects with $z < 0.65$ and for type-1.9 the ones with $z < 0.2$, as these cuts ensure complete classification for each class. From type-1.0 to type-1.8 the most populated bins are at $A_V < 1$ mag, with an increasing rise of a high A_V tail. Type-1.9 AGN on the other hand show the bulk of the extinction at $A_V \gtrsim 2$ mag, being the most different in terms of the mean extinction of the subclass. In Fig. 5.6 we show boxplots for each distribution, where is more visual the increase of the optical extinction with the subtype by looking at the boxes and the median of each distribution. Clearly, we can conclude that there is a direct relation between A_V and AGN subclass.

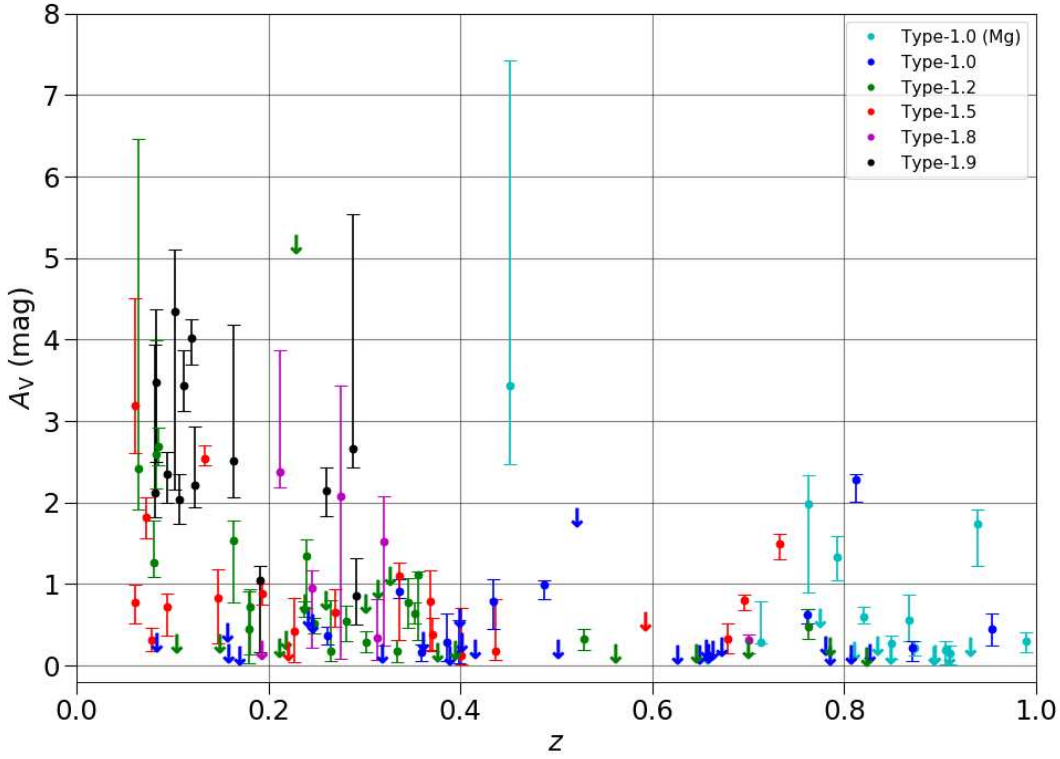

FIGURE 5.2: A_V versus z for the objects in the full BUXS type-1 sample. The arrows are 1σ upper limits.

The combination of the sample selection method (hard X-rays), the detailed optical classification and the accurate decomposition of the rest-frame UV/optical continuum into host galaxy and AGN emission makes it possible to detect highly reddened type-1 AGN that can be easily missed or misclassified by other selection methods. AGN surveys selected using blue optical colors preferentially miss obscured AGN (Padovani *et al.* 2017). This is why our sample includes more optically obscured objects than samples selected with optical colors, with $A_V \sim 0-1$ mag (Baron *et al.* 2016, Zafar *et al.* 2015). To put in context our results, in the color-selection method from Richards *et al.* (2003), AGN reddened with $A_V > 1.5$ mag will be missed, and even though this question is not formally addressed in their study, they roughly estimated that their selection method misses about 10 per cent of QSO (those with $A_V > 1.5$ mag). Our selection is able to find at least 15.15 per cent of objects above that limit, with an additional 8.33 per cent of sources with the mentioned limit within 1σ. The Faint Images of the Radio Sky and Two Micron All-Sky Survey (FIRST-2MASS) Red QSO survey (Glikman *et al.* 2007, Urrutia *et al.* 2009), using NIR color-based selection to identify obscured AGN, includes objects with $A_V = 0.3-4.5$ mag, a range of optical extinction that we are able to detect in our hard X-ray selected sample. In our study we obtained more type-1 AGN with higher extinction than other hard X-ray selected samples where the optical extinction is obtained using SED analysis (e.g. Lusso *et al.* 2010, 2013, Hao *et al.* 2013), probably because many samples similar to BUXS classify AGN based on the shape of the SED. We found that there is a non negligible fraction of sources that have been classified by us as type-1 AGN based on their UV/optical spectra while they show a SED characteristic of type-2

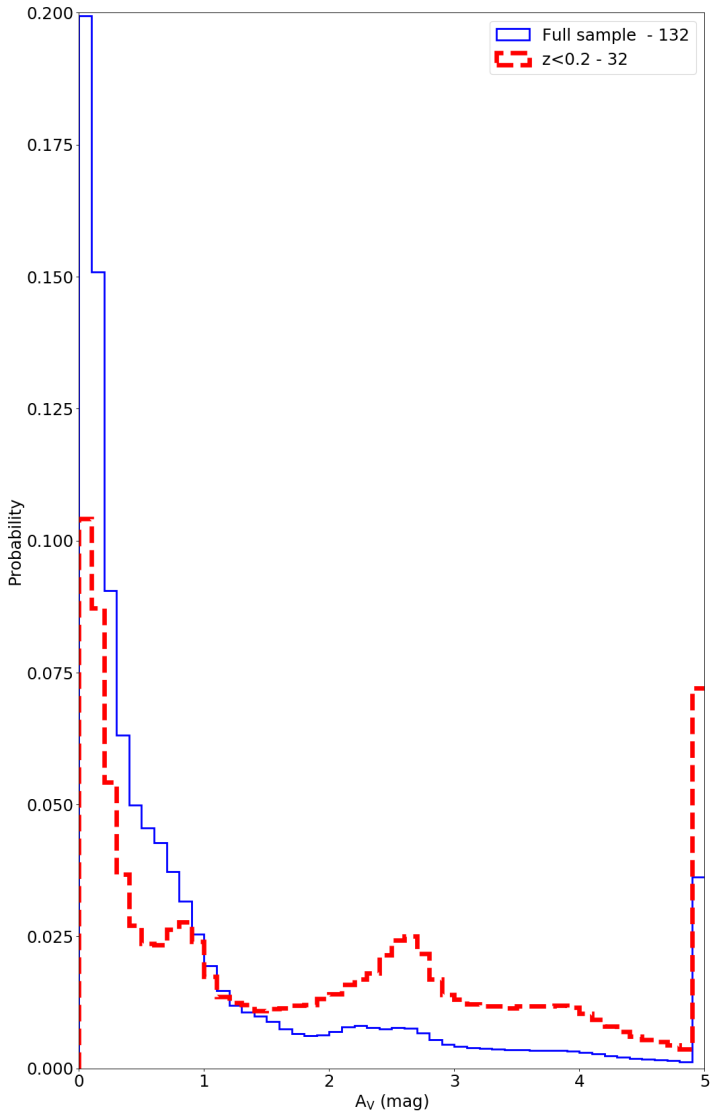

FIGURE 5.3: Normalized histograms of the optical extinction for the full BUXS type-1 sample and the $z < 0.2$ subsample. The last include all values higher than the maximum value shown in the X-axis.

objects.

We checked whether the distributions of A_V are statistically different using a rigorous statistical bootstrapping method with the Kolmogorov-Smirnov (KS) test. This approach developed by us is rather conservative. We need to test the null hypothesis that the A_V distributions for the two samples that we are comparing are extracted from the same parent population. To do so we compared the distance of the KS test of the two real samples with the distribution of distances of KS tests from two randomly generated samples drawn from parent samples of objects. In our simulations we computed d_0 (statistic of the KS test, the maximum difference in cumulative fraction) of the two samples (e.g. A and B with numbers of objects N_A and N_B, respectively) we want to compare. Each object contributes with 10000 points randomly drawn from the probability of A_V. For the original sample we compared the $10000 \times N_A$ points from sample A with the $10000 \times N_B$ points from sample B, obtaining a maximum distance

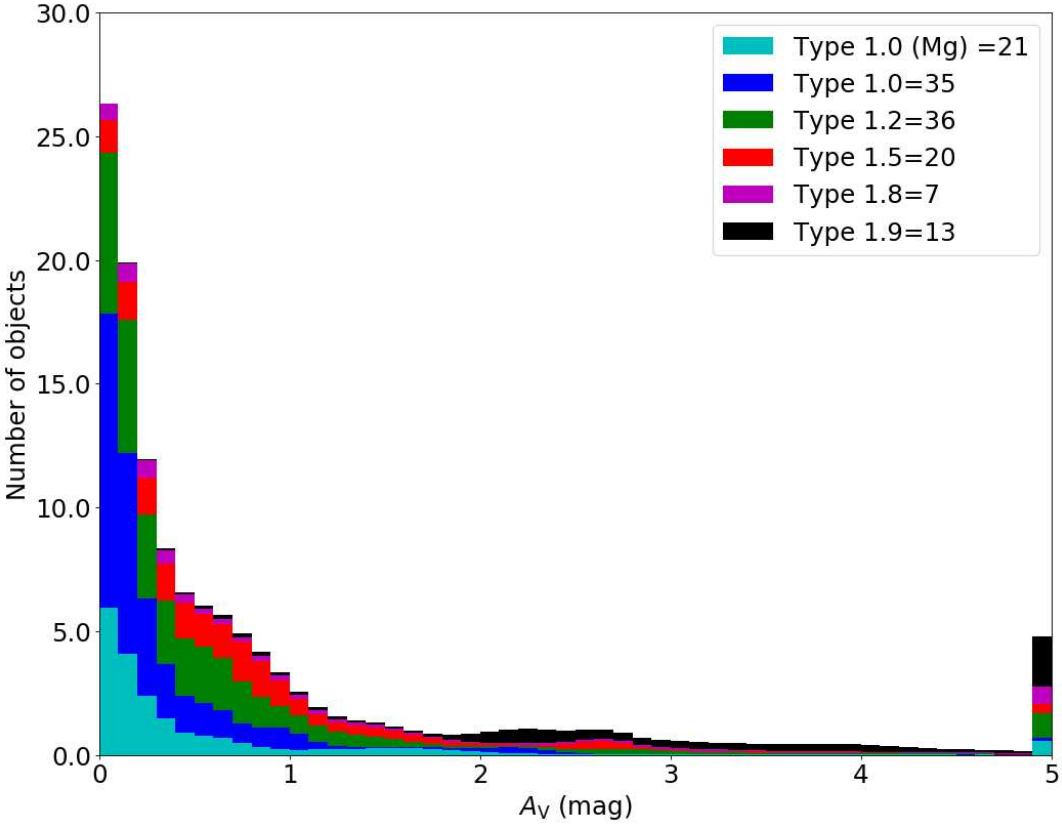

FIGURE 5.4: Histogram of the optical extinction for the full BUXS type-1 sample and the subtypes of AGN. Each object is represented by its probability distribution of A_V, and each individual distribution contributes in the histogram with an area equal to one. The last include all values higher than the maximum value shown in the X-axis.

d_0 from the KS test. We then repeat this procedure by pooling together the N_A and N_B objects and extracting at random N_A objects (simulated sample A′) and N_B objects (simulated sample B′) without repetition, obtaining a maximum KS distance of d_i for each simulation. We conducted this test 10000 different times, obtaining 10000 different d_i. If two parent samples are statistically similar, d_0 will have a value among the distribution of d_i. If they are very different, very few (or none) will have higher distance than the observed KS test (d_0), and therefore we can discard the hypothesis that they are equal. We show the results from these KS tests with bootstrapping in Table 5.4.

Type-1.0 and type-1.2 AGN are statistically different with a significance between 2σ and 3σ, while types-1.2/5/8/9 show $<1\sigma$ significance in consecutive pairs. This is explained if type-1.0 are mostly populated by sources with low optical extinction (almost the totality of the distribution is at $A_V < 1$ mag). With increasing classification, the low A_V area of the histogram decreases while the high A_V tail increases. Lastly, type-1.9 objects present an A_V probability distribution that is mostly dominated by high optical extinction ($A_V > 2$ mag). We also compared the significance of: a) type-1.0 vs type-1.2/5, b) type-1.2/5 vs type-1.8/9, and c) type-1.0/2/5 vs type-1.8/9. We obtained that the significance is higher than 3σ for all three a), b) and c) comparisons. In conclusion, we can distinguish between the

TABLE 5.4: Summary of the results from the KS test.

	A_V	N_H
Type-1.0 vs Type-1.2	0.0155	0.5309
Type-1.2 vs Type-1.5	0.3199	0.8069
Type-1.5 vs Type-1.8	0.3386	0.0275
Type-1.8 vs Type-1.9	0.3449	0.0305
Type-1.0 vs Type-1.2/5	0.0009	0.3966
Type-1.2/5 vs Type-1.8/9	0.0	0.0
Type-1.0/2/5 vs Type-1.8/9	0.0	0.0

Notes: Results from the KS test simulations conducted in this study for the optical extinction and the X-ray absorption (see Sec. 5.4.2). We show the fraction of KS simulations that have d_i smaller than the value derived for the parent samples. For 1.0/2/5/8 we used the $z < 0.65$ sample and for 1.9 and for the combined 1.8/1.9 we used the $z < 0.2$ sample.

following groups: the type-1.0, the intermediate classes of type-1.2/5 AGN, and the type-1.8/9, often grouped with the pure type-2 AGN in other works.

5.3.3 Fraction of optically reddened type-1 AGN

We have derived the fraction of type-1 AGN with an optical extinction typical of type-2 sources based on the individual probability distributions of A_V. As stated in Sec. 5.1, some studies consider type-1.8/9 AGN as type-2 objects, and using the probability distributions we have proven that these populations are normally affected by significant optical extinction. Using our distributions of A_V for the type-1.0/2/5 and type-1.8/9 AGN we checked at which A_V the latter classes begin to dominate, and thus the value of A_V that best divides the two AGN groups. We found that this limit is $A_V = 1.6$ mag, close to the value from Liu *et al.* (2018), i.e. $A_V = 1.4$ mag. To allow direct comparison we used this last value, as the results would not change significantly. We show in Table 5.5 the percentage of the combined probability distribution of each subclass and each selection with $A_V > 1.4$ mag at the top of each cell. The three numbers in brackets at the bottom of each cell stand for the number of sources with low optical extinction according to the mentioned threshold with more than 1σ confidence (i.e. the 1σ upper limit is below $A_V = 1.4$ mag), the ones whose 1σ confidence interval includes that value, and the sources with high optical extinction (i.e., the sources whose 1σ lower limit is below $A_V = 1.4$ mag), respectively. In addition, we include in Appendix A the results obtained using a more conservative limit, $A_V = 2$ mag from Caccianiga *et al.* (2008), where we show that the results are similar with this threshold. To help to understand our results, in Fig. 5.7 we represent the optical extinction fraction with a threshold of $A_V = 1.4$ mag and $A_V = 2$ mag from the combined A_V probability distribution of each class or subsample (combination of all individual probability distributions of the objects in each sample). We found that the extinction fraction gradually increases with the subtype of AGN.

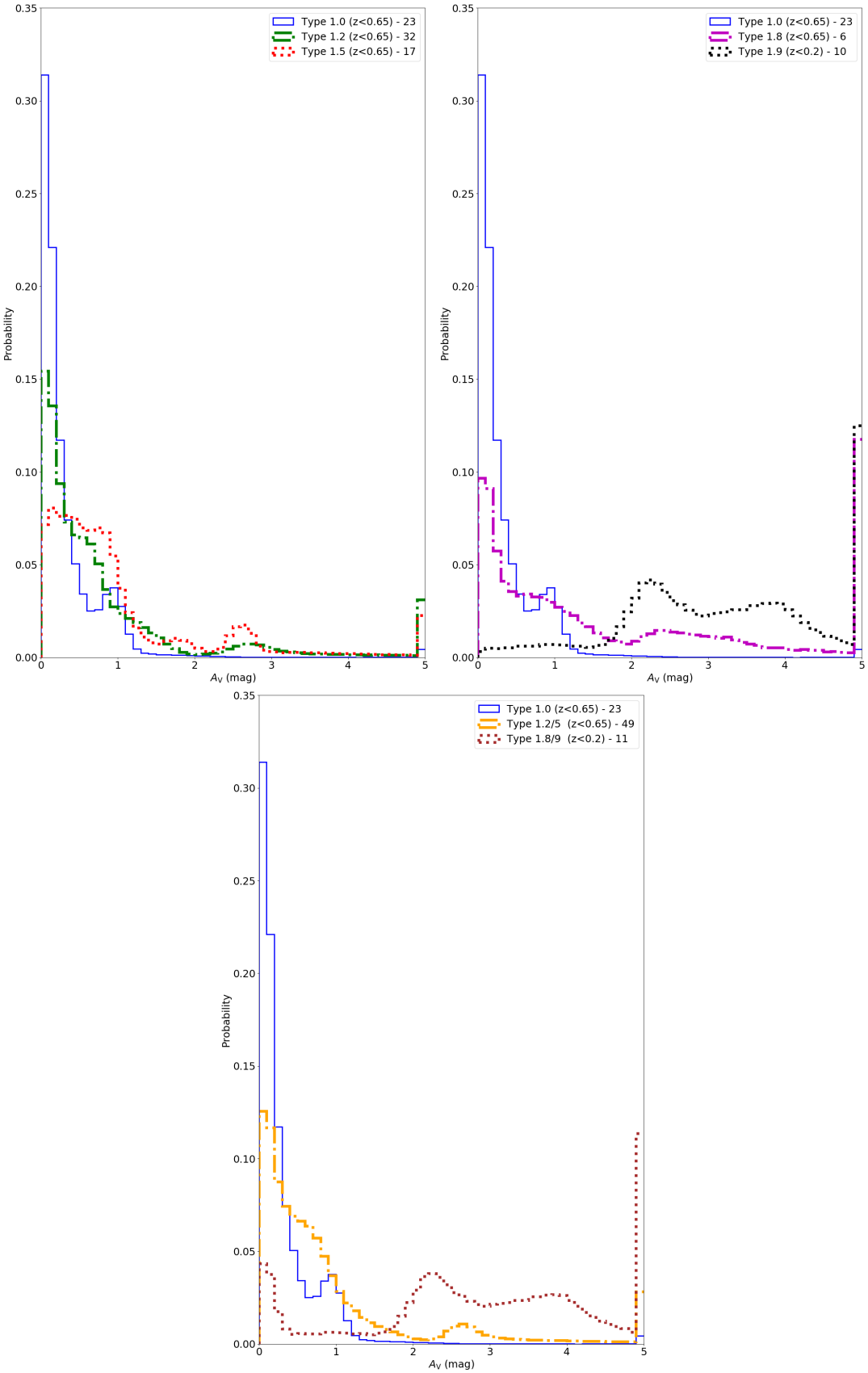

FIGURE 5.5: Normalized histograms of the optical extinction for the different subclasses in the BUXS type-1 sample. Each object is represented by its probability distribution of A_V. We include in each panel the type-1.0 A_V distribution as a reference. The last include all values higher than the maximum value shown in the X-axis.

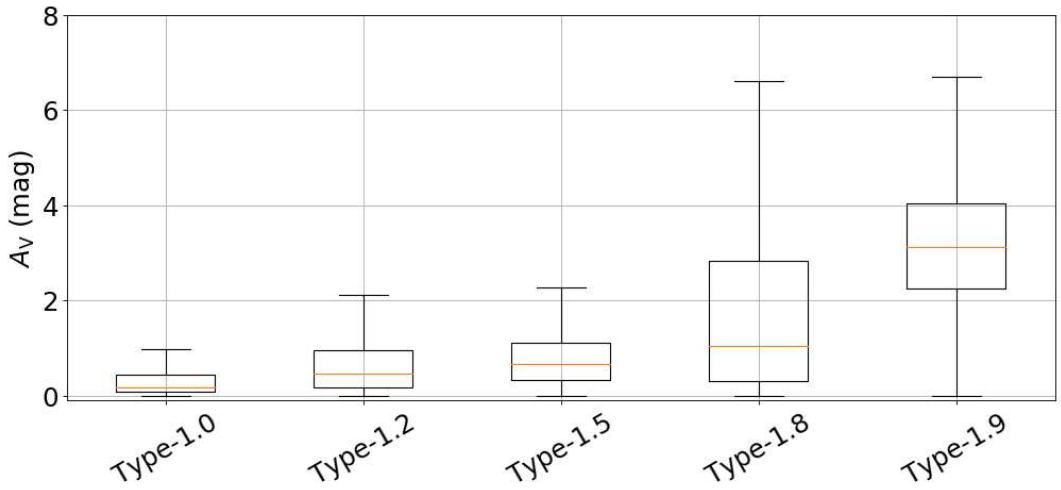

FIGURE 5.6: Boxplot of the optical extinction A_V of each subclass showing median values in orange. The box marks the first and third quartiles, and the whiskers represent the last datum at a distance less than 1.5 times the interquartile range (IQR). For 1.0/2/5/8 we used the $z < 0.65$ sample and for 1.9 we used the $z < 0.2$ sample.

The full sample composed by the 132 type-1 AGN in BUXS shows an optically reddened fraction of 21 per cent. If we consider only the types-1.0/2/5, as other studies do, the fraction drops to 12 per cent. The latter fraction is similar to the $\sim 5-10$ per cent of optically reddened AGN ($A_V > 1.4$ mag) estimated in other studies (e.g. Richards *et al.* 2003, Lusso *et al.* 2014), while the optically reddened fraction for the full sample is higher. The complete sample at $z < 0.2$ has a much higher extinction fraction (51 per cent) than previous studies, and a factor ~2.5 higher than the full sample. This contribution of optically reddened AGN is high due to the significant contribution of type-1.8/9 AGN at low z, as at higher z these objects are misclassified as type-2 sources.

5.3.4 A_V from the Balmer decrement of the broad emission lines

In the literature it is frequently seen that the optical extinction of the innermost region of AGN is measured using the observed flux ratio of the broad emission lines and assuming an intrinsic flux ratio of lines, normally a Baker-Menzel case B (e.g. Dong *et al.* 2008, Gaskell 2017). To check the validity of this approach, we have investigated whether, in the 51 AGN with covered and detected H_β and H_α broad emission lines (we hence exclude type-1.9 AGN), the optical extinction can be computed using the broad emission line flux ratio of the H_α and H_β lines. To do so we assumed that the same material is obscuring both the BLR and the accretion disk. This implies that the A_V estimation from the Balmer decrement should be the same, within errors, as the one calculated using the broad band UV/optical continuum, coming from the disk. We used the formula from Lyu, Hao, and Li (2014),

$$A_V = 1.086 \times \xi \times ln\left(\frac{\left(H_\alpha/H_\beta\right)_{observed}}{\left(H_\alpha/H_\beta\right)_{intrinsic}}\right) \tag{5.1}$$

Table 5.5: Type-1 AGN fraction with levels of obscuration typical of type-2 AGN.

	A_V = 1.4 mag	N_H = 21.5 cm^{-2}
Full sample	0.2065 (20/10/102)	0.2054 (103/4/25)
$z < 0.2$	0.5098 (15/2/15)	0.3957 (19/1/12)
Type-1 (MgII)	0.1294 (17/3/1)	0.0782 (19/1/1)
Type-1.0 ($z < 0.65$)	0.0192 (22/1/0)	0.0651 (21/1/1)
Type-1.2 ($z < 0.65$)	0.1564 (25/4/3)	0.1250 (28/0/4)
Type-1.5 ($z < 0.65$)	0.2019 (14/0/3)	0.1155 (15/0/2)
Type-1.8 ($z < 0.65$)	0.4225 (3/2/1)	0.6370 (2/0/4)
Type-1.9 ($z < 0.2$)	0.9178 (1/0/9)	0.7775 (2/1/7)
Type-1.0/2/5 ($z < 0.65$)	0.1241 (61/5/6)	0.1047 (64/1/7)
Type-1.8/9 ($z < 0.2$)	0.8347 (2/0/9)	0.7919 (2/1/8)

Notes: The top value in each cell represents the fraction of the combined A_V or N_H probability distribution of each class or subsample (combination of all individual probability distributions of the objects in each sample) with extinction/absorption typical of type-2 AGN, according to different thresholds reported in the literature. The three numbers in brackets at the bottom of each cell stand for the number of sources with low optical extinction or low X-ray absorption according to the correspondent threshold with more than 1σ confidence (i.e. the 1σ upper limit is below A_V = 1.4 mag or $\log(N_H/\mathrm{cm}^{-2}) = 21.5$), the ones whose 1σ confidence interval includes that value, and the sources with high optical extinction or high X-ray absorption (i.e., the sources whose 1σ lower limit is above A_V = 1.4 mag or $\log(N_H/\mathrm{cm}^{-2}) = 21.5$), respectively. The X-ray absorbed fraction will be discussed in Sec. 5.4.3.

where A_V is the optical extinction from the broad-band continuum emission, $(H_\alpha/H_\beta)_{observed}$ is the observed flux ratio of the H_α and H_β broad emission lines and $(H_\alpha/H_\beta)_{intrinsic}$ is the intrinsic flux ratio. The value ξ depends on the extinction curve, and has the mathematical expression

$$\xi = \left(\frac{A_V}{A_{H_\alpha}}\right) \times \left(\frac{A_{H_\beta}}{A_{H_\alpha}} - 1\right)^{-1} \tag{5.2}$$

where A_{H_α} and A_{H_β} stand for the extinction at H_α and H_β bands, respectively. For the SMC ξ = 2.38 (Lyu, Hao, and Li 2014).

To compute the intrinsic Balmer decrement we performed 50000 numerical realizations of A_V for each object using its probability distribution. We calculated 50000 numerical realizations of broad H_α and

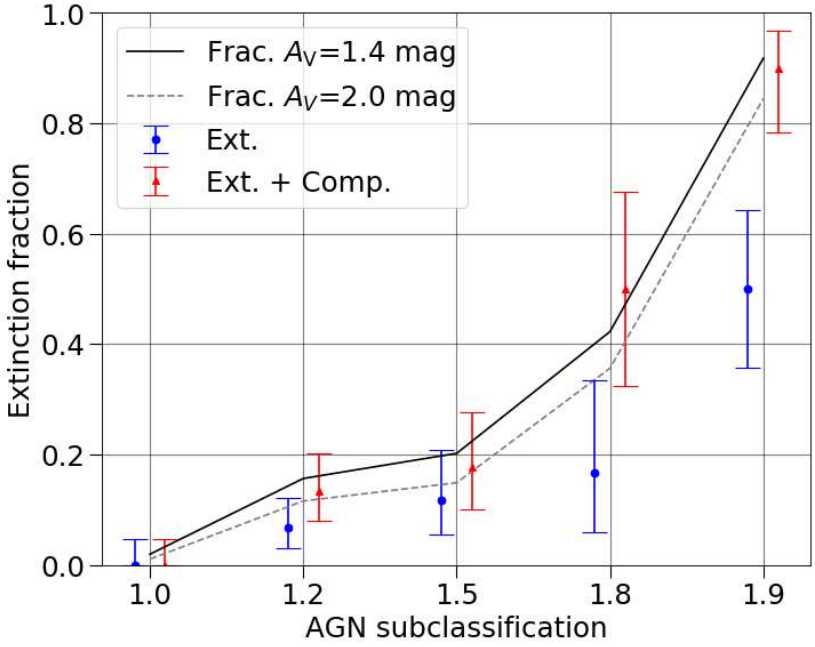

FIGURE 5.7: Fraction of AGN with optical extinction typical of a type-2 AGN within each subclass. The solid black line and the dashed grey line represent the fraction of the distribution of each class above the corresponding threshold (A_V = 1.4 and A_V = 2 mag, respectively first row in the corresponding cell in Tables 5.5 and B.1). The blue circles represent the fraction of objects whose A_V is above A_V = 1.4 mag within 1σ significance (second row in the corresponding cell in Table 5.5), with its 1σ error computed using binomial statistics. We represent with red triangles the fraction of objects whose A_V are higher or consistent with A_V = 1.4 mag at 1σ. The errors on the latter fractions are calculated using binomial statistics at 1σ significance.

H_β fluxes using an asymmetrical Gaussian as a probability distribution based on the asymmetrical 1σ error of the broad H_α and H_β fluxes, avoiding negative fluxes. For each numerical realization, we compute the intrinsic intrinsic H_α/H_β given a certain A_V and an $(H_\alpha/H_\beta)_{observed}$ pair.

We obtained an intrinsic $H_\alpha/H_\beta = 3.17^{+1.70}_{-1.34}$, computed using the median of the distribution of the intrinsic flux ratio, and the errors using the 1σ percentiles. The results do not change if we use instead the mode and the 1σ interval that minimizes the error range (intrinsic $H_\alpha/H_\beta = 3.15^{+1.33}_{-1.60}$). We show in Fig. 5.8 the observed H_α/H_β versus A_V from the spectral fits, where is clear that the data points are not grouped around a fixed ratio of H_α/H_β vs A_V and hence hints that there is no fixed value for the intrinsic broad H_α/H_β line flux ratio. In Fig. 5.9 we represent the histogram of the predicted intrinsic Balmer decrement. The distribution indicates that there is a wide spread without any particular skew towards higher or lower values (the median of the distribution is essentially equal to the mode).

Our estimate is consistent within the uncertainties with the most commonly used values, 3.0 – 3.4, and our error bars include the values, as well as the ones that deviate the most. Estimating the optical extinction through the Balmer decrement of the H_α and the H_β lines could be problematic for a fraction of sources. For example, in the hypothetical case of an observed ratio of H_α/H_β = 5 for one particular source, the optical extinction could range from A_V = 0.26 to A_V = 2.23 mag using the 1σ error intervals of the intrinsic ratio of H_α/H_β. In summary, the scatter is large, pointing to an important

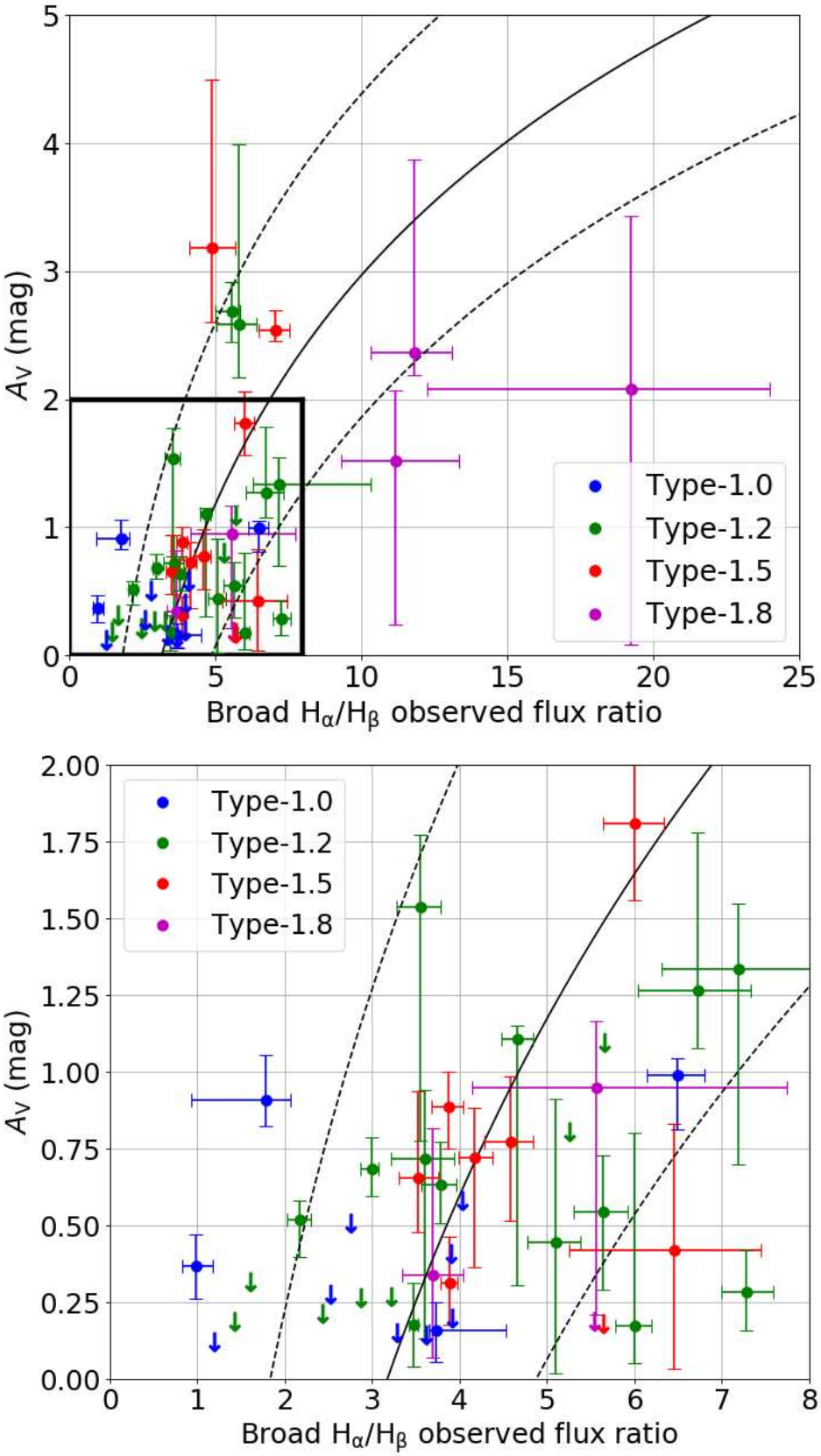

FIGURE 5.8: A_V from the continuum fits versus the H_α/H_β observed flux ratio. Top: full sample of objects with detected broad H_α and H_β, Bottom: zoom at low A_V and H_α/H_β observed ratio. The solid and dashed lines indicate the median of the H_α/H_β intrinsic ratio distribution computed in this work and its 1σ percentiles, respectively. Down pointing arrows are upper limits.

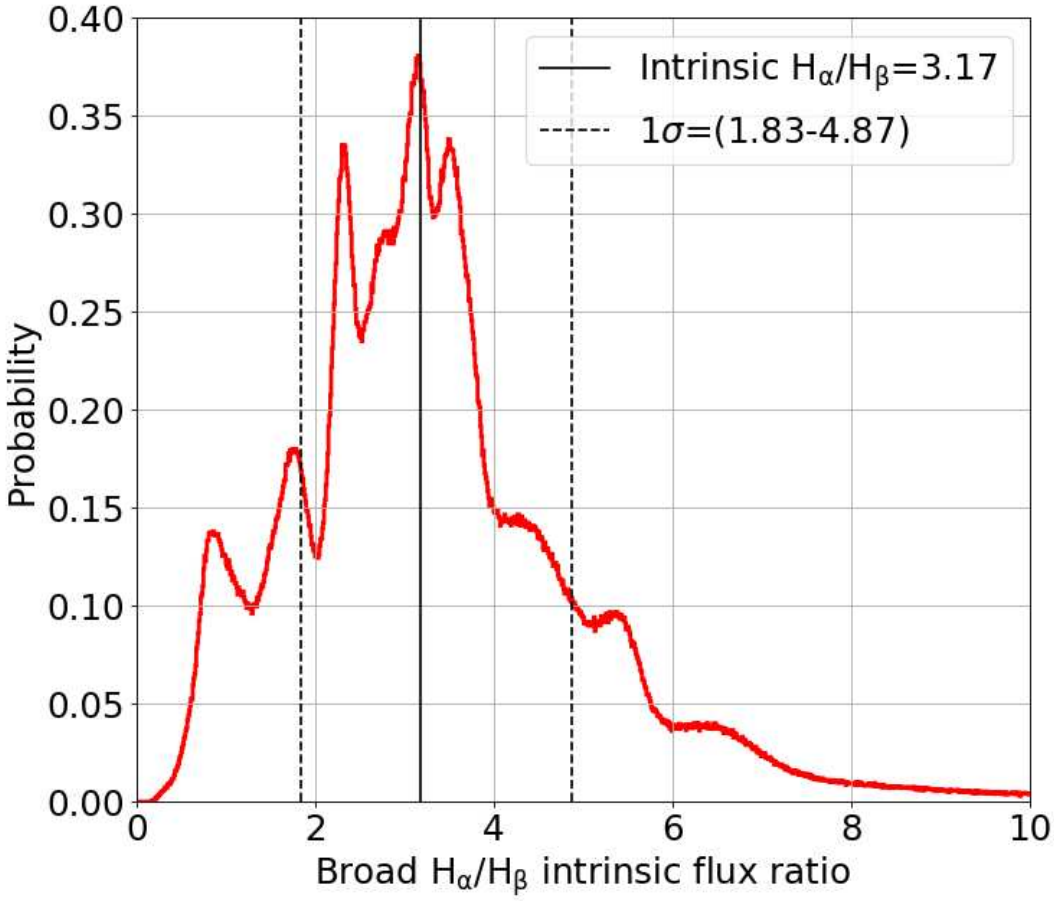

FIGURE 5.9: Probability distribution of the H_α/H_β intrinsic ratio. The solid and dashed lines show the median of the distribution and the 1σ percentiles, respectively.

dependence on the conditions of the BLR (e.g. optical depths and collisional effects), so we conclude that the extinction calculated from the BLR should be taken with extreme caution, if not discarded as extinction measurement altogether.

5.4 X-ray absorption

5.4.1 Complete classification subsample at $z < 0.2$

A similar discussion as in Sec. 5.3 can be done for the $N_{\rm H}$ column density. In Fig. 5.10 we represent the X-ray absorption versus z, and we note that, on average, $N_{\rm H}$ decreases with z. In Fig 5.11 we show the histogram of the probability distribution of $N_{\rm H}$ for the full sample and the one for the $z < 0.2$ sample. Instead of plotting the best fit values of the X-ray absorption of each AGN, we used the $N_{\rm H}$ probability distributions, so each object in the histogram contributes with an equal area. It is clear that the $N_{\rm H}$ probability distribution is skewed to lower X-ray absorption for the full sample in comparison with the sample with $z < 0.2$, as this subsample has a higher contribution of high $N_{\rm H}$ objects. Similar

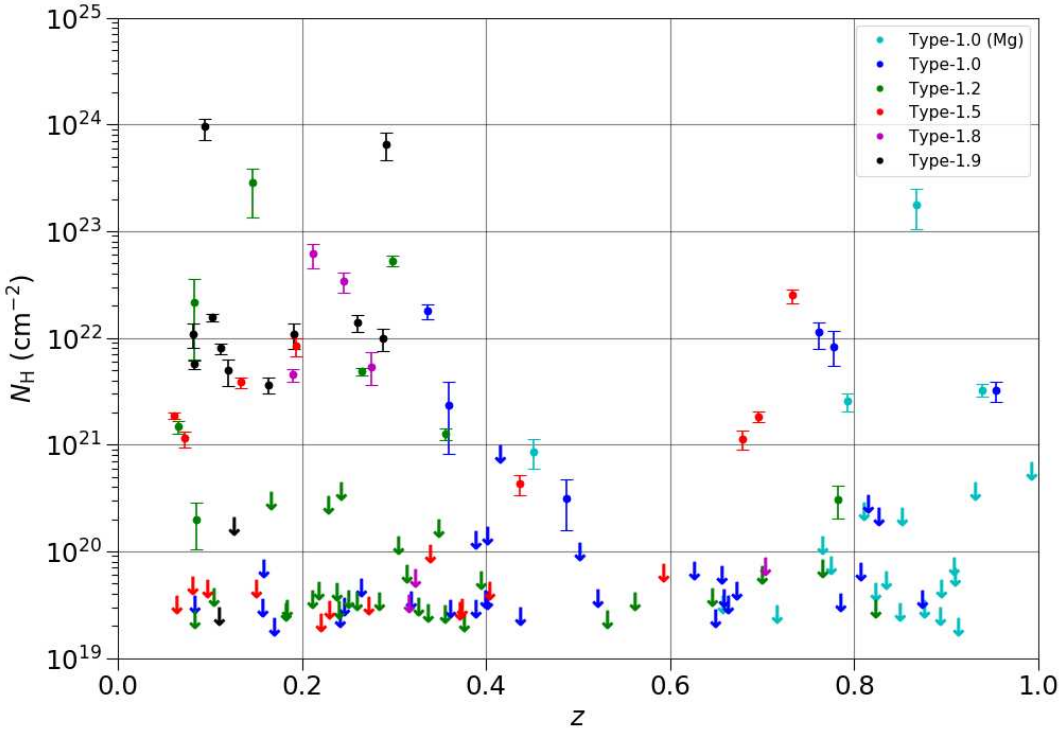

FIGURE 5.10: N_H versus z for the objects in the full BUXS type-1 sample. The error bars indicate objects with measured N_H, and the arrows indicate upper limits.

to what happens with the optical extinction, the samples without H_α wavelength coverage are biased against high N_H. Likewise, type-2 samples that do not cover the H_α wavelength region will include some type-1.9 AGN, affecting their N_H distributions.

In the following section we study the N_H probability distributions of each subclass.

5.4.2 Absorption of the subsamples

In Fig. 5.12 we show the distribution of the N_H of the full sample separated in subtypes using probability distributions as in Fig. 5.3. The type-1.8/9 AGN mainly contribute at $\log(N_H/\mathrm{cm}^{-2}) \gtrsim 21.5$, whereas the type 1.0/2/5 sources occupy the lower N_H bins preferentially, as well as the type-1 (MgII) AGN.

In Fig. 5.13 we plot the N_H probability distribution of every subclass, as previously done for A_V. In every subclass of AGN, even the type-1.8/9 objects, there are objects with low N_H for which we can only compute an upper limit on their column density. The N_H distributions for type-1.0/2/5 AGN are very similar, while those for type-1.8/1.9 sources have a larger fraction of objects with high column densities ($\log(N_H/\mathrm{cm}^{-2}) > 21.5 - 22$). To better visualize the results we show in Fig. 5.14 the boxplots of N_H for each AGN subtype. The IQR for the type-1.0/2/5 are below $\log(N_H/\mathrm{cm}^{-2}) = 21.5 - 22$, thresholds often used to separate absorbed and unabsorbed AGN (Ueda *et al.* 2003, Merloni *et al.* 2014). There is no increase in N_H from type-1.0 to type-1.5 objects. Instead, a substantial change in

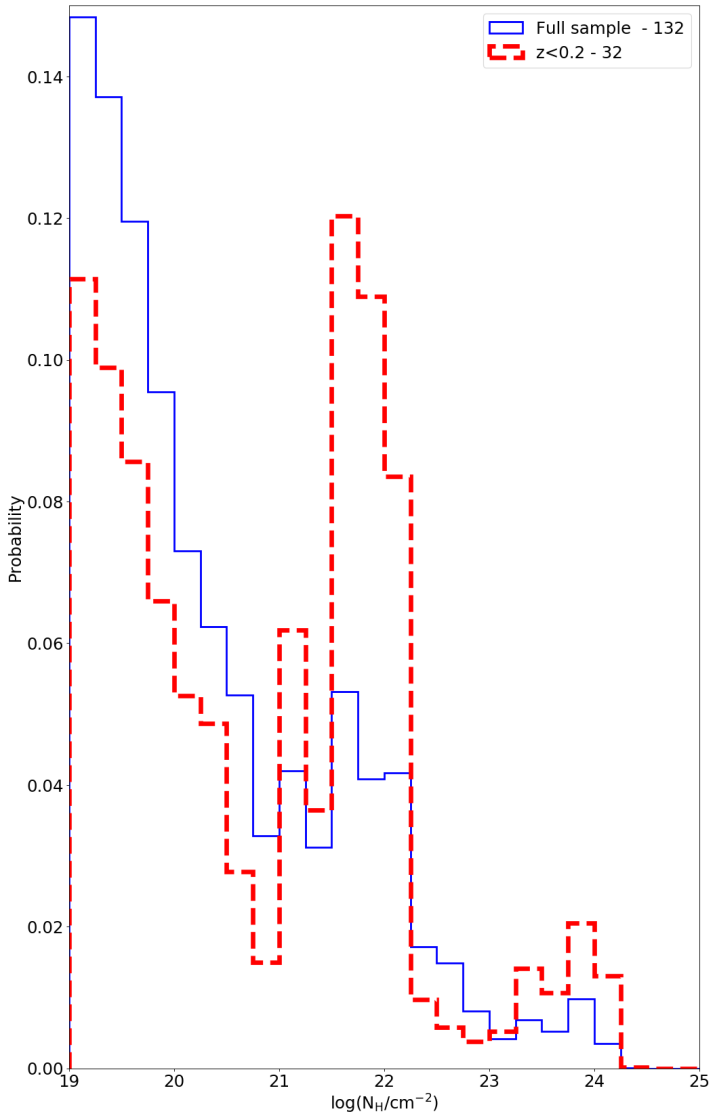

FIGURE 5.11: Normalized histograms of the X-ray absorption for the full BUXS type-1 sample and the $z < 0.2$ sample. Each object is represented by its probability distribution of $N_{\rm H}$.

$N_{\rm H}$ is seen between type-1.5 and type-1.8 AGN, and in type-1.9 objects this is more evident than in type-1.8 sources as seen in Fig. 5.14 . The IQR in the type-1.8/9 AGN reaches substantially higher $N_{\rm H}$ values than for type-1.0/2/5 sources.

We checked in a quantitative way using our KS method with bootstrapping as shown in Sec. 5.3.2 and in Table 5.4 the statistical difference of the $N_{\rm H}$ probability distribution between subtypes of AGN. In consecutive pairs, the significance of the difference of the $N_{\rm H}$ probability distribution of types-1.0/2/5 AGN are below 1σ. The turnover is produced between the type-1.5 and type-1.8 sources, because in type-1.8/9 AGN the fraction of X-ray absorbed sources is increasingly rising. The statistical difference of type-1.8 and type-1.9 AGN is between $2\sigma - 3\sigma$ significance, which is still high, probably due to the fact that absorbed sources have different levels of $N_{\rm H}$ and hence their probability distributions do nor overlap as much as in other cases. We also compared the significance of the pairs type-1.0 vs

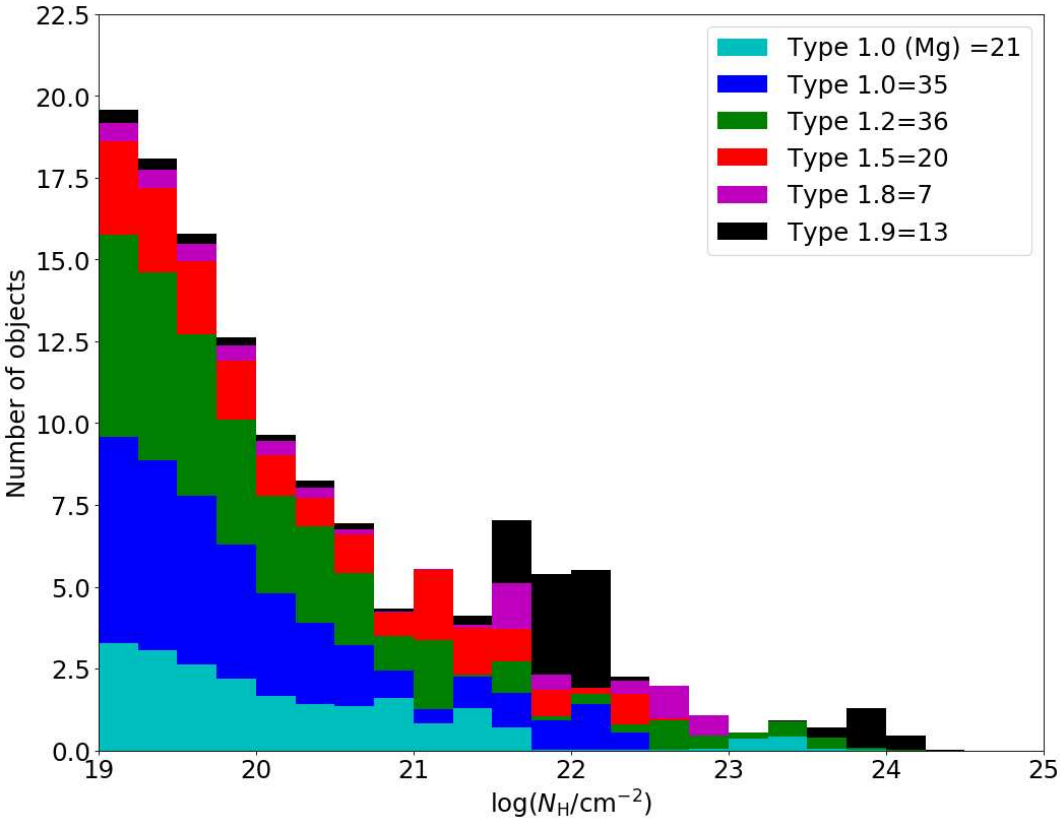

FIGURE 5.12: Histogram of the X-ray absorption for the subtypes of AGN. Each object is represented by its probability distribution of N_H, and each distribution contributes in the histogram with an area equal to one.

type-1.2/5, type-1.2/5 vs type-1.8/9 and type-1.0/2/5 vs type-1.8/9. The only pairs that are statistically significantly different are the type-1.2/5 vs type-1.8/9 and type-1.0/2/5 vs type-1.8/9 ones.

5.4.3 Fraction of X-ray absorbed type-1 AGN

As mentioned in Sec. 1.4, roughly between 10 and 23 per cent of optical type-1 AGN in the literature show X-ray absorption levels typical of type-2 AGN. Based on the N_H probability distribution of each object, we calculate the amount of X-ray absorption expected for a type-2 AGN. To do so, we proceed as with the optical extinction (see Sec. 5.3.2) and we checked the value that best divides the type-1.0/2/5 and type-1.8/9 AGN from our sample based on their N_H probability distributions. We find that the threshold that divides better the N_H distributions is $\log(N_H/\mathrm{cm}^{-2}) = 21.4$, that is close to $\log(N_H/\mathrm{cm}^{-2}) = 21.5$ from Merloni *et al.* (2014). Similar as done in Sec. 5.3.3, in this work we used the $\log(N_H/\mathrm{cm}^{-2}) = 21.5$ threshold to allow direct comparison. We include in Table 5.5 the percentage of X-ray absorption of each subclass and each subsample. The three numbers in brackets at the bottom of each cell stand for the number of sources with low X-ray absorption according to the mentioned threshold with more than 1σ confidence (i.e. the 1σ upper limit is below $\log(N_H/\mathrm{cm}^{-2}) = 21.5$), the ones whose 1σ confidence interval includes that value, and the sources with high X-ray absorption

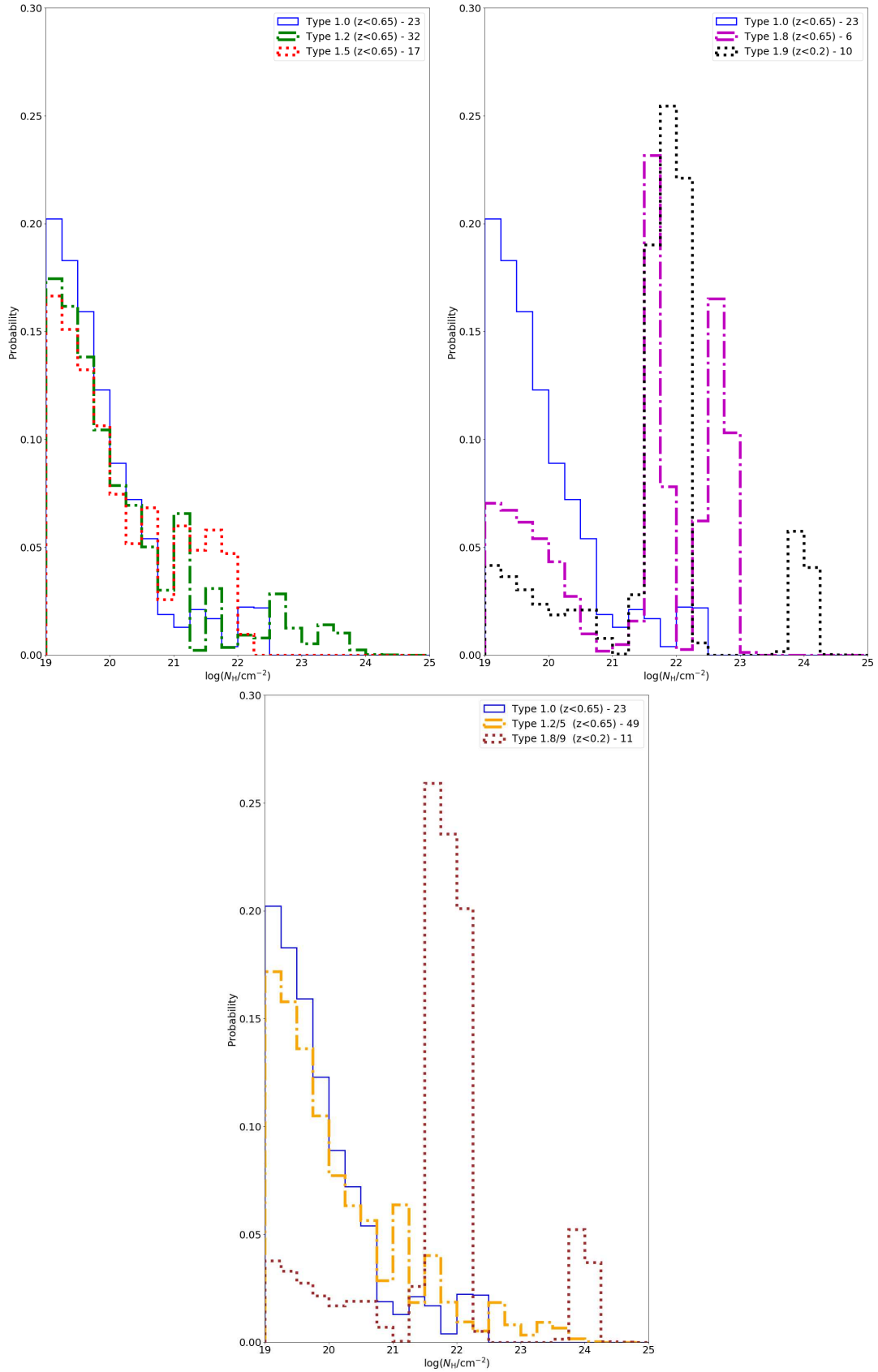

FIGURE 5.13: Normalized histograms of the X-ray absorption for the different subclasses. Each object is represented by its probability distribution of $N_{\rm H}$. We include in each panel the type-1.0 $N_{\rm H}$ distribution as a reference.

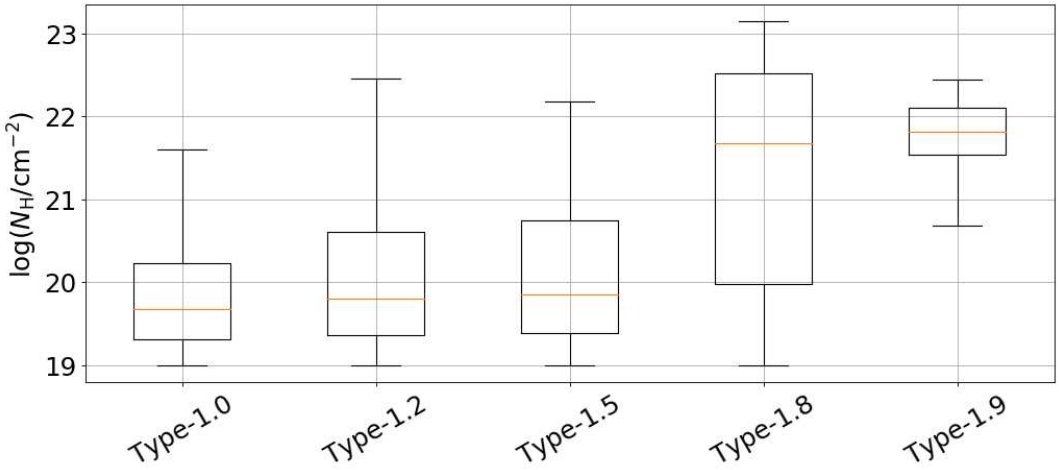

FIGURE 5.14: Boxplot of N_H for each subclass showing median values in orange. The box indicates the first and third quartiles, and the whiskers represent the last datum at a distance less than 1.5 times IQR. The z cuts for the subclasses are the same as the ones from Fig. 5.5.

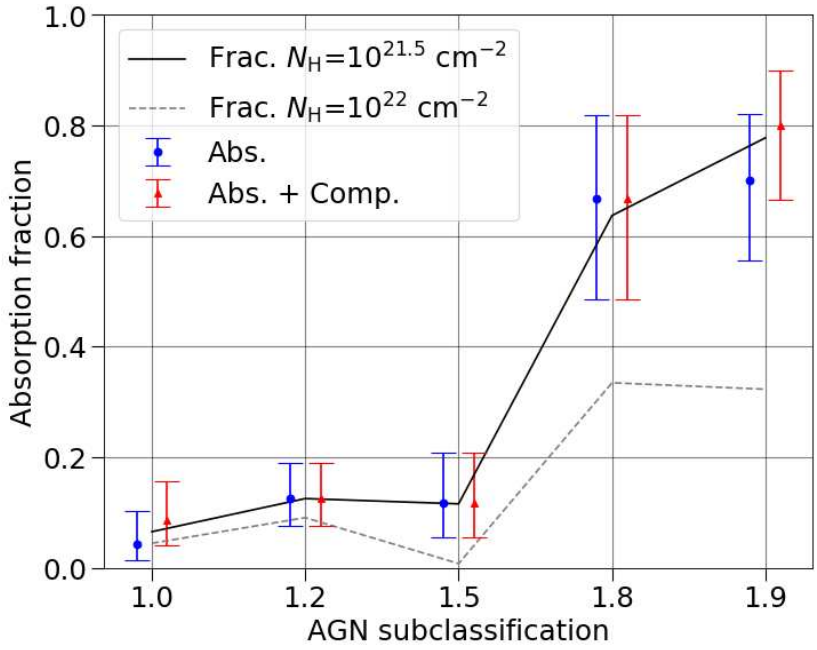

FIGURE 5.15: Fraction of AGN with X-ray absorption typical of a type-2 AGN within each subclass. The solid black line and the dashed grey line represent the fraction of the distribution of each class above the corresponding threshold ($\log(N_H/\mathrm{cm}^{-2}) = 21.5$ and $\log(N_H/\mathrm{cm}^{-2}) = 22$, respectively first row in the corresponding cell in Tables 5.5 and B.1). The blue circles represent the fraction of objects whose N_H is above $\log(N_H/\mathrm{cm}^{-2}) = 21.5$ within 1σ significance (second row in the corresponding cell in Table 5.5), with its 1σ error computed using binomial statistics. We represent with red triangles the fraction of objects whose N_H are higher or consistent with $\log(N_H/\mathrm{cm}^{-2}) = 21.5$ at 1σ. The errors on the latter fractions are calculated using binomial statistics at 1σ significance.

(i.e., the sources whose 1σ lower limit is above $\log(N_{\rm H}/{\rm cm}^{-2})= 21.5$), respectively. In Appendix A we calculate the X-ray absorbed fraction for $\log(N_{\rm H}/{\rm cm}^{-2}) = 22$ as a more conservative limit often used in the literature (Ueda *et al.* 2003). The results are similar using this threshold, but with lower absorbed fractions, in some cases about a factor ∼2 lower. In Fig. 5.15 we represent the absorbed fraction with both $N_{\rm H}$ thresholds from the combined $N_{\rm H}$ probability distribution of each class or subsample (combination of all individual probability distributions of the objects in each sample). It is evident the difference in the absorbed fraction between type-1.0/2/5 and type-1.8/9 AGN, where in the former only a few sources are absorbed and in the latter this fraction increases drastically.

In the full sample the X-ray absorbed fraction is 21 per cent. Considering only the type-1.0/2/5 AGN the X-ray absorbed fraction is 10 per cent. The percentage of absorbed type-1 AGN in BUXS is compatible with the 10-23 fraction typically found in previous studies (Caccianiga *et al.* 2004, Perola *et al.* 2004, Mateos *et al.* 2005b, Eckart *et al.* 2006, Garcet *et al.* 2007, Corral *et al.* 2011, Lusso *et al.* 2013, Merloni *et al.* 2014). The complete sample at $z < 0.2$, has a much higher absorbed fraction (40 per cent) than previous studies, and a factor ∼2 higher than the full sample. This fraction is higher due to the contribution of the type-1.8/9 AGN, because those sources are generally X-ray absorbed.

5.5 Optical extinction versus X-ray absorption

In Fig. 5.16 we plot $A_{\rm V}$ vs $N_{\rm H}$, as well as the curves corresponding to the Galactic $A_{\rm V}/N_{\rm H}$ ratio and 10, 0.1 and 0.01 times that value. It is clear that there is no direct relation between $N_{\rm H}$ and $A_{\rm V}$. Even though overall there is an increase of the extinction and X-ray absorption with AGN class, we can not assign an $N_{\rm H}$ given a certain $A_{\rm V}$, and vice versa. We find objects that are affected by significantly more obscuration in one band than in the other, without any clear bias towards higher $A_{\rm V}$ or $N_{\rm H}$.

We cannot calculate directly the dust-to-gas probability distributions as many of the $A_{\rm V}$-$N_{\rm H}$ pairs are upper limits because the distribution of the ratio may be not physical. In order to quantify the fraction of objects in our sample with dust-to-gas ratios compatible with the Galactic relation we used the $A_{\rm V}$ and $N_{\rm H}$ probability distributions previously determined. To do so we used 10000 random pairs of $N_{\rm H}$ and $A_{\rm V}$, and then we computed the percentage of $A_{\rm V}$-$N_{\rm H}$ pairs that falls above (and below) the Galactic $A_{\rm V}/N_{\rm H}$ standard. If the integral above the Galactic ratio is higher than a 83 per cent, the $A_{\rm V}/N_{\rm H}$ is higher than the Galactic ratio within a 1σ confidence. If the integral is less than a 17 per cent, the $A_{\rm V}/N_{\rm H}$ is lower than the Galactic ratio within a 1σ confidence. In the rest of the cases the dust-to-gas ratio could be compatible with a Galactic dust-to-gas ratio.

In addition, we investigated whether systematic errors, specially in low obscuration AGN, artificially extend the probability in $N_{\rm H}$ and/or $A_{\rm V}$ to higher values, resulting in wrong $A_{\rm V}/N_{\rm H}$ estimations, as the probability ratio would be artificially skewed to $A_{\rm V}$ or $N_{\rm H}$ due to these systematics. To check if this effect is important, we conducted a series of simulations. First, we fitted the low $A_{\rm V}$ and $N_{\rm H}$

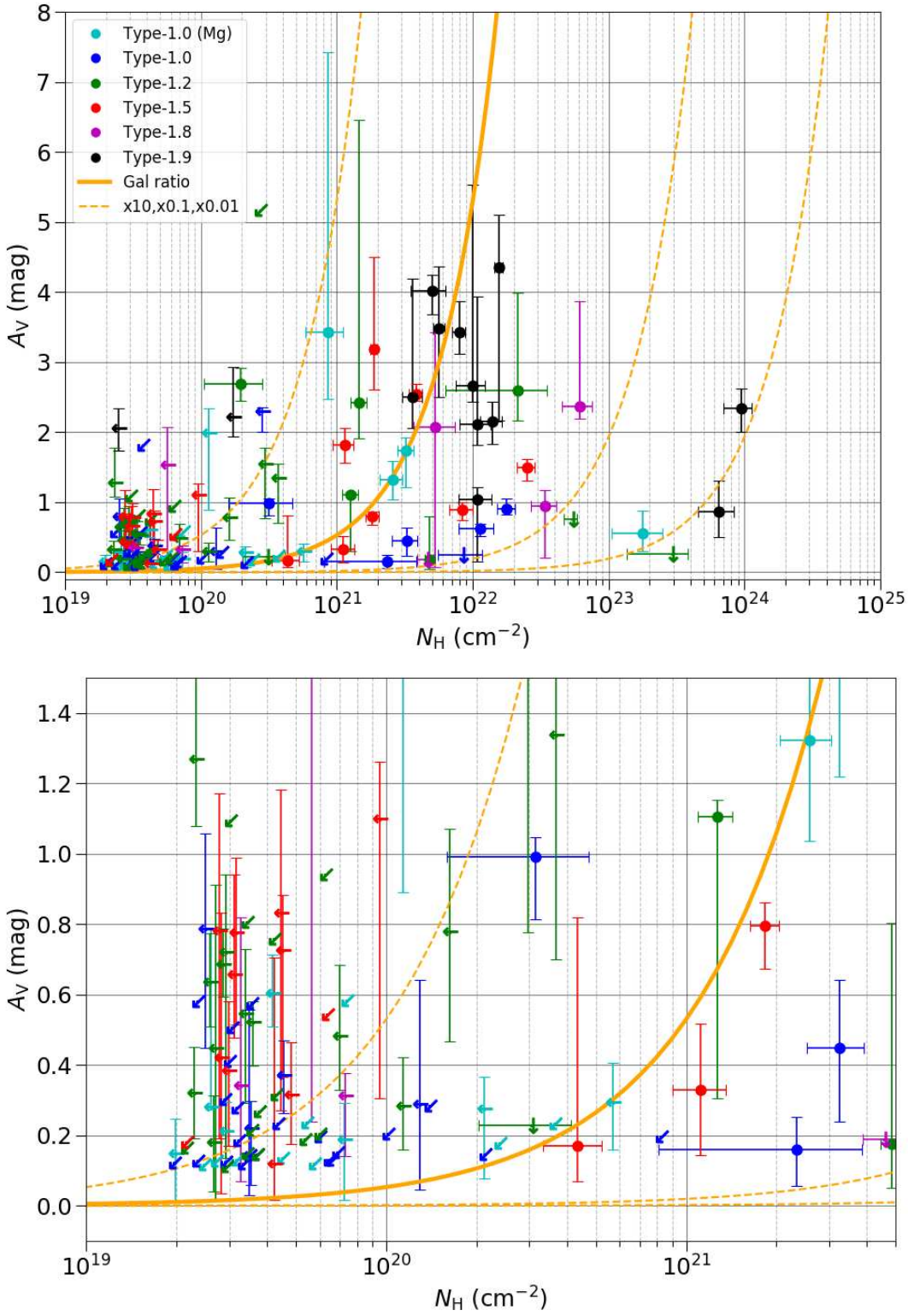

FIGURE 5.16: A_V versus N_H for the BUXS type-1 sample. Top: Full sample, Bottom: Zoom in the low A_V and N_H region of the diagram. We represent the detections with dots and the error bars indicate the 1σ percentiles. We represent the 1σ upper limits with an arrow. We use a down pointing arrow for upper limits in A_V, a left pointing arrow for upper limits in N_H, and down left pointing arrows for upper limits in both A_V and N_H. We plot with orange lines the Galactic dust-to-gas ratio (solid line) and 10, 0.1 and 0.01 times that value (dashed lines).

region of the probability distributions of type-1.0 to type-1.9 to a Gaussian, except for the type-1.9 A_V distribution, that does not present a low extinction structure able to fit to a Gaussian centred in $A_V = 0$ mag. We denote the σ of these Gaussian distributions as a systematic uncertainty for each subtype for A_V and N_H. For the systematic uncertainty in A_V for type-1.9 AGN we assumed that is the same as for type-1.8 AGN. The next step is to convert the individual N_H probability distributions to A_V using the Galactic dust-to-gas ratio and to add the Gaussian of the systematics from A_V for each type avoiding negative values. We do the same with the individual probability distributions of A_V converting them to N_H and adding the Gaussian of the systematic uncertainty of N_H for each subtype. In these simulations we compare the N_H with the A_V converted from the N_H plus the systematics (and the same thing for the A_V) and we obtain whether these values deviate significantly from the Galactic dust-to-gas relation which they should show by construction. We obtain that this effect is significant for $\log(N_H/cm^{-2}) < 21$ and $A_V < 0.5$ mag. This implies that we can only trust AGN dust-to-gas ratios for only half of the sample, missing the sources with the lowest A_V or N_H values where systematics are large enough to affect the A_V/N_H estimations, specially in low N_H objects. There are 78 objects with A_V below 0.5 mag (59 per cent) and 96 objects below $\log(N_H/cm^{-2}) < 21$ (72 per cent). With the two conditions together, the amount of AGN with $\log(N_H/cm^{-2}) < 21$ and $A_V < 0.5$ mag is 70 sources, 53 per cent of the sample.

We show in Table 5.6 the number of objects with higher A_V/N_H than the Galactic ratio, the number of AGN with compatible values and those with lower dust-to-gas ratios within a 1σ significance and the number of sources with lower A_V/N_H than the Galactic value, plus the number of AGN where it is not possible to discern between these scenarios as their low A_V and N_H provokes that the A_V/N_H ratio is biased due to the effect of systematics.

Among samples that are complete (all objects with $z < 0.2$, type-1.0/2/5 AGN with $z < 0.65$ and type-1.8/9 AGN with $z < 0.2$), despite being lower limits, we find a high fraction of objects with secure higher A_V/N_H than the Galactic standard (a minimum of 47, 32 and 36 per cent, respectively). This is in disagreement with some results previously reported where the dust-to-gas ratios are typically $3-100$ times lower than Galactic (Maiolino *et al.* 2001). The AGN sample in Maiolino *et al.* (2001) might not be comparable to our complete sample of type-1 AGN, as it is biased against both X-ray unabsorbed and highly reddened type-1 sources. Thus, our study better represents the intrinsic distribution of A_V/N_H for the type-1 population. Our results are more in the line of other studies that generally obtain that the dust-to-gas ratios are scattered around the Galactic standard (e.g. Vasudevan *et al.* 2009, Winter *et al.* 2010, Parisi *et al.* 2012, Schnorr-Müller *et al.* 2016, Glikman *et al.* 2017, Shimizu *et al.* 2018). We find that A_V-N_H points in Fig. 5.16 are scattered around the Galactic A_V/N_H without any particular skew towards higher or lower values.

TABLE 5.6: Dust-to-gas ratio of the different BUXS subsamples compared to the Galactic.

	A_V/N_H higher than Galactic	A_V/N_H compatible with Galactic	A_V/N_H lower than Galactic	Uncertain A_V/N_H
Full sample	32 (24%)	7 (5%)	23 (18%)	70 (53%)
$z < 0.2$	15 (47%)	2 (6%)	8 (25%)	7 (22%)
Type-1 (MgII)	3 (14%)	2 (10%)	1 (5%)	15 (71%)
Type-1.0 ($z < 0.65$)	2 (9%)	0 (0%)	2 (9%)	19 (82%)
Type-1.2 ($z < 0.65$)	12 (38%)	1 (3%)	4 (13%)	15 (46%)
Type-1.5 ($z < 0.65$)	9 (53%)	0 (0%)	1 (6%)	7 (41%)
Type-1.8 ($z < 0.65$)	1 (17%)	1 (17%)	3 (50%)	1 (17%)
Type-1.9 ($z < 0.2$)	4 (40%)	2 (20%)	4 (40%)	0 (0%)
Type-1.0/2/5 ($z < 0.65$)	23 (32%)	1 (1%)	7 (10%)	41 (57%)
Type-1.8/9 ($z < 0.2$)	4 (36%)	2 (18%)	5 (46%)	0 (0%)
A_V and N_H detected (full sample)	9 (25%)	7 (19%)	19 (53%)	1 (3%)
A_V and N_H detected ($z < 0.2$)	7 (47%)	2 (13%)	6 (40%)	(0%)

Notes: We list the number (fraction) of sources with A_V/N_H higher, compatible at 1σ or lower than Galactic, respectively. The last column indicates the number (fraction) of AGN for which we can not constrain the A_V/N_H scenario properly.

5.6 Discussion

5.6.1 Caveats

In this section we list some caveats that must be discussed in order to understand the results of this study:

- **UV/optical slope changes:** In our study we fixed the shape of the AGN featureless continuum to the one of the QSO template from Richards *et al.* (2006). We mentioned in Sec. 3.3.2 that the optical extinction measurements would not change dramatically, and we quantify here the possible deviations in A_V if other slopes were used. We obtain the maximum deviation that can be caused by different continua using the $\alpha = -1.9$ to -1.4 range (Polletta *et al.* 2007). We calculated the optical extinction needed to obtain the reddest continuum ($\alpha = -1.4$) using as a baseline the bluest one ($\alpha = -1.9$). This is computed between rest-frame 2000 and 9200 Å wavelengths, the rest-frame minimum and maximum wavelength values that we use. The measurements can deviate $A_V = 0.37$ mag at most. This conservative uncertainty does not explain the apparent lack of relationship in A_V-N_H that we find in our sample. So far, there are no indications that the shape of the rest-frame UV/optical continuum might be linked to the AGN subtype or the luminosity (e.g. Severgnini *et al.* 2003, Memola *et al.* 2007, Caccianiga *et al.* 2008, Shen *et al.* 2011, Jin *et al.* 2012a). Since the intrinsic slope is independent from the classification the A_V of the subtypes of AGN can be safely compared between them. The typical levels of obscuration of each subtype of AGN do not seem to change with z either, so we can

compare their combined distributions with complete classification even if they are built using different cuts in z.

- **Neutral gas versus ionized gas:** In this work we did not take into account that the gas responsible for the X-ray absorption might be ionized. This absorption is believed to be caused by outflows of the BLR gas (Reynolds and Fabian 1995, Kaastra *et al.* 2000, Kaspi *et al.* 2000a). An ionized gas would have a higher $N_{\rm H}$ density in comparison to a neutral absorber to produce the same effective absorption (Page *et al.* 2017). Thus, we might be underestimating the $N_{\rm H}$ column densities in this study, and so we would get $A_{\rm V}/N_{\rm H}$ values biassed too high. We can not introduce an ionized absorber to our X-ray spectral fits because our data have not enough quality to constrain the model parameters in a reliable enough way. Ionized absorbers have been detected in $20-50$ per cent of all AGN (Komossa and Hasinger 2003, Singh, Shastri, and Risaliti 2011, Ricci *et al.* 2017a). The distribution of ionization parameters in type-1 AGN is between $\log(\xi/\mathrm{erg\ cm\ s^{-1}}) = -2$ and 3.5, but the majority ($\sim$80 per cent) is in the $\log(\xi/\mathrm{erg\ cm\ s^{-1}}) = 0-2.5$ range (Ricci *et al.* 2017a). The deviation in the estimation of $N_{\rm H}$ is less than one order of magnitude for $\log(\xi/\mathrm{erg\ cm\ s^{-1}}) \simeq 3.5$, while for $\log(\xi/\mathrm{erg\ cm\ s^{-1}}) \lesssim 2.5$ the $N_{\rm H}$ is essentially the same as the one measured using neutral gas (Page *et al.* 2017). In conclusion, we might be underestimating the X-ray absorption in some AGN, but the values are not significantly different (at least in the vast majority of the AGN), and hence this effect cannot explain the scatter in the $A_{\rm V}$-$N_{\rm H}$ relation and it has only a marginal impact in our work.

- **Variability:** Our optical and X-ray spectra were not taken simultaneously. Variability in both the obscuration and flux is frequently observed in AGN (Risaliti *et al.* 2005, Trippe *et al.* 2010, LaMassa *et al.* 2015, De Cicco *et al.* 2015, Yang *et al.* 2016, Burtscher *et al.* (2016), Hernández-García *et al.* 2017, González-Martín 2018). Variability alone could spread $A_{\rm V}/N_{\rm H}$ ratios without invoking scenarios where the properties of the circumnuclear material can be more diverse than reported before. Markowitz, Krumpe, and Nikutta (2014) show that changes in the X-ray absorption can happen within one day to a few years, with column densities of the eclipsing clumps spanning $4-26\times10^{22}$ cm^{-2}. For type-1.0/2/5 AGN, the probability of an eclipse of a clump of gas is $0.3-16.6$ per cent, while for type-1.8/9 is $3.9-57.1$ per cent, so the probability that this effect is statistically affecting our results is low. Furthermore, our sample has 35 per cent of objects with more than one observation with time-scales between observations of years, so for these objects the $N_{\rm H}$ is averaged in years (since we combine all the X-ray spectra available for each source, see Sec. 3.2) and hence the variability impact is even lower. Regarding optical variability, we have 41 sources with more than one UV/optical spectrum. Of these, only 9 of the objects with multiple spectra show optical extinction variability with $>1\sigma$ confidence. This number is close to the expected number of spurious detections given the 1σ limit used. These results imply that variability could increase the scatter in the $A_{\rm V}$-$N_{\rm H}$ relation, but the observed scatter in our sample cannot be explained just by optical extinction and/or X-ray absorption variability and other scenarios must be explored.

5.6.2 Comparison between A_V from the continuum and from the Balmer decrement

Using our estimates of the optical extinction of the broad-band continuum emission (from the accretion disk), we investigated whether it correlates with the broad H_α and H_β flux ratio. The Balmer decrement, that is often used as an UV/optical extinction estimator, shows a big scatter when compared with the extinction from the continuum. The intrinsic broad H_α and H_β flux ratio is $H_\alpha/H_\beta = 3.17^{+1.70}_{-1.34}$, compatible with previous results but the error bars are large. These results are in concordance with other studies that find a wide spread in this quantity (Jin, Ward, and Done 2012b, Schnorr-Müller *et al.* 2016, Baron *et al.* 2016), and in agreement with the hypothesis that the intrinsic Balmer decrements can be very different depending on line optical depths and collisional effects in the BLR (Netzer 2013). We conclude that A_V estimations using Balmer decrements should be used with extreme caution.

5.6.3 Full sample vs. complete sample

This study is the first one that obtains the distribution of the optical extinction and X-ray absorption for a complete sample of type-1 AGN, which is based on the individual probability distributions of A_V and N_H from the modelling of their UV/optical and X-ray emission, respectively.

We analysed different subsamples of type-1 AGN in BUXS to conduct the studies presented in this Thesis. Our $z < 0.2$ sample allows us to analyse a type-1 AGN sample with complete and accurate classification in subtypes from type-1.0 to type-1.9, and compare it with the full sample to identify biases introduced in A_V and N_H that the latter has and determine their impact. Measuring the impact of working with a sample with incomplete classification is important since samples at higher z will be affected by these biases.

The fraction of optically reddened AGN in our complete sample is 51 per cent. This value is significantly higher than the 21 per cent in the full sample. Our results point out that there is a significant fraction of optically reddened objects (specially type-1.9 AGN with $z > 0.2$) missed by the full sample due to the lack of wavelength coverage of the H_α region (and H_β for the type-1.8/9 AGN at the highest z, that are classified as type-2). This implies that a sample of type-1 AGN without complete classification will have an A_V probability distribution biased to low optical extinction, and its optically reddened fraction would be underestimated by a factor ∼2.5.

The X-ray absorption fraction in the complete classification sample is 40 per cent, while in the full sample is 21 per cent. This finding is in line with the results obtained for the optical extinction, as the AGN with the highest X-ray absorption are preferentially found at low z. The misclassification of obscured type-1 sources as type-2 sources due to changes in wavelength coverage with z results in a N_H probability distribution biased to low X-ray absorption, as well as a decrease in the absorbed AGN fraction by a factor ∼2.

TABLE 5.7: Reddened and absorbed concordance for the complete sample ($z < 0.2$).

Complete sample (32)	Unreddened	A_V = 1.4 mag within 1σ	Reddened
Unabsorbed	11 (34 %)	2 (6 %)	6 (19 %)
$\log(N_H/cm^{-2}) = 21.5$ within 1σ	0 (0 %)	0 (0 %)	1 (3 %)
Absorbed	4 (13 %)	0 (0 %)	8 (25 %)

Notes: Number and fraction of AGN that are unreddened or unabsorbed, those whose 1σ confidence interval includes A_V = 1.4 mag or $\log(N_H/cm^{-2}) = 21.5$, and those that are reddened or absorbed.

Many studies only consider as type-1 AGN those objects whose classification are type-1.0/2/5, while type-1.8/9 are classified instead as type-2 AGN. If only type-1.0/2/5 AGN are considered, the fraction of reddened type-1 AGN drops to 12 per cent. With respect to the X-rays, the fraction of absorbed type-1.0/2/5 AGN is 10 per cent. Those fractions are a factor ∼2 lower than in the full sample, and hence a factor $\sim 4-5$ lower than the $z < 0.2$ sample. In conclusion, to study the properties of type-1 sources, as we have done with the A_V and N_H distributions in this Thesis, it is necessary to use a complete sample that includes type-1.8/9 AGN, as without complete classification the fraction of absorbed/reddened sources is underestimated by a factor $\sim 2-2.5$.

Lastly, in Table 5.7 we show, for the complete sample, the numbers and fractions of objects with both types of obscuration. 1σ errors were computed using binomial statistics. As expected, for the majority of AGN (a minimum of 59 ± 8 per cent) the optical and X-ray obscuration is correlated. In total, 32 ± 8 per cent of objects show discordant optical and X-ray obscuration, where 13 ± 6 per cent are unreddened but absorbed sources, and 19 ± 7 per cent of them are unabsorbed but reddened objects. As mentioned in Sec. 1.4.3, in the literature 10 – 23 per cent of AGN optically classified as type-1 show discordant optical and X-ray properties, so for the full sample this is a factor ∼2 higher than in the literature. In Table B.2 we show the same information but with $A_V = 2$ mag and $\log(N_H/cm^{-2}) = 22$.

5.6.4 Dependence of AGN obscuration with subclassification

The increase of the UV/optical extinction with the subtype of AGN indicates that, statistically, the main contribution to the optical spectroscopic classification of type-1 AGN is the extinction of the nuclear emission (Osterbrock 1981). Dust from the host galaxy (Maiolino and Rieke 1995, Alonso-Herrero *et al.* 2003, Prieto *et al.* 2014) and/or from the torus (Goodrich 1995, Komossa and Fink 1997, Heard and Gaskell 2016, Schnorr-Müller *et al.* 2016) partially blocks the accretion disk, BLR and X-ray corona. The narrow emission lines are not affected by the torus, as they are emitted further away from the SMBH.

The host galaxy obscuration has an impact in the nuclear emission (Baron *et al.* 2016). The inclination of the host galaxy disk is found to affect the classification with increasing inclination from type-1.0 to type-1.9, so type-1.0/2/5 AGN are found preferentially on face-on galaxies and type-1.8/9 on edge-on

galaxies (e.g. Maiolino and Rieke 1995, Curran 2000). There are studies that show that the classification in subtypes is provoked by foreground obscuration from the host galaxy. Specially in type-1.8/9 AGN it is proposed that the host extinction is the cause of this classification (e.g. Maiolino and Rieke 1995, Alonso-Herrero *et al.* 2003, Prieto *et al.* 2014). Koss *et al.* (2011) using a hard X-ray selected sample found that there are 41 per cent of spirals hosting AGN, while only 22 per cent of inactive galaxies are spirals, and there 10 per cent of elliptical galaxies hosting AGN versus 20 per cent of inactive elliptical galaxies. Spiral hosts, with cold gas and with presence of dust have more impact in the optical extinction and X-ray absorption than elliptical galaxies (Seward and Charles 1995, Binney and Merrifield 1998).

We tried to check the impact of the host galaxy morphology, so we cross correlated the sources in this study with the Galaxy Zoo 1 data release of morphological classification of galaxies (Lintott *et al.* 2011). Only for 23 sources there is Galaxy Zoo classification, so even for $z < 0.2$ we do not have complete classification. We visually inspected the morphology to check the classification and we noticed that for many cases it is very complicated to classify the host galaxies due to the quality of the SDSS images, specially between elliptical galaxies and face-on disk galaxies or with intermediate inclinations. This means that we can not estimate robustly the impact of the host galaxy morphology in our study. There are 3 galaxies where the most probable classification is of an edge-on galaxy: 2 of them are type-1.9 AGN and the other one is a type-1.5 AGN. Among the possible face-on and elliptical galaxies there are type-1.9 AGN, so even though edge-on galaxies are preferentially type-1.9 sources, not all of these objects reside in edge-on galaxies. With the data available in this work we can not estimate whether the obscuring material is mainly from the host galaxy or from the torus.

Alternative contributions to the extinction that may affect the classification (Trippe *et al.* 2010, Elitzur, Ho, and Trump 2014) might be as well present but given the clear relation between A_V and AGN subtype their contribution should be much less important than obscuration.

We obtained that we can differentiate type-1 AGN subtypes in three groups: objects with almost no N_H nor A_V (type-1.0), those with moderate A_V and no N_H (type-1.2/5), and finally those with substantial A_V and N_H (type-1.8/9). In Sec. 5.6.5 we examine further the dust-to-gas ratio of the sample by checking different scenarios based on the A_V and N_H probability distributions (higher or lower A_V/N_H ratios than the Galactic standard or compatible with it, if it is possible to discern between those scenarios).

5.6.5 Comparison between A_V and N_H

Due to the lack of dependence between the amount of A_V and N_H, our results favour scenarios where the bulk of the X-ray absorption takes place in a different region than the optical extinction (Weingartner and Murray 2002) or there is a wide span of dust-to-gas ratios from object to object (Maiolino *et al.* 2001, Malizia *et al.* 2012, Ordovás-Pascual *et al.* 2017, Shimizu *et al.* 2018). As mentioned in Sec. 5.5 we obtain dust-to-gas ratios for the AGN in this study scattering around the Galactic ratio.

From a conservative and rigorous analysis, we obtained that for 53 per cent of the full sample we can not constrain properly the dust-to-gas ratio scenario, as both A_V and N_H are too low and hence their probability distributions ratio are biased due to systematic effects. In these cases, the most likely explanation is that the line-of-sight does not intercept any material, or perhaps the material has low density and we are not able to constrain its properties. If we consider the complete classification sample, the fraction of objects with secure dust-to-gas ratios higher than the Galactic value rises to 47 per cent, while this subsample has less objects with no estimated A_V/N_H (22 per cent). An scenario where the dust is more abundant than the gas in comparison with the Galactic dust-to-gas ratio is reported in the literature, but only for $3-9$ per cent of the sources (Panessa and Bassani 2002, Trippe *et al.* 2010, Simmons *et al.* 2011, Malizia *et al.* 2012, Mehdipour, Branduardi-Raymont, and Page 2012, Huang *et al.* 2011, Ordovás-Pascual *et al.* 2017). Our higher fraction of A_V/N_H ratios higher than the Galactic standard compared to previous studies might be due to selection effects of previous samples (e.g. misclassification of type-1 objects or AGN selection methods that miss sources with high optical extinction) or because this analysis is not formally performed in these works (the fraction of high A_V/N_H AGN in Shimizu *et al.* 2018 might be comparable to the one in this Thesis). Our results point out that, accurately treating the probability distributions of A_V and N_H, the population of high dust-to-gas ratio AGN could be higher than reported before according to our analysis, as shown in Table 5.6 and looking at the A_V versus N_H plot in Fig. 5.16.

For the type-1.0/2/5 AGN with complete classification ($z < 0.65$), even though for 57 per cent we can not estimate A_V/N_H, there is a minimum of 32 per cent of sources with higher dust-to-gas ratio than the Galactic. In type-1.8/9 AGN with $z < 0.2$ we have complete identification of dust-to-gas ratio scenarios, and the fraction of objects with higher A_V/N_H than Galactic is 36 per cent.

For the AGN subsamples that are not affected by systematics and hence we can constrain the A_V/N_H for all objects (that are type-1.9 at $z < 0.2$, type-1.8/9 at $z < 0.2$ and the objects at $z < 0.2$ with A_V and N_H detected), we obtained that their fraction of A_V/N_H higher than the Galactic standard is roughly the same as the one with A_V/N_H lower than the Galactic ratio (40 per cent approximately). If we use all the objects in the sample with detected A_V and N_H, the fraction of AGN with lower dust-to-gas ratios than the Galactic standard is roughly twice as the one for higher A_V/N_H ratio than the Galactic (53 per cent versus 25 per cent, respectively). So if we consider only those objects with detected A_V and N_H, we would overestimate the fraction of AGN with lower dust-to-gas ratios than the Galactic. This sample, and the one of $z < 0.2$ objects with detected A_V and N_H, are not complete samples so we can not draw any further conclusions from them.

In conclusion, our sample of type-1 AGN has A_V/N_H ratios scattered around the Galactic value, as similar studies obtained, but the fraction of type-1 sources with higher dust-to-gas ratios is found to be higher than previously reported.

5.7 Conclusions

In this Thesis we analysed the dependence of the subclassification of AGN with the nuclear obscuration in the UV/optical and X-ray energy bands using the BUXS type-1 AGN sample. This is a large, flux limited sample of X-ray selected AGN with accurate spectroscopic classifications and z for all sources and with good quality spectra in the UV/optical and X-rays. We used a new analysis technique based on the individual probability distributions of $A_{\rm V}$ and $N_{\rm H}$ for each object in this sample. We isolated the AGN emission from the host galaxy starlight at UV/optical wavelengths to obtain the $A_{\rm V}$ from the modelling of the continuum emission. From our analysis we concluded that:

(i) The complete classification subsample ($z < 0.2$) shows $A_{\rm V}$ and $N_{\rm H}$ probability distributions with higher values than the full sample. This is quantified using the fraction of optically reddened and X-ray absorbed AGN. For the full sample is 21 per cent, for each one, while for the complete classification subsample are 51 and 40 per cent, respectively. This is a factor $2-2.5$ of difference. This indicates that type-1 AGN selected samples without complete classification (i.e. without H_α and H_β covered for all sources) miss a significant fraction of obscured sources, thus biasing the sample to low $A_{\rm V}$ and $N_{\rm H}$.

(ii) We find that 32 per cent of AGN in the complete sample show discordant optical and X-ray obscuration, where 19 per cent of them are unabsorbed but reddened objects, and 13 per cent are unreddened but absorbed sources. This percentage of discordant type-1 AGN is a factor ~2 higher than the one in the literature.

(iii) We obtained that the $A_{\rm V}$ probability distributions of type-1.0, type-1.2/5 and type-1.8/9 AGN form statistically different populations, while the $N_{\rm H}$ probability distributions divide the subtypes in type-1.0/2/5 and type-1.8/9 sources. $A_{\rm V}$ gradually increases from type-1.0 to type-1.9 objects, indicating that this is the main contribution to AGN subclassification. In the case of $N_{\rm H}$ type-1.0/2/5 are generally unabsorbed ($\log(N_{\rm H}/{\rm cm}^{-2}) < 21.5$), while there is a higher number of X-ray absorbed type-1.8/9 objects. The optical extinction and the X-ray absorption are tightly related with the AGN subtype.

(iv) The Balmer decrement of the H_α and H_β broad emission line flux ratios does not correlate tightly with the UV/optical continuum extinction. We obtained that the H_α/H_β intrinsic ratio is $H_\alpha/H_\beta = 3.17^{+1.70}_{-1.34}$, compatible with previous reported values, but the big scatter indicates that there is no universal value for all AGN. UV/optical extinction estimations from these ratios must be taken with caution.

(v) The lack of correlation between $A_{\rm V}$ and $N_{\rm H}$ suggests that either the material responsible for the X-ray absorption is located in a different structure than the region that obscures the optical extinction, or that the material that obscures the innermost emission of the AGN can have a wide variety of relative proportions of dust and gas.

(vi) The A_V-N_H pairs in our sample of type-1 AGN are scattered around the Galactic A_V/N_H ratio, as previously reported in other works. Even though for half of the sample we can not compute properly the A_V/N_H ratios, using a rigorous and conservative analysis we obtained a minimum of 47 per cent of objects with higher dust-to-gas ratios than the Galactic for the complete sample. This fraction is higher than the $3-9$ per cent previously reported. If we consider only type-1.0/2/5 AGN with $z < 0.65$, as other works do, there is a minimum of 32 per cent of objects with higher dust-to-gas ratios than the Galactic, which is still higher than previously reported.

Chapter 6

Conclusions and future work

6.1 Conclusions of this Thesis

In this Thesis we present the results of a complete study of the extinction (in the optical) and absorption (in X-rays) of the nuclear emission by material in the line-of-sight to the SMBH for AGN optically classified as type-1. This topic has direct bearings in the band-dependent (and sometimes inconsistent) classification of AGN as obscured or unobscured. There have been a few studies on the topic of the relation between optical and X-ray classifications, and the extinction processes related to each band. Roughly $10-23$ per cent of type-1 AGN present are X-ray absorbed, while $3-17$ per cent of type-2 AGN are X-ray unabsorbed. The dust-to-gas ratios show a wide spread of values in type-1 AGN, while only a $3-9$ per cent show $A_{\rm V}/N_{\rm H}$ higher than the Galactic ratio. Often, these samples are affected by biases against reddened AGN due to misclassification of type-1 objects or AGN selection methods that miss sources with low extinction, and do not work with complete and representative samples.

In Sec. 6.1.1 we will point out the main conclusions from the detailed study of the two particularly interesting unabsorbed type-1.9 sources. After that, in Sec. 6.1.2 we analyse the general results and consequences that we can extract from the statistical study of a larger and representative sample of type-1 AGN. Finally, this Thesis has provided an important quantity of information with remarkable quality to the BUXS sample, that can be used to study other research topics. In Sec. 6.2 we point out several topics that can be studied as a follow up of the work provided in the present Thesis.

6.1.1 Detailed analysis of two X-ray unabsorbed type-1.9 objects

In Chap. 4 we presented in detail the case of two type-1.9 (generally reddened in the UV/optical) AGN: 2XMMiJ000441.2+000711 and 2XMMJ025218.5-011746 (called here J00 and J02, respectively), whose $N_{\rm H}$ was below the threshold commonly used for X-ray absorbed sources ($\log(N_{\rm H}/{\rm cm}^{-2})$

= 21.5 − 22). After a careful removal of the host galaxy emission we could recover the AGN emission at rest-frame UV-to-NIR wavelengths and compute, not only the optical extinction but other nuclear emission parameters such as the flux of several broad and narrow emission lines or the SMBH masses. Relating this information with the host galaxy we could examine whether the mismatch between UV/optical and X-ray properties was due to intrinsic nuclear properties and/or dilution of the AGN emission by their host galaxies.

Our results confirmed that in the case of J00 the obscuring medium in the line-of-sight is a material with more dust content than the average AGN population. This is more than 5 times more dusty than the standard Galactic dust-to-gas ratio in terms of A_V/N_H. This peculiar composition provokes that the UV/optical emission from the nuclei is more affected by obscuration than the X-ray photons, causing a mismatch between the optical and X-ray classifications of J00. An environment more dusty than the average is reported in the literature in 3 – 9 per cent (Caccianiga *et al.* 2004, Malizia *et al.* 2012). This is a possible explanation for type-2 AGN with slightly absorbed X-ray emission or not absorbed at all (Trippe *et al.* 2010, Mehdipour, Branduardi-Raymont, and Page 2012, Huang *et al.* 2011), where there is a host-galaxy related dusty structure or the circumnuclear region is more dusty than the average. For the particular case of J00, the NLR Balmer decrement gives an A_V smaller than for the nuclear continuum, so a dusty host-galaxy related structure is less likely in this case. In conclusion, a higher dust-to-gas ratio than the Galactic relation is the best explanation to the classification mismatch in J00.

With respect to J02, in the public spectrum of 6dF there is no broad H_α emission visible. Using our dedicated long slit spectrum from VLT/X-Shooter we uncovered a broad emission line in H_α, thanks to the detailed modelling of the emission lines and because with the slit we got rid of an important fraction of the host galaxy starlight. In fact, for J02, the host galaxy emission is the main factor that provokes the mismatch of the optical and X-ray classifications, as the host galaxy is more than one order of magnitude more massive than expected by the host-SMBH relation. Host galaxy dilution of the AGN emission could be the explanation of XBONGs (Smith, Koss, and Mushotzky 2014), those whose optical spectrum is of a quiescent galaxy but whose large X-ray luminosity is difficult to explain without invoking nuclear activity. We conclude that is crucial to separate host galaxy starlight from the AGN emission, as it can disturb the results in a critical way, as in the case of J02.

In the first work of this Thesis we have proven that the discrepancy of AGN classification between the optical and X-ray bands can be originated by very different phenomena, and hence they do not form a physical family with similar properties.

6.1.2 Optical extinction and X-ray absorption of a complete type-1 sample

Focusing in the statistical approach from Chap. 5, we analysed the $z = 0.05 - 1$ BUXS type-1 AGN sample, excluding those objects with $\log(L_{2-10\,\mathrm{keV}}/\mathrm{erg\ s^{-1}}) < 42$, to increase the contrast between

AGN and host galaxy. This leads to our full sample of 132 type-1 AGN. By combining all the XMM-Newton observations publicly available at the time of the analysis, we obtained high quality XMM-Newton spectra. This allowed the X-ray absorption to be measured with a minimum column density of $\log(N_{\rm H}/{\rm cm}^{-2}) \gtrsim 19$, whereas in previous studies normally set a minimum of $\log(N_{\rm H}/{\rm cm}^{-2})= 20$ when no absorption is detected. In this Thesis we accurately decomposed the observed rest-frame UV/optical spectrum of AGN into host galaxy and nuclear emission, the latter taking into account the Balmer continuum and the FeII emission, as well as the intrinsic optical extinction. For both $A_{\rm V}$ and $N_{\rm H}$ we obtained individual probability distributions for each object, being the first study that uses these distributions to conduct a detailed analysis of the obscuration in type-1 AGN in each energy band. By modelling the broad and narrow emission lines we classified our type-1 sources into type-1.0/2/5/8/9 AGN, allowing us to work with an unique cosmological sample with accurate classification.

It is very common in the literature that the optical extinction is estimated through broad H_α and H_β emission line flux ratios, that is the Balmer decrement. By comparing the $A_{\rm V}$ values from the accretion disk with the broad H_α/H_β ratio, we obtained that these quantities do not correlate well. The intrinsic H_α/H_β ratio that we obtained is $H_\alpha/H_\beta = 3.17^{+1.70}_{-1.34}$, similar to the one from previous studies, but with a significant scatter. We conclude that reddening values using the Balmer decrement should be taken with caution.

We compared the full sample with the subsample with $z < 0.2$, that has complete classification. This means that we do not misclassify any type-1.8/9 AGN as a type-2 object due to the lack of coverage of the rest-frame H_α or H_β wavelength region. We obtained that without working with complete classification type-1 samples a significant fraction of obscured sources would be missed. This provokes a bias in the sample to low $A_{\rm V}$, as in the full sample there is 21 per cent of reddened AGN versus 51 per cent in the complete sample. The same bias is observed when analysing the X-ray absorption, that in the full sample there is 21 per cent of absorbed AGN, while in the complete sample is 40 per cent. The fraction of discordant reddening and absorption in type-1 AGN for the complete sample of AGN is 32 per cent, that compared with a $10-23$ per cent of AGN optically classified as type-1 that show discordant optical and X-ray properties as found in the literature, we obtain a fraction $\sim$2 times higher. At $z > 0.2$, the type-1.8/9 objects, that normally present high optical extinction, would be classified as type-2 AGN, as the optical spectrum misses the H_α or H_β regions, observed at NIR frequencies. The fraction of optically obscured and X-ray absorbed type-1 sources is likely to increase at higher z with respect to the $10-23$ per cent obtained by previous studies.

Based on the $A_{\rm V}$ levels of subtypes of AGN, we can statistically distinguish between type-1.0 (almost not reddened), type-1.2/5 (with moderate extinction) and type-1.8/9 AGN (with high extinction, $A_{\rm V} \gtrsim 1.4$ mag). The gradual increase of $A_{\rm V}$ from type-1.0 to type-1.9 sources implies that the optical extinction is the main contribution to the subclassification of AGN. There are contributions that may affect the classification without invoking reddening of the nuclear emission (Trippe *et al.* 2010, Elitzur, Ho, and Trump 2014) but these should be much less important than the optical extinction. We found

that the X-ray absorption has as well a direct relation with the subtype of AGN. We can statistically distinguish between type-1.0/2/5 (generally with $\log(N_{\rm H}/{\rm cm}^{-2}) < 21.5 - 22$) and type-1.8/9 AGN (generally with $\log(N_{\rm H}/{\rm cm}^{-2}) > 21.5 - 22$).

Although the optical extinction and the X-ray absorption have a direct relation with the AGN classification, we cannot associate a certain level of $A_{\rm V}$ to a certain amount of $N_{\rm H}$ column density and vice versa. We obtained a wide scatter of $A_{\rm V}$-$N_{\rm H}$ around the Galactic relation, as obtained by similar studies in the literature. Contributions like variability, ionization of the obscuring material and different UV/optical AGN continuum slopes can contribute to this spread to a certain degree, but they can not explain completely the observed scatter.

Lastly, we analysed the dust-to-gas ratios of the type-1 AGN in BUXS. For half of the sample we can not compute properly the $A_{\rm V}/N_{\rm H}$ ratios. This is because, as this is a type-1 AGN sample, the sources are generally affected by low optical extinction and low X-ray absorption. This implies that systematic effects associated with the precision of the measurements can not be ignored as they affect the probability distributions. The $A_{\rm V}/N_{\rm H}$ estimations are then artificially skewed, hence preventing us from being able to draw conclusions from half of the sample. Even so, using a rigorous and conservative analysis using the individual $A_{\rm V}$ and $N_{\rm H}$ probability distributions, we are able to identify a lower limit of 47 per cent of objects with higher dust-to-gas ratios than the Galactic for the complete sample, a higher fraction than obtained by previous studies ($3 - 9$ per cent). If only type-1.0/2/5 AGN are considered, as other studies do, we obtain a minimum of 32 per cent of objects with higher dust-to-gas ratios than the Galactic.

6.2 Future work

In the previous sections we provided a series of conclusions on several issues that this Thesis has brought light into. Nevertheless, there are still various topics related to obscuration and the material that provokes it in the UV/optical and X-rays that still need better understanding. In this section we propose a series of topics that could extend and complete the results provided here based on the work conducted in this Thesis.

In the complete classification sample of $z < 0.2$ (see Chap. 5) we have noted that the contribution of the type-1.8/9 sources can be important in samples of AGN with broad line emission. The contribution of these objects drops in samples at higher z due to wavelength coverage, as the UV lines are suppressed even with only moderate amounts of optical extinction. For this kind of objects, only the most conspicuous lines, H_α and perhaps H_β, may be detectable. Extending the coverage of the available BUXS spectra of type-2 AGN to NIR wavelengths would allow to build a complete sample at higher z. The extension of the sample with complete classification at higher z would allow to study the dependence of our results with the intrinsic luminosity. In addition, by increasing the number of objects, will improve

the statistical significance of the results. At this time we have already started with this extension of the study with an observing campaign using the Especrografo Multiobjeto Infra-Rojo (EMIR), a NIR instrument located at GTC. We are currently reducing these spectra from EMIR.

Apart from identifying the misclassified type-1 AGN at $z > 0.2$ using NIR spectra, we can extend the study to identify those type-1 objects that are misclassified as type-2 due to host galaxy contrast, as seen in Chap. 4. This issue has no significant impact in the results of our study as in the complete sample there are only 3 unabsorbed type-2 AGN, less than 8 per cent of that sample. By extending the H_α spectral coverage at $z > 0.2$, and in order to assess the importance of this contribution, we could obtain narrow slit spectra for the type-2 objects for which we only have a fibre spectrum to reduce as much as possible the host stellar starlight. To give an idea of the extension of this exercise, using the $z = 0.05 - 1$ and $\log(L_{2-10\ \mathrm{keV}}/\mathrm{erg\ s^{-1}}) > 42$ cuts as in the total BUXS sample of 132 objects, there are 60 type-2 AGN, of which 12 are X-ray unabsorbed and hence possible misclassified sources.

We can extend the work from this Thesis studying the effects of the Eddington ratio on the classification by obtaining the SMBH masses and comparing them with the bolometric luminosities. Studying the accretion of the sources in this Thesis can clarify the dependence of the classification on the luminosity and the Eddington ratio, as hinted by Elitzur, Ho, and Trump (2014).

Appendix A

Results of the UV/optical and X-ray analysis

In this appendix we show the results of the optical and X-ray spectral fits. We summarize in Table A the $A_{\rm V}$ and the reddening corrected monochromatic flux at 5100 Å from the optical fits, and the $N_{\rm H}$ and the intrinsic luminosity in the 2-10 keV energy range from the X-ray fits. We list as well other important information to better understand the fits in both energy bands.

TABLE A.1: Results of the optical spectral fits of the BUXS type-1 sample.

Source	Class	Instrument	SNR	A_V mag	5100 Å Flux $\times 10^{17}$ erg s^{-1} cm^{-2} Å^{-1}	Model	$\log(N_{H,G}/\mathrm{cm}^{-2})$	$\log(N_H/\mathrm{cm}^{-2})$	$\log(L_{2-10\ \mathrm{keV}}/\mathrm{erg\ s}^{-1})$
2XMMiJ000441.2+000711	1.9	XSHOOTER	27.3	$2.04^{+0.3}_{-0.3}$	$0.9^{+0.09}_{-0.09}$	zwapecpo	20.49	<19.78	$42.76^{+0.02}_{-0.03}$
2XMMiJ002244.5+001825	1.0	SDSS	6.1	<0.58	$2.53^{+1.61}_{-0.71}$	zwapo	20.43	<20.07	$43.71^{+0.03}_{-0.03}$
2XMMJ003430.8-213351	1 (MgII)	FORS2	17.1	$1.98^{+0.36}_{-1.09}$	$8.76^{+12.63}_{-7.12}$	zwapo	20.18	<20.76	$44.25^{+0.04}_{-0.04}$
2XMMJ004003.8+005853	1.2	FORS2	28.6	$2.28^{+0.07}_{-0.27}$	$53.5^{+6.4}_{-22.0}$	zwapecpo	20.36	<20.94	$44.78^{+0.03}_{-0.03}$
2XMMJ004341.4+005610	1 (MgII)	SDSS	6.0	<0.24	$2.25^{+0.39}_{-0.27}$	zwapo	20.37	<20.3	$44.63^{+0.02}_{-0.02}$
2XMMJ004350.2+005750	1 (MgII)	DOLORES	6.5	$1.32^{+0.27}_{-0.29}$	$7.9^{+4.05}_{-2.57}$	zwapof	20.37	$21.41^{+0.07}_{-0.1}$	$44.81^{+0.02}_{-0.02}$
2XMMJ004404.6+010153	1.9	SDSS	15.8	$3.43^{+0.44}_{-0.31}$	$185.0^{+28.0}_{-35.0}$	zwapopo	20.37	$21.9^{+0.04}_{-0.05}$	$43.48^{+0.02}_{-0.02}$
2XMMiJ011829.6+004549	1.8	SDSS	4.3	$0.34^{+0.48}_{-0.27}$	$2.64^{+3.8}_{-1.45}$	zwapo	20.52	<19.98	$43.78^{+0.03}_{-0.03}$
2XMMJ012447.7+320727	1 (MgII)	DOLORES	49.8	<0.13	$15.5^{+0.4}_{-0.7}$	zwapecpo	20.75	<19.93	$45.08^{+0.01}_{-0.01}$
2XMMJ013943.0+061254	1.5	BOSS	9.0	$0.33^{+0.19}_{-0.18}$	$2.63^{+1.24}_{-1.24}$	zwapecpo	20.61	$21.05^{+0.08}_{-0.09}$	$44.44^{+0.01}_{-0.01}$
2XMMJ014804.3+055055	1.2	FORS2	62.7	<0.26	$3.49^{+0.13}_{-0.34}$	zwapecpo	20.64	$23.46^{+0.13}_{-0.33}$	$43.27^{+0.21}_{-0.19}$
2XMMJ020011.5-093125	1.0	BOSS	36.3	$0.16^{+0.09}_{-0.1}$	$45.0^{+2.5}_{-2.1}$	zwapecpo	20.31	$21.37^{+0.12}_{-2.36}$	$44.25^{+0.03}_{-0.03}$
2XMMJ023234.3-073102	1.2	SDSS	20.6	<0.21	$10.8^{+0.5}_{-0.5}$	zwapo	20.49	<20.36	$44.52^{+0.04}_{-0.04}$
2XMMJ024325.4-000412	1.2	BOSS	10.3	$1.11^{+0.05}_{-0.8}$	$9.94^{+2.15}_{-9.15}$	zwapo	20.56	$21.1^{+0.05}_{-0.06}$	$43.49^{+0.02}_{-0.02}$
2XMMJ030742.6-000121	1.2	DOLORES	20.4	$0.78^{+0.29}_{-0.31}$	$7.05^{+5.72}_{-3.42}$	zwapo	20.83	<20.86	$43.78^{+0.04}_{-0.05}$
2XMMJ033729.5+004227	1.5	FORS2	9.9	$0.78^{+0.39}_{-0.59}$	$0.95^{+1.81}_{-0.72}$	zwapecpo	20.92	<19.89	$43.72^{+0.02}_{-0.02}$
2XMMJ073534.9+435414	1.9	SDSS	11.4	$1.04^{+0.18}_{-0.88}$	$10.9^{+14.2}_{-9.1}$	zwapecpo	20.78	$22.04^{+0.1}_{-0.14}$	$43.05^{+0.04}_{-0.04}$
2XMMJ080608.0+244421	1.0	SDSS	15.3	<0.3	$9.08^{+1.61}_{-1.13}$	zwapo	20.59	<19.89	$43.92^{+0.02}_{-0.02}$
2XMMJ081014.5+280337	1.2	BOSS	36.8	<0.11	$14.3^{+0.1}_{-0.5}$	zwapecpo	20.57	<19.91	$44.89^{+0.02}_{-0.02}$
2XMMJ085835.2+275543	1.2	DOLORES	8.3	<0.76	$1.66^{+7.66}_{-0.52}$	zwapopo	20.49	$22.72^{+0.04}_{-0.05}$	$43.73^{+0.03}_{-0.03}$
2XMMiJ091557.3+292618	1.2	SDSS	13.6	$0.32^{+0.13}_{-0.13}$	$10.1^{+1.4}_{-1.1}$	zwapecpo	20.33	<19.72	$44.08^{+0.02}_{-0.02}$
2XMMJ091636.5+301749	1.9	SDSS	17.6	$2.2^{+0.73}_{-0.27}$	$63.6^{+25.6}_{-6.0}$	zwapo	20.32	<20.65	$42.88^{+0.04}_{-0.04}$
2XMMJ092129.2+370103	1.0	SDSS	9.1	<0.51	$3.76^{+1.34}_{-0.56}$	zwapecpo	20.18	<19.94	$43.31^{+0.03}_{-0.03}$
2XMMJ092313.0+511742	1.0	ACAM	9.5	$0.78^{+0.27}_{-0.34}$	$4.47^{+2.84}_{-2.35}$	zwapecpo	20.16	<19.81	$43.91^{+0.02}_{-0.02}$

Continued on next page

Table A.1 – *Continued from previous page*

Source	Class	Instrument	SNR	A_V mag	5100 Å Flux $\times 10^{17}$ erg s^{-1} cm^{-2} Å^{-1}	Model	$\log(N_{H,G}/\mathrm{cm}^{-2})$	$\log(N_H/\mathrm{cm}^{-2})$	$\log(L_{2-10\ \mathrm{keV}}/\mathrm{erg\ s}^{-1})$
2XMMiJ092619.6+362714	1 (MgII)	ACAM	36.8	<0.18	$5.1^{+0.27}_{-0.17}$	zwapo	20.15	<20.77	$44.46^{+0.02}_{-0.02}$
2XMMJ093347.9+551846	1 (MgII)	OSIRIS	23.1	$1.73^{+0.18}_{-0.52}$	$5.39^{+1.16}_{-2.7}$	zwapo	20.28	$21.51^{+0.06}_{-0.07}$	$44.79^{+0.01}_{-0.01}$
2XMMJ093458.2+611234	1.8	SDSS	11.9	$0.95^{+0.22}_{-0.74}$	$10.0^{+16.3}_{-8.8}$	zwapopo	20.42	$22.53^{+0.08}_{-0.11}$	$43.49^{+0.05}_{-0.06}$
2XMMJ094057.1+032401	1.5	SDSS	20.0	$0.77^{+0.21}_{-0.26}$	$42.1^{+17.0}_{-15.6}$	zwapecpo	20.58	<19.95	$42.56^{+0.02}_{-0.02}$
2XMMJ094350.2+035913	1.0	BOSS	15.0	$0.62^{+0.07}_{-0.1}$	$11.7^{+0.5}_{-0.7}$	zwapopo	20.58	$22.06^{+0.09}_{-0.16}$	$44.45^{+0.04}_{-0.04}$
2XMMJ094404.3+480647	1.0	BOSS	26.8	<0.19	$8.88^{+1.06}_{-0.39}$	zwapecpo	20.08	<20.35	$43.74^{+0.02}_{-0.02}$
2XMMJ094439.8+034940	1.0	SDSS	32.8	<0.15	$56.3^{+2.3}_{-0.8}$	zwapecpo	20.58	<20.49	$43.25^{+0.03}_{-0.03}$
2XMMJ094509.0+040817	1.9	SDSS	18.4	$4.01^{+0.23}_{-0.33}$	$180.0^{+20.0}_{-33.0}$	zwapo	20.56	$21.7^{+0.1}_{-0.16}$	$43.03^{+0.06}_{-0.06}$
2XMMiJ095630.7-003437	1.5	SDSS	5.0	$0.65^{+0.29}_{-0.18}$	$6.16^{+1.97}_{-1.13}$	zwapecpo	20.56	<19.93	$43.66^{+0.03}_{-0.03}$
2XMMJ095732.0+024302	1 (MgII)	EFOSC	16.2	$0.27^{+0.09}_{-0.2}$	$3.72^{+0.56}_{-1.59}$	zwapo	20.46	<20.8	$44.73^{+0.02}_{-0.02}$
2XMMJ100025.2+015852	1.2	SDSS	14.1	<0.17	$6.31^{+0.2}_{-0.13}$	zwapecpo	20.41	<19.66	$44.05^{+0.01}_{-0.01}$
2XMMJ100035.4+052428	1.5	SDSS	16.3	$0.31^{+0.15}_{-0.14}$	$26.8^{+5.4}_{-3.6}$	zwapecpo	20.42	<20.21	$42.66^{+0.03}_{-0.03}$
2XMMJ100057.4+684230	1.0	SDSS	13.2	<0.21	$5.32^{+0.69}_{-0.54}$	zwapecpo	20.6	<20.5	$44.05^{+0.02}_{-0.02}$
2XMMJ100205.0+023731	1.0	DOLORES	4.5	<1.82	$0.76^{+9.3}_{-0.49}$	zwapo	20.4	<20.03	$44.24^{+0.01}_{-0.01}$
2XMMJ100237.8+024701	1.8	BOSS	8.8	$2.37^{+1.5}_{-0.18}$	$25.0^{+8.6}_{-3.7}$	zwapopo	20.39	$22.79^{+0.09}_{-0.13}$	$43.0^{+0.07}_{-0.07}$
2XMMJ101616.7+391143	1.0	BOSS	23.1	<0.2	$14.1^{+0.5}_{-0.7}$	zwapecpo	20.14	<21.58	$43.89^{+0.05}_{-0.05}$
2XMMiJ101733.1-000144	1.5	SDSS	24.3	$3.18^{+1.32}_{-0.58}$	$106.0^{+41.0}_{-26.0}$	zwapo	20.61	$21.27^{+0.03}_{-0.03}$	$43.22^{+0.01}_{-0.01}$
2XMMJ101922.6+412050	1.0	SDSS	9.0	<0.58	$3.18^{+1.61}_{-0.6}$	zwapecpo	20.05	<19.72	$43.49^{+0.03}_{-0.02}$
2XMMJ102147.4+130850	1.0	SDSS	12.7	<0.15	$4.6^{+0.27}_{-0.24}$	zwapecpo	20.6	<20.07	$44.37^{+0.02}_{-0.02}$
2XMMJ102147.8+131227	1.2	SDSS	29.0	$2.69^{+0.23}_{-0.24}$	$209.0^{+17.0}_{-23.0}$	zwapo	20.6	$20.3^{+0.16}_{-0.27}$	$43.3^{+0.01}_{-0.01}$
2XMMJ102551.1+384008	1.5	ACAM	34.8	$0.83^{+0.35}_{-0.56}$	$9.15^{+15.03}_{-7.61}$	zwapof	20.14	<20.13	$42.79^{+0.03}_{-0.03}$
2XMMJ103739.4+414149	1 (MgII)	OSIRIS	36.4	$0.29^{+0.11}_{-0.13}$	$1.56^{+0.46}_{-0.03}$	zwapof	20.13	<21.02	$44.91^{+0.02}_{-0.02}$
2XMMJ104048.4+061819	1.2	BOSS	11.3	$1.54^{+0.24}_{-0.76}$	$16.6^{+8.0}_{-6.4}$	zwapo	20.45	<20.7	$42.88^{+0.03}_{-0.03}$
2XMMJ104522.0-012844	1.0	FORS2	79.6	<0.12	$2.69^{+0.01}_{-0.21}$	zwapecpo	20.62	<19.98	$44.77^{+0.02}_{-0.02}$
2XMMJ104522.1+212614	1 (MgII)	SDSS	19.6	<0.12	$9.07^{+0.06}_{-0.41}$	zwapecpo	20.33	<19.77	$44.6^{+0.01}_{-0.01}$

Continued on next page

Table A.1 – *Continued from previous page*

Source	Class	Instrument	SNR	A_V mag	5100 Å Flux $\times 10^{17}$ erg s^{-1} cm^{-2} Å^{-1}	Model	$\log(N_{H,G}/\mathrm{cm}^{-2})$	$\log(N_H/\mathrm{cm}^{-2})$	$\log(L_{2-10\ \mathrm{keV}}/\mathrm{erg\ s}^{-1})$
2XMMJ104912.6+330501	1.2	WFGS	15.8	<5.18	$8.74^{+8.79}_{-8.35}$	zwapo	20.29	<20.81	$43.44^{+0.04}_{-0.04}$
2XMMJ105932.0+242939	1 (MgII)	SDSS	20.7	<0.12	$7.46^{+0.24}_{-0.2}$	zwapecpo	20.19	<20.32	$44.75^{+0.02}_{-0.02}$
2XMMiJ111006.8+612522	1.0	SDSS	21.0	$0.37^{+0.1}_{-0.11}$	$23.2^{+1.5}_{-1.3}$	zwapecpo	19.82	<20.2	$43.58^{+0.03}_{-0.02}$
2XMMJ111121.6+482047	1.2	BOSS	17.1	$0.54^{+0.18}_{-0.25}$	$13.1^{+4.5}_{-5.1}$	zwapecpo	20.1	<19.99	$43.72^{+0.03}_{-0.03}$
2XMMJ111135.6+482945	1.2	SDSS	13.6	<0.15	$6.05^{+0.45}_{-0.45}$	zwapecpo	20.1	<20.06	$44.74^{+0.01}_{-0.01}$
2XMMJ111606.9+423645	1.0	SDSS	10.1	<0.23	$4.13^{+0.72}_{-0.42}$	zwapecpo	20.25	<20.17	$44.58^{+0.01}_{-0.02}$
2XMMJ111750.7+075710	1.5	FORS2	60.5	$0.79^{+0.07}_{-0.12}$	$7.58^{+0.07}_{-0.23}$	zwapo	20.53	$21.26^{+0.05}_{-0.05}$	$44.81^{+0.01}_{-0.01}$
2XMMJ111832.4+130732	1.0	BOSS	8.3	$0.22^{+0.08}_{-0.16}$	$1.95^{+0.37}_{-0.83}$	zwapecpo	20.3	<20.03	$44.42^{+0.02}_{-0.02}$
2XMMJ112328.0+052823	1.2	SDSS	17.4	<0.27	$18.6^{+1.5}_{-1.0}$	zwapecpo	20.64	<20.1	$42.75^{+0.02}_{-0.02}$
2XMMJ113121.7+310254	1.8	ALFOSC-FASU	9.6	<0.19	$2.545^{+0.001}_{-0.001}$	zwapopo	20.3	$21.66^{+0.05}_{-0.07}$	$43.52^{+0.02}_{-0.03}$
2XMMJ113129.2+310944	1.2	SDSS	10.0	$0.45^{+0.47}_{-0.43}$	$3.93^{+12.09}_{-2.46}$	zwapecpo	20.3	<19.79	$43.29^{+0.02}_{-0.02}$
2XMMJ120518.6+443926	1.8	OSIRIS	32.5	$1.52^{+0.55}_{-1.28}$	$1.88^{+0.4}_{-1.63}$	zwapo	20.12	<20.28	$43.59^{+0.03}_{-0.03}$
2XMMJ120529.5+442106	1.0	OSIRIS	78.5	$0.91^{+0.15}_{-0.09}$	$14.3^{+3.8}_{-1.6}$	zwapecpo	20.1	$22.25^{+0.06}_{-0.08}$	$43.7^{+0.04}_{-0.03}$
2XMMJ120952.6+393143	1.5	BOSS	9.7	$0.89^{+0.11}_{-0.14}$	$15.8^{+1.1}_{-2.4}$	zwapecpo	20.3	$21.92^{+0.08}_{-0.09}$	$43.12^{+0.02}_{-0.02}$
2XMMJ121118.8+503653	1.9	SDSS	16.7	$4.35^{+0.75}_{-2.18}$	$127.0^{+135.0}_{-68.0}$	zwapopo	20.28	$22.19^{+0.03}_{-0.04}$	$43.41^{+0.01}_{-0.01}$
2XMMJ121122.4+130936	1.2	SDSS	6.9	<1.1	$1.3^{+4.54}_{-0.59}$	zwapecpo	20.4	<19.9	$44.06^{+0.03}_{-0.03}$
2XMMJ121356.1+140431	1.0	SDSS	20.5	<0.41	$11.5^{+3.6}_{-0.8}$	zwapecpo	20.44	<19.92	$43.439^{+0.003}_{-0.003}$
2XMMJ121509.4+135450	1 (MgII)	SDSS	17.9	<0.13	$7.85^{+0.26}_{-0.36}$	zwapecpo	20.44	<19.8	$44.61^{+0.01}_{-0.01}$
2XMMJ121808.5+471613	1.0	SDSS	5.2	$0.14^{+0.42}_{-0.11}$	$2.71^{+2.21}_{-0.76}$	zwapecpo	20.07	<19.95	$43.83^{+0.01}_{-0.01}$
2XMMJ121839.4+470627	1.9	SDSS	16.8	$2.34^{+0.28}_{-0.34}$	$98.7^{+4.0}_{-15.4}$	zwapectorus	20.07	$23.98^{+0.08}_{-0.13}$	$43.38^{+0.05}_{-0.05}$
2XMMJ121930.9+064334	1.0	SDSS	37.9	<0.28	$62.7^{+1.2}_{-1.6}$	zwapo	20.19	<19.88	$42.93^{+0.02}_{-0.02}$
2XMMJ121952.2+472058	1.0	SDSS	10.2	<0.2	$4.08^{+0.41}_{-0.27}$	zwapecpo	20.06	<20.4	$44.4^{+0.01}_{-0.01}$
2XMMJ122137.8+043025	1.5	SDSS	22.9	$0.72^{+0.16}_{-0.36}$	$65.1^{+22.8}_{-22.4}$	zwapecpo	20.22	<20.26	$42.87^{+0.02}_{-0.02}$
2XMMJ122330.7+154507	1.2	SDSS	21.6	$1.27^{+0.52}_{-0.19}$	$47.1^{+16.3}_{-11.8}$	zwapecpo	20.38	<19.73	$42.75^{+0.02}_{-0.02}$
2XMMJ122649.5+311735	1.9	SDSS	20.4	$3.48^{+0.88}_{-0.98}$	$137.0^{+62.0}_{-40.0}$	zwapopo	20.15	$21.75^{+0.04}_{-0.04}$	$42.86^{+0.02}_{-0.02}$

Continued on next page

Table A.1 – *Continued from previous page*

Source	Class	Instrument	SNR	A_V mag	5100 Å Flux $\times 10^{17}$ erg s^{-1} cm^{-2} Å^{-1}	Model	$\log(N_{H,G}/\mathrm{cm}^{-2})$	$\log(N_H/\mathrm{cm}^{-2})$	$\log(L_{2-10\ \mathrm{keV}}/\mathrm{erg\ s}^{-1})$
2XMMJ122656.4+013124	1.5	FORS2	34.5	$1.49^{+0.12}_{-0.19}$	$13.4^{+1.4}_{-2.8}$	zwapo	20.26	$22.4^{+0.06}_{-0.08}$	$44.66^{+0.03}_{-0.04}$
2XMMJ123305.8+001438	1.2	EFOSC	14.5	<0.76	$1.6^{+0.99}_{-0.46}$	zwapecpo	20.27	<20.35	$43.46^{+0.02}_{-0.02}$
2XMMJ123356.1+074755	1.5	SDSS	13.3	$0.38^{+0.2}_{-0.21}$	$10.9^{+3.9}_{-2.9}$	zwapecpo	20.22	<19.95	$44.13^{+0.01}_{-0.01}$
2XMMJ123538.5+621643	1 (MgII)	DOLORES	8.2	$0.28^{+0.51}_{-0.01}$	$2.51^{+0.0}_{-0.32}$	zwapecpo	20.18	<19.81	$44.4^{+0.01}_{-0.01}$
2XMMiJ123604.0+264135	1.2	SDSS	24.4	<0.22	$25.2^{+3.2}_{-1.0}$	zwapecpo	20.12	<20.04	$43.66^{+0.01}_{-0.02}$
2XMMJ123725.2+114158	1.5	FORS2	14.3	<0.54	$0.2^{+0.11}_{-0.05}$	zwapo	20.39	<20.39	$44.18^{+0.03}_{-0.03}$
2XMMJ123759.5+621102	1 (MgII)	SDSS	7.1	$0.15^{+0.1}_{-0.14}$	$2.86^{+0.72}_{-1.16}$	zwapecpo	20.16	<19.59	$44.62^{+0.01}_{-0.01}$
2XMMJ124213.8-112510	1 (MgII)	DOLORES	13.2	$0.6^{+0.11}_{-0.09}$	$11.4^{+1.6}_{-1.1}$	zwapecpo	20.56	<20.15	$44.48^{+0.02}_{-0.02}$
2XMMJ124408.9+113334	1.5	SDSS	4.0	$0.12^{+0.59}_{-0.1}$	$1.98^{+3.0}_{-0.57}$	zwapecpo	20.35	<20.21	$43.75^{+0.02}_{-0.02}$
2XMMJ135628.7+052144	1.9	SDSS	4.6	$2.51^{+1.68}_{-0.45}$	$14.7^{+7.2}_{-4.1}$	zwapo	20.22	$21.56^{+0.07}_{-0.08}$	$42.83^{+0.04}_{-0.04}$
2XMMJ125453.1+272008	1.9	BOSS	8.5	$2.66^{+2.87}_{-0.23}$	$26.1^{+5.2}_{-6.5}$	zwapo	19.95	$22.0^{+0.09}_{-0.12}$	$43.4^{+0.05}_{-0.05}$
2XMMJ125553.0+272405	1.0	SDSS	24.1	<0.14	$12.2^{+0.9}_{-1.2}$	zwapecpo	19.96	<20.05	$44.12^{+0.01}_{-0.02}$
2XMMJ130936.2+082815	1.0	BOSS	8.5	<0.25	$1.76^{+0.58}_{-0.5}$	zwapecpo	20.32	$21.92^{+0.15}_{-0.18}$	$44.58^{+0.04}_{-0.04}$
2XMMJ131046.7+271645	1.2	SDSS	11.2	$0.28^{+0.14}_{-0.12}$	$10.9^{+1.3}_{-1.0}$	zwapecpo	19.99	<20.71	$44.22^{+0.01}_{-0.01}$
2XMMJ131246.8+275219	1 (MgII)	OSIRIS	36.9	$0.55^{+0.32}_{-0.25}$	$1.42^{+1.1}_{-0.68}$	zwapof	20.0	$23.25^{+0.15}_{-0.23}$	$44.52^{+0.15}_{-0.28}$
2XMMJ132037.8+341126	1.2	ALFOSC-FASU	6.5	$2.42^{+4.04}_{-0.51}$	$77.3^{+8564.4}_{-1637.6}$	zwapecpo	20.0	$21.17^{+0.05}_{-0.06}$	$42.36^{+0.02}_{-0.02}$
2XMMJ132101.4+340658	1.2	SDSS	25.5	$0.18^{+0.14}_{-0.14}$	$9.74^{+3.42}_{-1.92}$	zwapecpo	20.0	<19.78	$43.75^{+0.02}_{-0.02}$
2XMMJ132105.4+341500	1 (MgII)	ALFOSC-FASU	5.4	$3.43^{+3.99}_{-0.96}$	$138.0^{+530.0}_{-135.0}$	zwapo	20.0	$20.94^{+0.11}_{-0.16}$	$44.02^{+0.03}_{-0.03}$
2XMMJ132349.6+654148	1.0	OSIRIS	179.9	<0.12	$124.97^{+0.01}_{-1.26}$	zwapecpo	20.3	<19.59	$44.02^{+0.01}_{-0.01}$
2XMMJ132419.0+300042	1.5	BOSS	19.3	$1.81^{+0.25}_{-0.25}$	$12.7^{+4.6}_{-2.1}$	zwapecpo	20.06	$21.06^{+0.07}_{-0.09}$	$42.29^{+0.03}_{-0.03}$
2XMMJ132958.6+242435	1.8	ALFOSC-FASU	16.3	$0.31^{+0.07}_{-0.17}$	$1.65^{+0.12}_{-0.1}$	zwapo	20.06	<20.44	$44.5^{+0.03}_{-0.03}$
2XMMJ133904.2+281240	1.0	BOSS	6.1	$0.45^{+0.19}_{-0.21}$	$1.56^{+1.04}_{-0.87}$	zwapo	20.05	$21.51^{+0.08}_{-0.11}$	$44.76^{+0.02}_{-0.03}$
2XMMJ134044.5-004516	1.0	SDSS	43.1	<0.13	$34.6^{+0.4}_{-0.5}$	zwapecpo	20.32	<19.86	$43.9^{+0.03}_{-0.03}$
2XMMJ134113.9-005314	1.2	SDSS	27.7	$0.68^{+0.1}_{-0.09}$	$46.2^{+2.9}_{-1.7}$	zwapo	20.34	<19.81	$44.36^{+0.01}_{-0.01}$
2XMMJ134133.1+353252	1.2	SDSS	10.7	<0.23	$3.27^{+0.48}_{-0.8}$	zwapo	19.98	$20.48^{+0.13}_{-0.18}$	$44.85^{+0.01}_{-0.01}$

Continued on next page

Table A.1 – *Continued from previous page*

Source	Class	Instrument	SNR	A_V mag	5100 Å Flux $\times 10^{17}$ erg s^{-1} cm^{-2} Å^{-1}	Model	$\log(N_{H,G}/\mathrm{cm}^{-2})$	$\log(N_H/\mathrm{cm}^{-2})$	$\log(L_{2-10\ \mathrm{keV}}/\mathrm{erg\ s}^{-1})$
2XMMJ134252.9+403202	1 (MgII)	SDSS	4.9	$0.19^{+0.11}_{-0.17}$	$2.18^{+0.38}_{-1.29}$	zwapo	19.94	<20.41	$44.76^{+0.02}_{-0.02}$
2XMMJ134256.5+000057	1.0	SDSS	12.9	<0.13	$3.14^{+0.2}_{-0.21}$	zwapo	20.28	<20.37	$44.72^{+0.02}_{-0.02}$
2XMMJ134323.6+001223	1 (MgII)	SDSS	16.2	$0.21^{+0.08}_{-0.1}$	$8.95^{+0.7}_{-0.54}$	zwapecpo	20.28	<19.9	$44.68^{+0.02}_{-0.02}$
2XMMJ134749.8+582109	1.0	BOSS	38.3	<0.13	$29.8^{+1.3}_{-1.3}$	zwapecpo	20.11	<19.71	$45.05^{+0.01}_{-0.01}$
2XMMiJ135436.3+051524	1.9	SDSS	16.0	$2.11^{+1.82}_{-0.3}$	$46.9^{+8.8}_{-7.3}$	zwapecpo	20.32	$22.04^{+0.09}_{-0.13}$	$42.43^{+0.05}_{-0.05}$
2XMMJ125414.5+101605	1.9	BOSS	13.0	$2.15^{+0.29}_{-0.32}$	$18.4^{+6.0}_{-6.2}$	zwapecpo	20.32	$22.15^{+0.07}_{-0.1}$	$43.46^{+0.04}_{-0.04}$
2XMMJ140127.6+025606	1.2	SDSS	7.5	$0.17^{+0.63}_{-0.12}$	$2.84^{+0.62}_{-0.6}$	zwapopo	20.37	$21.68^{+0.03}_{-0.04}$	$43.84^{+0.01}_{-0.01}$
2XMMJ140353.8+540939	1.5	DOLORES	8.4	$1.1^{+0.16}_{-0.79}$	$4.81^{+2.0}_{-4.56}$	zwapo	20.06	<20.54	$43.54^{+0.03}_{-0.03}$
2XMMJ140515.4+542459	1.2	SDSS	20.0	$2.59^{+1.4}_{-0.42}$	$69.9^{+43.4}_{-12.0}$	zwapo	20.06	$22.33^{+0.22}_{-0.53}$	$42.44^{+0.18}_{-0.12}$
2XMMJ140745.3+283028	1.2	SDSS	13.4	<0.15	$6.14^{+0.17}_{-0.69}$	zwapo	20.15	<20.08	$44.73^{+0.02}_{-0.02}$
2XMMJ141449.5+361239	1.2	SDSS	9.6	$0.72^{+0.22}_{-0.58}$	$8.12^{+11.16}_{-6.29}$	zwapo	20.03	<20.04	$42.85^{+0.05}_{-0.04}$
2XMMJ141512.6+360813	1.2	BOSS	11.1	$1.34^{+0.21}_{-0.64}$	$7.58^{+4.36}_{-3.79}$	zwapo	20.04	<20.84	$43.16^{+0.04}_{-0.04}$
2XMMJ141531.4+113156	1.2	SDSS	12.5	<0.81	$3.66^{+7.12}_{-0.65}$	zwapo	20.26	<19.94	$43.62^{+0.01}_{-0.01}$
2XMMiJ142656.4+602903	1.0	SDSS	21.6	<0.13	$11.0^{+0.3}_{-0.3}$	zwapo	20.2	<20.45	$44.26^{+0.03}_{-0.03}$
2XMMJ142759.5+262150	1 (MgII)	SDSS	9.5	<0.14	$2.71^{+0.18}_{-0.36}$	zwapo	20.25	<20.2	$44.79^{+0.02}_{-0.02}$
2XMMJ143025.8+415957	1.2	SDSS	9.0	$0.63^{+0.14}_{-0.13}$	$17.8^{+2.1}_{-1.8}$	zwapo	20.15	<19.81	$43.77^{+0.02}_{-0.02}$
2XMMJ144404.5+291412	1.0	SDSS	28.3	<0.19	$16.1^{+0.8}_{-0.4}$	zwapecpo	20.19	<19.95	$44.46^{+0.02}_{-0.03}$
2XMMJ145426.6+182956	1.0	SDSS	23.6	$0.52^{+0.06}_{-0.12}$	$42.1^{+1.2}_{-1.8}$	zwapecpo	20.38	<20.05	$43.36^{+0.03}_{-0.03}$
2XMMJ145459.4+184452	1.0	BOSS	13.0	$0.99^{+0.05}_{-0.18}$	$20.5^{+1.3}_{-2.6}$	zwapo	20.39	$20.5^{+0.18}_{-0.3}$	$44.52^{+0.01}_{-0.01}$
2XMMJ145717.5+223332	1 (MgII)	OSIRIS	18.7	<0.23	$0.28^{+0.04}_{-0.05}$	zwapo	20.51	<21.03	$44.7^{+0.03}_{-0.03}$
2XMMJ150431.2+474151	1.0	SDSS	11.9	<0.15	$5.36^{+0.35}_{-0.39}$	zwapo	20.34	<20.76	$45.02^{+0.02}_{-0.02}$
2XMMJ151703.6+562338	1.5	OSIRIS	12.1	$0.17^{+0.65}_{-0.1}$	$0.89^{+0.14}_{-0.17}$	zwapo	20.16	$20.64^{+0.08}_{-0.12}$	$43.86^{+0.01}_{-0.01}$
2XMMJ153228.8+045358	1.5	SDSS	19.4	<0.18	$18.6^{+1.0}_{-0.6}$	zwapof	20.62	<19.67	$44.11^{+0.01}_{-0.01}$
2XMMJ153304.0+302508	1.5	SDSS	5.5	$0.42^{+0.41}_{-0.39}$	$4.44^{+11.65}_{-2.79}$	zwapo	20.34	<19.85	$42.93^{+0.03}_{-0.03}$
2XMMiJ155850.7+023539	1 (MgII)	DOLORES	6.4	<0.58	$0.87^{+1.07}_{-0.5}$	zwapof	20.78	<20.46	$44.8^{+0.03}_{-0.03}$

Continued on next page

Table A.1 – *Continued from previous page*

Source	Class	Instrument	SNR	A_V mag	5100 Å Flux $\times 10^{17}$ erg s^{-1} cm^{-2} Å^{-1}	Model	$\log(N_{H,G}/\mathrm{cm}^{-2})$	$\log(N_H/\mathrm{cm}^{-2})$	$\log(L_{2-10\ \mathrm{keV}}/\mathrm{erg\ s}^{-1})$
2XMMJ163331.8+570520	1.0	DOLORES	16.5	$0.29^{+0.36}_{-0.24}$	$2.94^{+3.85}_{-1.36}$	zwapo	20.27	<20.46	$43.63^{+0.02}_{-0.02}$
2XMMJ164119.4+385407	1.2	SDSS	6.2	<0.94	$1.64^{+2.67}_{-0.58}$	zwapo	20.06	<20.38	$43.41^{+0.04}_{-0.04}$
2XMMiJ164723.9+270547	1.9	BOSS	15.4	$0.86^{+0.45}_{-0.36}$	$1.4^{+1.28}_{-1.4}$	zwapof	20.65	$23.81^{+0.1}_{-0.15}$	$43.86^{+0.16}_{-0.16}$
2XMMiJ173104.7+365800	1.8	ISIS	6.1	$2.08^{+1.35}_{-2.0}$	$6.3^{+2.39}_{-4.78}$	zwapopo	20.52	$21.72^{+0.14}_{-0.16}$	$43.41^{+0.04}_{-0.04}$
2XMMJ173821.9+655056	1.2	OSIRIS	17.3	$0.48^{+0.2}_{-0.15}$	$0.76^{+0.17}_{-0.12}$	zwapecpo	20.57	<20.52	$43.98^{+0.07}_{-0.08}$
2XMMJ211516.5+060840	1.0	DOLORES	11.7	<0.29	$7.04^{+1.49}_{-0.65}$	zwapecpo	20.82	<20.66	$43.95^{+0.01}_{-0.01}$
2XMMJ212932.8+001044	1.5	ISIS	19.3	$2.54^{+0.16}_{-0.08}$	$52.8^{+6.2}_{-7.6}$	zwapecpo	20.63	$21.58^{+0.04}_{-0.05}$	$43.12^{+0.02}_{-0.02}$
2XMMiJ232807.6+144207	1.2	SDSS	14.6	<0.32	$6.37^{+1.09}_{-0.59}$	zwapecpo	20.62	<20.25	$43.48^{+0.05}_{-0.06}$

Notes: (1): X-ray source identifier as listed in the Second XMM-Newton Serendipitous Source Catalogue (2XMM-DR3; Watson *et al.* 2009); (2): classification of the source; (3): spectroscopic instrument that was used to obtain the optical spectrum (see Sec. 2.2.2); (4): median signal-to-noise ratio of the continuum windows used to fit the spectrum; (5): optical reddening A_V; (6): reddening corrected 5100 Å monochromatic flux; (7): best fit X-ray spectral model (see Sec. 3.2.2); (8): logarithm of the Galactic N_H column density from the Dickey & Lockman HI map (Dickey and Lockman 1990); (9); logarithm of the intrinsic N_H column density and the 1σ interval or the 1σ upper limit; (10): logarithm of the intrinsic luminosity in the rest-frame 2-10 keV energy range and the 1σ interval.

Appendix B

Fraction of obscured sources using conservative limits

We list in Table B.1 the fraction of optically reddened and the X-ray absorbed AGN for more conservative limits than used in Chap. 5: the $A_V = 2$ mag from Caccianiga *et al.* (2008) $\log(N_H/cm^{-2}) = 22$ (Ueda *et al.* 2003). The three numbers in brackets at the bottom of each cell stand for the number of sources with low optical extinction according to each threshold with more than 1σ confidence, the ones whose 1σ error includes that value, and the sources with high optical extinction, respectively.

In Table 5.7 we indicate, for the complete sample, the correlation between both quantities fraction of AGN that are reddened ($A_V > 2$ mag) and the one that are absorbed ($\log(N_H/cm^{-2}) > 22$). In total, 25^{+8}_{-7} per cent of objects show discordant optical and X-ray obscuration, where 3^{+4}_{-3} per cent are unreddened but absorbed sources, and 22 ± 7 per cent of them are unabsorbed but reddened objects. As mentioned in Sec. 1.4.3, $10-23$ per cent of AGN optically classified as type-1 present an X-ray absorbed spectrum while $3-17$ per cent of type-2 AGN are X-ray unabsorbed. With this thresholds, the discordant type-1 AGN fraction is only slightly higher than the fraction in the literature.

TABLE B.1: Type-1 AGN fraction with obscuration levels typical of type-2 AGN.

	A_V = 2 mag	$\log(N_H/cm^{-2})$ = 22
Full sample	0.1610 (108/11/13)	0.1114 (115/6/11)
z<0.2	0.4390 (17/6/9)	0.1664 (26/3/3)
Type-1 (MgII)	0.0605 (19/1/1)	0.0476 (20/0/1)
Type-1.0 (z<0.65)	0.0103 (23/0/0)	0.0442 (22/0/1)
Type-1.2 (z<0.65)	0.1156 (28/2/2)	0.0905 (29/1/2)
Type-1.5 (z<0.65)	0.1487 (14/1/2)	0.0074 (17/0/0)
Type-1.8 (z<0.65)	0.3562 (3/2/1)	0.3345 (4/0/2)
Type-1.9 (z<0.2)	0.8448 (1/4/5)	0.3228 (6/2/2)
Type-1.0/2/5 (z<0.65)	0.0900 (65/2/4)	0.0559 (68/1/3)
Type-1.8/9[(1)] (z<0.2)	0.7699 (2/4/5)	0.2971 (7/2/2)

Notes: The upper value in each cell represents the fraction of sources with extinction/absorption typical of type-2 AGN for the combined A_V or N_H probability distribution of each class or subsample (combination of all individual probability distributions of the objects in each sample), according to different thresholds reported in the literature.

TABLE B.2: Reddened and absorbed concordance for the complete sample.

Complete sample (32)	Unreddened	A_V = 2 mag within 1σ	Reddened
Unabsorbed	15 (47 %)	4 (13 %)	7 (22 %)
$\log(N_H/cm^{-2})$ = 22 within 1σ	1 (3 %)	1 (3 %)	1 (3 %)
Absorbed	1 (3 %)	1 (3 %)	1 (3 %)

Notes: Number and fraction of AGN that are unreddened or unabsorbed, those whose 1σ confidence interval includes A_V = 2 mag or $\log(N_H/cm^{-2})$ = 22, and those that are reddened or absorbed.

References

Abazajian, K.N., Adelman-McCarthy, J.K., Agüeros, M.A., Allam, S.S., Allende Prieto, C., An, D., Anderson, K.S.J., Anderson, et al.: 2009, *The Astrophysical Journal Supplement Series* **182**, 543-558.

Abolfathi, B., Aguado, D.S., Aguilar, G., Allende Prieto, C., Almeida, A., Tasnim Ananna, T., Anders, F., Anderson, S.F., et al.: 2018, *The Astrophysical Journal Supplement Series* **235**, 42.

Akylas, A. and Georgantopoulos, I.: 2009, *Astron. Astroph.* **500**, 999.

Akylas, A., Georgakakis, A., Georgantopoulos, I., Brightman, M., and Nandra, K.: 2012, *Astron. Astroph.* **546**, A98.

Allen, C.W.: 1973, *London: University of London, Athlone Press, —c1973, 3rd ed.*.

Alonso-Herrero, A., Quillen, A.C., Simpson, C., Efstathiou, A., and Ward, M.J.: 2001, *The Astronomical Journal* **121**, 1369.

Alonso-Herrero, A., Quillen, A.C., Rieke, G.H., Ivanov, V.D., and Efstathiou, A.: 2003, *The Astronomical Journal* **126**, 81.

Alonso-Herrero, A., Ramos Almeida, C., Mason, R., Asensio Ramos, A., Roche, P.F., Levenson, N.A., Elitzur, M., Packham, C., et al.: 2011, *Astrophys. J.* **736**, 82.

Anders, E. and Grevesse, N.: 1989, *Geochimica et Cosmochimica Acta* **53**, 197.

Antonucci, R.R.J. and Miller, J.S.: 1985, *Astrophys. J.* **297**, 621.

Antonucci, R.: 1993, *Annual Review of Astronomy and Astrophysics* **31**, 473.

Arnaud, K.A.: 1996, *Astronomical Data Analysis Software and Systems V* **101**, 17.

Bañados, E., Venemans, B.P., Mazzucchelli, C., Farina, E.P., Walter, F., Wang, F., Decarli, R., Stern, D., Fan, X., Davies, F.B., Hennawi, J.F., Simcoe, R.A., Turner, M.L., and, ...: 2018, *Nature* **553**, 473.

Barger, A.J., Cowie, L.L., Mushotzky, R.F., Yang, Y., Wang, W.-H., Steffen, A.T., and Capak, P.: 2005, *The Astronomical Journal* **129**, 578.

Baron, D., Stern, J., Poznanski, D., and Netzer, H.: 2016, *Astrophys. J.* **832**, 8.

Bassani, L., Dadina, M., Maiolino, R., Salvati, M., Risaliti, G., Della Ceca, R., Matt, G., and Zamorani, G.: 1999, *The Astrophysical Journal Supplement Series* **121**, 473.

Beckmann, V. and Shrader, C.R.: 2012, *Active Galactic Nuclei, ISBN-13: 978-3527410781. 350 pages. Wiley-VCH Verlag GmbH, 2012*.

Beckmann, V. and Shrader, C.: 2012, *Proceedings of "An INTEGRAL view of the high-energy sky (the first 10 years)" - 9th INTEGRAL Workshop and celebration of the 10th anniversary of the launch (INTEGRAL 2012). 15-19 October 2012. Bibliotheque Nationale de France, Paris, France. Published online at ¡A href="http://pos.sissa.it/cgi-bin/reader/conf.cgi?confid=176"¿http://pos.sissa.it/cgi-bin/reader/conf.cgi?confid=176¡/A¿, id.69*, 69.

Bell, E.F. and de Jong, R.S.: 2001, *Astrophys. J.* **550**, 212.

Bianchi, S., Corral, A., Panessa, F., Barcons, X., Matt, G., Bassani, L., Carrera, F.J., and Jiménez-Bailón, E.: 2008, *Monthly Notices of the Royal Astronomical Society* **385**, 195.

Bianchi, S., Panessa, F., Barcons, X., Carrera, F.J., La Franca, F., Matt, G., Onori, F., Wolter, A., Corral, A., Monaco, L., Ruiz, Á., and Brightman, M.: 2012, *Monthly Notices of the Royal Astronomical Society* **426**, 3225.

Binney, J. and Merrifield, M.: 1998, *Galactic astronomy. Princeton, NJ : Princeton University Press*.

Bohlin, R.C., Savage, B.D., and Drake, J.F.: 1978, *Astrophys. J.* **224**, 132.

Boissay, R., Ricci, C., and Paltani, S.: 2016, *Astron. Astroph.* **588**, A70.

Braito, V., Franceschini, A., Della Ceca, R., Severgnini, P., Bassani, L., Cappi, M., Malaguti, G., Palumbo, G.G.C., et al.: 2003, *Astron. Astroph.* **398**, 107.

Braito, V., Reeves, J.N., Sambruna, R.M., and Gofford, J.: 2011, *Monthly Notices of the Royal Astronomical Society* **414**, 2739.

Brightman, M. and Nandra, K.: 2011, *Monthly Notices of the Royal Astronomical Society* **413**, 1206.

Brightman, M., Nandra, K., Salvato, M., Hsu, L.-T., Aird, J., and Rangel, C.: 2014, *Monthly Notices of the Royal Astronomical Society* **443**, 1999.

Bruzual, G. and Charlot, S.: 2003, *Monthly Notices of the Royal Astronomical Society* **344**, 1000.

Burtscher, L., Davies, R.I., Graciá-Carpio, J., Koss, M.J., Lin, M.-Y., Lutz, D., Nandra, P., Netzer, H., et al.: 2016, *Astron. Astroph.* **586**, A28.

Caccianiga, A., Severgnini, P., Braito, V., Della Ceca, R., Maccacaro, T., Wolter, A., Barcons, X., Carrera, F.J., et al.: 2004, *Astron. Astroph.* **416**, 901.

Caccianiga, A., Severgnini, P., Della Ceca, R., Maccacaro, T., Carrera, F.J., and Page, M.J.: 2007, *Astron. Astroph.* **470**, 557.

Caccianiga, A., Severgnini, P., Della Ceca, R., Maccacaro, T., Cocchia, F., Barcons, X., Carrera, F.J., Matute, I., et al.: 2008, *Astron. Astroph.* **477**, 735.

Calzetti, D., Armus, L., Bohlin, R.C., Kinney, A.L., Koornneef, J., and Storchi-Bergmann, T.: 2000, *Astrophys. J.* **533**, 682.

Cappellari, M., Bacon, R., Bureau, M., Damen, M.C., Davies, R.L., de Zeeuw, P.T., Emsellem, E., Falcón-Barroso, J., et al.: 2006, *Monthly Notices of the Royal Astronomical Society* **366**, 1126.

Cardelli, J.A., Clayton, G.C., and Mathis, J.S.: 1989, *Astrophys. J.* **345**, 245.

Carrera, F.J., Page, M.J., and Mittaz, J.P.D.: 2004, *Astron. Astroph.* **420**, 163.

Cash, W.: 1979, *Astrophys. J.* **228**, 939.

Castelló-Mor, N., Carrera, F.J., Alonso-Herrero, A., Mateos, S., Barcons, X., Ranalli, P., Pérez-González, P.G., Comastri, A., et al.: 2013, *Astron. Astroph.* **556**, A114.

Castelló-Mor, N.,: 2014, *PhD thesis*, Univ. de Cantabria

Cid Fernandes, R., Mateus, A., Sodré, L., Stasińska, G., and Gomes, J.M.: 2005, *Monthly Notices of the Royal Astronomical Society* **358**, 363.

Comastri, A.: 2004, *Supermassive Black Holes in the Distant Universe* **308**, 245.

Corral, A., Barcons, X., Carrera, F.J., Ceballos, M.T., and Mateos, S.: 2005, *Astron. Astroph.* **431**, 97.

Corral, A., Page, M.J., Carrera, F.J., Barcons, X., Mateos, S., Ebrero, J., Krumpe, M., Schwope, A., et al.: 2008, *Astron. Astroph.* **492**, 71.

Corral, A., Della Ceca, R., Caccianiga, A., Severgnini, P., Brunner, H., Carrera, F.J., Page, M.J., and Schwope, A.D.: 2011, *Astron. Astroph.* **530**, A42.

Corral, A., Georgantopoulos, I., Watson, M.G., Rosen, S.R., Page, K.L., and Webb, N.A.: 2015, *Astron. Astroph.* **576**, A61.

Crenshaw, D.M.: 1986, *The Astrophysical Journal Supplement Series* **62**, 821.

Curran, S.J.: 2000, *Astronomy and Astrophysics Supplement Series* **144**, 271.

De Cicco, D., Paolillo, M., Covone, G., Falocco, S., Longo, G., Grado, A., Limatola, L., Botticella, M.T., et al.: 2015, *Astron. Astroph.* **574**, A112.

de Ruiter, H.R., Willis, A.G., and Arp, H.C.: 1977, *Astronomy and Astrophysics Supplement Series* **28**, 211.

de Vaucouleurs, G., de Vaucouleurs, A., Corwin, H.G., Jr., Buta, R.J., Paturel, G., and Fouqué, P.: 1991, *Third Reference Catalogue of Bright Galaxies. Volume I: Explanations and references. Volume II: Data for galaxies between 0^h and 12^h. Volume III: Data for galaxies between 12^h and 24^h, by de Vaucouleurs, G.; de Vaucouleurs, A.; Corwin, H. G., Jr.; Buta, R. J.; Paturel, G.; Fouqué, P.. Springer, New York, NY (USA), 1991, 2091 p., ISBN 0-387-97552-7, Price US 198.00. ISBN 3-540-97552-7, Price DM 448.00. ISBN 0-387-97549-7 (Vol. I), ISBN 0-387-97550-0 (Vol. II), ISBN 0-387-97551-9 (Vol. III).* **I**.

Del Moro, A., Alexander, D.M., Bauer, F.E., Daddi, E., Kocevski, D.D., McIntosh, D.H., Stanley, F., Brandt, W.N., et al.: 2016, *Monthly Notices of the Royal Astronomical Society* **456**, 2105.

Della Ceca, R., Pellegrini, S., Bassani, L., Beckmann, V., Cappi, M., Palumbo, G.G.C., Trinchieri, G., and Wolter, A.: 2001, *Astron. Astroph.* **375**, 781.

den Herder, J.W., Brinkman, A.C., Kahn, S.M., Branduardi-Raymont, G., Thomsen, K., Aarts, H., Audard, M., Bixler, J.V., et al.: 2001, *Astron. Astroph.* **365**, L7.

Deo, R.P., Crenshaw, D.M., Kraemer, S.B., Dietrich, M., Elitzur, M., Teplitz, H., and Turner, T.J.: 2007, *Astrophys. J.* **671**, 124.

Di Matteo, T., Blackman, E.G., and Fabian, A.C.: 1997, *Monthly Notices of the Royal Astronomical Society* **291**, L23.

Dickey, J.M. and Lockman, F.J.: 1990, *Annual Review of Astronomy and Astrophysics* **28**, 215.

Dong, X., Wang, T., Wang, J., Yuan, W., Zhou, H., Dai, H., and Zhang, K.: 2008, *Monthly Notices of the Royal Astronomical Society* **383**, 581.

Eckart, M.E., Stern, D., Helfand, D.J., Harrison, F.A., Mao, P.H., and Yost, S.A.: 2006, *The Astrophysical Journal Supplement Series* **165**, 19.

Elitzur, M.: 2012, *Astrophys. J.* **747**, L33.

Elitzur, M., Ho, L.C., and Trump, J.R.: 2014, *Monthly Notices of the Royal Astronomical Society* **438**, 3340.

Fabian, A.C.: 2012, *Annual Review of Astronomy and Astrophysics* **50**, 455.

Fanaroff, B.L. and Riley, J.M.: 1974, *Monthly Notices of the Royal Astronomical Society* **167**, 31P.

Ferguson, J.W., Korista, K.T., and Ferland, G.J.: 1997, *The Astrophysical Journal Supplement Series* **110**, 287.

Ferrarese, L. and Merritt, D.: 2000, *Astrophys. J.* **539**, L9.

Freeman, P., Doe, S., and Siemiginowska, A.: 2001, in J. L. Starck & F. D. Murtagh (ed.), *Society of Photo-Optical Instrumentation Engineers (SPIE) Conference Series*, Vol. 4477 of *Presented at the Society of Photo-Optical Instrumentation Engineers (SPIE) Conference*, pp 76–87

Galbiati, E., Caccianiga, A., Maccacaro, T., Braito, V., Della Ceca, R., Severgnini, P., Brunner, H., Lehmann, I., et al.: 2005, *Astron. Astroph.* **430**, 927.

Gandhi, P., Lansbury, G.B., Alexander, D.M., Stern, D., Arévalo, P., Ballantyne, D.R., Baloković, M., Bauer, F.E., et al.: 2014, *Astrophys. J.* **792**, 117.

Garcet, O., Gandhi, P., Gosset, E., Sprimont, P.G., Surdej, J., Borkowski, V., Tajer, M., Pacaud, F., et al.: 2007, *Astron. Astroph.* **474**, 473.

García-Bernete, I., Ramos Almeida, C., Alonso-Herrero, A., Ward, M.J., Acosta-Pulido, J.A., Pereira-Santaella, M., Hernán-Caballero, A., et al.: 2019, *Monthly Notices of the Royal Astronomical Society* **486**, 4917.

García-Burillo, S., Combes, F., Ramos Almeida, C., Usero, A., Krips, M., Alonso-Herrero, A., Aalto, S., Casasola, V., et al.: 2016, *Astrophys. J.* **823**, L12.

García-González, J., Alonso-Herrero, A., Pérez-González, P.G., Hernán-Caballero, A., Sarajedini, V.L., and Villar, V.: 2015, *Monthly Notices of the Royal Astronomical Society* **446**, 3199.

Gaskell, C.M. and Goosmann, R.W.: 2013, *Astrophys. J.* **769**, 30.

Gaskell, C.M.: 2017, *Monthly Notices of the Royal Astronomical Society* **467**, 226.

Gebhardt, K., Bender, R., Bower, G., Dressler, A., Faber, S.M., Filippenko, A.V., Green, R., Grillmair, C., et al.: 2000, *Astrophys. J.* **539**, L13.

Georgantopoulos, I., Rovilos, E., Akylas, A., Comastri, A., Ranalli, P., Vignali, C., Balestra, I., Gilli, R., et al.: 2011, *Astron. Astroph.* **534**, A23.

Georgantopoulos, I., Rovilos, E., Xilouris, E.M., Comastri, A., and Akylas, A.: 2011, *Astron. Astroph.* **526**, A86.

Georgantopoulos, I. and Georgakakis, A.: 2005, *Monthly Notices of the Royal Astronomical Society* **358**, 131.

Ghez, A.M., Salim, S., Weinberg, N.N., Lu, J.R., Do, T., Dunn, J.K., Matthews, K., Morris, M.R., et al.: 2008, *Astrophys. J.* **689**, 1044.

Gilli, R., Risaliti, G., Severgnini, P., Maiolino, R., Marconi, A., and Salvati, M.: 2001, *X-ray Astronomy 2000* **234**, 459.

Gilli, R., Salvati, M., and Hasinger, G.: 2001, *Astron. Astroph.* **366**, 407.

Gilli, R., Comastri, A., and Hasinger, G.: 2007, *Astron. Astroph.* **463**, 79.

Glikman, E., Helfand, D.J., White, R.L., Becker, R.H., Gregg, M.D., and Lacy, M.: 2007, *Astrophys. J.* **667**, 673.

Glikman, E., LaMassa, S., Piconcelli, E., Urry, M., and Lacy, M.: 2017, *Astrophys. J.* **847**, 116.

González-Martín, O.: 2018, *Astrophys. J.* **858**, 2.

Goodman, J. and Weare, J.: 2010, *Communications in Applied Mathematics and Computational Science, Vol. 5, No. 1, p. 65-80, 2010* **5**, 65.

Goodrich, R.W., Veilleux, S., and Hill, G.J.: 1994, *Astrophys. J.* **422**, 521.

Goodrich, R.W.: 1995, *Astrophys. J.* **440**, 141.

Gordon, K.D., Clayton, G.C., Misselt, K.A., Landolt, A.U., and Wolff, M.J.: 2003, *Astrophys. J.* **594**, 279.

Granato, G.L., Danese, L., and Franceschini, A.: 1997, *Astrophys. J.* **486**, 147.

Grandi, S.A.: 1982, *Astrophys. J.* **255**, 25.

Greene, J.E. and Ho, L.C.: 2005, *Astrophys. J.* **630**, 122.

Greene, J.E. and Ho, L.C.: 2006, *Astrophys. J.* **641**, 117.

Gunn, J.E., Siegmund, W.A., Mannery, E.J., Owen, R.E., Hull, C.L., Leger, R.F., Carey, L.N., Knapp, G.R., et al.: 2006, *The Astronomical Journal* **131**, 2332.

Hall, P.B., Gallagher, S.C., Richards, G.T., Alexander, D.M., Anderson, S.F., Bauer, F., Brandt, W.N., and Schneider, D.P.: 2006, *The Astronomical Journal* **132**, 1977.

Hao, H., Elvis, M., Bongiorno, A., Zamorani, G., Merloni, A., Kelly, B.C., Civano, F., Celotti, A., et al.: 2013, *Monthly Notices of the Royal Astronomical Society* **434**, 3104.

Hawkins, M.R.S.: 2007, *Astron. Astroph.* **462**, 581.

Heard, C.Z.P., and Gaskell, C.M.: 2016, *Monthly Notices of the Royal Astronomical Society* **461**, 4227.

Hernández-García, L., Masegosa, J., González-Martín, O., and Márquez, I.: 2015, *Astron. Astroph.* **579**, A90.

Hernández-García, L., Masegosa, J., González-Martín, O., Márquez, I., Guainazzi, M., and Panessa, F.: 2017, *Astron. Astroph.* **602**, A65.

Hickox, R.C., and Alexander, D.M.: 2018, *Annual Review of Astronomy and Astrophysics* **56**, 625.

Hirschmann, M., Khochfar, S., Burkert, A., Naab, T., Genel, S., and Somerville, R.S.: 2010, *Monthly Notices of the Royal Astronomical Society* **407**, 1016.

Hogg, D.W. and Foreman-Mackey, D.: 2018, *The Astrophysical Journal Supplement Series* **236**, 11.

Hopkins, P.F., Strauss, M.A., Hall, P.B., Richards, G.T., Cooper, A.S., Schneider, D.P., Vanden Berk, D.E., Jester, S., et al.: 2004, *The Astronomical Journal* **128**, 1112.

Hopkins, P.F., Hernquist, L., Cox, T.J., and Kereš, D.: 2008, *The Astrophysical Journal Supplement Series* **175**, 356.

Huang, X.-X., Wang, J.-X., Tan, Y., Yang, H., and Huang, Y.-F.: 2011, *Astrophys. J.* **734**, L16.

Hubble, E.P.: 1929, *Astrophys. J.* **69**.

Hönig, S.F., Watson, D., Kishimoto, M., Gandhi, P., Goad, M., Horne, K., Shankar, F., Banerji, M., et al.: 2017, *Monthly Notices of the Royal Astronomical Society* **464**, 1693.

Jansen, F., Lumb, D., Altieri, B., Clavel, J., Ehle, M., Erd, C., Gabriel, C., Guainazzi, M., et al.: 2001, *Astron. Astroph.* **365**, L1.

Jeffreys, H.: 1946, *Proceedings of the Royal Society of London Series A* **186**, 453.

Jin, C., Ward, M., Done, C., and Gelbord, J.: 2012a, *Monthly Notices of the Royal Astronomical Society* **420**, 1825.

Jin, C., Ward, M., and Done, C.: 2012b, *Monthly Notices of the Royal Astronomical Society* **422**, 3268.

Jones, D.H., Read, M.A., Saunders, W., Colless, M., Jarrett, T., Parker, Q.A., Fairall, A.P., Mauch, T., et al.: 2009, *Monthly Notices of the Royal Astronomical Society* **399**, 683.

Kaastra, J.S.: 1992, *An X-Ray Spectral Code for Optically Thin Plasmas*, **SRON-Leiden** (Internal Report, updated version 2.0)

Kaastra, J.S., Mewe, R., Liedahl, D.A., Komossa, S., and Brinkman, A.C.: 2000, *Astron. Astroph.* **354**, L83.

Kant, I.: 1755. *Allgemeine Naturgeschichte und Theorie des Himmels* , Part I, J.F. Peterson, Königsberg and Leipzig.

Kaspi, S., Brandt, W.N., Netzer, H., Sambruna, R., Chartas, G., Garmire, G.P., and Nousek, J.A.: 2000, *Astrophys. J.* **535**, L17.

Kaspi, S., Smith, P.S., Netzer, H., Maoz, D., Jannuzi, B.T., and Giveon, U.: 2000, *Astrophys. J.* **533**, 631.

Kishimoto, M., Hönig, S.F., Antonucci, R., Barvainis, R., Kotani, T., Tristram, K.R.W., Weigelt, G., and Levin, K.: 2011, *Astron. Astroph.* **527**, A121.

Komossa, S., and Fink, H.: 1997, *Astron. Astroph.* **327**, 555.

Komossa, S., and Hasinger, G.: 2003, *XEUS - Studying the Evolution of the Hot Universe*, 285.

Koratkar, A. and Blaes, O.: 1999, *Publications of the Astronomical Society of the Pacific* **111**, 1.

Kormendy, J. and Ho, L.C.: 2013, *Annual Review of Astronomy and Astrophysics* **51**, 511.

Koss, M., Mushotzky, R., Veilleux, S., Winter, L.M., Baumgartner, W., Tueller, J., Gehrels, N., and Valencic, L.: 2011, *Astrophys. J.* **739**, 57.

Koulouridis, E., Georgantopoulos, I., Loukaidou, G., Corral, A., Akylas, A., Koutoulidis, L., Jiménez-Andrade, E.F., León-Tavares, J., et al.: 2016, *Astron. Astroph.* **586**, A3.

Kovačević, J., Popović, L.Č., and Kollatschny, W.: 2014, *Advances in Space Research* **54**, 1347.

Krolik, J.H. and Begelman, M.C.: 1988, *Astrophys. J.* **329**, 702.

Krumpe, M., Lamer, G., Markowitz, A., and Corral, A.: 2010, *Astrophys. J.* **725**, 2444.

LaMassa, S.M., Cales, S., Moran, E.C., Myers, A.D., Richards, G.T., Eracleous, M., Heckman, T.M., Gallo, L., et al.: 2015, *Astrophys. J.* **800**, 144.

Lanzuisi, G., Civano, F., Elvis, M., Salvato, M., Hasinger, G., Vignali, C., Zamorani, G., Aldcroft, T., et al.: 2013, *Monthly Notices of the Royal Astronomical Society* **431**, 978.

Lawrence, A., and Elvis, M.: 2010, *Astrophys. J.* **714**, 561.

Liedahl, D.A., Osterheld, A.L., and Goldstein, W.H.: 1995, *Astrophys. J.* **438**, L115.

Lintott, C., Schawinski, K., Bamford, S., Slosar, A., Land, K., Thomas, D., Edmondson, E., Masters, K., et al.: 2011, *Monthly Notices of the Royal Astronomical Society* **410**, 166.

Liu, Z., Yuan, W., Lu, Y., Carrera, F.J., Falocco, S., and Dong, X.-B.: 2016, *Monthly Notices of the Royal Astronomical Society* **463**, 684.

Liu, T., Merloni, A., Wang, J.-X., Tozzi, P., Shen, Y., Brusa, M., Salvato, M., Nandra, K., et al.: 2018, *Monthly Notices of the Royal Astronomical Society* **479**, 5022.

Lusso, E., Comastri, A., Vignali, C., Zamorani, G., Brusa, M., Gilli, R., Iwasawa, K., Salvato, M., et al.: 2010, *Astron. Astroph.* **512**, A34.

Lusso, E., Hennawi, J.F., Comastri, A., Zamorani, G., Richards, G.T., Vignali, C., Treister, E., Schawinski, K., et al.: 2013, *Astrophys. J.* **777**, 86.

Lusso, E., Decarli, R., Dotti, M., Montuori, C., Hogg, D.W., Tsalmantza, P., Fumagalli, M., and Prochaska, J.X.: 2014, *Monthly Notices of the Royal Astronomical Society* **441**, 316.

Lyu, J., Hao, L., and Li, A.: 2014, *Astrophys. J.* **792**, L9.

López, S., D'Odorico, V., Ellison, S.L., Becker, G.D., Christensen, L., Cupani, G., Denney, K.D., Pâris, I., et al.: 2016, *Astron. Astroph.* **594**, A91.

Lopez-Rodriguez, E., Packham, C., Roche, P.F., Alonso-Herrero, A., Díaz-Santos, T., Nikutta, R., González-Martín, O., Álvarez, C.A., et al.: 2016, *Monthly Notices of the Royal Astronomical Society* **458**, 3851.

Magorrian, J., Tremaine, S., Richstone, D., Bender, R., Bower, G., Dressler, A., Faber, S.M., Gebhardt, K., et al.: 1998, *The Astronomical Journal* **115**, 2285.

Mainieri, V., Rosati, P., Tozzi, P., Bergeron, J., Gilli, R., Hasinger, G., Nonino, M., Lehmann, I., et al.: 2005, *Astron. Astroph.* **437**, 805.

Maiolino, R. and Rieke, G.H.: 1995, *Astrophys. J.* **454**, 95.

Maiolino, R., Marconi, A., Salvati, M., Risaliti, G., Severgnini, P., Oliva, E., La Franca, F., and Vanzi, L.: 2001, *Astron. Astroph.* **365**, 28.

Malizia, A., Bassani, L., Bazzano, A., Bird, A.J., Masetti, N., Panessa, F., Stephen, J.B., and Ubertini, P.: 2012, *Monthly Notices of the Royal Astronomical Society* **426**, 1750.

Malizia, A., Molina, M., Bassani, L., Stephen, J.B., Bazzano, A., Ubertini, P., and Bird, A.J.: 2014, *Astrophys. J.* **782**, L25.

Marchese, E., Della Ceca, R., Caccianiga, A., Severgnini, P., Corral, A., and Fanali, R.: 2012, *Astron. Astroph.* **539**, A48.

Marconi, A., Risaliti, G., Gilli, R., Hunt, L.K., Maiolino, R., and Salvati, M.: 2004, *Monthly Notices of the Royal Astronomical Society* **351**, 169.

Markowitz, A.G., Krumpe, M., and Nikutta, R.: 2014, *Monthly Notices of the Royal Astronomical Society* **439**, 1403.

Masetti, N., Parisi, P., Jiménez-Bailón, E., Palazzi, E., Chavushyan, V., Bassani, L., Bazzano, A., Bird, A.J., et al.: 2012, *Astron. Astroph.* **538**, A123.

Mason, K.O., Breeveld, A., Much, R., Carter, M., Cordova, F.A., Cropper, M.S., Fordham, J., Huckle, H., et al.: 2001, *Astron. Astroph.* **365**, L36.

Mateos, S., Barcons, X., Carrera, F.J., Ceballos, M.T., Caccianiga, A., Lamer, G., Maccacaro, T., Page, M.J., et al.: 2005, *Astron. Astroph.* **433**, 855.

Mateos, S., Barcons, X., Carrera, F.J., Ceballos, M.T., Hasinger, G., Lehmann, I., Fabian, A.C., and Streblyanska, A.: 2005, *Astron. Astroph.* **444**, 79.

Mateos, S., Barcons, X., Carrera, F.J., Page, M.J., Ceballos, M.T., Hasinger, G., and Fabian, A.C.: 2007, *Astron. Astroph.* **473**, 105.

Mateos, S., Saxton, R.D., Read, A.M., and Sembay, S.: 2009, *Astron. Astroph.* **496**, 879.

Mateos, S., Carrera, F.J., Page, M.J., Watson, M.G., Corral, A., Tedds, J.A., Ebrero, J., Krumpe, M., et al.: 2010, *Astron. Astroph.* **510**, A35.

Mateos, S., Alonso-Herrero, A., Carrera, F.J., Blain, A., Watson, M.G., Barcons, X., Braito, V., Severgnini, P., et al.: 2012, *Monthly Notices of the Royal Astronomical Society* **426**, 3271.

Mateos, S., Carrera, F.J., Alonso-Herrero, A., Rovilos, E., Hernán-Caballero, A., Barcons, X., Blain, A., Caccianiga, A., et al.: 2015, *Monthly Notices of the Royal Astronomical Society* **449**, 1422.

Mateos, S., Carrera, F.J., Barcons, X., Alonso-Herrero, A., Hernán-Caballero, A., Page, M., Ramos Almeida, C., Caccianiga, A., et al.: 2017, *Astrophys. J.* **841**, L18.

Mateus, A., Sodré, L., Cid Fernandes, R., Stasińska, G., Schoenell, W., and Gomes, J.M.: 2006, *Monthly Notices of the Royal Astronomical Society* **370**, 721.

Mehdipour, M., Kaastra, J.S., Kriss, G.A., Arav, N., Behar, E., Bianchi, S., Branduardi-Raymont, G., Cappi, M. et al. 2017, *Astron. Astroph.* **607**, A28.

Mehdipour, M., Branduardi-Raymont, G., and Page, M.J.: 2012, *Astron. Astroph.* **542**, A30.

Memola, E., Caccianiga, A., Cocchia, F., Della Ceca, R., Maccacaro, T., Severgnini, P., Fyfe, D.J., Mateos, S., et al.: 2007, *Astron. Astroph.* **465**, 759.

Merloni, A., Bongiorno, A., Brusa, M., Iwasawa, K., Mainieri, V., Magnelli, B., Salvato, M., Berta, S., et al.: 2014, *Monthly Notices of the Royal Astronomical Society* **437**, 3550.

Merritt, D. and Ferrarese, L.: 2001, *Monthly Notices of the Royal Astronomical Society* **320**, L30.

Meusinger, H., and Brunzendorf, J.: 2002, *Astron. Astroph.* **390**, 439.

Mewe, R., Gronenschild, E.H.B.M., and van den Oord, G.H.J.: 1985, *Astronomy and Astrophysics Supplement Series* **62**, 197.

Mewe, R., Lemen, J.R., and van den Oord, G.H.J.: 1986, *Astronomy and Astrophysics Supplement Series* **65**, 511.

Miller, J.S. and Goodrich, R.W.: 1990, *Astrophys. J.* **355**, 456.

Miniutti, G., Sanfrutos, M., Beuchert, T., Agís-González, B., Longinotti, A.L., Piconcelli, E., Krongold, Y., Guainazzi, M., et al.: 2014, *Monthly Notices of the Royal Astronomical Society* **437**, 1776.

Mushotzky, R.: 2004, *Supermassive Black Holes in the Distant Universe*, 53.

Nenkova, M., Ivezić, Ž., and Elitzur, M.: 2002, *Astrophys. J.* **570**, L9.

Nenkova, M., Sirocky, M.M., Ivezić, Ž., and Elitzur, M.: 2008, *Astrophys. J.* **685**, 147.

Netzer, H.: 1990 *Active Galactic Nuclei*, AGN Emission Lines, eds. R.D. Blandford, H. Netzer and L. Woltjer.

Netzer, H.: 2013, *The Physics and Evolution of Active Galactic Nuclei, by Hagai Netzer, Cambridge, UK: Cambridge University Press, 2013*.

Netzer, H.: 2015, *Annual Review of Astronomy and Astrophysics* **53**, 365.

Nisini, B., Giannini, T., Antoniucci, S., Alcalá, J.M., Bacciotti, F., and Podio, L.: 2016, *Astron. Astroph.* **595**, A76.

Noll, S. and Pierini, D.: 2005, *Astron. Astroph.* **444**, 137.

Ordovás-Pascual, I., Mateos, S., Carrera, F.J., Wiersema, K., Barcons, X., Braito, V., Caccianiga, A., Del Moro, A., et al.: 2017, *Monthly Notices of the Royal Astronomical Society* **469**, 693.

Osterbrock, D.E.: 1977, *Astrophys. J.* **215**, 733.

Osterbrock, D.E.: 1981, *Astrophys. J.* **249**, 462.

Osterbrock, D.E. and Pogge, R.W.: 1985, *Astrophys. J.* **297**, 166.

Osterbrock, D.E.: 1989, *Research supported by the University of California, John Simon Guggenheim Memorial Foundation, University of Minnesota, et al. Mill Valley, CA, University Science Books, 1989, 422 p.*.

Osterbrock, D.E.: 1991, *Reports on Progress in Physics* **54**, 579.

Padovani, P.: 2016, *Astronomy and Astrophysics Review* **24**, 13.

Padovani, P., Alexander, D.M., Assef, R.J., De Marco, B., Giommi, P., Hickox, R.C., Richards, G.T., Smolčić, V., et al.: 2017, *Astronomy and Astrophysics Review* **25**, 2.

Page, M.J., Carrera, F.J., Stevens, J.A., Ebrero, J., and Blustin, A.J.: 2011, *Monthly Notices of the Royal Astronomical Society* **416**, 2792.

Page, M.J., Carrera, F.J., Ceballos, M., Corral, A., Ebrero, J., Esquej, P., Krumpe, M., Mateos, S., et al.: 2017, *Monthly Notices of the Royal Astronomical Society* **464**, 4586.

Panessa, F. and Bassani, L.: 2002, *Astron. Astroph.* **394**, 435.

Panessa, F., Bassani, L., Cappi, M., Dadina, M., Barcons, X., Carrera, F.J., Ho, L.C., and Iwasawa, K.: 2006, *Astron. Astroph.* **455**, 173.

Panessa, F., Baldi, R.D., Laor, A., Padovani, P., Behar, E., and McHardy, I.: 2019, *arXiv e-prints* , arXiv:1902.05917.

Pappa, A., Georgantopoulos, I., Stewart, G.C., and Zezas, A.L.: 2001, *Monthly Notices of the Royal Astronomical Society* **326**, 995.

Parisi, P.: 2011, *PhD thesis*, Univ. di Bologna

Parisi, P., Masetti, N., Jiménez-Bailón, E., Chavushyan, V., Palazzi, E., Landi, R., Malizia, A., Bassani, L., et al.: 2012, *Astron. Astroph.* **545**, A101.

Park, D., Kelly, B.C., Woo, J.-H., and Treu, T.: 2012, *The Astrophysical Journal Supplement Series* **203**, 6.

Perola, G.C., Puccetti, S., Fiore, F., Sacchi, N., Brusa, M., Cocchia, F., Baldi, A., Carangelo, N., et al.: 2004, *Astron. Astroph.* **421**, 491.

Pineau, F.-X., Motch, C., Carrera, F., Della Ceca, R., Derrière, S., Michel, L., Schwope, A., and Watson, M.G.: 2011, *Astron. Astroph.* **527**, A126.

Polletta, M., Tajer, M., Maraschi, L., Trinchieri, G., Lonsdale, C.J., Chiappetti, L., Andreon, S., Pierre, M., et al.: 2007, *Astrophys. J.* **663**, 81.

Popović, L.Č.: 2003, *Astrophys. J.* **599**, 140.

Press, W.H., Teukolsky, S.A., Vetterling, W.T., and Flannery, B.P.: 1992, *Cambridge: University Press*.

Prieto, M.A., Mezcua, M., Fernández-Ontiveros, J.A., and Schartmann, M.: 2014, *Monthly Notices of the Royal Astronomical Society* **442**, 2145.

Raimundo, S.I. and Fabian, A.C.: 2009, *Monthly Notices of the Royal Astronomical Society* **396**, 1217.

Ramos Almeida, C., Martínez González, M.J., Asensio Ramos, A., Acosta-Pulido, J.A., Hönig, S.F., Alonso-Herrero, A., Tadhunter, C.N., and González-Martín, O.: 2016, *Monthly Notices of the Royal Astronomical Society* **461**, 1387.

Ramos Almeida, C., and Ricci, C.: 2017, *Nature Astronomy* **1**, 679.

Reynolds, C.S., and Fabian, A.C.: 1995, *Monthly Notices of the Royal Astronomical Society* **273**, 1167.

Ricci, C., Ueda, Y., Paltani, S., Ichikawa, K., Gandhi, P., and Awaki, H.: 2014, *Monthly Notices of the Royal Astronomical Society* **441**, 3622.

Ricci, C., Trakhtenbrot, B., Koss, M.J., Ueda, Y., Del Vecchio, I., Treister, E., Schawinski, K., Paltani, S., et al: 2017, *The Astrophysical Journal Supplement Series* **233**, 17.

Ricci, C., Trakhtenbrot, B., Koss, M.J., Ueda, Y., Schawinski, K., Oh, K., Lamperti, I., Mushotzky, R., et al.: 2017, *Nature* **549**, 488.

Richards, G.T., Hall, P.B., Vanden Berk, D.E., Strauss, M.A., Schneider, D.P., Weinstein, M.A., Reichard, T.A., York, D.G., et al.: 2003, *The Astronomical Journal* **126**, 1131.

Richards, G.T., Strauss, M.A., Fan, X., Hall, P.B., Jester, S., Schneider, D.P., Vanden Berk, D.E., Stoughton, C., et al.: 2006, *The Astronomical Journal* **131**, 2766.

Risaliti, G., Elvis, M., and Nicastro, F.: 2002, *Astrophys. J.* **571**, 234.

Risaliti, G. and Elvis, M.: 2004, *Supermassive Black Holes in the Distant Universe* **308**, 187.

Risaliti, G., Elvis, M., Fabbiano, G., Baldi, A., and Zezas, A.: 2005, *Astrophys. J.* **623**, L93.

Risaliti, G., Nardini, E., Salvati, M., Elvis, M., Fabbiano, G., Maiolino, R., Pietrini, P., and Torricelli-Ciamponi, G.: 2011, *Monthly Notices of the Royal Astronomical Society* **410**, 1027.

Schmidt, K.B., Rix, H.-W., Shields, J.C., Knecht, M., Hogg, D.W., Maoz, D., and Bovy, J.: 2012, *Astrophys. J.* **744**, 147.

Schnorr-Müller, A., Davies, R.I., Korista, K.T., Burtscher, L., Rosario, D., Storchi-Bergmann, T., Contursi, A., Genzel, R., et al.: 2016, *Monthly Notices of the Royal Astronomical Society* **462**, 3570.

Schutte, Z., Reines, A., and Greene, J.: 2019, *arXiv e-prints* , arXiv:1908.00020.

Schwartz, D.A., Marshall, H.L., Miller, B.P., Worrall, D.M., Birkinshaw, M., Lovell, J.E.J., Jauncey, D.L., Perlman, E.S., et al.: 2003, *New Astronomy Reviews* **47**, 461.

Scott, A.E., Stewart, G.C., and Mateos, S.: 2012, *Monthly Notices of the Royal Astronomical Society* **423**, 2633.

Selsing, J., Fynbo, J.P.U., Christensen, L., and Krogager, J.-K.: 2016, *Astron. Astroph.* **585**, A87.

Severgnini, P., Caccianiga, A., Braito, V., Della Ceca, R., Maccacaro, T., Wolter, A., Sekiguchi, K., Sasaki, T., et al.: 2003, *Astron. Astroph.* **406**, 483.

Seward, F.D. and Charles, P.A.: 1995, *Exploring the X-Ray Universe, pp. 414. ISBN 0521437121. Cambridge, UK: Cambridge University Press, November 1995.*, 414.

Seyfert, C.K.: 1943, *Astrophys. J.* **97**, 28.

Shen, Y., Richards, G.T., Strauss, M.A., Hall, P.B., Schneider, D.P., Snedden, S., Bizyaev, D., Brewington, H., et al.: 2011, *The Astrophysical Journal Supplement Series* **194**, 45.

Shields, G.A., Ludwig, R.R., and Salviander, S.: 2010, *Astrophys. J.* **721**, 1835.

Shimizu, T.T., Davies, R.I., Koss, M., Ricci, C., Lamperti, I., Oh, K., Schawinski, K., Trakhtenbrot, B., et al.: 2018, *Astrophys. J.* **856**, 154.

Silk, J., Di Cintio, A., and Dvorkin, I.: 2014, *Proceedings of the International School of Physics 'enrico Fermi' Course 186 'new Horizons for Observational Cosmology' Vol. 186*, 137.

Simmons, B.D., Van Duyne, J., Urry, C.M., Treister, E., Koekemoer, A.M., Grogin, N.A., and GOODS Team: 2011, *Astrophys. J.* **734**, 121.

Singh, K.P.: 2013, *Bulletin of the Astronomical Society of India* **41**, 137.

Smee, S.A., Gunn, J.E., Uomoto, A., Roe, N., Schlegel, D., Rockosi, C.M., Carr, M.A., Leger, F., et al.: 2013, *The Astronomical Journal* **146**, 32.

Smith, K.L., Koss, M., and Mushotzky, R.F.: 2014, *Astrophys. J.* **794**, 112.

Singh, V., Shastri, P., and Risaliti, G.: 2011, *Astron. Astroph.* **532**, A84.

Sparke, L.S. and Gallagher, J.S., III: 2007, *Galaxies in the Universe: An Introduction. Second Edition. ISBN-13 978-0-521-85593-8 (HB); ISBN-13 978-0-521-67186-6 (PB). Published by Cambridge University Press, Cambridge, UK, 2007.*.

Spiegelhalter D. J., Best N. G., Carlin B. P., van der Linde A.: 2002, *Journal of the Royal Statistical Society, Series B.* **64** (4), 583

Spiniello, C., Trager, S.C., Koopmans, L.V.E., and Chen, Y.P.: 2012, *Astrophys. J.* **753**, L32.

Steidel, C.C., Dickinson, M., Meyer, D.M., Adelberger, K.L., and Sembach, K.R.: 1997, *Astrophys. J.* **480**, 568.

Steinhardt, C.L., Schramm, M., Silverman, J.D., Alexandroff, R., Capak, P., Civano, F., Elvis, M., Masters, D., et al.: 2012, *Astrophys. J.* **759**, 24.

Stern, J. and Laor, A.: 2012, *Monthly Notices of the Royal Astronomical Society* **426**, 2703.

Stoehr, F., White, R., Smith, M., Kamp, I., Thompson, R., Durand, D., Freudling, W., Fraquelli, D., et al.: 2008, *Astronomical Data Analysis Software and Systems XVII* **394**, 505.

Storey, P.J. and Hummer, D.G.: 1995, *Monthly Notices of the Royal Astronomical Society* **272**, 41.

Strüder, L., Briel, U., Dennerl, K., Hartmann, R., Kendziorra, E., Meidinger, N., Pfeffermann, E., Reppin, C., et al.: 2001, *Astron. Astroph.* **365**, L18.

Sulentic, J.W., Marziani, P., and Dultzin-Hacyan, D.: 2000, *Annual Review of Astronomy and Astrophysics* **38**, 521.

Szokoly, G.P., Bergeron, J., Hasinger, G., Lehmann, I., Kewley, L., Mainieri, V., Nonino, M., Rosati, P., et al.: 2004, *The Astrophysical Journal Supplement Series* **155**, 271.

Taylor, E.N., Franx, M., Brinchmann, J., van der Wel, A., and van Dokkum, P.G.: 2010, *Astrophys. J.* **722**, 1.

Tozzi, P., Gilli, R., Mainieri, V., Norman, C., Risaliti, G., Rosati, P., Bergeron, J., Borgani, S., et al.: 2006, *Astron. Astroph.* **451**, 457.

Tran, H.D., Miller, J.S., and Kay, L.E.: 1992, *Astrophys. J.* **397**, 452.

Treister, E., Urry, C.M., and Virani, S.: 2009, *Astrophys. J.* **696**, 110.

Tremonti, C.A., Heckman, T.M., Kauffmann, G., Brinchmann, J., Charlot, S., White, S.D.M., Seibert, M., Peng, E.W., et al.: 2004, *Astrophys. J.* **613**, 898.

Trippe, M.L., Crenshaw, D.M., Deo, R.P., Dietrich, M., Kraemer, S.B., Rafter, S.E., and Turner, T.J.: 2010, *Astrophys. J.* **725**, 1749.

Trump, J.R., Impey, C.D., McCarthy, P.J., Elvis, M., Huchra, J.P., Brusa, M., Hasinger, G., Schinnerer, E., et al.: 2007, *The Astrophysical Journal Supplement Series* **172**, 383.

Turner, M.J.L., Abbey, A., Arnaud, M., Balasini, M., Barbera, M., Belsole, E., Bennie, P.J., Bernard, J.P., et al.: 2001, *Astron. Astroph.* **365**, L27.

Turner, T.J. and Miller, L.: 2009, *Astronomy and Astrophysics Review* **17**, 47.

Ueda, Y., Akiyama, M., Ohta, K., and Miyaji, T.: 2003, *Astrophys. J.* **598**, 886.

Ulrich, M.-H., Maraschi, L., and Urry, C.M.: 1997, *Annual Review of Astronomy and Astrophysics* **35**, 445.

Urrutia, T., Becker, R.H., White, R.L., Glikman, E., Lacy, M., Hodge, J., and Gregg, M.D.: 2009, *Astrophys. J.* **698**, 1095.

Urry, C.M. and Padovani, P.: 1995, *Publications of the Astronomical Society of the Pacific* **107**, 803.

van Dokkum, P.G.: 2001, *Publications of the Astronomical Society of the Pacific* **113**, 1420.

Vasudevan, R.V., Mushotzky, R.F., Winter, L.M., and Fabian, A.C.: 2009, *Monthly Notices of the Royal Astronomical Society* **399**, 1553.

Verner E., Bruhweiler F., Johansson S., Peterson B., 2009, *Physica Scripta* **134**, 014006

Vernet, J., Dekker, H., D'Odorico, S., Kaper, L., Kjaergaard, P., Hammer, F., Randich, S., Zerbi, F., et al.: 2011, *Astron. Astroph.* **536**, A105.

Vitale, M., Mignoli, M., Cimatti, A., Lilly, S.J., Carollo, C.M., Contini, T., Kneib, J.-P., Le Fevre, O., et al.: 2013, *Astron. Astroph.* **556**, A11.

Véron-Cetty, M.P. and Véron, P.: 2000, *Astronomy and Astrophysics Review* **10**, 81.

Véron-Cetty, M.-P. and Véron, P.: 2001, *Astron. Astroph.* **374**, 92.

Watson, M.G., Schröder, A.C., Fyfe, D., Page, C.G., Lamer, G., Mateos, S., Pye, J., Sakano, M., et al.: 2009, *Astron. Astroph.* **493**, 339.

Weingartner, J.C. and Murray, N.: 2002, *Astrophys. J.* **580**, 88.

Whittle, M.: 1992, *The Astrophysical Journal Supplement Series* **79**, 49.

Wilkes, B.J., Schmidt, G.D., Cutri, R.M., Ghosh, H., Hines, D.C., Nelson, B., and Smith, P.S.: 2002, *Astrophys. J.* **564**, L65.

Wilkes, B.: 2004, *AGN Physics with the Sloan Digital Sky Survey* **311**, 37.

Willott, C.J., Albert, L., Arzoumanian, D., Bergeron, J., Crampton, D., Delorme, P., Hutchings, J.B., Omont, A., et al.: 2010, *The Astronomical Journal* **140**, 546.

Wilman, R.J. and Fabian, A.C.: 1999, *Monthly Notices of the Royal Astronomical Society* **309**, 862.

Winkler, H.: 1992, *Monthly Notices of the Royal Astronomical Society* **257**, 677.

Winter, L.M., Mushotzky, R.F., Tueller, J., and Markwardt, C.: 2008, *Astrophys. J.* **674**, 686.

Winter, L.M., Mushotzky, R.F., Reynolds, C.S., and Tueller, J.: 2009, *Astrophys. J.* **690**, 1322.

Winter, L.M., Mushotzky, R., Lewis, K., Veilleux, S., Koss, M., and Keeney, B.: 2010, *X-ray Astronomy 2009; Present Status, Multi-wavelength Approach and Future Perspectives*, 369.

Yang, G., Brandt, W.N., Luo, B., Xue, Y.Q., Bauer, F.E., Sun, M.Y., Kim, S., Schulze, S., et al.: 2016, *Astrophys. J.* **831**, 145.

Young, M., Elvis, M., and Risaliti, G.: 2008, *Astrophys. J.* **688**, 128-147.

Zafar, T., Møller, P., Watson, D., Fynbo, J.P.U., Krogager, J.-K., Zafar, N., Saturni, F.G., Geier, S., et al.: 2015, *Astron. Astroph.* **584**, A100.